4-9-2019 10:00 AM

Ultra-High Field Magnetic Resonance Imaging for Stereotactic Neurosurgery

Jonathan Lau, *The University of Western Ontario*

Supervisor: Peters, Terry M., *The University of Western Ontario*
Co-Supervisor: Khan, Ali R., *The University of Western Ontario*
A thesis submitted in partial fulfillment of the requirements for the Doctor of Philosophy degree in Biomedical Engineering

Recommended Citation

Lau, Jonathan, "Ultra-High Field Magnetic Resonance Imaging for Stereotactic Neurosurgery" (2019). *Electronic Thesis and Dissertation Repository*. 6194.
https://ir.lib.uwo.ca/etd/6194

Abstract

Stereotactic neurosurgery is a subspecialty within neurosurgery concerned with accurate targeting of brain structures. Deep brain stimulation (DBS) is a specific type of stereotaxy in which electrodes are implanted in deep brain structures. It has proven therapeutic efficacy in Parkinson's disease and Essential Tremor, but with an expanding number of indications under evaluation including Alzheimer's disease, depression, epilepsy, and obesity, many more Canadians with chronic health conditions may benefit. Accurate surgical targeting is crucial with millimeter deviations resulting in unwanted side effects including muscle contractions, or worse, vessel injury. Lack of adequate visualization of surgical targets with conventional lower field strengths (1.5/3 Tesla) has meant that standard-of-care surgical treatment has relied on indirect targeting using standardized landmarks to find a correspondence with a histological "template" of the brain. For this reason, these procedures routinely require awake testing and microelectrode recording, which increases operating room time, patient discomfort, and risk of complications. Advances in ultra-high field (≥ 7 Tesla or 7T) imaging have important potential implications for targeting structures enabling better visualization as a result of its increased (sub-millimeter) spatial resolution, tissue contrast, and signal-to-noise ratio. The work in this thesis explores ways in which ultra-high field magnetic resonance imaging can be integrated into the practice of stereotactic neurosurgery. In Chapter 2, an ultra-high field MRI template is integrated into the surgical workflow to assist with planning for deep brain stimulation surgery cases. Chapter 3 describes a novel anatomical fiducial placement protocol that is developed, validated, and used prospectively to quantify the limits of template-assisted surgical planning. In Chapter 4, geometric distortions at 7T that may impede the ability to perform accurate surgical targeting are characterized in participant data, and generally noted to be away from areas of interest for stereotactic targeting. Finally, Chapter 5 discusses a number of important stereotactic targets that are directly visualized and described for the first time *in vivo*, paving the way for patient-specific surgical planning using ultra-high field MRI.

Keywords: accuracy, deep brain stimulation, magnetic resonance imaging, neuromodulation, stereotactic neurosurgery, surgical planning.

Tools used by the surgeon must be adapted
to the task and where the human brain is
concerned, no tool can be too refined.
– LARS LEKSELL

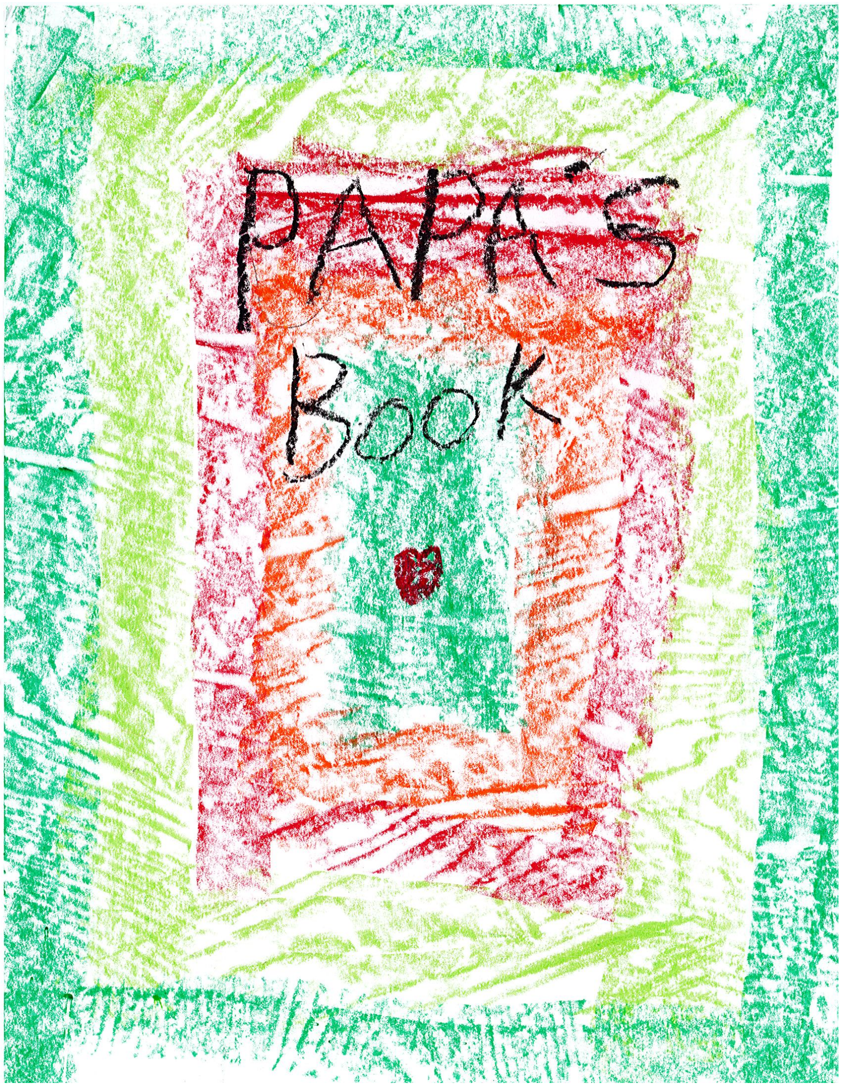
PAPA'S
BOOK

Acknowledgments

I would like to thank Terry and Ali for their academic mentorship. I had no intention of embarking on further academic training, but happened to fall in with the perfect people to make this pursuit worthwhile. The academic environment at Robarts Research Institute is truly one of a kind allowing active engagement between clinicians and researchers. In particular, I would like to thank Goli Ameri, Jordan DeKraker, Pierre Jannin (who came to visit on his sabbatical), Jonathan McLeod, John Moore, and Yiming Xiao for many helpful discussions. Thanks must also go to the many students who participated in the anatomical fiducials project and encouraged me to develop it as a tool for teaching anatomy.

My research on ultra-high field MRI would not have been possible without the tremendous support from colleagues at the Centre for Functional and Metabolic Mapping. Specifically, thanks must go to Ravi Menon, Joe Gati, and Trevor Szekeres.

Thanks to my colleagues and mentors in the Department of Clinical Neurological Sciences for encouraging me to pursue further academic training and providing time and initial salaried support, which enabled me to successfully obtain my own independent funding. In particular, I would like to thank Joe Megyesi for his advice and providing an opportunity to help mentor students on our many research collaborations together. I would like to acknowledge Greydon Gilmore for his incessant enthusiasm about data informatics and deep brain stimulation. I must also thank Andy Parrent, Keith MacDougall, David Steven, and Jorge Burneo for keeping my research questions grounded and encouraging me to obtain the skills necessary to become a successful clinician researcher.

Last, but definitely not least, thank you to my family! Mom and Dad: I am grateful to you for teaching me to have the curiosity and resilience to succeed, and always reminding me about the importance of enjoying the process. Alison: I am so lucky to have a professional editor in the family (and the best sister). Hélène, Charlotte, and Oscar: I love you! Thank you for your support and understanding through it all.

Co-Authorship Statement

Chapter 1:

J. C. Lau — sole author

Chapter 2:

J. C. Lau — study design, software development, data collection, wrote manuscript

M. F. Arango — reviewed manuscript

K. W. MacDougall, A. G. Parrent, Terry M. Peters — study design, reviewed manuscript

A. R. Khan — study design, software development, reviewed manuscript

Chapter 3:

J. C. Lau — developed protocol, study design, software development, validation, data collection, statistical analysis, wrote manuscript

A. G. Parrent — developed protocol, study design, reviewed manuscript

J. Demarco, G. Gupta, P. J. Park, K. Ferko — data collection, reviewed manuscript

A. R. Khan, T. M. Peters — study design, reviewed manuscript

Chapter 4:

J. C. Lau — study design, software development, validation, data collection, statistical analysis, wrote manuscript

T. Y. Zeng — validation, reviewed manuscript

K. W. MacDougall, A. G. Parrent — reviewed manuscript

A. R. Khan, T. M. Peters — study design, reviewed manuscript

Chapter 5:

J. C. Lau — study design, software development, data collection, statistical analysis, wrote manuscript

A. G. Parrent, G. G. Gilmore, J. Demarco, K. W. MacDougall — study design, reviewed manuscript

C. Currie — data collection, reviewed manuscript

Y. Xiao — software development, reviewed manuscript

Chapter 6:

J. C. Lau — sole author

Contents

List of Figures

List of Tables

List of Abbreviations and Nomenclature

General Terminology

3D	three-dimensional
7T	seven Tesla
AC	anterior commissure
AC-PC	anterior-posterior commissure
AChA	anterior choroidal artery
al	ansa lenticularis
cZI	caudal zona incerta
CC	corpus callosum
CNR	contrast-to-noise ratio
CSF	cereberospinal fluid
DBS	deep brain stimulation
DRTT	dentatorubrothalamic tract
ET	essential tremor
fct	fasciculus cerebellothalamicus
fl	fasciculus lenticularis
FDR	false discovery rate
FLE	fiducial localization error
FRE	fiducial registration error
ft	fasciculus thalamicus
GM	gray matter
GPe	globus pallidus externus
GPi	globus pallidus internus
ICBM	International Consortium for Brain Mapping
IG	indusium griseum
IPF	interpeduncular fossa
lin	linear
LMS	lateral mesencephalic sulcus
LV	lateral ventricle
MB	mamillary bodies
MER	microelectrode recording
MMSE	mini-mental state examination
MNI	Montreal Neurological Institute
MPTP	1-methyl-4-phenyl-1,2,3,6-tetrahydropyridine
nlin	nonlinear
OR	operating room
PC	posterior commissure
PD	Parkinson's disease
PMJ	pontomesencephalic junction
PSA	posterior subthalamic area

General Terminology (Continued)

raprl	prelemniscal radiations
RN	red nucleus
ROI	region-of-interest
rZI	rostral zona incerta
SNpc	substantia nigra pars compacta
SNpr	substantia nigra pars reticulata
SNR	signal-to-noise ratio
STN	subthalamic nucleus
UHF	ultra-high field
VIM	ventral intermediate nucleus of the thalamus
VLp	ventrolateral posterior nucleus of the thalamus
VPL	ventral posterolateral nucleus of the thalamus
WM	white matter
ZI	zona incerta

Medical Imaging Terminology

BIDS	Brain Imaging Data Structure
CT	computed tomography
DICOM	Digital Imaging and Communications in Medicine
DTI	diffusion tensor imaging
FA	fractional anisotropy
HCP	Human Connectome Project
MD	mean diffusivity
MPRAGE	magnetization prepared rapid acquisition gradient echoes
MP2RAGE	magnetization prepared 2 rapid acquisition gradient echoes
MRI	magnetic resonance imaging
NIfTI	Neuroimaging Informatics Technology Initiative
NMR	nuclear magnetic resonance
PAT	parallel acceleration technique
PD	proton density
RF	radiofrequency
SA2RAGE	saturation- prepared with 2 rapid gradient echoes
SPACE	Sampling Perfection with Application-optimized Contrasts by using different flip angle
QMRI	quantitative MRI
QSM	quantitative susceptibility mapping
T1w	T1-weighted
T2w	T2-weighted
TE	echo time
TI	inversion time
TR	repetition time
TSE	turbo spin echo

Terms Introduced by this Thesis

AFID	anatomical fiducial
AFLE	anatomical fiducial localization error
AFRE	anatomical fiducial registration error

Chapter 1

Introduction

Neurological disorders represent the predominant contributor to the global burden of disease [Feigin et al., 2017]. For the vast majority of these diseases, effective treatments have unfortunately remained elusive. Neuromodulatory therapy is broadly aimed at providing treatments that improve upon quality of life by either overriding or compensating for pathological activity. The need for improved treatments is paramount particularly with an aging population.

Stereotactic neurosurgery is a subspecialty within the practice of neurosurgery concerned with accurate targeting of brain structures for diagnostic and therapeutic purposes. The word *stereotaxy* is derived from the Greek words "stereos-", for *three-dimensional* (3D), and "-taxy", for *arrangement*[1] first used by Horsley and Clarke in 1908 [Horsley and Clarke, 1908]. The pioneering work of Leksell and others has resulted in focal surgical treatment options for previously intractable disorders, such as essential tremor and Parkinson's disease [Spiegel et al., 1947, Leksell, 1949, Peters, 2006]. While the mechanical techniques used to accurately target regions with millimetric accuracy have improved relatively modestly in the intervening half century, a variety of neuromodulatory technologies such as biocompatible implanted electrodes and drug delivery systems have since been developed and are available as part of the stereotactic surgeon's armamentarium. Concurrent developments in noninvasive imaging are leading to increasingly robust biomarkers of anatomical and functional substrates of disease that may represent putative therapeutic targets for a wide range of neurodegenerative and chronic illnesses.

This dissertation explores a gap in stereotaxy, namely the continued reliance by neurosurgeons on histological spatial references rather than patient-specific imaging, and presents novel techniques using magnetic resonance imaging (MRI), specifically in the use of high-field images, validation of the correspondence between images, and high-resolution methods to visualize structures not previously seen *in vivo*.

In this introductory chapter, stereotactic neurosurgery is reviewed from the initial stages of development to present day. The impact of the invention of novel non-invasive imaging methods, i.e. magnetic resonance imaging (MRI), on the practice of stereotaxy is reviewed. Recent MRI advancements, specifically ultra-high field imaging and quantitative MRI, are explored in detail as well as implications of these developments on improving therapeutic targeting of brain structures.

1.1 Stereotactic Neurosurgery

Invention and innovation have been central to the evolution of the field of stereotactic neurosurgery, leading to increasingly safer and accurate surgical targeting of brain regions. The history of stereotaxy began in the late 19th century (see [Peters, 2001, Grunert et al., 2003, Peters,

---

[1] Contemporary use of the word "stereotactic" may actually have mixed origins, "tactus" being Latin for *touch*.

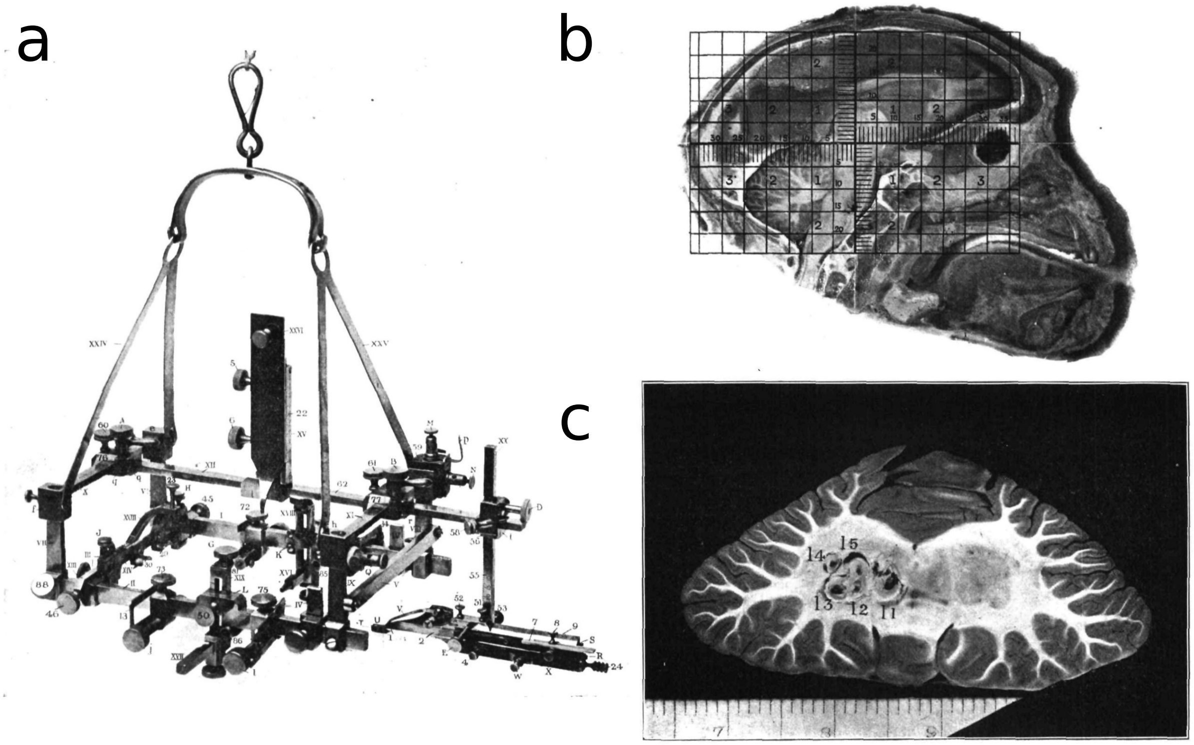

Figure 1.1: The pioneering work of Victor Horsley and Robert Clarke who coined the term "stereotaxy" and proposed a system involving the combination of (a) a mechanical frame with (b) a histological reference space using frozen sections for (c) electrolytic study of the deep cerebellar nuclei [Horsley and Clarke, 1908].

2006, Gildenberg and Krauss, 2009] for reviews on this topic). The first attempts at mechanical localization were reported by Russian physician, D. N. Zernov, who invented a device called an "encephalometer" for localizing brain structures based on skull landmarks [Kandel and Shchavinskii, 1973, Blomstedt et al., 2007, Gildenberg and Krauss, 2009]. This work was further extended by his student N. V. Altukhov for targeting deeper structures including the basal ganglia [Grunert et al., 2003, Gildenberg and Krauss, 2009]. However, it was Victor Horsley and Robert Clarke who were the true pioneers and coined the term "stereotaxy" in 1908, reporting the development of a surgical apparatus for targeting of the deep cerebellar nuclei in experimental animals [Horsley and Clarke, 1908] (Figure 1.1). The frame of this instrument was designed to be rigidly fixed to the cranium allowing for the description of points within the frame based on 3D Cartesian (x,y,z) coordinates. Concurrent with this physical apparatus, Clarke and Horsley devised a brain atlas from histological sections, providing a mapping between the subject under investigation and a prepared cadaveric specimen (Figure 1.1; covered in Section 1.1.2). While Clarke and Horsley alluded to the use of the apparatus in humans, it was not until 1947 that Ernest Spiegel and Henry Wycis reported the first human device, which they called the Model V [Spiegel et al., 1947]. After visiting Spiegel, Lars Leksell developed a significant modification by introducing the first "centre-of-arc" based system (Figure 1.2) [Leksell, 1949, Meyerson and Linderoth, 2009]. The stereotactic methodology was further refined in Paris by Jean Talairach [Talairach et al., 1957] into a meticulous system integrated with collinear x-ray pneumoencephalography and cerebral angiography, allowing precise *réperage direct* (direct investigation) [Gildenberg and Krauss, 2009, Bancaud et al., 1965].

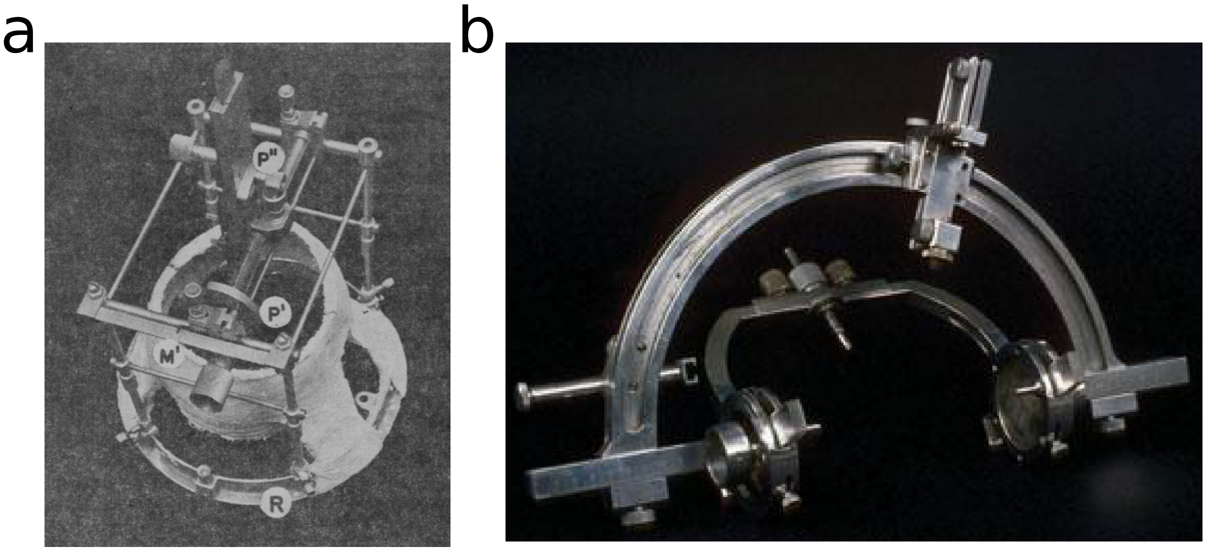

Figure 1.2: Stereotactic equipment in humans. (a) The Model V instrument of Spiegel and Wycis introduced in 1947 requiring plaster casting as a means to fix the frame to the head. (b) The first "centre-of-arc" system invented by Lars Leksell in 1949.

1.1.1 Early Indications and Treatment Modalities

While the indications for stereotaxy are growing, here we focus on two classic neurological disorders: Parkinson's disease (PD) and essential tremor (ET). Parkinson's disease, which was first described by James Parkinson [Parkinson, 2002] as the "shaking palsy" or paralysis agitans in 1817, is characterised by a number of involuntary clinical manifestations including resting tremor, stiffness of motor movements (also called rigidity), slowed movements (bradykinesia), and postural imbalance (or instability). Essential tremor is a common disorder affecting up to 5% of patients older than 60 characterized by appendicular (arms or legs) or axial tremor typically action-related and occurring in the 6-8 Hz range. Despite best medical management, this disorder can remain debilitating in around half of patients (Figure 1.3) [Hallett, 2014].

Preceding the development of good pharmacological treatments, clinicians explored surgical therapy as an option for their patients. However, as Gildenberg notes in his historical review [Gildenberg and Krauss, 2009], the consideration of surgical therapy of the basal ganglia was

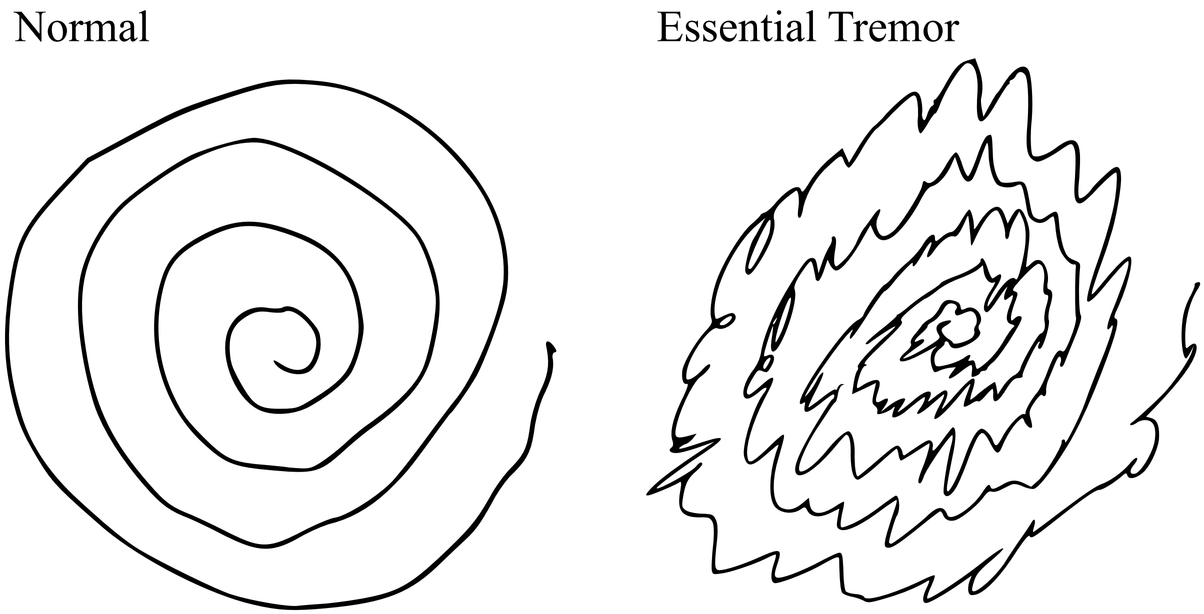

Figure 1.3: Spiral drawing under normal conditions and for a patient with essential tremor.

initially stalled due to the influential opinion of pioneering neurosurgeon, Walter Dandy, who contended that "basal ganglia resections were universally lethal" and who considered the caudate nucleus the "seat of consciousness" [Dandy, 1946, Gildenberg and Krauss, 2009].

Eventually, these views were challenged by a few surgeons who developed open neurosurgical approaches to the deep brain. Russell Meyers began performing surgical procedures in the caudate nucleus with modest benefit [Meyers, 1951a] without the mortality previously reported by Dandy. He went on to develop surgical approaches to the basal ganglia facilitating interruptions of connections, including open approaches to resection of the fiber connections in the deep nuclei [Meyers, 1951b]. Irving Cooper was credited with accidentally discovering that ligation of the anterior choroidal artery (AChA) [Cooper, 1953] resulted in relief of Parkinsonism in a few patients, and went on to produce a larger series where he intentionally ligated the AChA and while some good effect was achieved, observed that unfortunately a subset of patients became either transiently or permanently hemiplegic [Cooper, 1960]. Further investigation revealed that the arterial distribution of the AChA was non-specific to Parkinsonism and not uncommonly supplied blood to important regions including the posterior limb of the internal capsule along the corticospinal tract. These findings resulted in a shift in interest from vascular to parenchymal targeting, with a specific focus on investigating the specific role of deep structures perfused by the AChA. Overall these reports resulted in an understanding that the interruption and disruption of specific deep brain regions could provide effective treatment for movement disorders.

These discoveries using open neurosurgical techniques enabled Spiegel and Wycis, with their innovations in stereotactic instrumentation, to propose the use of more targeted approaches to the region. In this context, the first reported stereotactic case, a thalamotomy of the medial nucleus of the thalamus was successfully performed by Spiegel and Wycis [Spiegel et al., 1947, Grunert et al., 2003]. The first successful treatments of Parkinson's disease via stereotactic surgery were performed in the 1950's [Narabayashi and Okuma, 1953, Guiot and Brion, 1953, Spiegel and Wycis, 1954, Svennilson et al., 1960, Laitinen et al., 1992]. Cooper began to use more focal treatments, experimenting with different methods for ablation, and played an important role in the development of chemoablation and cryoablation [Cooper, 1960]. Multiple different targets were being explored for ablative (radiofrequency) treatment of Parkinson's disease and debilitating tremor including the posterior ventrolateral area of the thalamus (VLp), globus pallidus internus (GPi), and subthalamic nucleus [Andy et al., 1963, Mundinger, 1965, Houdart et al., 1966, Velasco et al., 1972].

With two exceptions, further technical developments in physical devices for stereotactic treatment were relatively modest until recently. First, Lars Leksell developed an arc-based frame enabling a physical system whereby Cartesian and polar coordinates could be combined (**??**b). The arc frame simplified the process of determining the trajectory. Once a target location was determined, the trajectory location could be optimized by manipulating the ring and arc angles with the target remaining centered. Second, the invention of frameless computer-aided navigation systems [Kelly et al., 1986] revolutionized standard cranial surgery for the localization of intracranial lesions (e.g. tumours), which are now routinely used in clinical practice. Please see [Peters, 2001, Grunert et al., 2003, Peters, 2006] for more details on the development of stereotaxy.

1.1.2 Brain Atlases

Brain atlases are a fundamental aspect of stereotactic neurosurgery, and central to the focus of this thesis. The practice of stereotaxy can be considered analogous to geographical exploration and the reliance on a topographic atlas or map. One key distinction must be made between what constitutes a *template* versus an *atlas*. A template refers to the brain section, or raw image data prepared in a way that can be described in terms of spatial coordinates, while an *atlas* refers to an overlay or annotation of the structures in the template. The choice of "reference space" can impact the accuracy of surgical targeting. However, while taking a wrong turn due an inaccurate map can often be compensated for, a deviation from the expected path in a stereotactic procedure could represent the difference between optimal therapy and a devastating complication for the patient. In the following section, we discuss the development of brain atlases leading to the present day.

When neurosurgeons first began considering therapy for deep brain structures, they relied on knowledge from cadaveric specimens and sections [Horsley and Clarke, 1908, Spiegel et al., 1947, Talairach et al., 1957]. A template brain specimen was developed in parallel with the Horsley and Clarke instrument, consisting of glass-mounted frozen sections from a *Macaca mulatta* (rhesus macaque) specimen [Horsley and Clarke, 1908] (Figure 1.1). Several decades later, these same principles were used to devise a brain template for humans [Spiegel et al., 1947]. These post-mortem brain atlases continued to evolve with two of the most commonly referenced stereotactic atlases being created by Jean Talairach [Talairach et al., 1957] and Schaltenbrand and Wahren [Schaltenbrand and Wahren, 1977].

Computing the correspondence between an external template and the patient or subject is central to the process of atlas-assisted sterotaxy. Without access to other resources, these decisions were originally made by inferring the location of structures based on external cranial landmarks [Grunert et al., 2003]. Talairach appreciated that external cranial landmarks were unreliable for describing the location of structures within the cranial vault employing intra-operative adjuncts such as x-ray and more specifically ventriculographic and angiographic techniques to provide internal references for correspondence, a process which he referred to as a *réperage indirect* [Talairach et al., 1957]. Ventriculographic studies allowed for alignment based on observed features in both the template and patient images. To establish correspondence between the postmortem brain and the patient under investigation, Talairach observed that several salient features could be visible on ventriculographic studies, specifically, the *anterior commissure* (AC) and *posterior commissure* (PC), two dense white matter tracts connecting the hemispheres. Talairach's *réperage* procedure was refined over time into a more comprehensive system for alignment of individual patient datasets with a template space through a series of axes-specific scaling steps, since referred to as the *Talairach proportional grid normalization* [Talairach et al., 1957, Talairach and Tournoux, 1988, Brett et al., 2002]. Under this process, each subject was brought into alignment using first an AC-PC transformation followed by scaling in the standard cardinal (x,y,z) directions relative to AC-PC. This would be considered a 9 degree-of-freedom transformation (consisting of 3 degrees for translation, 3 for rotation, and 3 for scaling). It became possible to thus relate different anatomical labels onto the Talairach template.

Atlas representations have continued to evolve and the process, increasingly refined. Talairach's initial template had several limitations: it was devised from a single subject (a 60 year-old female) and also the left and right hemispheres had to be sectioned in two different orientations (one axial and the other coronal). Symmetry between hemispheres was thus a necessary assumption. Another commonly used atlas developed by Schaltenbrand and Wahren [Schaltenbrand and Wahren, 1977] used three separate brains cut in each of the standard cardinal planes. To prepare the transparent atlas overlays, 10 brains were used in the preparation of the coronal overlays, 13 sagittal, and 7 transverse [Schaltenbrand and Wahren, 1977]. The spatial correspondence between the same structures (particularly thalamic nuclei) in the different orientations has been reported to be poor [Niemann and Van Nieuwenhofen, 1999] as a result of inter-subject variability which is a confound in atlas-based studies. To complicate matters further, tears and processing artifacts (e.g. tissue distortions) were encountered and required substitution with additional brain sections, which in total amounted to 111 brains being used in the preparation of the atlas [Schaltenbrand and Wahren, 1977]. Finally despite high detail in the plane of the sections, individual sections were variably spaced from between 0.5-1.5 mm presenting some problems to their use for accurate stereotactic targeting. The process of improving the correspondence between the atlas and subject or template continues to be refined [Brett et al., 2002, Amunts et al., 2014]. How the correspondence between templates and subject datasets can be quantified, is the subject of study in Chapter 3 of this thesis.

1.1.3 The Importance of Imaging

The development of stereotaxy coincided with a number of important imaging innovations crucial to improving targeting accuracy. The discovery of x-rays and the development of x-ray imaging by Wilhelm Roentgen [Roentgen, 1895] followed by ventriculography [Dandy, 1918], and cerebral angiography by Egaz Moniz [Doby, 1992] enabled visualization of the patient's cranial anatomy, ventricles, and cerebral vasculature respectively. These innovations allowed for more accurate correspondence with histological atlases by permitting linear alignment of the atlas to these anatomical features [Spiegel et al., 1947]. The ability to see the cerebral vessels also enabled Talairach's *réperage* [Talairach et al., 1957], and to directly avoid vessels seen on angiograms [Talairach et al., 1957, Bancaud et al., 1965]. Calcification of the pineal gland could also be used as an internal reference frame for anatomy, and was used, as such, for the first successful thalamotomy [Spiegel et al., 1947, Grunert et al., 2003]. Targeting of specific parenchymal regions remained elusive with x-ray technology since, compared to bone or contrast-enhanced regions, x-ray contrast between different soft tissues is very low, and thus these tissues still had to be targeted using indirect methods based on atlas correspondence.

1.1.4 Deep Brain Stimulation

Over the last several decades, deep brain stimulation (DBS) has become established as an effective and *reversible* means of providing focal surgical therapy for patients with movement disorders [The Deep-Brain Stimulation for Parkinson's Disease Study Group, 2001, Hariz, 2017]. These efforts were driven in part by increased recognition of side effects of systemic pharmacotherapy for the treatment of movement disorders, namely levodopa for Parkinson's disease [Shoulson et al., 1975, Marsden and Parkes, 1976, Lees et al., 1977, Krack et al., 1999, Poewe, 2009, Williams et al., 2010], and thus renewed interest in other treatment options including surgery. DBS was pioneered by Alim Benabid [Benabid et al., 1988, Benabid et al., 1996], who demonstrated that high-frequency (> 100 Hz) electrical stimulation applied to specific deep brain targets could be effective for treating motor symptoms, coinciding with new insights into the basal ganglia circuitry (Figure 1.4) derived from microelectrode recordings of primate PD models by Mahlon Delong and colleagues [Bergman et al., 1990, DeLong, 1990]. Neuromodulatory therapy to specific basal ganglia targets such as the globus pallidus and subthalamic nucleus (STN) were being explored as candidate regions for focal electrical stimulation [Poewe, 2009].

Benabid reported on the efficacy of DBS of the STN region in 1993 [Pollak et al., 1993, Benabid et al., 1994, Limousin et al., 1995]. For Parkinson's disease, DBS allows reduction of dopaminergic therapy [Deuschl et al., 2006], thus decreasing drug-induced motor symptoms like dyskinesia, while enabling more consistent efficacy and minimization of on/off fluctuations [Tomlinson et al., 2010, Okun, 2012]. A recent cost-analysis reported that DBS may be associated with lower medical costs at follow-up due to reductions in the long-term need of polypharmacy ($65K over 10 years in the United States) [Hacker et al., 2016]. These findings have also motivated earlier intervention in PD patients with demonstration of superiority to medical therapy with respect to motor symptoms, quality of life, and levodopa-related dyskinesias [Schuepbach et al., 2013], as well as evidence for decreased medication costs [Hacker et al., 2016].

Benabid also proposed the use of DBS for the treatment of medically refractory essential tremor (ET), specifically suggesting the ventralis intermedius (VIM) nucleus as the target, which is also known as the ventrolateral posterior (VLp) nucleus[2] [Benabid et al., 1988, Benabid et al., 1991]. Microelectrode recordings (MER) studies have revealed that neurons in the VIM are synchronous with tremor in the contralateral extremity, and as such believed to play a crucial role in tremor modulation [Narabayashi, 1986]. Other groups have found success with stimulation of other regions including the caudal zona incerta (cZI) within the posterior subthalamic area [Plaha et al., 2006, Blomstedt et al., 2007, Fiechter et al., 2017, Nowacki et al., 2018], based on previous lesional work from Spiegel [Spiegel et al., 1964] and Mundinger [Mundinger, 1965, Mohadjer et al., 1990]. Studies have suggested that the cZI may require comparatively reduced amplitude of stimulation to achieve a therapeutic benefit [Blomstedt et al., 2010], which may result in longer life of the stimulator battery, although this has not been evaluated as a randomized controlled trial. Nowadays, DBS is considered the first-line

---

[2] Not to be confused with the ventral posterolateral (VPL) or main somatosensory nucleus of the thalamus

surgical treatment option for patients with essential tremor, given it is a reversible treatment [Tasker et al., 1997, Pahwa et al., 1999, Schuurman et al., 2000, Pahwa et al., 2001].

The exact mechanism by which electrical stimulation works as therapy remains poorly understood. Early on, Benabid and colleagues posited that DBS induced “functional inhibition” of the target region [Benabid et al., 1988, Benabid et al., 1996]. Studies employing neuronal recording methods demonstrate evidence of neuronal suppression in the vicinity of the stimulation target [Kiss et al., 2002, Hamani et al., 2004], which may be mediated by alterations of the extracellular milieu, particularly increased potassium concentrations [Shin et al., 2007, Florence et al., 2016]. Beyond local suppression, evidence suggests more far-reaching interactions with projected regions [Anderson et al., 2004, Miocinovic et al., 2006, Shimamoto et al., 2013, Horn et al., 2017c]. At the level of the local field, these findings may manifest as changes in the oscillatory background activity and suppressed with stimulation, which have been observed in the beta (12-30 Hz) range in patients with PD [Kuhn et al., 2008] and at the tremor frequency (6-8 Hz), a concept referred to as thalamocortical dysrhythmia [Gallay et al., 2008], in patients with ET [Hua and Lenz, 2005, Raethjen and Deuschl, 2012, Hallett, 2014, Hariz and Blomstedt, 2017]. Overall, high-frequency DBS likely involves a dynamic interplay between inhibitory and excitatory mechanisms at both the local and network levels, and also involving a range of time scales of clinical effect from immediate (for tremor) to long-term (weeks to months) for obsessive compulsive disorder and refractory depression (see [Herrington et al., 2016] for a recent review).

1.1.5 Conventional Approaches for Stereotactic Targeting

The work by Delong and colleagues elucidated clear functional roles in different pathways of the basal ganglia and how dysfunction within this circuit could produce symptoms like Parkinson’s disease [Bergman et al., 1990, DeLong, 1990, Poewe, 2009]. Delong studied experimental models of PD (1-methyl-4-phenyl-1,2,3,6-tetrahydropyridine; MPTP) investigating neuronal activity in these deep circuits using microelectrode recordings. Coupled with the routine use of awake MER by Benabid and colleagues, with few exceptions, MER has remained a central component of DBS procedures. Awake MER surgery has been central to DBS surgery and the origins of how the technique was discovered. However, use of MER results in increased operating room time, patient discomfort, and risk of complications [Zrinzo et al., 2012]. Systematic reviews have identified that MER results in a higher hemorrhage rate [Zrinzo et al., 2012].

Side effects include pyramidal effects (stimulation-locked clonic movements), dysarthrophonia, cognitive, behavioural side effects [Krack et al., 2002, Lambert et al., 2012], eye devi-

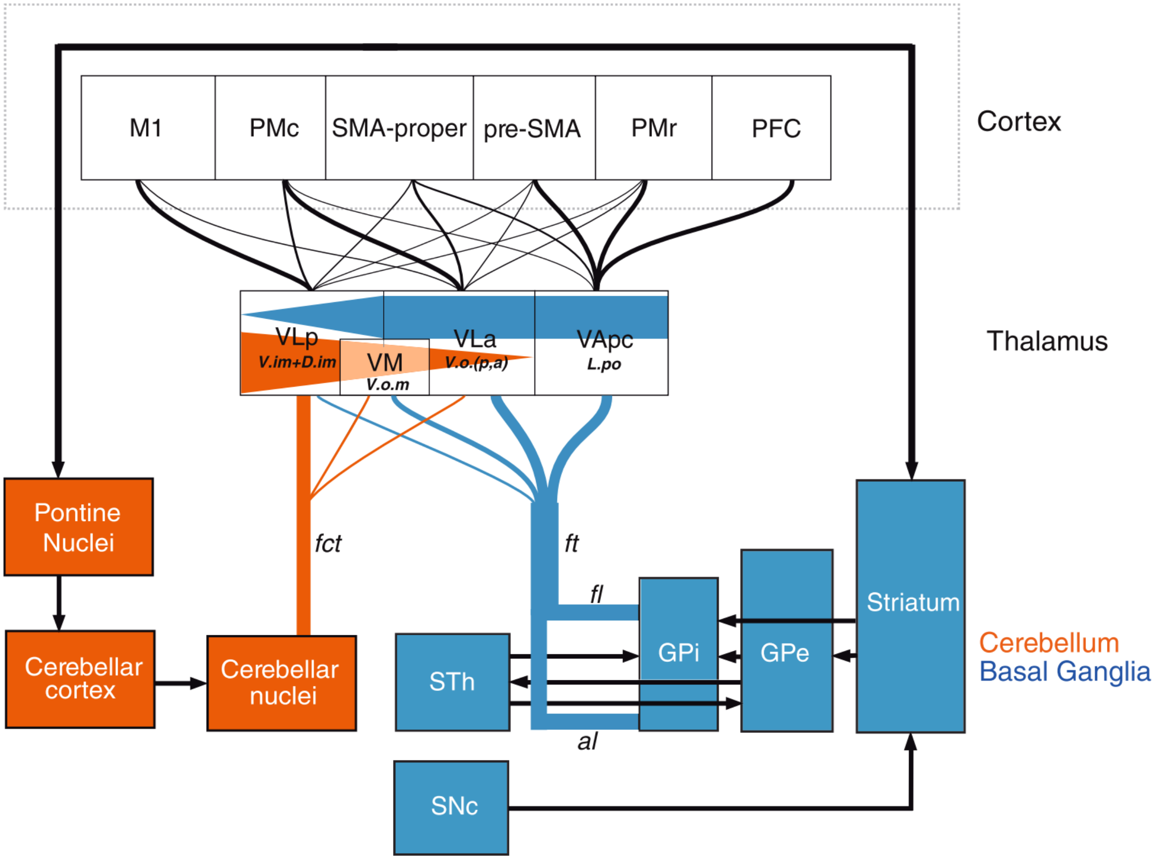

Figure 1.4: Schematic of the cerebellothalamocortical and pallidothalamocortical circuits based on tract-tracing studies in primates [Gallay et al., 2008]. All major cerebellar, basal ganglia, and cortical regions are represented. M1 = primary motor cortex; PMc = caudal premotor ; SMA = supplementary motor area; PMr = rostral premotor; PFC = prefrontal cortex; VLp = ventrolateral posterior thalamus; VM = ventral medial nucleus; VLa = ventrolateral anterior; VApc = ventral anterior parvocellular division; fct = fasciculus cerebellothalamicus; ft = fasciculus thalamicus; fl = fasciculus lenticularis; al = ansa lenticularis; STh = subthalamic nucleus; SNc = substantia nigra pars compacta; GPi = globus pallidus internus; GPe = globus pallidus externus.

ation [Shields et al., 2007], and speech effects [Tripoliti et al., 2008, Åström et al., 2010]. In 2000, Hariz first reported an increased risk of complications in those with pre-existing speech and cognitive decline [Hariz et al., 2000, Hariz, 2017]. Beyond complication avoidance, all these factors motivate the need for better ways of optimizing the target location [Delong and Wichmann, 2012], for which improving the quality of pre-operative patient imaging has been crucial.

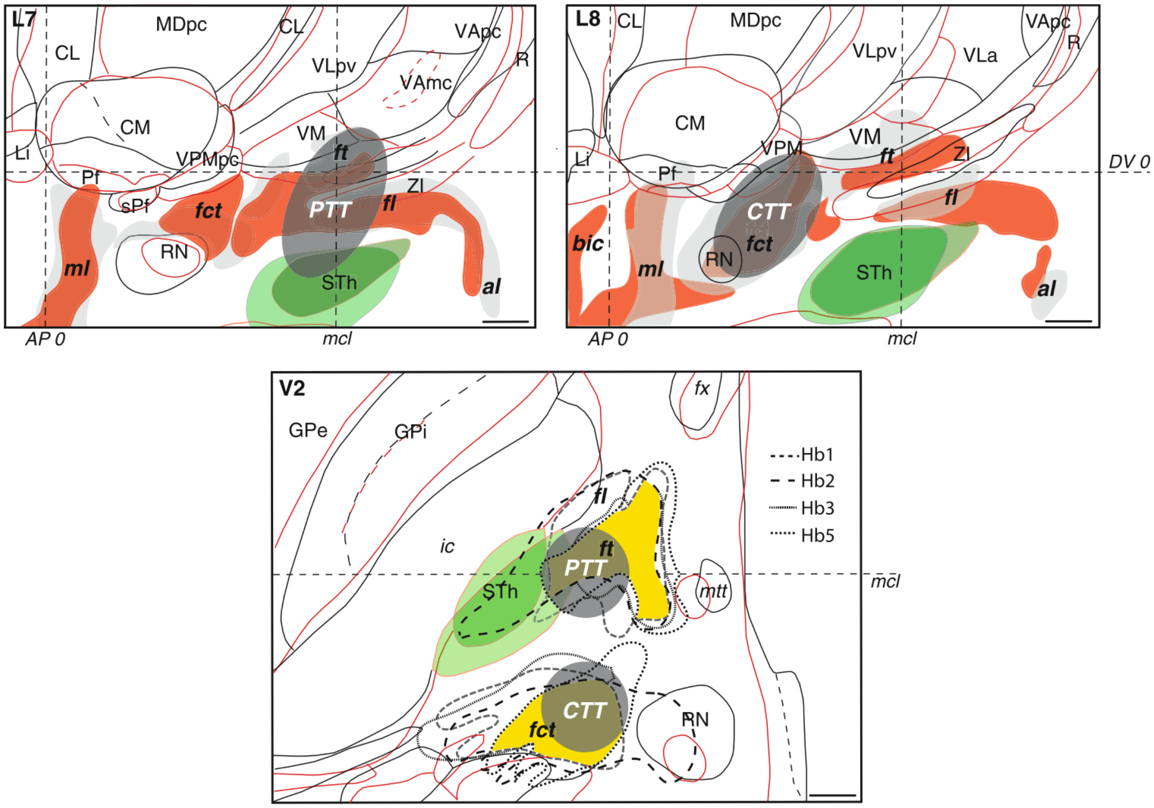

Figure 1.5: Demonstration of the intersubject variability in the location of anatomical structures of the deep brain and specifically the subthalamic region. The upper subfigures represent sagittal sections of the brain from two different cadavers (Hb1 is shown with red outlines and filled shapes while Hb2 is shown with black outlines and light gray filling). The lower subfigure demonstrates variability in the locations for four specimens (Hb1, Hb2, Hb3, Hb5). PTT = pallidothalamic tractotomy. CTT = cerebellothalamic tractotomy. Figure taken from the open access article by [Gallay et al., 2008].

1.2 Magnetic Resonance Imaging

The development of MRI began with nuclear magnetic resonance (NMR) when two researchers Felix Bloch and Edward Purcell independently discovered that they could “listen” to atonic nuclei [Bloch, 1946, Purcell et al., 1946]. Further developments were related to the idea that the magnetic field of a sample could be manipulated by applying an external electromagnetic field [Ernst et al., 1987], termed “pulsed NMR” and eventually the suggestion by Richard Ernst that encoding of space within a sample was possible using frequency and phase [Ernst and Anderson, 1966]. These discoveries formed a foundation by which Paul Lauterbur and Peter Mansfield could independently describe magnetic resonance imaging (MRI) [Mansfield and Grannell, 1973, Lauterbur, 1973, Mansfield, 1977]. Here we outline some of the important concepts necessary to provide context for the application of MRI to stereotactic neurosurgery.

1.2.1 Fundamentals of Magnetic Resonance Imaging

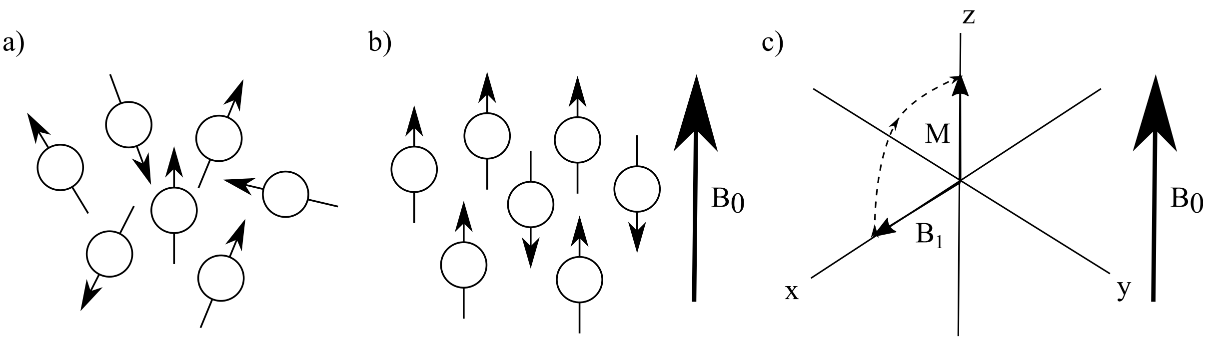

Figure 1.6: (a) Protons spinning in free space, (b) protons spinning under the influence of B_0, (c) A B_1 radiofrequency pulse tips the magnetization vector, $\vec{M}$ into the transverse plane and over time relaxes back to equilibrium in alignment with B_0 (rotating frame). The arrows in (a) and (b) refer to the magnetic moment of the spinning nuclei.

Nuclear magnetic resonance (NMR) is based on the absorption and emission of energy in the radiofrequency (MHz) range by atomic nuclei. Atoms with an odd number of protons or neutrons have a net spin or magnetic moment, μ, behaving, at a macroscopic level, like tiny magnets. The strength of the magnetic moment quantifies the strength of this magnetism. When placed under the influence of a static magnetic field (B_0), atoms with net spin align either parallel with or antiparallel to the field producing a net magnetization, $\vec{M}$ (Figure 1.6). This net magnetization is in the direction of B_0, which is conventionally known as the longitudinal, or $\vec{z}$, direction. There is no net magnetization in the transverse plane, i.e. in the $\vec{x}$ and $\vec{y}$ components, since the orientation of the spins is random in this plane and thus cancel out. Different nuclei precess at a predefined *frequency* (i.e. Hertz = Hz) for a given B_0, also known as the *Larmor frequency*:

$$f_0 = B_0 \times (\gamma/2\pi) \tag{1.1}$$

where $\gamma/2\pi$ is the gyromagnetic ratio, which is constant for a given atomic nucleus and magnetic field strength. For hydrogen nuclei, which in water make up the most abundant source measured in biological tissues, $\gamma/2\pi$ is 42.575 MHz/Tesla. The net magnetization at equilibrium, $\vec{M}_0$, under the influence of B_0 can be described by the following equation:

$$\vec{M}_0 = \frac{N_s \gamma^2 \hbar^2 \vec{B}_0}{4 k_B T} \tag{1.2}$$

where N_s is the number of spinning atomic nuclei, $\hbar$ is Planck's constant, k_B is Boltzmann's constant, and T is the temperature (in degrees K). Overall, this equation demonstrates that sensitivity to detection of NMR signal is dependent on having an abundance of detectable nuclei (i.e. protons in water) and a higher main magnetic field strength (see Section 1.2.2). Decreasing the temperature also has the effect of increasing net magnetization but is not feasible in living subjects.

When a radiofrequency (transmit) pulse (B_1) is applied at an angle relative to B_0 (classically perpendicular), the aligned nuclei are excited into a higher energy state (Figure 1.6c). Upon cessation of the pulse, the stimulated nuclei return to the equilibrium state (M_0) in alignment with the main magnet, a phenomenon known as *relaxation*, which is described by the Bloch equations:

$$\frac{d\vec{M}}{dt} = \vec{M} \times \gamma \vec{B} + \frac{M_x\vec{x} + M_y\vec{y}}{T_2} - \frac{(M_z - M_0)\vec{z}}{T_1} \tag{1.3}$$

where T_1 and T_2 relaxation times represent two independent processes that describe how the spins recover after the application of a radiofrequency (B_1) pulse to return to equilibrium (i.e. in alignment with B_0). More specifically, T_1 represents the longitudinal relaxation time constant for nuclei to recover to equilibrium and T_2 represents the transverse relaxation time constant for nuclei to dephase or decay to equilibrium. In an NMR experiment, this process of relaxation back to equilibrium can be recorded using radiofrequency receiver coils. T_1 and T_2 relaxation can be modeled as exponential curves with net magnetization in the component longitudinal (M_z) and transverse (M_{xy}) directions described using the following:

$$M_z(t) = M_z(0)(1 - e^{\frac{-t}{T_1}}) \tag{1.4}$$

$$M_{xy}(t) = M_{xy}(0)(e^{\frac{-t}{T_2}}) \tag{1.5}$$

noting that $M_z(0)$ is equivalent to M_0. Specifically, T_1 is defined as the length of time for M_0 to recover by a factor of $(1 - 1/e)$, where e is Euler's number, that is to 63.2% of its original value. T_2 is defined as the length of time for $M_{xy}(0)$ to decay to $1/e$, or 36.8% of its maximal value. Example relaxation curves are demonstrated in Figure 1.7.

A basic NMR experiment requires a static (B_0) field, transmit RF (B_1+) field, and receiver RF (B_1-) coil for detecting magnetic parameters in a test tube with a homogeneous sample. To produce images, gradient coils are a crucial additional element that allows encoding of information about two key properties of spinning atomic nuclei: *frequency* and *phase*. Coils are constructed that produce a spatially varying magnetic field by manipulating the frequency and phase of the atomic spins to be unique at every point in the scanned region by using frequency encoding (G_f) and phase encoding (G_ϕ) gradients, respectively. These magnetic manipulations occur at a much smaller scale than B_0 and are in the range of milli-Tesla per meter (mT/m). For a gradient G_x, the resonance frequency at each location can thus be expressed using a linear

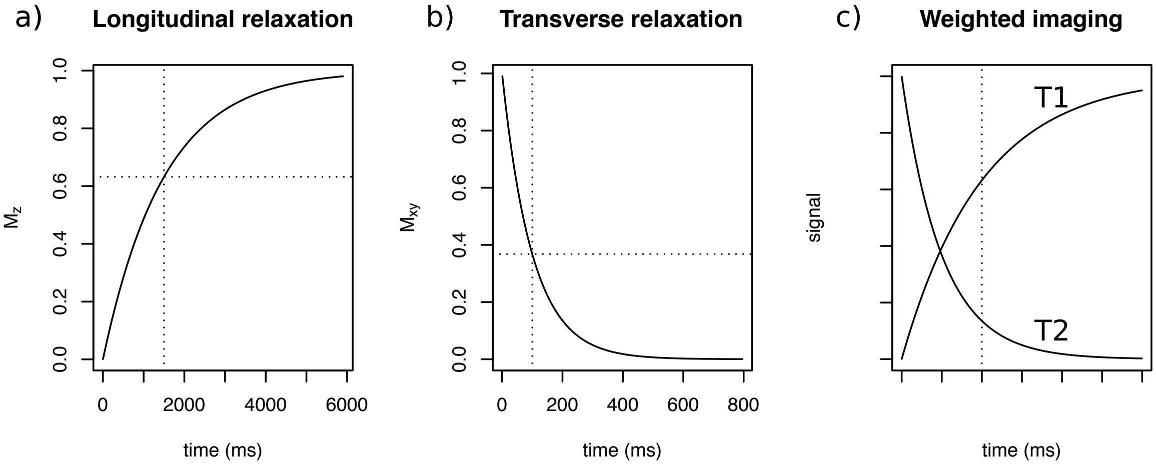

Figure 1.7: T_1 (a) and T_2 (b) relaxation can be modeled using exponential functions as demonstrated in Equations 1.4 and 1.5. The T_1 and T_2 relaxation times were set at 1500 ms and 50 ms respectively in these simulated examples (dashed lines). (c) Demonstration of how for a given echo time (marked by the dashed line) for recording, a mix of both T_1 and T_2-based signal is recorded, as is typical with conventional imaging methods.

equation:

$$\omega(x) = \omega_0 + \gamma G_x x \tag{1.6}$$

The faster and slower precession of atomic nuclei along this *gradient* is used to spatially encode information about local net magnetization and stored in Fourier space, also known as k-space. In k-space, information across the entire region of interest being scanned is summed together and represented in *spatial frequency* space. The frequency differences can be recovered from the raw signals recorded from the receiver RF using Fourier transformation to produce the images in magnetic resonance imaging (MRI). The interested reader is referred to the following references for a more thorough description of the theoretical and practical foundations of MRI and Fourier transformation [Nishimura, 1996, McRobbie et al., 2003]. Finally, there are inherent inhomogeneities introduced during the construction of gradient coils that can result in geometric distortion that is important to understand in the context of stereotactic neurosurgery. These issues are further explored in Chapter 4 as are other sources of MRI distortion.

1.2.2 Ultra-High Field MRI

Measuring signal from precessing nuclei is an inherently noisy process requiring sensors capable of detecting signal differences on the order of parts per million. As demonstrated in Equation 1.2, one way to increase sensitivity to magnetization is to increase B_0, which scales at least linearly with magnetic field strength. The increased signal can be exploited in different ways, permitting investigation of small structures in the deep brain to be imaged at higher resolution. Ultimately, going to higher main magnetic field strength presents an opportunity to improve *in vivo* visualization of putative stereotactic targets for neuromodulation.

As an exercise, we specifically consider the STN and the impact of resolution. The STN is one of the smaller deep brain nuclei and one of the key targets for Parkinson's disease, that has been better characterized over the the last few years. The volume of the STN as estimated from histological studies at 240 mm^3 with a maximal extent of $\sim$ 10 mm in the dorsolateral to ventromedial direction and containing approximately 560000 neurons, thus containing approximately 2300-2400 neurons within a 1 mm^3 voxel [Hardman et al., 2002, Hamani et al., 2004], the standard clinical resolution acquired for surgical planning. Increasing the resolution by 40% isotropically (i.e. reducing the voxel dimensions to 0.7 mm^3) results in an improvement in the overall number of voxels from 240 with 10 along the maximal extent to 700 voxels (almost 3-fold) with 15 voxels along the maximal extent. Estimates within a voxel also improve from 2300-2400 neurons to $\sim$ 800 neurons per voxel. The numbers are more drastic with improvements to 0.5 mm isotropic voxels, representing an 8-fold increase in number of STN voxels to 1920 with a 2-fold increase in a single dimension to 20 voxels along the maximal extent. Increasing B_0 permits an increase in signal that can be used to offset the increased noise associated with higher resolution imaging.

There are also smaller structures in the vicinity of the STN such as the fields of Forel and zona incerta that have not been reliably visualized *in vivo*, although they have historically been considered potential therapeutic targets. Spiegel and Wycis initially had proposed *ansotomy*, that is lesioning of the *ansa lenticularis*, and *campotomy*, that is lesioning of the *nuclei campi perizonalis* or Fields of Forel as a means of treating Parkinson's disease [Spiegel and Wycis, 1954, Spiegel et al., 1962, Spiegel et al., 1964]. Later, Mundinger and colleagues described lesioning of the cZI [Mundinger, 1965]. However, it is unclear how well the original pioneers of stereotaxy were able to accurately localize the location of their lesions. To our knowledge, no clear estimates of the size of the cZI or fields of Forel have been made using histology or MRI. Direct visualization of these structures at high-fields will be the subject of Chapter 5.

Moving to higher fields introduces many new challenges (see [Uğurbil, 2017] for review). Most directly, B_0 inhomogeneities increase with the static magnetic field strength inducing "phase accruals" that lead to distortion and signal loss particularly at tissue interfaces. Of particular concern, these spatial distortions could render the use of 7T impractical for surgical targeting purposes and is explored in detail in Chapter 4. An increase in B_0 also results in an increase in the resonance (Larmor) frequency and smaller wavelengths. The increased resonance frequency leads to higher attenuation and thus the need for higher B_1 intensity; that is, the RF transmit pulses need to be stronger to excite the atoms in an MR experiment. The excitation

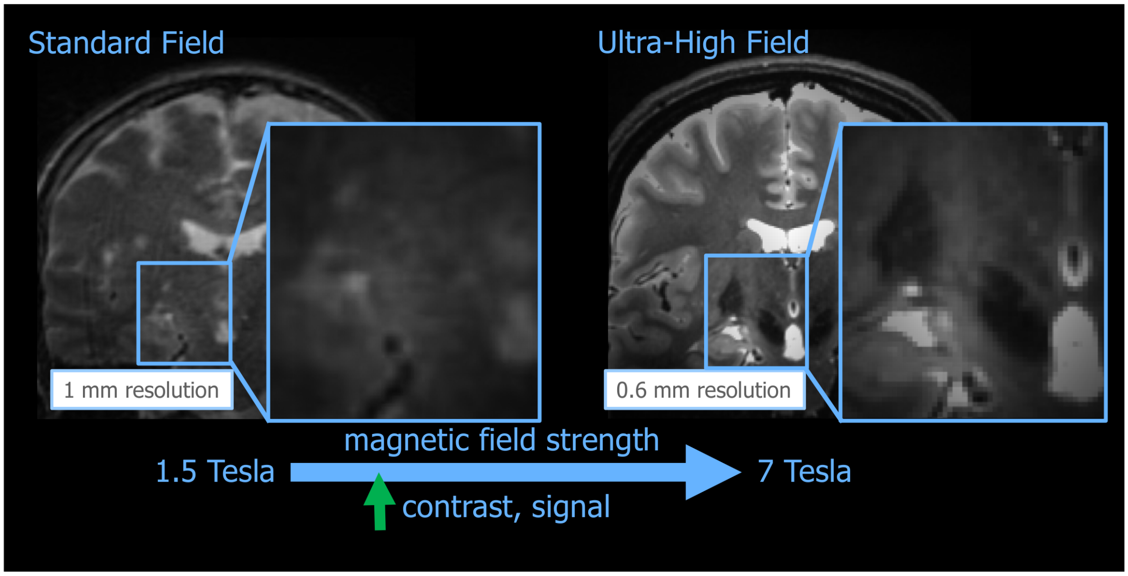

Figure 1.8: One way to increase sensitivity to magnetization (i.e. signal) is to increase B_0, which scales at least linearly with magnetic field strength. Selected T2-weighted coronal images taken at standard clinical field strength (1.5T) and at 7T demonstrating the improvement in image contrast in deep brain structures with an increase in B_0. The zoomed in regions demonstrate the increased detail in structures of the basal ganglia, specifically the pallidum, subthalamic nucleus, and substantia nigra.

angles transmitted to the entire volume, which in ideal circumstances are stable throughout, are inhomogeneous due to both the increased attenuation and standing wave effects. This results in variable intensities throughout the sample in the reconstructed image. Second, the strong RF pulse implies that there is an increase in the power deposited into the subject, which is regulated by the FDA by a measurement called the *specific absorption rate*. Finally, other features that can be perceived as advantages or disadvantages are the changes in the inherent relaxation parameters of different tissues. T_1 relaxation times increase with field strength, while T2 relaxation times shorten.

To date, all ultra-high field MRI systems are attached to academic institutions and require highly complex and specialized hardware in order to achieve optimal performance. The process to achieve this performance, the delays in imaging and complex decisions regarding hardware design are well-documented by Kamil Ugurbil in his recent commentary [Uğurbil, 2017]. While not standard with ultra-high field MRI systems, radiofrequency coil design innovations have been crucial for mitigating problems with B_1 inhomogeneity and SAR. Specifically, the development of parallel transmit (pTx) technology, that is the use of multichannel transmit coil elements rather than a single element, has presented an elegant means of appropriately distributing power across the object being imaged, all while maintaining homogeneous excitation and limiting power deposition.

1.2.3 Quantitative MRI

Standard anatomical MRI images are "weighted" by a combination of magnetic parameters (T_1, T_2, PD) and scanner-related idiosyncracies (e.g. B_1 field inhomogeneities) limiting interpretability. While a radiologist may be able to qualitatively identify any relative differences in intensity for a given image, high variability exists not only between scanners and subjects, but also for single subjects across different sessions. Post-processing using intensity normalization techniques enable some degree of between participant comparison; however, the local tissue value is devoid of meaning (Figure 1.9). Quantitative MRI (QMRI) involves a shift in paradigm from using MRI as a tool strictly for producing images to one that is also used for measurement.

QMRI sequences measure individual MRI contrast-generating parameters in isolation (see [Weiskopf et al., 2015] for a review). QMRI-based methods typically require the acquisition of multiple scans in order to estimate specific magnetic resonance properties (e.g. T_1 or T_2 relaxation). These local parameters are inherently more robust than weighted images, which involve a mix of parameters, and thus better reflect intrinsic tissue properties and can be used to identify specific brain structures and also pathology on the basis of a local measurement. These measurements are also more directly comparable between scanners allowing better standardization compared with conventional weighted images [Deoni et al., 2008, Weiskopf et al., 2013].

Chapter 5 of this thesis focusses on examining the utility of longitudinal relaxometry (T_1 = $1/R_1$) at ultra-high fields for delineating deep brain structures relevant to stereotactic neurosurgery. T_1 relaxation is also referred to as *spin-lattice* relaxation as it involves the transfer of energy between local nuclear spins and the surrounding environment, or lattice. Thus, the structure of the environment heavily impacts the local T_1 values measured. On the one hand, areas of relatively restricted water mobility (i.e. in the axons of white matter), collisions and interactions with surrounding lipid molecules in myelin result in more rapid relaxation, and thus shorter, T_1 values. On the other hand, areas of high relative water mobility (e.g. cerebrospinal fluid) have longer relaxation times, relying on random interactions with other water molecules rather than any sort of inherently structured lattice. Generally, as it relates to brain tissue, T_1 values are highest in cerebrospinal fluid, intermediately high in gray matter, and lowest in white matter (see Table 1.1).

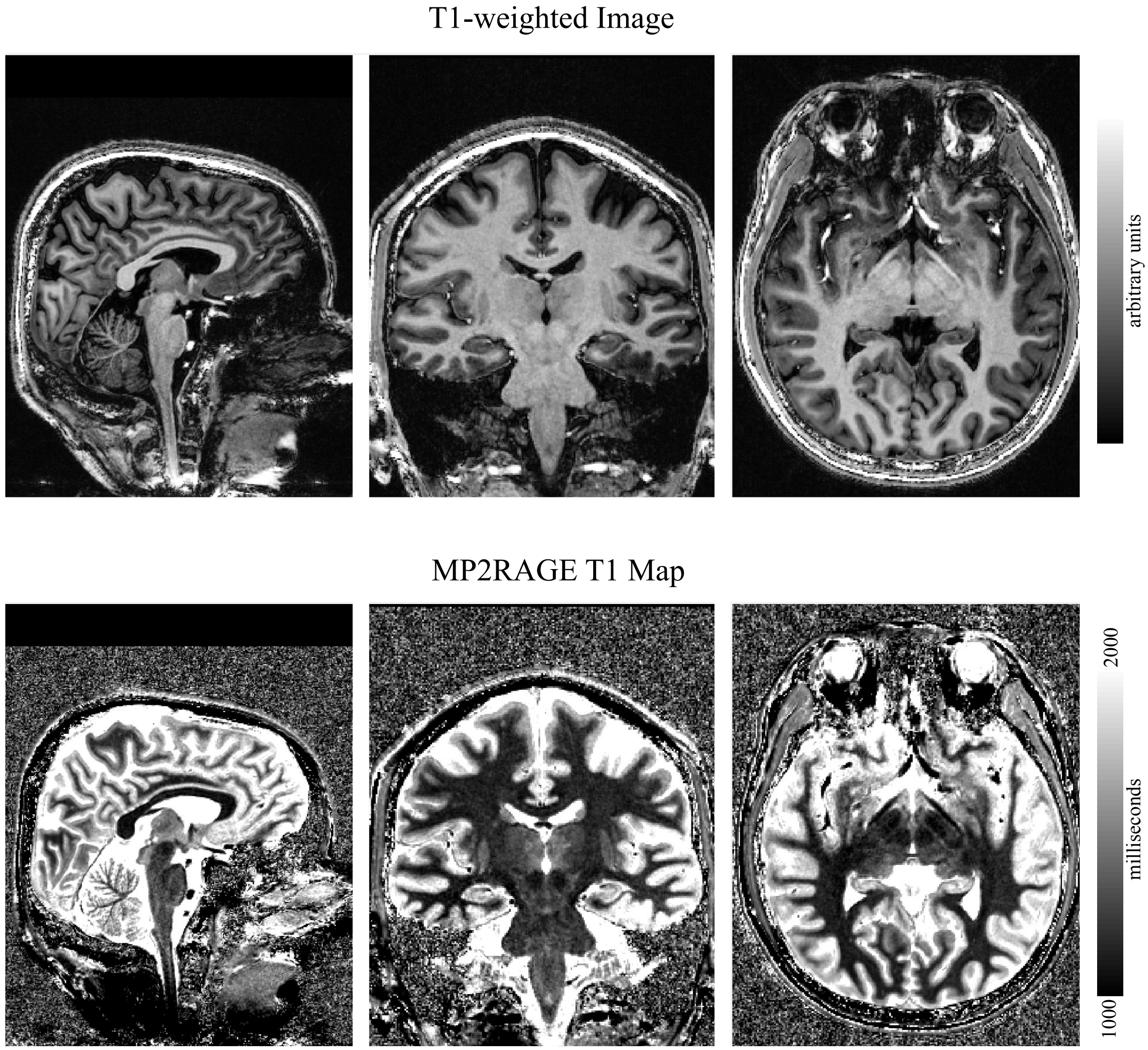

Figure 1.9: Comparison of conventional T_1-weighted imaging where the units are arbitrary with quantitative T_1 mapping where the values reflect inherent local tissue properties. Individual subject scan at 7-Tesla using the MP2RAGE sequence [Marques et al., 2010].

Many groups have focussed on the inherent contrast-related advantages of T2-based protocols at high field, due to the rich iron content of many basal ganglia nuclei. However, the advantages are not limited to this contrast type, with T_1 values not only increasing in a field-dependent manner, but also the dispersion between different tissue types; thus increasing the contrast and thus salience between neighbouring structures with different properties [Rooney et al., 2007, Tourdias et al., 2014].

Table 1.1: T_1 values at 7-Tesla as acquired from the literature [Marques and Norris, 2017]

region	T_1 (ms)	T_2 (ms)
White Matter	1100–1400	55
Cortical Gray Matter	1900–2100	50
Cerebrospinal Fluid	4400	NA
Blood	2600	7
Putamen	1520–1700	NA
Caudate Nucleus	1630–1700	NA
Globus Pallidus	1180–1200	NA
Red Nucleus / Substantia Nigra	~ White Matter	NA

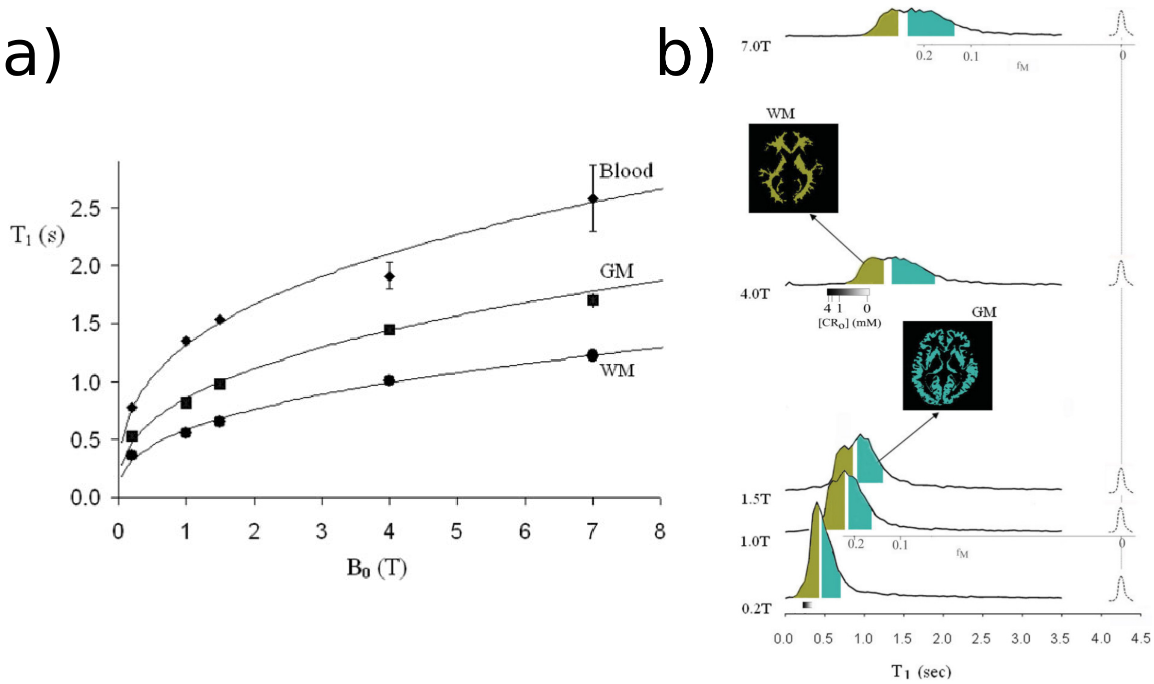

Figure 1.10: Figures from Rooney et al. demonstrating the field-dependent increase in T_1 values and dispersion in different tissue types [Rooney et al., 2007]. The increase in dispersion of T1 manifests as improved contrast that can be exploited for better delineating boundaries between brain structures. This will be the subject of Chapter 5.

1.3 Thesis Outline

Despite significant advances in stereotactic targeting, a recent analysis of multiple national databases in North America (over 28000 procedures) revealed a surprisingly high rate of hardware revision and removal for deep brain stimulation procedures at a rate of up to 48.5% related to improper targeting or lack of therapeutic effect [Rolston et al., 2016]. This suggests that further work is necessary in both patient and target selection in patients being considered for neuromodulation. Lack of adequate visualization with conventional lower field strengths (1.5/3 Tesla) has meant that standard-of-care surgical treatment has relied on indirect targeting using standardized landmarks as described in Section 1.1.2. For this reason, these procedures routinely require awake testing and microelectrode recording, which increases operating room (OR) time, patient discomfort, and risk of complications.

In this manuscript-based thesis, the feasibility of using ultra-high field MRI for stereotactic surgery is explored. The fundamental motivation behind this line of work is that the ability to see structures better will allow for more focal, targeted therapy. To answer this question, this work begins in *Chapter 2* with a practical clinical example of integrating a 7T template into the clinical workflow for surgical planning. This technical report is followed with a study examining the practical limits of accuracy using traditional template-assisted stereotaxy in *Chapter 3*. In *Chapter 4*, the impact of geometric distortion on our ability to use 7T for surgical targeting is investigated. Finally, in *Chapter 5*, we demonstrate how quantitative MRI acquired at 7T can be used to visualize stereotactic targets never before seen *in vivo*. The implications of the thesis and future considerations are summarized in *Chapter 6*.

Chapter 2

Ultra-high field template-assisted deep brain stimulation surgery

This chapter is based on the following manuscript:

- Lau, J. C., MacDougall, K. W., Arango, M. F., Peters, T. M., Parrent, A. G., & Khan, A. R. (2017). Ultra-High Field Template-Assisted Target Selection for Deep Brain Stimulation Surgery. World Neurosurgery, 103, 531–537.

2.1 Introduction

Surgical planning for deep brain stimulation (DBS) surgery is variable from centre to centre as a result of a number of factors including availability of imaging modalities, access to stereotactic equipment, and the institutional and neurosurgical experience. Results of a recent international survey highlighted important procedural differences in DBS workflow steps, identifying five distinct procedural clusters among respondents [Abosch et al., 2013]. Many centres continue to depend on lower field magnetic resonance imaging (MRI) at 1.5 Tesla as part of the clinical workflow where direct visualization of traditional DBS targets can be challenging. Even where more high field scanners are available, acquired images may be suboptimal due to patient movement, poorly optimized MRI protocols, and patient-specific considerations (e.g. oblique image acquisitions as a result of torticollis).

Template or atlas guidance has been a fundamental part of stereotactic neurosurgery since Jean Talairach described the réperage radiologique to describe the process of establishing the stereotactic positions of neuroanatomical structures by aligning an anatomical atlas, derived from histological sectioning of a single individual, with patient-specific fluoroscopic images [Bancaud et al., 1965, Talairach and Tournoux, 1988]. Semantically, template assistance involves planning using the unprocessed underlying dataset, while atlas guidance involves using the labeled version of the template. While modern imaging has enabled subcortical visualization not possible with classical x-ray based studies, growing evidence points to the need for even more precise targeting of subcortical substructures [Accolla et al., 2016, Lambert et al., 2012, Vanegas-Arroyave et al., 2016]. In this technical report, we describe our initial experiences with using an ultra-high field (UHF) template to assist neurosurgeons with stereotactic planning for conventional deep brain stimulation targets.

2.2 Materials and Methods

2.2.1 Deep Brain Stimulation Surgery Workflow

In the typical DBS workflow at our centre, the patient is referred to Neurosurgery for DBS implantation by a movement disorders neurologist. After consenting to the procedure, the patient undergoes clinical (1.5T) MRI for surgical planning in the weeks leading up to the surgery with an 8-channel head/neck/spine (GE Healthcare, Milwaukee, Wisconsin). Sequences acquired include a three dimensional (3D) T1-weighted image using an axial inversion recovery spoiled gradient recalled echo sequence: echo time (TE) = 4.1 ms, inversion time (TI) = 300 ms, flip angle = 20 degrees, resolution = 1.25×1.25×1.50 mm, receiver bandwidth = 22.73 kHz, field of view (FOV) = 26×26 cm^2, matrix size = 256×256. Selected two dimensional (2D) T2-weighted fast spin echo (FSE) sequences in axial and coronal sections are also acquired to better visualize the target region (TE = 110 ms, TR = 2800 ms, receiver bandwidth = 20.83 kHz, FOV = 26×26 cm^2, matrix size = 256×224, slice thickness = 1.5 mm, resolution = 1.25×1.25×1.50 mm). After importing the relevant pre-operative images, the anterior and posterior commissures (AC-PC) are identified using the surgical navigation system (StealthStation S7 Framelink software version 5.4.1, Medtronic Inc., Minneapolis, Minnesota). Indirect targeting based on AC-PC coordinates is performed by the neurosurgeon, aided by direct visualization when feasible. However, it is our experience that the clinical MRI protocols at our centre often do not clearly delineate conventional DBS targets. The total surgical planning process of image import, fusion, and planning requires approximately 60-90 minutes.

The morning of surgery, a Leksell stereotactic frame is secured to the patient's head after a bilateral field block with a 50:50 mixture of 0.5% bupivacaine and 2% lidocaine, both with epinephrine. A stereotactic computed tomography (CT) scan is acquired with double-dose contrast while the patient is in the headframe. The CT is fused with the 1.5T MRI using the image guidance system bringing the surgical plan into the reference frame of the patient. The Leksell target and entry point coordinates are extracted from the surgical navigation workstation requiring roughly 15-30 minutes for CT-MRI fusion and final coordinate calculations. The patient is brought to the operating room where the frame is secured to the operating table in the typical manner. The patient is attached to American Society of Anesthesiologists (ASA) standard monitoring, a non-central IV line is inserted, and IV sedation is initiated (dexmedetomidine continuous infusion at 0.4–0.6 mcg/kg/hr). In our experience, dexmedetomidine, contrary to other sedative medications, has almost no respiratory depression effects and minimal interaction with the microelectrode recording.

The surgical field is prepped and draped in the usual manner. The Leksell frame is set to the specified target coordinates, local anaesthetic is infiltrated, the incision opened, and the cortex exposed via a cranial burr hole. A lead fixation device is attached to the skull surrounding the burr hole (Medtronic Stimloc, Medtronic Inc., Minneapolis, Minnesota). The dura is opened and coagulated, as is the overlying brain. Fibrin sealant is introduced to limit brain shift from pneumocephaly. The microdriver system is attached to the frame and, using Ben's gun [Limousin et al., 1995], up to five microelectrodes are slowly advanced towards the target by a dedicated neurophysiologist while the electrical activity is recorded (Medtronic Leadpoint, Medtronic Inc., Minneapolis, Minnesota). Once the target region has been mapped physiologically, the patient is awoken to test for effects from stimulation. The macroelectrode is inserted along the course of the best candidate microelectrode. The same procedure is repeated on the opposite side, if indicated. Regarding sedation, the dexmedetomidine infusion is stopped 30 minutes before stimulation, and re-instituted once the surgeon and neurophysiologist are satisfied, continuing until the end of the procedure. The lead or leads are tunnelled to the parietal scalp. The frame is removed and the patient is placed in the supine position and general anaesthetic is administered. The DBS electrodes are tunnelled and connected to the implantable pulse generator (IPG). A post-operative 1.5T MRI is completed the day following surgery to confirm placement. Once the appropriate position is confirmed and the patient is mobilizing well, they are discharged home. The patient is followed by a neurologist for optimizing stimulation parameters with stimulation commencing as early as two weeks post-implantation.

2.2.2 7T Group Template Creation

While a number of different ultra-high field templates have been proposed in the literature, for the current report, we have elected to use an unbiased group average created at our institution [Wang et al., 2016]. In brief, 12 healthy control subjects (6 female; age: 27.6 +/- 4.4 years) were scanned on a 7T scanner (Agilent, Santa Clara, CA, USA/Siemens, Erlangen, Germany) using a 24-channel transmit-receive head coil array constructed in-house with a receiver bandwidth of 50 kHz. A T1-weighted (T1w) MPRAGE sequence was acquired (TR = 8.1 ms, TE = 2.8 ms, TI = 650 ms, flip angle=11°, 256×512, 230 slices, resolution = $0.59 \times 0.43 \times 0.75$ mm^3). A T2-weighted (T2w) turbo spin-echo (TSE) 3D (TR = 3D sagittal, matrix: 260×366, 266 slices, resolution = 0.6 mm^3, 4 averages). High-resolution *in vivo* templates were created by performing group-wise linear and nonlinear registration of 12 normal subjects scanned on a human 7T scanner using both T1w and T2w contrasts (available for download at http://www.nitrc.org/projects/deepbrain7t/) resulting in an unbiased group nonlinear T1w average and T2w averages at submillimeter resolution. These templates demonstrate improved visualization of subcortical nuclei compared to lower field templates.

2.2.3 Template-to-Patient Registration Workflow

We propose to assist with target selection by fusing the ultra-high field template to the patient reference (T1w) space (Figure 2.1). The procedures are performed using standard-of-care clinical imaging as described above, but the planning is augmented by the integration of patient-aligned high resolution templates. The patient 1.5T T1w volume, the reference image,

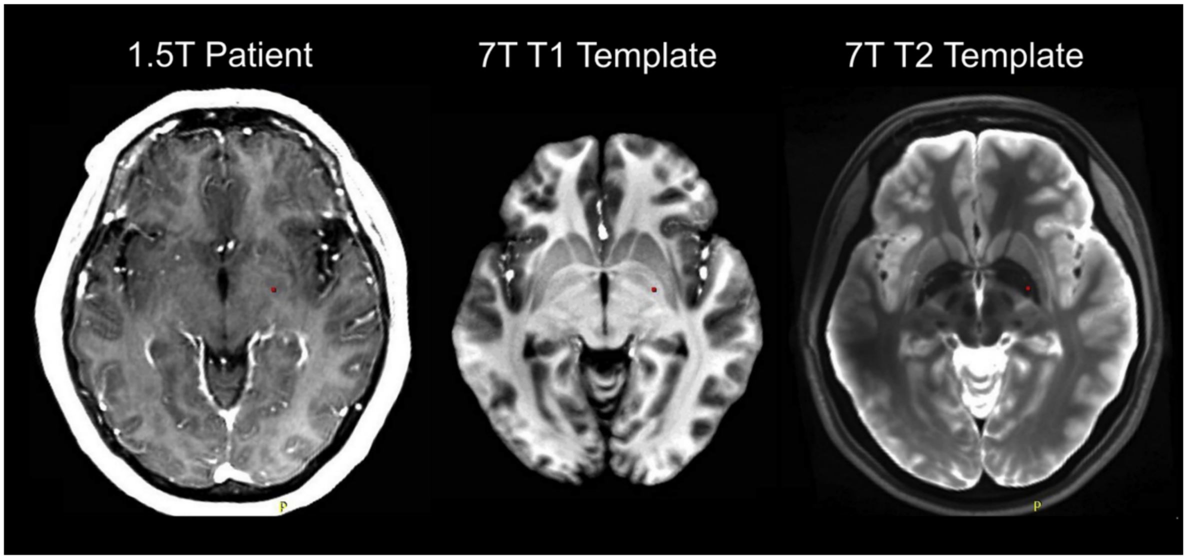

Figure 2.1: Side-by-side visualization of standard clinical 1.5T T1 magnetic resonance imaging (MRI) next to the fused ultra-high field MRI T1 and T2 templates in the axial plane. The red dot marks the location of the globus pallidus internus.

is exported from PACS and converted to NiFTI file format using dcm2niix [Li et al., 2016]. The reference image is first corrected for intensity inhomogeneities [Sled et al., 1998, Tustison et al., 2010], and subsequently, brain masking is performed using the Brain Extraction Toolkit from the FSL package at a fractional intensity threshold of 0.4 [Smith, 2002]. Through a series of successive image registration steps using NiftyReg [Modat et al., 2010] (default settings in version 1.3.9), the UHF T1w and T2w templates are warped into the patient T1w image space. Registration is initiated with a rigid body (6 degrees-of-freedom) registration, and is followed by affine (12 degrees-of-freedom). Finally, the template is nonlinearly registered to the reference space using the NiftyReg block-matching deformation technique. The duration of image fusion and registration is 20 minutes. All processing was performed on a modern workstation (Intel Core i5-6400 CPU @ 2.70 GHz x 4; 64-bit; 32 Gb of RAM; Ubuntu 16.04 Long Term Support version), and automated using a bash shell script.

The quality of registration is assessed by the treating neurosurgeon via visual inspection of the spatial correspondence between key neuroanatomical features on both images. Once satisfactory, the transformed templates are exported back to DICOM format using NifTI2Dicom. The DICOM IDs of the newly created DICOM files are unified with the patient pre-operative T1w dataset with one modification to the Study Description header using OsiriX. The aligned UHF templates are imported to the StealthStation as separate image datasets. At several stages throughout processing, the images are quality controlled by the clinical team for salient features that correctly identify the sidedness of each hemisphere in comparison with unprocessed clinical images (i.e. based on cortical and vascular landmarks). The fusion of the CT with the pre-operative MRI was performed on the day of surgery using the commercial neuronavigation software. This was independent of the template fusion process, but ultimately permitted overlaying of UHF templates and the stereotactic CT in the image space of the pre-operative MRI for visualization, resulting in a transformation of the planned trajectory into physical Leksell coordinates.

2.3 Results: Two Cases

We demonstrate the utility of UHF template-assisted stereotactic targeting in two cases: unilateral globus pallidus internus implantation and bilateral subthalamic nucleus implantation.

2.3.1 Right GPi Implantation for Dystonia

The first patient was a 51 year-old otherwise healthy right-handed female with severe progressive left-sided dystonia and supranuclear palsy of unknown etiology. Her painful dystonia progressed to the point of complete loss of left upper extremity function requiring an arm sling and she suffered from recurrent severe left shoulder dislocations, despite trials of systemic and local baclofen therapy and a failed orthopedic intervention to correct her dislocation. She opted to undergo implantation of her right internal pallidum to improve her mostly unilateral (left-sided) symptoms.

She underwent a clinical pre-operative MRI scan several weeks prior to her procedure (Figure 2.2a). The basal ganglia structures were not well visualized, made more challenging by her left-sided torticollis (head rotated in the scanner). We employed template-to-patient registration bringing our high resolution T1 and T2 templates into the patient space (Figure 2.2d and 2.2e). Quality of registration was assessed manually by the neurosurgeon but was noticeably improved compared to the built-in Schaltenbrand-Wahren atlas provided as part of the commercial software package (Figure 2.2b). Target selection was performed using a combination of indirect (AC-PC coordinate based) and direct targeting techniques, and furthermore assisted by the inclusion of the aligned 7T templates. The final trajectory was decided after ensuring that the trajectory choice using conventional clinical imaging appeared appropriate. The stereotactic CT was registered to the pre-operative patient MRI on the day of surgery using the commercial neuronavigation system (Figure 2.2c). Three microelectrodes were used for recording. Unit potentials were obtained at the expected depth with the central electrode trajectory being chosen after demonstrating the fewest side effects. A 3387 electrode (Medtronic Inc., Minneapolis, Minnesota) was then implanted at the target site (Figure 2.2f). Figure 2.3

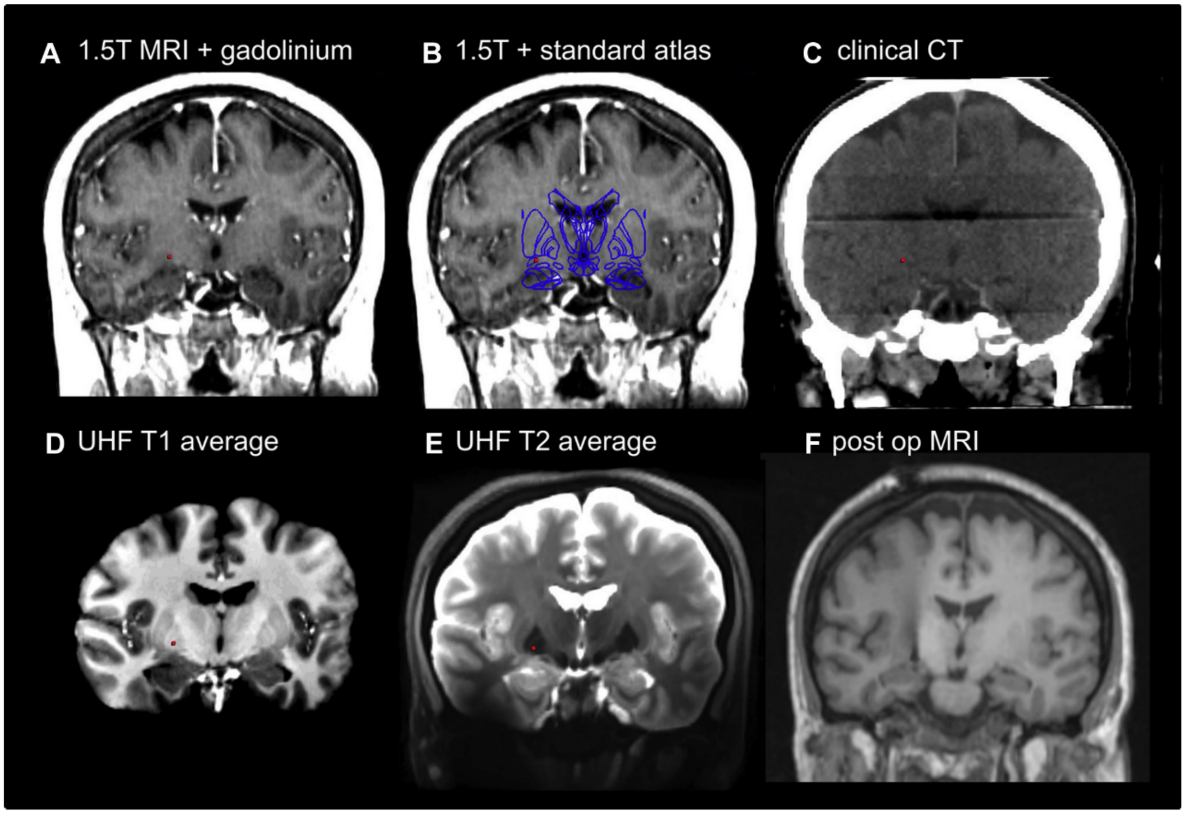

Figure 2.2: Right internal pallidum implantation assisted by ultra-high field (UHF) fusion to standard clinical images (1.5T magnetic resonance imaging [MRI] and computed tomography [CT]). The red dot marks the same location fused between modalities for (A) 1.5T MRI with gadolinium, (B) with the Schaltenbrand-Wahren atlas overlay provided in the clinical neuronavigation software, (C) CT in Leksell frame, (D) UHF T1 average, and (E) UHF T2 average. Also included is the best corresponding coronal section in the post-insertion MRI (F).

shows a screenshot of the UHF T2 average integrated into the commercial neuronavigation software.

The patient noted an immediate improvement in her dystonia after surgery. Post-op imaging revealed that the electrode was in the appropriate position with no complications. At four months follow-up, she no longer required an arm sling, and demonstrated significant improvement in her pain and her dystonia with the following stimulation settings: effective contact = 2, amplitude = 3.5V, pulse width = 60 us, frequency = 130 Hz.

2.3.2 Bilateral STN Implantation for Parkinson's Disease

The second patient was a 66 year-old left-handed male with a 14-year history of Parkinson's disease. He was referred as a surgical candidate due to significant bradykinesia, dyskinesias, and on/off fluctuations. He consented to bilateral subthalamic nucleus implantation.

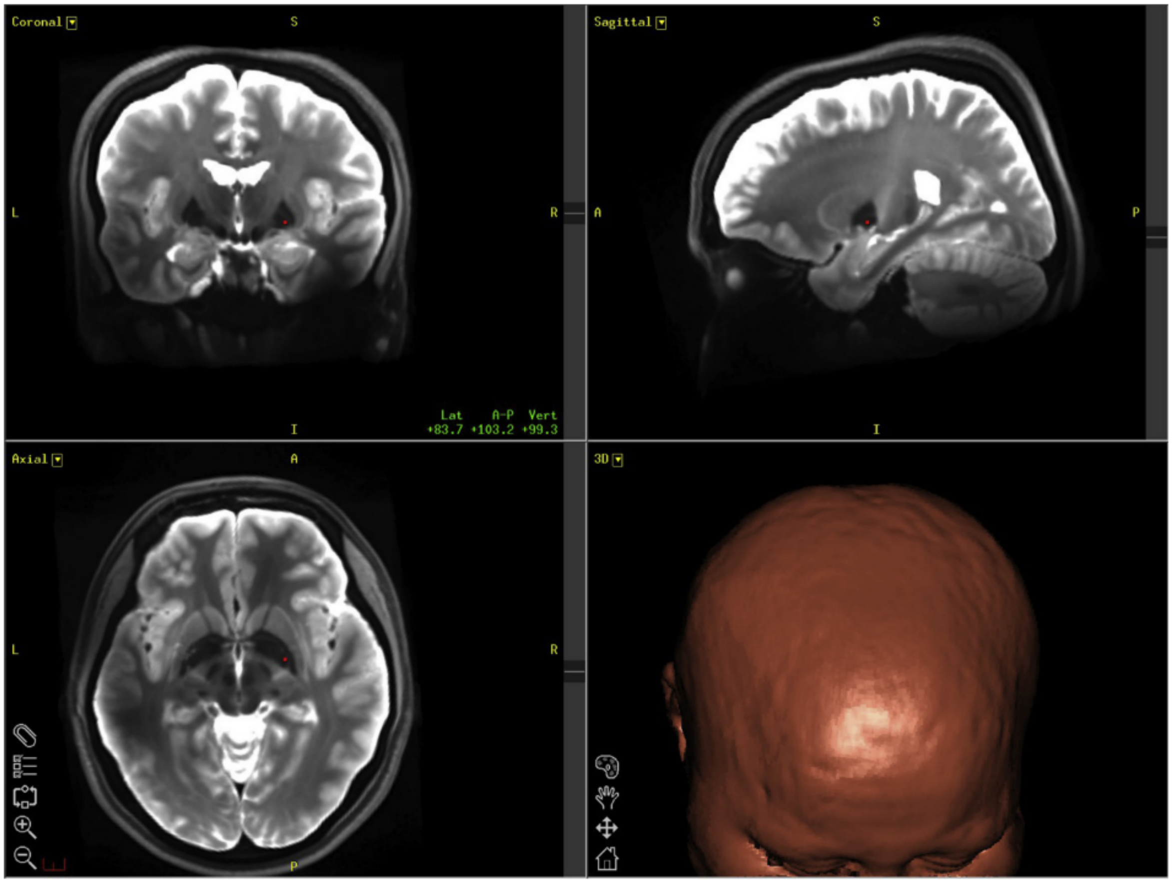

Figure 2.3: Example screenshot demonstrating the integration of the 7T T2 average into the commercial surgical planning software (Case 1: right internal pallidum insertion). The red dot marks the location of the globus pallidus internus.

Preoperative imaging again revealed poor visualization of subcortical structures including the STN (Figure 2.4a). Template-to-patient registration was performed (Figure 2.4c and d), and compared against the standard atlas integrated into the neuronavigation software (Figure 2.4b). Target selection was performed using a combination of indirect (AC-PC coordinate based) and direct targeting techniques with assistance from the 7T templates. For each side, all five microelectrodes were used for recording. Unit recordings were best identified along lateral and anterior trajectories. The left anterior trajectory was chosen due to no side effects except for mild right hemi-body symptoms at high threshold. On the right, good unit activity was observed in the central, anterior, and medial recordings. The medial electrode demonstrated the best side effect profile. Bilateral Medtronic 3389 leads were implanted (Figure 2.4e and 2.4f).

Postoperatively, this patient noted immediate improvement, likely due to an insertional effect. However, this effect dissipated within two weeks, at which point stimulation was initi-

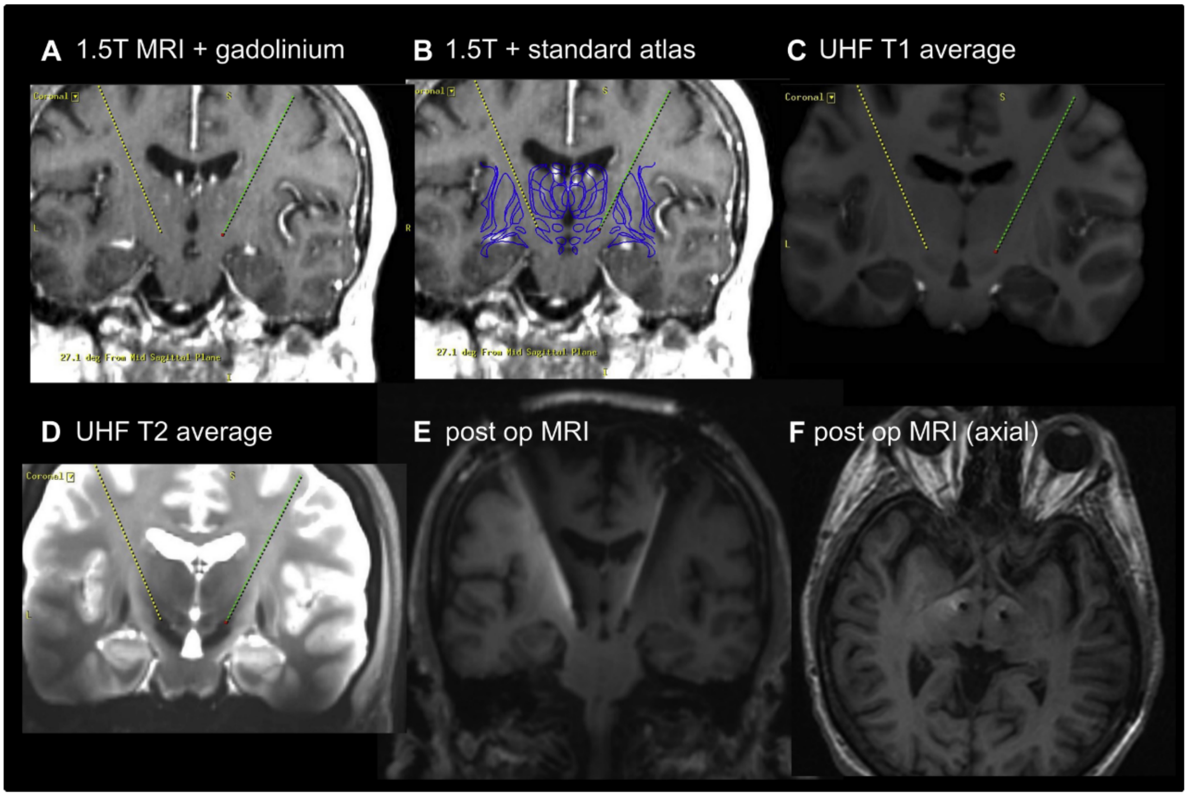

Figure 2.4: Bilateral subthalamic nucleus implantation assisted by ultra-high field (UHF) fusion to standard clinical images. The left and right trajectories (yellow and green, respectively) are fused across modalities for (A) 1.5T magnetic resonance imaging (MRI) with gadolinium, (B) with the Schaltenbrand-Wahren atlas overlay, (C) UHF T1 average, and (D) UHF T2 average. Bilateral subthalamic nuclei were implanted successfully, as demonstrated with select (E) coronal and (F) axial views on postoperative MRI.

ated. At three months post-op, he has halved his levocarbidopa dosage and no longer has any off periods. He is now independent in all activities of daily living. His stimulation settings are the following: L STN bipolar stimulation with effective contacts = 1 positive and 2 negative, amplitude = 3V, pulse width = 90 us, frequency = 130 Hz; R STN bipolar stimulation with effective contacts = 9 positive and 10 negative, amplitude = 3V, pulse width = 90 us, frequency = 130 Hz.

2.4 Discussion

In this technical report, we have described a workflow for the integration of high-resolution *in vivo* ultra-high field templates into the surgical navigation system to assist with DBS planning. We have demonstrated that UHF assistance can be helpful for internal pallidum and subthalamic nucleus implantations.

Ultra-high field MRI delivers an over two-fold improvement in signal-to-noise (SNR) compared with standard clinical scanners, allowing *in vivo* visualization at submillimeter spatial resolution. The improved resolution has enabled clear delineation of small structures like the subthalamic nucleus and pallidum, overall enriching 3D context in the subcortex invaluable for surgical targeting. To date, patient-specific UHF imaging has been limited to research protocols and has not been used directly for surgical planning. While interest in UHF imaging is growing, availability remains limited. By using an unbiased UHF template, our workflow does not require the candidate DBS patient to undergo any additional scans beyond what is conventionally performed at a given institution, and could be used by centers without access to UHF imaging.

Numerous alternative templates exist both with and without atlas labeling. Histological atlases, while capable of providing microscopic detail, may be more difficult to accurately register with clinical images due to differences in scale and contrast, as well as the challenge of spatial correspondences between the histological atlas (derived from a single individual) with the patient. Atlases created at low field are abundant and typically involve larger datasets (e.g. the MNI152 atlas which has 152 subjects). However, the poorer spatial resolution limits visualization of subcortical targets like the STN. Our initial experiences suggest that UHF *in vivo* templates may serve as an alternative option enabling improved signal and resolution but also improved registration with patient datasets since context regarding expected location of subcortical structures is maintained at a group level. This report has focused on the use of T1 and T2 UHF templates created from a dataset of young healthy volunteers at our centre. This could be considered a limitation of the current work since they may not best represent our patient groups, both in terms of age and pathology. Certain subcortical structures are displaced and atrophic in Parkinson's compared to normal age-matched controls [Xiao et al., 2014], suggesting that a disease-specific atlas could be ideal for DBS planning. One practical problem with such a choice is that it remains unclear how optimal a Parkinson's specific atlas would be for other patient populations encountered in a DBS practice, for example in dystonia or essential tremor. Finally, there is growing evidence that there are separate subtypes of Parkinson's, some of which could be more responsive to DBS than others, suggesting that ultimately subtype specific templates may be more representative. Overall, the choice of atlas is a complex decision, and is an area of further study. Eventually, patient-specific ultra-high field imaging may be feasible. However, calibration and correction of distortion remain challenges [Duchin et al., 2012, Lau et al., 2018a] (also see Chapter 4).

As is routine in clinical practice, the neurosurgeon must be rigorous in establishing the correspondence between any fused images (e.g. CT and MRI), which is performed by manual inspection on the surgical navigation system. When using the proposed workflow, the same level of rigor is necessary for assuring adequate alignment of the template to the patient dataset. Design and implementation requires a close working relationship with biomedical engineers and medical physicists to debug any software problems and develop safeguards to minimize errors of spatial alignment and data conversion, including DICOM import and export. Our 7T template-assisted workflow serves as an enhancement of the conventional workflow of MRI to CT fusion. The surgeon still performs the target planning using clinical images, but can choose to augment or confirm their targeting with template-assistance by windowing between the template and clinical scan within the neuronavigation software. It should be emphasized that the UHF template is helpful for target placement but obviously not for entry point localization since patient-specific gyral patterns and cortical vessel anatomy would not be accounted for.

Our proposed image fusion workflow could be better optimized through more systematic evaluation of the impact of different pipeline modifications. For example, in our experience, a coarse-to-fine registration approach results in better registration of our template to a patient target image due to better initialization of global image correspondence prior to nonlinear registration. While we have not assessed this systematically, the additional time required for each of the linear (rigid-body and affine) registration components is minimal (less that 1 minute). Ongoing goals in this collaborative project with biomedical engineers include more robust evaluation of the impact of brain extraction and nonlinear fusion methods on speed and accuracy. Overall, we feel that the time required for our current workflow (20 minutes) is reasonable given that DBS cases are performed on an elective basis.

2.5 Conclusions

We have described a technique for integrating an ultra-high field MRI template into the surgical planning workflow that may serve as a valuable adjunct to standard clinical imaging for stereotactic target selection. The method does not require any additional cost or time to the patient. Prospective studies would help to identify ideal template selection and how this information is best used along with high-quality patient-specific pre-operative imaging.

Chapter 3

A framework for evaluating correspondence between brain images using anatomical fiducials

This chapter is based on the following manuscript:

- Lau, J. C., Parrent, A. G., Demarco, J., Gupta, G., Park, P. J., Ferko, K., Khan, A. R., & Peters, T. M. (2019). A framework for evaluating correspondence between brain images using anatomical fiducials. Human Brain Mapping, Under Review.

3.1 Introduction

Establishing spatial correspondence between images is a crucial step in neuroimaging studies enabling fusion of multimodal information, analysis of focal morphological differences, and comparison of within- and between-study data in a common coordinate space. Stereotaxy arose as a result of questions raised by scientists and surgeons interested in the physiology and treatment of focal brain structures [Evans et al., 2012, Horsley and Clarke, 1908, Peters, 2006]. Jean Talairach played a crucial role, observing consistent anatomical features on lateral pneumoencephalograms [Dandy, 1918], or “air studies”, that could be consistently localized, specifically the anterior commissure (AC) and posterior commissure (PC) [Schaltenbrand and Wahren, 1977, Talairach et al., 1957], and could thus be mapped to prepared post-mortem brain sections in a 3D coordinate system. The AC-PC line has remained important in the era since magnetic resonance imaging (MRI) has risen to prominence for aligning brain images to create population atlases [Collins et al., 1994, Evans et al., 1992, Talairach and Tournoux, 1988] as well as to project data from structural and functional investigations. Further optimizations enabled by deformable registration have led to atlas enhancements [Fonov et al., 2011] where many more structural features are preserved. The adoption of standard templates has allowed researchers to compile cytoarchitectonic, functional, and structural data across studies via image-based meta-analysis of peak coordinates and statistical maps [Eickhoff et al., 2009, Gorgolewski et al., 2015, Yarkoni et al., 2011].

Ever since the first linearly aligned population templates [Evans et al., 1992, Talairach and Tournoux, 1988], there have been a number of advances in the development of robust higher order nonlinear registration tools. As the options became more numerous, several studies investigated the performance of the different nonlinear registration algorithms [Chakravarty et al., 2009, Evans et al., 2012, Hellier et al., 2003, Klein et al., 2009]. Over the past decade, the most common metrics used to evaluate spatial correspondence are related to voxel overlap between regions-of-interest (ROIs) segmented in both reference and target images. Typically, large subcortical structures well-visualized on standard structural MRIs such as the globus pallidus (pallidum), striatum, and thalamus are used [Chakravarty et al., 2009, Chakravarty et al., 2008, Klein et al., 2009]. While these measures are effective for evaluating spatial correspondence on the macroscale, here we argue that they remain relatively coarse measures of registration quality and are insensitive to focal misregistration between images. In addition, they do not permit facile identification or description of where these local biases are occurring. These issues are particularly critical as technical advancements in both imaging and stereotaxy are enabling more accurate therapeutic modulation of brain regions where several millimeters could represent the difference between optimal therapy and complications.

In this paper, we sought inspiration from classical stereotactic methods [Schaltenbrand and Wahren, 1977, Talairach et al., 1957], and propose that point-based distances provide a more sensitive metric by which brain image correspondence can be evaluated. Anatomical points have been referred to in the literature using a variety of terms including fiducials, landmarks, markups (sometimes used in combination) but ultimately involve representing an anatomical feature by a three-dimensional (x,y,z) Cartesian coordinate. For this manuscript, we have chosen to use the term AFIDs, short for anatomical fiducials, “fiducia” being Latin for trust or confidence. We argue that the advent of automatic segmentation-based methods has led to a relative underemphasis of point correspondence between brain structures. We first sought to determine whether we could define a set of AFIDs that were both consistently identifiable across multiple datasets while also providing a distributed sampling about the brain. Following this, we demonstrate how AFIDs are complementary to segmentation-based metrics for providing a quantitative report of spatial correspondence between structural magnetic resonance images of the brain using more intuitive distance-based measures of alignment. Central to this work was the development of our protocol using an open source framework, enabling reproducibility across sites and centers. The overall study organization is shown schematically in Figure 3.1.

3.2 Methods

3.2.1 Protocol development

A series of anatomical fiducials (AFIDs) were identified by the lead author (JCL; 10 years experience in neuroanatomy) in consultation with an experienced neurosurgeon (AGP; 20+ years experience practicing stereotactic and functional neurosurgery) with consensus achieved on a set of 32 points, which we refer to as AFID32 (see Figure 3.2; RRID:SCR_016623). AFIDs could generally be classified as midline (10/32 = 31.25%) or lateral (22/32; i.e. 11 structures that could be placed on each of the left and right sides). Regions prone to geometric distortion were avoided [Lau et al., 2018b]. We limited our initial set of AFID locations to deep brain regions where less inter-subject variability exists (millimeter scale) compared to the cortical sulci and gyri (centimeter scale) [Thompson et al., 1996].

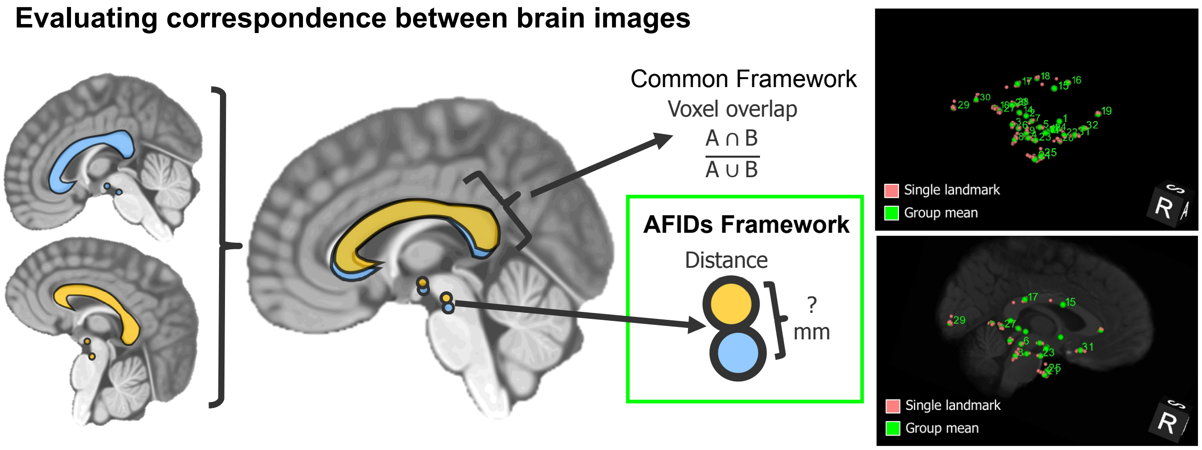

Figure 3.1: Metrics for evaluating spatial correspondence between brain images include voxel overlap (i.e. ROI-based) metrics as well as point-based distance metrics. The proposed framework involves the identification of point-based anatomical fiducials (AFIDs) in a series of brain images, which provide an intuitive millimetric estimate of correspondence error between images and is also a useful tool for teaching neuroanatomy.

The AFID points were placed using the Markups Module of 3D Slicer version 4.6.2 [Fedorov et al., 2012] (RRID:SCR_005619). One key feature of 3D Slicer is that it allows markup points to be placed in the 3D coordinate system of the software as opposed to the voxel coordinate system of the image being annotated permitting more refined (sub-voxel) localization. Images are automatically linearly interpolated by the software on zoom. After importing the structural MRI scan to be annotated into 3D Slicer, the anterior commissure (AC) and posterior commissure (PC) points were placed, specifically the center of each commissure rather than the intraventricular edge. After defining an additional midline point (typically the pontomesencephalic junction or intermamillary sulcus), an AC-PC transformation was performed using the built-in Slicer module (AC-PC Transform). For all subsequent AFID placements, the AC-PC aligned image was used. The AFID32 protocol is shown in MNI2009bAsym space in Figure 3.2.

The rest of the methods are organized into four separate phases. Phase 1 involved AFID32 placement in three open access brain templates. Phase 2 involved further placement of the AFIDs in individual subject scans. In Phase 3, AFIDs were used to evaluate subject-to-template registration; and finally, in Phase 4, they were used to assess template-to-template registration quality.

For validation and assessment, we adopted the terminology of Fitzpatrick and colleagues [Fitzpatrick and West, 2001, Fitzpatrick et al., 1998] who defined fiducial localization error (FLE) and fiducial registration error (FRE) as metrics used to evaluate the real-world accuracy of image-guidance systems used in neurosurgery. FLE is defined as error related to the placement (i.e. localization) of fiducials, while FRE is defined as error related to registration. This body of work has been most concerned with describing the correspondence between preoperative images of a patient and the physical location of the patient and surgical site in the operating room. Here, we use these terms to describe (virtual, image-based) anatomical fiducials (AFIDs) annotated in structural T1-weighted MRI scans.

3.2.2 Phase 1: Protocol validation for brain templates

Novice participants (N=8) were trained over a series of neuroanatomy tutorials to place AFIDs on a number of publicly available brain images: Agile12v2016 [Lau et al., 2017, Wang et al., 2016], Colin27 [Holmes et al., 1998], MNI2009bAsym (nonlinear asymmetric; version 2009b; RRID:SCR_008796) [Fonov et al., 2011]. Each participant then performed 4 rating sessions independently for each template, for a total of 12 point sets resulting in a total of 96 AFID32 protocols. We computed several different metrics for describing the accuracy (and reliability) of our proposed protocol, all of which are variations of anatomical fiducial localization error (AFLE): mean AFLE, intra-rater AFLE, and inter-rater AFLE as shown in Figure 3.3.

To compute the mean AFLE, the mean AFID coordinate for each brain image was used as an approximation of the ideal coordinate location. Mean AFLE was calculated as the Euclidean distance between the individual position and the group mean. We furthermore calculated intra-rater AFLE as the mean pairwise distance between AFIDs placed by the same rater. The individual measures were averaged across all raters as a summary metric. To calculate inter-rater AFLE, a mean coordinate was computed by averaging the coordinates for each rater as an estimate of the ideal coordinate location for the rater; the mean pairwise distance between AFIDs placed across raters was then calculated as a summary metric. We summarized global and location-specific mean AFLE according to a number of variables: template (group versus individual), rating session (1-4), rater, and AFID.

Time required to complete AFID32 placement for a single MRI was documented by each rater. Outliers were defined as any fiducials deviating from the mean fiducial point by greater than 10 mm. Furthermore, patterns of variability in AFID placement were assessed using K-means clustering of fiducial locations (point clouds) relative to the mean fiducial location.

3.2.3 Phase 2: Protocol validation for individual subjects

The same participants and the lead author (total N=9) performed additional AFID placement on a series of 30 independent brain images from the OASIS-1 database [Marcus et al., 2010] (RRID:SCR_007385). Subjects from the OASIS-1 database were selected from the broad range of ages encountered in the database, restricted to cognitively intact (MMSE 30) participants.

Figure 3.2: Each anatomical fiducial in the full AFID32 protocol is demonstrated with crosshairs at the representative location in MNI2009bAsym space using the standard cardinal planes. AC = anterior commissure; PC = posterior commissure; AL = anterolateral; AM = anteromedial; IG = indusium griseum; IPF = interpeduncular fossa; LMS = lateral mesencephalic sulcus; LV = lateral ventricle; PMJ = pontomesenphalic junction.

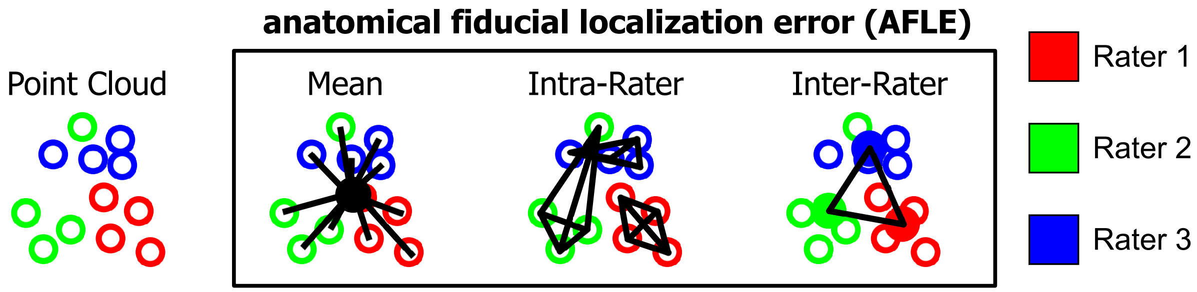

Figure 3.3: Metrics used for validating AFID placements are shown here in schematic form. Mean, intra-rater, and inter-rater AFLE can be computed for an image that has been rated by multiple raters multiple times.

Although we controlled for normal cognition by MMSE, we selected for qualitatively challenging images with more complex anatomy (asymmetric anatomy and/or variably-sized ventricles). Details on the 30 scans are provided in Appendix Section A.2 and organized into the Brain Imaging Data Structure (BIDS) format [Gorgolewski et al., 2016] (RRID:SCR_016124).

Each of the 9 participants placed 10 independent AFID32 protocols for a total of 90 AFID32 protocols and 2880 individual points. Each of the 30 MRI scans from the OASIS-1 database had AFIDs placed by 3 raters to establish inter-rater AFLE (as described in Methods Section Phase 1: Protocol Validation for Brain Templates). Intra-rater AFLE was not evaluated in Phase 2. Quality of rigid registration was visually inspected by an experienced rater (JL).

Region-of-interest segmentation

BIDS formatting permitted automatic processing of each included OASIS-1 subject using fMRIPrep version 1.1.1 [Esteban et al., 2018, Gorgolewski et al., 2016] (RRID:SCR_016216) with anatomical image processing only. Briefly, the fMRIPrep pipeline involves linear and deformable registration to the MNI2009cAsym template [Avants et al., 2008, Fonov et al., 2011] then processing of the structural MRI through Freesurfer for cortical surface and subcortical volumetric labeling [Dale et al., 1999, Fischl, 2012] (RRID:SCR_001847). We focused on using ROIs commonly used in the literature to evaluate quality of registration in the subcortex [Chakravarty et al., 2009, Hellier et al., 2003, Klein et al., 2009], i.e. the pallidum, striatum, and thalamus provided as part of the fMRIPrep output run through FreeSurfer. The striatum label required combining the ipsilateral caudate nucleus, accumbens, and putamen labels.

3.2.4 Phase 3: Evaluating subject-to-template registration

We evaluated the quality of subject-to-template registration using the output provided as part of fMRIPrep version 1.1.1 using conventional ROI-based metrics (i.e. voxel overlap) as well as distance metrics derived from our manual AFID32 annotations from Phases 1 and 2. The default template for fMRIPrep 1.1.1 was the MNI2009cAsym template. We started by visually inspecting the images qualitatively from the output fMRIPrep html pages. For each individual subject scan, we used the mean fiducial location as the optimal location calculated in Phase 2. The distance between the individual subject AFID location and the corresponding mean AFID location in the template was computed and defined as the anatomical fiducial registration error (AFRE) and computed for linear transformation alone (lin) and combined linear and nonlinear transformation (nlin). Our definition of AFRE differs from the FRE used by Fitzpatrick whose framework for neuronavigation was necessarily limited to rigid-body transformations [Fitzpatrick et al., 1998]. This was compared with ROI-based measures of spatial correspondence, specifically, the Jaccard similarity coefficient ($(A \cap B)/(A \cup B)$) and the Dice kappa coefficient ($(2 \times A \cap B)/(A + B)$), where A and B are the number of voxels in the source and reference images, respectively.

We were able to use the AFID32 points placed in Phase 1 for the MNI2009bAsym template since the only difference between the MNI2009bAsym and MNI2009cAsym templates was the resampling from 0.5 mm to 1 mm isotropic resolution. AFRE was computed for each AFID location and OASIS-1 subject, along with voxel overlap for the pallidum, striatum, and thalamus. Comparisons between AFRE and voxel overlap were made using Kendall's tau.

3.2.5 Phase 4: Evaluating template-to-template registration

BigBrain is a publicly available ultrahigh-resolution (20 micron) human brain model that has enabled bridging of macroscale anatomy with near cellular anatomy [Amunts et al., 2013] (RRID:SCR_001593). A deformable mapping provided by the MNI group has permitted the exploration of high-resolution BigBrain neuroanatomy in MNI2009bSym space (BigBrainRelease.2015; Last modified August 21, 2016; accessed August 2, 2018; Available at: `ftp://bigbrain.loris.ca/BigBrainRelease.2015/3D_Volumes/MNI-ICBM152_Space/`). In this manuscript, we refer to the registered BigBrain image as BigBrainSym. We quantify the spatial correspondence between BigBrainSym and MNI2009bSym as well as BigBrainSym and MNI2009bAsym templates using the AFID32 protocol to determine whether any significant AFRE could be identified. For MNI2009bAsym, we used mean coordinates for each AFID using rater data from Phase 1. BigBrainSym and MNI2009bSym templates were annotated de novo by three experienced raters (GG, JL, KF). The mean AFID coordinate was used as an approximation of the ideal coordinate location for each template. Spatial correspondence was estimated as the AFRE (i.e. Euclidean distance between points) for each AFID. Correlation between AFLE and AFRE were assessed using Kendall's tau.

Table 3.1: Summary of fiducial localization error across brain templates.

	Before QC		After QC			
Template	mean AFLE (mm)	# of outliers (%)	mean AFLE (mm)	# of outliers (%)	intra-rater AFLE (mm)	inter-rater AFLE (mm)
Agile12v2016	1.10 ± 1.59	3/1024 (0.29%)	1.01 ± 0.93	0/1021 (0.00%)	1.13 ± 0.86	1.14 ± 0.48
Colin27	1.71 ± 2.78	20/1024 (1.95%)	1.11 ± 1.05	1/1004 (0.10%)	1.14 ± 0.92	1.36 ± 0.88
MNI2009bAsym	0.99 ± 1.11	1/1024 (0.10%)	0.97 ± 0.80	0/1023 (0.00%)	1.03 ± 0.78	1.07 ± 0.46
Total	1.27 ± 1.98	24/3072 (0.78%)	1.03 ± 0.94	1/3048 (0.03%)	1.10 ± 0.86	1.19 ± 0.64

3.2.6 Source code and data availability

All data analysis was performed using R-project version 3.5.1. The AFIDs protocol, raw and processed data, processing scripts, and scripts used in this manuscript are available at: `https://github.com/afids`.

3.3 Results

3.3.1 Phase 1: Protocol validation for brain templates

The 8 raters had a mean experience of 11.5 ± 11.2 months in medical imaging (range: 0-24 months), 14.3 ± 17.0 months in neuroanatomy (range: 0-48 months), and 7.0 ± 8.8 months in 3D Slicer (range: 0-24 months). During the template validation phase, the raters placed a total of 3072 individual points (number of sessions = 4; templates = 3; points = 32). Average AFID32 placement time was estimated at between 20-40 minutes. Thus, a total of 1920-3840 minutes (or 32-64 hours) were logged in this phase of the study. The mean, intra-rater, and inter-rater AFLE metrics are summarized in Table 3.1.

For the raw data, the mean AFLE was 1.27 ± 1.98 mm (1.10 ± 1.59 mm for Agile12v2016; 1.71 ± 2.78 mm for Colin27; 0.99 ± 1.11 mm for MNI2009bAsym). Using a threshold of mean AFLE greater than 10 mm from the group mean, we identified 24 outliers out of 3072 independent points (0.78%). 20/24 (83.33%) of outliers were the result of variable placement in the bilateral ventral occipital horns (i.e. AFID29 and AFID30) of the Colin27 template. One pair (2/24; 8.33%) of outliers was due to left-right mislabeling (indusium griseum; AFID27 and AFID28). One additional point was mislabeled; i.e. the left anterolateral temporal horn point (AFID22) was placed at the left inferior anteromedial horn location (AFID26). After quality control (QC) and filtering outliers, mean AFLE improved to 1.03 ± 0.94 mm (1.01 ± 0.93 mm for Agile12v2016; 1.11 ± 1.05 mm for Colin27; 0.97 ± 0.80 mm for MNI2009bAsym).

Intra-rater AFLE was 1.10 ± 0.86 mm (1.13 ± 0.86 mm for Agile12v2016; 1.14 ± 0.92 mm for Colin27; 1.03 ± 0.78 mm); and inter-rater AFLE was 1.19 ± 0.65 mm (1.15 ± 0.49 mm for Agile12v2016; 1.36 ± 0.88 mm for Colin27; 1.07 ± 0.46 mm for MNI2009bAsym). Mean, intra-rater, and inter-rater AFLE for each AFID post-QC are summarized in Appendix Section

A.1.

All subsequent analyses were performed using the mean AFLE metric. We performed a one-way analysis of variance observing evidence of statistically different variance between templates (F-value = 7.88; p-value < 0.001). Differences in mean AFLE between templates were identified on subgroup analysis for the right superior lateral mesencephalic sulcus (AFID-06), culmen (AFID10), genu of the corpus callosum (AFID19), and left superior anteromedial temporal horn (AFID24), suggesting differences between templates that may contribute to errors in placement. The results for each AFID are also summarized in the Appendix Section A.1.

Furthermore, we observed several distinct patterns of AFID placement using K-means clustering of fiducial locations (point clouds) relative to the mean fiducial location (see Figure 3.4). We identified three different general patterns of point cloud distributions ranging from highly anisotropic to moderately anisotropic to isotropic.

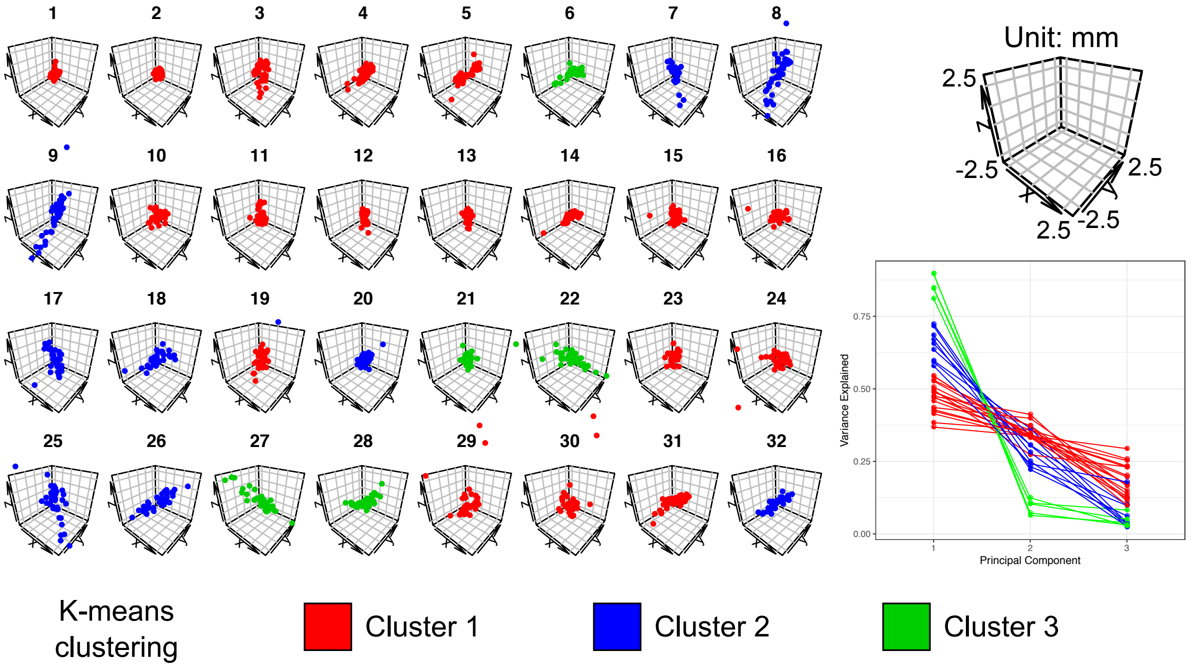

Figure 3.4: K-means clustering of point clouds relative to the mean fiducial location for each of the 32 AFIDs (left). Principle components analysis (bottom right) revealed three different general patterns were identified ranging from highly isotropic (Cluster 1: red) to moderately anisotropic (Cluster 2: blue) to anisotropic (Cluster 3: green). Results are shown for the MNI2009bAsym template. See Appendix Section A.1 for similar plots for Agile12v2016, Colin27, and the templates combined.

As a secondary analysis, we explored whether any evidence of learning over the 4 independent rating sessions could be identified (Appendix Section A.1). Using linear modeling, we identified a general decrease in mean AFLE with increasing session number although this did not meet thresholds of statistical significance (estimate = -0.02 mm/session; p-value = 0.11).

These trends were explored on the individual rater level. For two out of 8 raters, AFLE varied with session number. Rater04 demonstrated a general linear improvement of -0.17 mm/session from an initial mean AFLE of 1.64 mm (i.e. the worst performing initial session); however Rater02 worsened at a rate of 0.12 mm/session from an initial mean AFLE of 0.59 mm (i.e. the best performing initial session). No significant effect with individual AFIDs was identified. All subgroup analyses were multiple comparisons corrected using FDR (q-value < 0.05).

3.3.2 Phase 2: Protocol validation for individual subjects

During the individual subject validation phase, 9 participants completed 10 AFID protocols (= 90 total protocols) and a total of 2880 individual points distributed equally among 30 OASIS-1 datasets. We identified 28 outliers (0.97%), defined as individual point placements greater than 1 cm (10 mm) away from the group mean. 8/28 outliers (28.57%) were the result of mislabeled points: three pairs of lateral (non-midline) AFIDs and only one pair due to gross mislabeling of the target AFID structure (placement in bilateral frontal ventricular horns rather than occipital horns). Beyond left-right swapping, the AFIDs most susceptible to outliers were the following points: bilateral ventral occipital horns (AFID29-30) and bilateral indusium griseum origins (AFID27-28). Mean AFLE across the 30 scans and points was 1.28 ± 3.03 mm improving to 0.94 ± 0.73 after filtering out the outliers. Inter-rater AFLE was 1.58 ± 1.02 mm across all AFIDs. Mean AFLE and inter-rater AFLE are summarized for each AFID in Table 3.2 and subject in Appendix Section A.2. FMRIPrep ran successfully on 30/30 datasets (100.0%).

3.3.3 Phase 3: Evaluating subject-to-template registration

The following section uses the AFIDs to evaluate the quality of spatial correspondence between the Phase 2 subject data with the MNI2009cAsym template as processed through fMRIPrep. Visual inspection of the fMRIPrep generated reports revealed no gross misregistrations between MNI2009c and the individual subject scans although a pattern of worse deformable registration in subjects with enlarged ventricles was observed. The rest of this section is concerned with examining the comparative utility of conventional voxel overlap (ROI-based) metrics against the point-based (AFRE) metric proposed in this study (see Figure 3.5a).

Improvements in overlap were identified when going from linear to combined (linear and nonlinear) transformations (Table 3.3). Some heterogeneity in values was noted between ROIs with voxel overlap measures observed to be lowest for the pallidum (the smallest structure evaluated). All Jaccard values after nonlinear transformation were greater than 0.7 (greater than 0.8 for Dice kappa), generally considered to represent good correspondence between two registered images. For simplicity, we report the Jaccard coefficient as our measure of voxel

Table 3.2: Mean and inter-rater fiducial localization error pre- and post-QC for the included OASIS-1 subjects for all AFIDs.

		Before QC	After QC	
AFID	Description	Mean AFLE	Mean AFLE	Inter-Rater AFLE
01	AC	0.36 ± 0.21 (1.29)	0.36 ± 0.21 (1.29)	0.60 ± 0.25 (1.38)
02	PC	0.34 ± 0.16 (0.88)	0.34 ± 0.16 (0.88)	0.57 ± 0.21 (1.22)
03	infracollicular sulcus	0.78 ± 0.48 (3.07)	0.78 ± 0.48 (3.07)	1.34 ± 0.64 (3.84)
04	PMJ	0.83 ± 0.49 (2.44)	0.83 ± 0.49 (2.44)	1.41 ± 0.55 (2.55)
05	superior interpeduncular fossa	1.20 ± 0.75 (3.50)	1.20 ± 0.75 (3.50)	2.04 ± 0.90 (4.25)
06	R superior LMS	1.30 ± 1.74 (14.25)	1.01 ± 0.55 (2.85)	1.70 ± 0.68 (3.13)
07	L superior LMS	1.36 ± 1.71 (13.99)	1.06 ± 0.61 (3.45)	1.72 ± 0.71 (3.89)
08	R inferior LMS	1.13 ± 0.75 (5.13)	1.03 ± 0.57 (2.99)	1.77 ± 0.74 (3.43)
09	L inferior LMS	1.10 ± 0.80 (5.31)	1.01 ± 0.62 (2.72)	1.71 ± 0.86 (3.71)
10	culmen	0.99 ± 0.99 (5.66)	0.83 ± 0.62 (3.07)	1.35 ± 0.82 (3.42)
11	intermammillary sulcus	0.60 ± 0.31 (1.62)	0.60 ± 0.31 (1.62)	1.02 ± 0.41 (1.86)
12	R MB	0.40 ± 0.23 (1.11)	0.40 ± 0.23 (1.11)	0.69 ± 0.32 (1.52)
13	L MB	0.36 ± 0.20 (1.20)	0.36 ± 0.20 (1.20)	0.62 ± 0.29 (1.62)
14	pineal gland	0.68 ± 0.47 (1.98)	0.68 ± 0.47 (1.98)	1.16 ± 0.69 (2.63)
15	R LV at AC	1.00 ± 0.90 (5.28)	0.91 ± 0.72 (4.45)	1.55 ± 1.08 (5.86)
16	L LV at AC	1.01 ± 0.80 (4.53)	0.94 ± 0.70 (4.53)	1.60 ± 1.08 (5.47)
17	R LV at PC	0.92 ± 0.54 (3.42)	0.92 ± 0.54 (3.42)	1.54 ± 0.77 (3.84)
18	L LV at PC	0.87 ± 0.42 (2.20)	0.87 ± 0.42 (2.20)	1.46 ± 0.55 (2.80)
19	genu of CC	0.97 ± 0.81 (5.16)	0.89 ± 0.63 (3.69)	1.50 ± 0.89 (4.30)
20	splenium	0.54 ± 0.25 (1.24)	0.54 ± 0.25 (1.24)	0.91 ± 0.35 (1.66)
21	R AL temporal horn	1.44 ± 1.09 (7.01)	1.30 ± 0.86 (4.45)	2.21 ± 1.13 (5.92)
22	L AL temporal horn	1.22 ± 0.77 (4.11)	1.22 ± 0.77 (4.11)	2.04 ± 1.01 (4.47)
23	R superior AM temporal horn	1.28 ± 1.27 (8.22)	1.12 ± 0.88 (4.69)	1.86 ± 1.19 (4.97)
24	L superior AM temporal horn	1.09 ± 1.22 (7.54)	0.83 ± 0.61 (3.66)	1.39 ± 0.85 (4.60)
25	R inferior AM temporal horn	1.69 ± 1.43 (9.03)	1.44 ± 0.91 (4.72)	2.39 ± 1.23 (5.07)
26	L inferior AM temporal horn	1.99 ± 1.75 (8.79)	1.49 ± 1.09 (4.70)	2.42 ± 1.47 (6.64)
27	R indusium griseum origin	3.13 ± 4.19 (23.44)	1.77 ± 0.99 (4.77)	2.95 ± 1.20 (5.75)
28	L indusium griseum origin	2.99 ± 4.30 (24.30)	1.68 ± 1.00 (5.00)	2.75 ± 1.29 (5.78)
29	R ventral occipital horn	3.64 ± 10.36 (78.74)	0.69 ± 0.39 (2.11)	1.14 ± 0.54 (2.53)
30	L ventral occipital horn	3.43 ± 10.38 (80.42)	0.86 ± 0.67 (4.94)	1.39 ± 0.98 (5.72)
31	R olfactory sulcal fundus	0.99 ± 0.53 (2.29)	0.99 ± 0.53 (2.29)	1.71 ± 0.60 (2.84)
32	L olfactory sulcal fundus	1.21 ± 0.74 (4.53)	1.21 ± 0.74 (4.53)	2.11 ± 0.92 (5.81)

AFLE values summarized as: mean ± standard deviation (max value)

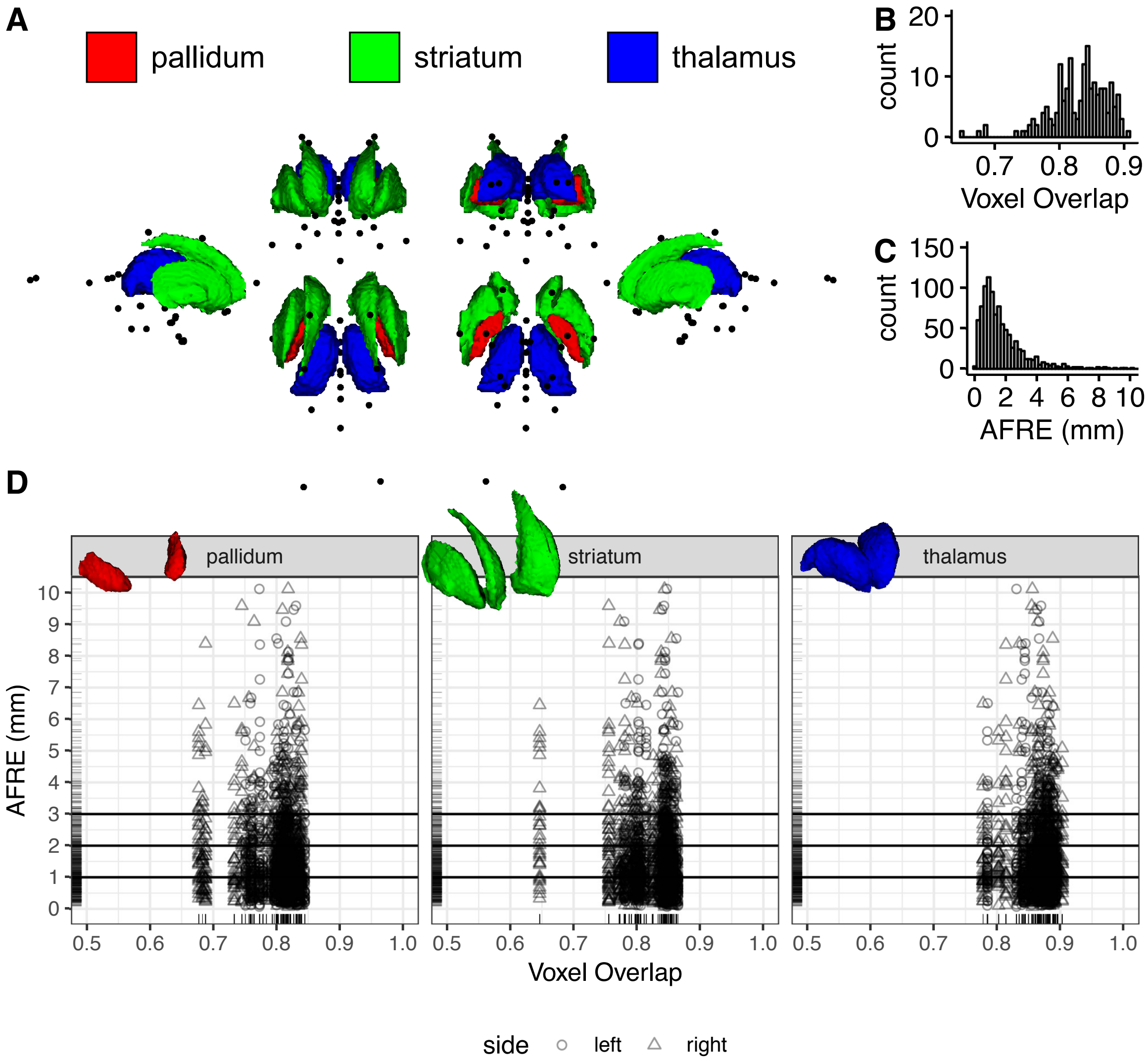

Figure 3.5: A comparison of voxel overlap and distance metrics for establishing spatial correspondence between brain regions as evaluated on fMRIPrep output. (A) Multiple views showing the location of AFIDs (black dots) relative to three commonly used ROIs used in voxel overlap measures (the pallidum, striatum, and thalamus). (B,C) The histograms for voxel overlap (Jaccard index) and AFRE, respectively. The distribution for AFRE is more unimodal with a more interpretable dynamic range (in mm) compared to voxel overlap. Trellis plots demonstrate evidence of focal misregistrations identified by AFRE not apparent when looking at ROI-based voxel overlap alone (D).

overlap for all subsequent analyses.

Mean AFRE improved from 3.40 ± 2.55 mm with linear transformation alone to 1.80 ± 2.09 with combined linear/nonlinear transformation (p-value < 0.001). AFRE was significantly decreased with nonlinear registration for all AFIDs except the pineal gland (AFID14). AFRE was observed to be higher than mean AFLE measures (see Phase 2: 0.93 ± 0.73 mm) across the same subjects providing evidence that registration error is detectable beyond the

Table 3.3: Voxel overlap (Jaccard and Kappa) of the pallidum, striatum, and thalamus after linear registration only and combined linear /nonlinear registration.

		Jaccard			Kappa		
roi	side	lin	nlin		lin	nlin	
pallidum	left	0.54 ± 0.13	0.80 ± 0.03	*	0.69 ± 0.11	0.89 ± 0.02	*
	right	0.55 ± 0.12	0.79 ± 0.05	*	0.70 ± 0.11	0.88 ± 0.03	*
striatum	left	0.53 ± 0.14	0.83 ± 0.03	*	0.68 ± 0.13	0.91 ± 0.02	*
	right	0.55 ± 0.15	0.82 ± 0.05	*	0.70 ± 0.13	0.90 ± 0.03	*
thalamus	left	0.70 ± 0.11	0.86 ± 0.03	*	0.82 ± 0.08	0.93 ± 0.02	*
	right	0.69 ± 0.11	0.87 ± 0.03	*	0.81 ± 0.08	0.93 ± 0.02	*

* significant after FDR corrected (q-value < 0.05)

limits of localization error. The number of outlier AFIDs with AFRE > 3 mm (more than 2 standard deviations above the mean AFLE found in Phase 2 for the same subjects) was 135/960 (14.06%), representing 22/32 (68.75%) unique AFIDs identified as misregistered. Each independent OASIS-1 subject had at least one AFID with AFRE > 3 mm with a mean maximum AFRE of 7.5 mm (Range: 3.16-32.78 mm). Although AFLE and AFRE were statistically correlated, the effect size was small (Kendall tau = 0.15; p-value < 0.001; Appendix Section A.3).

Subgroup analysis for each AFID is summarized in Table 3.4. AC and PC had the lowest mean AFRE at 0.36 ± 0.21 and 0.57 ± 0.29 mm, respectively. However, registration errors as high as 1.64 mm were observed for PC. The ventricles appeared particularly difficult to align on subgroup analysis of the AFIDs. The highest AFRE among all 32 AFIDs was observed for the right and left ventral occipital horns (AFID29-30) at 3.44 ± 5.77 and 4.51 ± 6.28 mm respectively with errors in certain cases over 20 mm (OAS1_0109 and OAS1_0203; Appendix Section A.3). Similarly, the lateral ventricle features (AFID15-18) also demonstrated high AFRE ranging from 2.11-3.01 mm on average and up to 7 mm or more. Finally, the alignment of the temporal horn features (AFID21-26) also support this observation with mean errors of 1.67-2.41 mm with observed errors over 5 mm.

AFRE was negatively correlated with voxel overlap but the estimates were small (tau = -0.02; p = 0.03). Subgroup analysis demonstrated the same negative trends for the right pallidum and striatum but these results did not survive multiple comparisons correction (Figure 3.5d). No correlation between voxel overlap measures and individual AFID AFREs survived multiple comparisons correction. Comparing histograms, AFRE demonstrated a more unimodal distribution peaking between 1-2 mm (Figure 3.5b) while voxel overlap exhibited two peaks within the 0.8-0.9 range (Figure 3.5c). The AFRE plot also demonstrated a longer tail up to 10 mm, thus permitting a broader dynamic range in which to judge the quality of registration. In contrast, voxel overlap metrics were sparse in the lower range making interpretation more difficult. Finally, we observed that even where voxel overlap was high, suggesting good spatial correspondence, high AFRE values were also observed for certain AFIDs (see Figure 3.5d). These represent focal AFID locations where two images are misregistered despite stable voxel overlap results (Figure 3.6).

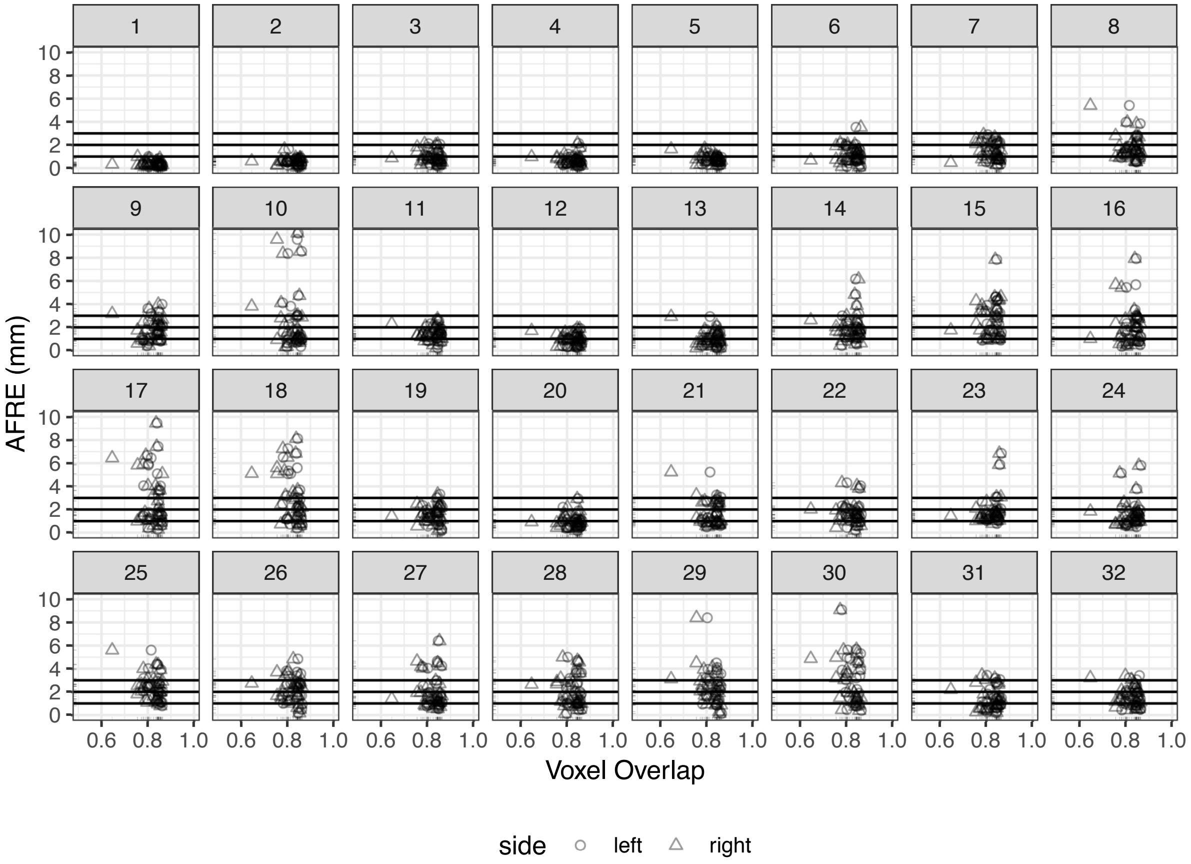

Figure 3.6: Investigating relationships between voxel overlap of the striatum and AFRE for each AFID. Focal misregistrations are identified using AFRE for the following AFIDs: 8-10, 14-18, 21-30. The most commonly misregistered regions include the inferior mesencephalon, superior vermis, pineal gland, indusium griseum, and ventricular regions. Horizontal lines are used to demarcate tiers of AFLE error above which AFRE values are beyond a threshold of localization error alone, i.e. the top horizontal line at 3 mm represents more than 2 standard deviations beyond the mean AFLE. Separate plots for the pallidum and thalamus ROIs are provided in Appendix Section A.3.

3.3.4 Phase 4: Evaluating template-to-template registration

Mean AFLE for BigBrainSym and MNI2009bSym was 0.59 ± 0.40 mm combined with no outliers (BigBrainSym: 0.63 ± 0.50 mm; MNI2009bSym: 0.55 ± 0.26 mm). We highlighted

Table 3.4: AFRE after linear registration alone and combined linear/nonlinear registration.

		Mean AFRE		
AFID	Description	lin	nlin	
01	AC	2.15 ± 0.97 (4.96)	0.36 ± 0.21 (0.99)	*
02	PC	1.83 ± 0.96 (4.58)	0.57 ± 0.29 (1.64)	*
03	infracollicular sulcus	2.20 ± 1.23 (5.71)	0.93 ± 0.53 (2.11)	*
04	PMJ	2.50 ± 1.36 (6.06)	0.68 ± 0.43 (2.13)	*
05	superior interpeduncular fossa	2.35 ± 1.06 (4.75)	0.76 ± 0.37 (1.69)	*
06	R superior LMS	2.07 ± 0.95 (4.32)	1.17 ± 0.74 (3.52)	*
07	L superior LMS	2.03 ± 0.85 (4.22)	1.43 ± 0.77 (2.88)	*
08	R inferior LMS	2.45 ± 1.37 (7.50)	1.78 ± 1.11 (5.41)	*
09	L inferior LMS	2.54 ± 1.26 (6.63)	1.83 ± 0.96 (3.99)	*
10	culmen	4.50 ± 2.93 (12.72)	2.73 ± 2.81 (10.12)	*
11	intermammillary sulcus	2.81 ± 1.62 (6.30)	1.44 ± 0.60 (2.73)	*
12	R MB	2.72 ± 1.67 (6.90)	0.93 ± 0.48 (1.90)	*
13	L MB	2.84 ± 1.70 (6.14)	1.01 ± 0.62 (2.93)	*
14	pineal gland	2.53 ± 1.39 (5.70)	2.01 ± 1.24 (6.16)	
15	R LV at AC	4.44 ± 1.84 (7.90)	2.70 ± 1.59 (7.85)	*
16	L LV at AC	4.50 ± 1.95 (8.40)	2.11 ± 1.72 (7.92)	*
17	R LV at PC	4.81 ± 2.54 (10.07)	2.96 ± 2.42 (9.46)	*
18	L LV at PC	4.80 ± 2.64 (10.34)	3.01 ± 2.22 (8.13)	*
19	genu of CC	3.73 ± 1.82 (7.88)	1.56 ± 0.76 (3.32)	*
20	splenium	2.96 ± 1.88 (7.57)	0.97 ± 0.60 (2.93)	*
21	R AL temporal horn	3.79 ± 1.71 (7.50)	1.70 ± 1.09 (5.23)	*
22	L AL temporal horn	3.62 ± 1.45 (6.98)	1.67 ± 0.98 (4.31)	*
23	R superior AM temporal horn	3.34 ± 1.63 (7.25)	1.93 ± 1.34 (6.85)	*
24	L superior AM temporal horn	3.44 ± 1.80 (8.20)	1.67 ± 1.25 (5.80)	*
25	R inferior AM temporal horn	4.02 ± 1.97 (8.32)	2.41 ± 1.16 (5.61)	*
26	L inferior AM temporal horn	4.13 ± 1.70 (8.20)	2.21 ± 1.09 (4.84)	*
27	R indusium griseum origin	3.36 ± 2.07 (8.46)	2.06 ± 1.49 (6.40)	*
28	L indusium griseum origin	3.60 ± 1.68 (8.83)	2.05 ± 1.37 (5.00)	*
29	R ventral occipital horn	5.86 ± 6.32 (36.26)	3.44 ± 5.77 (32.78)	*
30	L ventral occipital horn	6.99 ± 6.72 (33.74)	4.51 ± 6.28 (29.76)	*
31	R olfactory sulcal fundus	2.83 ± 1.36 (7.50)	1.37 ± 0.95 (3.44)	*
32	L olfactory sulcal fundus	2.94 ± 1.28 (6.49)	1.57 ± 0.84 (3.41)	*

AFRE values summarized as: mean ± standard deviation (max value)

* significant after FDR corrected (q-value < 0.05)

AFRE values beyond a threshold of 2 mm given this represents more than 2 standard deviations beyond the mean AFLE in the templates being studied. AFRE values beyond this minimum were flagged as highlighting focal misregistrations between templates.

The mean AFRE between BigBrainSym and MNI2009bSym was 2.16 ± 1.99 mm and between BigBrainSym and MNI2009bAsym was 2.30 ± 1.83 mm, both above threshold. The largest error was 9.27 mm (MNI2009bSym) and 9.38 mm (MNI2009bAsym), found at the culmen (AFID10). Out of the 32 AFIDs defined, 11 (34.4%) were above threshold for the symmetric template and 12 (37.5%) for the asymmetric template. The most prominent misregistrations tended to occur in the posterior brainstem with the infracollicular sulcus (AFID03) and pineal gland (AFID14) quantified as 6.36 mm and 4.42 mm AFRE, respectively. These registration errors can be seen in Figure 3.7 and are summarized by AFID in Table 3.5. In addition, AFRE up to 2.78 mm were observed for AFIDs placed along the lateral mesencephalic sulcus (AFID06-09) and at the superior interpeduncular fossa (AFID05), which represent features demarcating the lateral and superior bounds of midbrain registration. Registration differences between these templates was also above threshold for the left lateral ventricle at the anterior commissure (AFID16), splenium (AFID20), left anterolateral temporal horn (AFID22), bilateral ventral occipital horns (AFID29-30), and bilateral olfactory sulcal fundi (AFID31-32). No correlation between AFRE and AFLE was found using BigBrainSym AFLE (tau = 0.071; p-value = 0.57) or MNI2009bSym AFLE (tau = -0.046; p-value = 0.71). Interestingly, AFRE was somewhat lower with MNI2009bAsym in many midline AFIDs but higher for certain lateral landmarks, i.e. the left inferior anteromedial temporal horn and bilateral origin of the indusium griseum (AFID26-28).

Finally, we explored the differences in correspondence between the MNI2009bSym and MNI2009bAsym. Note that these differences are not registration errors per se, as the two are not meant to be in the exact same coordinate space. The differences were generally more subtle (0.88 ± 0.68 mm) but 4 AFIDs (12.5%) were found to be above threshold. As expected, correspondence differences greater than 2 mm occurred in lateral rather than midline AFIDs, specifically at the left anterolateral temporal horn (AFID22), bilateral origins of the indusium griseum (AFID27-28), and left lateral ventral occipital horn (AFID30). No correlations between correspondence and AFLE were found (tau = 0.210; p-value = 0.09).

3.4 Discussion

The present findings demonstrate that a series of anatomical fiducials, referred to here as AFIDs, can be consistently placed on standard structural MR images and can be used to quantify the degree of spatial alignment between brain images in millimeters. We found that AFIDs

Table 3.5: AFIDs demonstrating evidence of template-to-template misregistration for BigBrainSym with MNI2009bSym and BigBrainSym with MNI2009bAsym as well as correspondence differences between MNI2009bAsym and MNI2009bSym.

		AFRE (mm)				Distance** (mm)	
AFID	Description	BigBrainSym vs MNI2009bSym		BigBrainSym vs MNI2009bAsym		MNI2009bAsym vs MNI2009bSym	
3	infracollicular sulcus	6.36	*	5.48	*	0.98	
9	L inferior LMS	2.78	*	2.48	*	0.68	
10	culmen	9.27	*	9.39	*	0.21	
14	pineal gland	4.42	*	4.16	*	0.41	
16	L LV at AC	2.05	*	1.22		0.86	
20	splenium	2.23	*	2.2	*	0.1	
22	L AL temporal horn	4.69	*	3.44	*	2.45	*
26	L inferior AM temporal horn	1.88		2.58	*	0.98	
27	R indusium griseum origin	1.21		3.6	*	2.81	*
28	L indusium griseum origin	0.74		2.88	*	2.29	*
29	R ventral occipital horn	2.54	*	3.99	*	1.63	
30	L ventral occipital horn	5.88	*	4.22	*	2	*
31	R olfactory sulcal fundus	2.62	*	1.84		1.1	
32	L olfactory sulcal fundus	3.06	*	4.21	*	1.24	

* AFRE > 2 mm

** Distance between fiducials (not truly a registration error since templates are designed to be in different spaces)

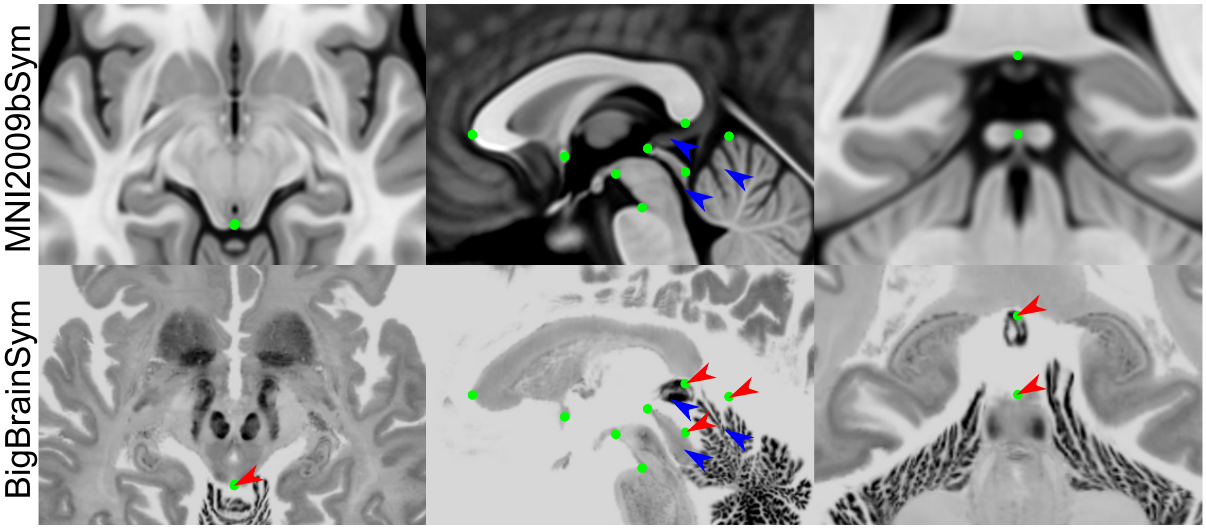

Figure 3.7: Select views demonstrating registration errors between BigBrainSym and MNI2009bSym. The green dots represent the optimal AFID coordinates in MNI2009bSym space superimposed in both templates to provide a basis for comparing registration differences. While many of the midline AFIDs are stable across both templates, the infracollicular sulcus, pineal gland, splenium, and culmen are misregistered in BigBrainSym (red arrows). The AFIDs draw attention to registration differences in the BigBrainSym space in the tectal plate, pineal gland, and superior vermis (blue arrows).

are reproducible, not overtly manually intensive (20-40 minutes once trained), and more sensitive to local registration errors than standard voxel overlap measures. Our entire protocol and study framework leverages open resources and tools, and has been developed with full transparency in mind so that others may freely use, adopt, and modify.

The work presented here is inspired heavily by classical stereotactic methods [Talairach et al., 1957], where point-based correspondence has been used to align brain templates with patient anatomy to enable atlas-based surgical targeting. The anterior and posterior commissure were originally identified as prominent intraventricular features based on air studies, prior to the invention of computed tomography or MRI. The AC and PC have proven to be reliable features on MRI and were adopted by neuroscientists for the alignment of brain images to templates, in what is referred to as the Talairach grid normalization procedure [Brett et al., 2002, Talairach and Tournoux, 1988]. The advent of robust and openly available software for automatic or semi-automatic labeling of regions-of-interest in brain images has led to a relative underemphasis of point-based alignment. We demonstrate here that point-based metrics are more sensitive to focal misregistrations than voxel overlap measures and quantified in millimeters.

Tolerance to focal misregistration in images undoubtedly will depend on the application; but there is no doubt that poor image correspondence can result in inaccurate (and possibly erroneous) predictions and conclusions in neuroimaging studies. Our results evaluating correspondence error in an fMRI preprocessing pipeline revealed local template misregistrations of 1.80 ± 2.09 mm. For many fMRI or diffusion-based applications, this mean error is about the size of a voxel; and thus may be within an acceptable tolerance. However, mean maximum errors of over 7 mm were also observed and may begin to impact the sensitivity to discovery as well as the accuracy of localization of affected brain regions in a task or connectivity analyses. These misregistrations also may affect the interpretation of voxel-based and deformation-based morphometry studies that seek to investigate subtle shape differences between study populations. Finally, minimizing registration error becomes particularly critical for analyses pertaining to stereotactic interventions like deep brain stimulation (DBS) where millimeters can represent the difference between optimal therapy and side effects.

3.4.1 Protocol development and validation

After a single training session, novice raters could place AFIDs at a mean AFLE of approximately 1-1.5 mm across all AFID32 points. Placement error varied from one template to another and among AFIDs (Appendix Section A.1). Raters had the least amount of error with placements for the MNI2009bAsym and Agile12v2016 templates. In contrast, fiducial placement errors were higher when raters were asked to place AFIDs for individual subjects, i.e. Colin27 as well as the OASIS-1 database. Repeatability was assessed using measures of intra-rater and inter-rater AFLE. Intra-rater AFLE was lowest for the MNI2009bAsym and highest in Colin27 (Table 3.1). Inter-rater AFLE was again lowest for MNI2009bAsym and highest in Colin27 and the OASIS-1 datasets. This demonstrates how AFIDs are more difficult to place due to individual variability versus in population templates where the individual nuances of these features may be effectively blurred out. Overall, the placement error remains acceptable (1-2 mm) among all annotated images.

The AC and PC were the most reliably identifiable AFIDs with mean AFLE of less than 0.5 mm and inter-rater AFLE of 0.5-1 ± 0.3 mm observed. These results compared favorably to an analysis of experienced neurosurgeons by Pallaravam and colleagues placing the same AC-PC points where they observed a point placement error (equivalent to the inter-rater AFLE metric used here) that was surprisingly higher at 1-2 mm ± 1.5 mm [Pallavaram et al., 2008]. We speculate that the higher variability in the referenced study was the lack of restriction on how the AC-PC landmarks were placed; that is, some stereotactic neurosurgeons continue to use the intraventricular edge of each commissure, which was the classical technique used by Talairach during air studies, while others used the center of each commissure [Horn et al., 2017a]. The distance from the center to the ventricular edge can be several millimeters likely accounting for this difference. Overall, our findings demonstrate that enforcing certain practices such as using the center of each commissure play an important role in the consistency and standardization of fiducial placement.

In contrast, certain fiducial points contributed substantially to worse overall estimates of fiducial localization error. In particular, the bilateral ventral occipital horns (AFID29-30) had higher placement errors. Placement was particularly inaccurate for individual subjects where the ventricular atrium tapered completely in many individual subject studies (including Colin27), and thus the posterior continuation into the occipital horn was sometimes difficult to visualize or resolve at all. The bilateral origins of the indusium griseum (AFID27-28) were also difficult for raters to place consistently.

3.4.2 Point-based versus ROI-based metrics

Previous work has shown that nonlinear registration improves alignment between structures [Chakravarty et al., 2009, Hellier et al., 2003, Klein et al., 2009], and that the choice of parameters matters. These existing studies have mostly used voxel overlap measures to support their findings. Our results are also in-line with prior work but also demonstrate how AFIDs are complementary and more sensitive than ROI-based metrics for evaluating both local and global spatial correspondence of brain images (see Figure 3.5).

We were able to compare the relative efficacy of AFRE and voxel overlap for subjects from the OASIS-1 database and several commonly used templates. AFRE had a more unimodal distribution and a longer tail facilitating identification of focal misregistrations between images (Figure 3.5). On the other hand, the Jaccard histogram was more sparse towards the tail of the distribution suggesting a poorer ability to discriminate. One key advantage of AFRE is its interpretability, representing the distance in millimeters between aligned neuroanatomical structures in two images, compared to voxel overlap, which is a relative measure and unitless. It is commonly perceived in segmentation studies that voxel overlap measures greater than 0.7 represent accurate correspondence between regions. However, our analysis demonstrates that even with generally high overlap after nonlinear registration, focal misregistrations of AFIDs above 7 mm may be identified (Figure 3.6 and Table 3.4).

3.4.3 Subject-to-template registration

We chose to evaluate the subject-to-template registrations computed as part of an fMRI processing pipeline, fMRIPrep [Esteban et al., 2018], as a use case for our AFIDs protocol. Functional MRI studies may not represent the optimal use case due to the relatively coarse spatial resolution relative to the size of misregistration effects we can detect with AFIDs, and because most fMRI researchers are focused on cortical activation while our protocol emphasizes and detects misregistrations in the deep brain regions. Our choice to investigate fMRIPrep registration performance was motivated by their transparent approach to the development of preprocessing software for neuroimaging and BIDS integration [Gorgolewski et al., 2016, Gorgolewski and Poldrack, 2016]. The active developer and support base, as well as growing adoption by many end-users were other contributing factors. Our analysis revealed misregistrations on the order of 1.80 ± 2.09 mm and as high as over 30 mm that would be more difficult to identify by qualitative evaluation or ROI-based analysis alone.

While this points to potential caution with the use of standardized pipelines like fMRIPrep for template registration, it should be noted that fMRIPrep was designed with a focus on robustness, rather than accuracy. The underlying parameters and processing steps used in fMRIPrep are fully transparent. In addition, the underlying deformable registration software used [Avants et al., 2008] has been demonstrated to achieve high performance in studies using traditional voxel overlap measures [Klein et al., 2009]. The focal template misregistrations we have identified in fMRIPrep with AFIDs are meant to serve as a baseline for refinement in future versions that can be compared transparently and potentially incorporated for testing new versions as part of a continuous integration workflow. Using additional image contrasts [Xiao et al., 2017] or subcortical tissue priors [Ewert et al., 2019] to drive template registration have been demonstrated using conventional voxel overlap techniques to result in more optimal registrations that can also be tested using the AFIDs framework.

3.4.4 Template-to-template registration

We recommend that imaging scientists exercise caution when displaying statistical maps using a template other than the one to which the original deformations were performed. For example, it has become increasingly common to project statistical maps and subject data registered to MNI space using BigBrain for visualization purposes. In this study, we identified clear evidence of registration differences between several templates commonly assumed to be in the same coordinate space: BigBrainSym and MNI2009bSym, and even greater between BigBrainSym and MNI2009bAsym because of the differences in AFID locations in MNI2009bSym and MNI2009bAsym. Specifically, misregistrations as high as over 9 mm have been identified. Many of these errors occur in the midbrain region (Table 3.5), which would have implications in particular if using BigBrainSym to project locations of electrode implantations. In support of other recent work (Horn et al., 2017), this study highlights the importance of understanding which exact template one is using for processing and analysis: that multiple "MNI" templates exist (with different version dates, types, and symmetry), as do registration differences between these templates.

3.4.5 Teaching neuroanatomy

Our AFID32 protocol may also hold particular value for teaching neuroanatomy. In fact, evidence from our study suggests that even relative novices can be trained to place AFIDs accurately, including the AC and PC, with comparable accuracy and variability to trained neurosurgeons (Table 3.2). By releasing the data acquired in this study, we provide a normative distribution of AFID placements that can be used to quantify how accurately new trainees can place points. These measures can be used to gauge the comprehension of students regarding the specific location of neuroanatomical structures in a quantitative (millimetric) manner and focus efforts on consolidating understanding based on where localization errors were higher. To date, over a series of locally-held workshops and tutorials, over 60 students have been trained to complete the AFID32 protocol.

3.4.6 Limitations and future work

While we have found the AFIDs proposed to be quite reliable, there is clearly location-related heterogeneity in placement error. We make no claims that this set of anatomical fiducials is optimal and in the future, other locations may prove to be more effective than others. Also, for this first proposed set of AFIDs, we limited our locations to deep structures where less inter-subject variability exists compared to cortical features (Thompson et al., 1996); future extensions could include linking our workflow with cortical surface-based [Fischl, 2004] and sulcal-based [Hellier et al., 2003, Perrot et al., 2011, Mangin et al., 2015] methods of spatial correspondence. Development of similar protocols for other neuroimaging modalities such as T2-weighted or diffusion-based contrasts may also be of value. In addition, fiducial localization error may be biased by how the raters were taught to place the fiducials; in our case, we organized an initial interactive tutorial session, and provided text and picture-based resources of how to place the AFIDs. It is also possible that AFLE would be lower if performed by a more experienced group of raters. Also, how AFID placement behaves in the presence of lesional pathology remains an open question. We have made the annotations and images available to allow other groups to propose other AFID locations and descriptions that could be similarly validated. We plan to post any modifications to the protocol as separate versions at the linked repository.

The AFIDs protocol requires correct placement of the anterior commissure (AFID01) and posterior commissure (AFID02) points. We made this decision as it helps to align the brain images into a more standard orientation for subsequent placement of bilateral fiducials. In particular, 4 of the AFIDs are dependent on AC-PC alignment (the lateral ventricles at AC and PC in the coronal plane). It is possible that error in AFID placements could be compounded by initial error in placement of AC and PC. Fortunately, AC and PC can be placed with high trueness and precision (< 1 mm) (Table 3.2), consistent with prior studies [Liu et al., 2015]. We made the decision to perform AC-PC alignment to permit more accurate placement of lateral AFIDs, which may otherwise have appeared quite oblique from each other if the individual's head was tilted in the scanner. Thus, on balance, AC-PC alignment probably mitigates placement error in lateral AFIDs compared to placing fiducials in the native MRI space. Further research can examine these potential spatial biases more systematically.

Beyond evaluating correspondence, AFIDs could be used for point-based inter-subject or subject-to-template registration. AFIDs used in combination with classic rigid registration algorithms such as Iterative Closest Point [Besl et al., 1992] may result in more optimal initial linear registration between images. In addition, point-based deformable registration using (B-splines) may produce more efficient, lower order deformable registrations between two images [Bookstein, 1997]. To prevent circular reasoning, we thought this would be best evaluated as independent studies. Finally one compelling extension of this work would be to automate or semi-automate AFID placement, which would enable inclusion of AFID-based metrics in standardized workflows involving template or intersubject registration.

3.5 Conclusions

Our proposed framework consists of the identification of anatomical fiducials, AFIDs, in structural magnetic resonance images of the human brain. Validity has been established using several openly available brain templates and datasets. We found that novice users could be trained to reliably place these points over a series of interactive training sessions to within millimeters of placement accuracy. As an example of different use cases, we examined the utility of our proposed protocol for evaluating subject-to-template and template-to-template registration revealing that AFIDs are sensitive to focal misregistrations that may be missed using other commonly used evaluation methods. This protocol holds value for a broad number of applications including intersubject alignment and teaching neuroanatomy.

Chapter 4

Quantification of local geometric distortion in structural magnetic resonance images: Application to ultra-high fields

This chapter is based on the following manuscript:

- Lau, J. C., Khan, A. R., Zeng, T. Y., MacDougall, K. W., Parrent, A. G., & Peters, T. M. (2018). Quantification of local geometric distortion in structural magnetic resonance images: Application to ultra-high fields. NeuroImage, 168, 141–151.

4.1 Introduction

Ultra-high field ($\geq$ 7 Tesla) magnetic resonance imaging (MRI) allows for improved *in vivo* visualization of neuroanatomical structures, facilitating detailed morphological and functional study. The superiority of 7T neuroimaging has been demonstrated for visualizing subcortical anatomy due to increased spatial resolution, tissue contrast, and improved signal-to-noise ratio [Abosch et al., 2010, Cho et al., 2010, Kerl et al., 2012]. The subthalamic nucleus (STN) and globus pallidus internus (GPi) are more clearly and reliably visualized at 7T, suggesting ultra-high field MRI can facilitate better understanding of these structures [Kerl et al., 2012, Keuken et al., 2013].

However, the increase in field strength can result in significant geometric artifacts that must be considered, not only in neuroscientific study, but also when considering the use of 7T for image-guided interventions where accuracy is critical [Sankar and Lozano, 2011, Sumanaweera et al., 1994a, Sumanaweera et al., 1994b, Wang et al., 2005]. Stereotactic neurosurgical procedures rely on submillimeter-to-millimeter ranges of accuracy for patient safety, and the presence of geometric distortion in MRI results in loss of spatial confidence in patient images. Geometric inhomogeneity in MR images is the result of multiple scanner and patient-related factors including gradient coil nonlinearity and magnetic susceptibility. Gradient coil nonlinearities are geometric errors introduced through the coil design process with regions closest to the magnet and coil isocenter being the most geometrically accurate. Magnetic susceptibility artifacts occur as a result of local magnetic field inhomogeneities at tissue interfaces, and since they increase linearly with field strength, can become increasingly problematic at ultra-high fields [Littmann et al., 2006].

Several studies have evaluated the problem of geometric distortion at ultra-high field [Cho et al., 2010, Duchin et al., 2012, Neumann et al., 2015]. Results using MRI phantoms have been inconsistent with one study reporting submillimeter accuracy with appropriate higher-order active shimming [Cho et al., 2010] and another claiming deviations in the 2-3 mm range [Neumann et al., 2015]. Furthermore, the extent to which a phantom approximates geometric distortion in *in vivo* patient data remains unclear. Phantom studies can characterize gradient nonlinearities but do not account for anatomical and physiological distortions resulting from magnetic susceptibilities at tissue interfaces. Another approach involves characterization of distortion in subjects scanned on both 7T and lower-field MRI. By using a combination of qualitative evaluation of registration, manual fiducial placement error, and analysis in 9 block-shaped regions, Duchin et al. [Duchin et al., 2012] showed that subcortical targets are minimally effected by geometric distortion and most significant in the orbital frontal block. Unfortunately, the results of existing studies are difficult to generalize to other sites as the distribution and magnitude of geometric distortion is known to vary from scanner to scanner [Caramanos et al., 2010]. Replicating these studies at each site with fiducial placement would be manually intensive, and prone to intra-rater and inter-rater variability.

In this work, we present a computational method for quantifying geometric distortion in 7T structural images. Our technique estimates distortion using deformation fields automatically derived from nonlinear registration of 7T data to corresponding subject data at lower fields. Voxel-wise statistical analysis in a common stereotactic space permits the identification of focal brain regions systematically affected by geometric distortion that should be accounted for in neuroimaging analysis and planning stereotactic interventions. Finally, for validation, we compared our automated measures against manual fiducial placement.

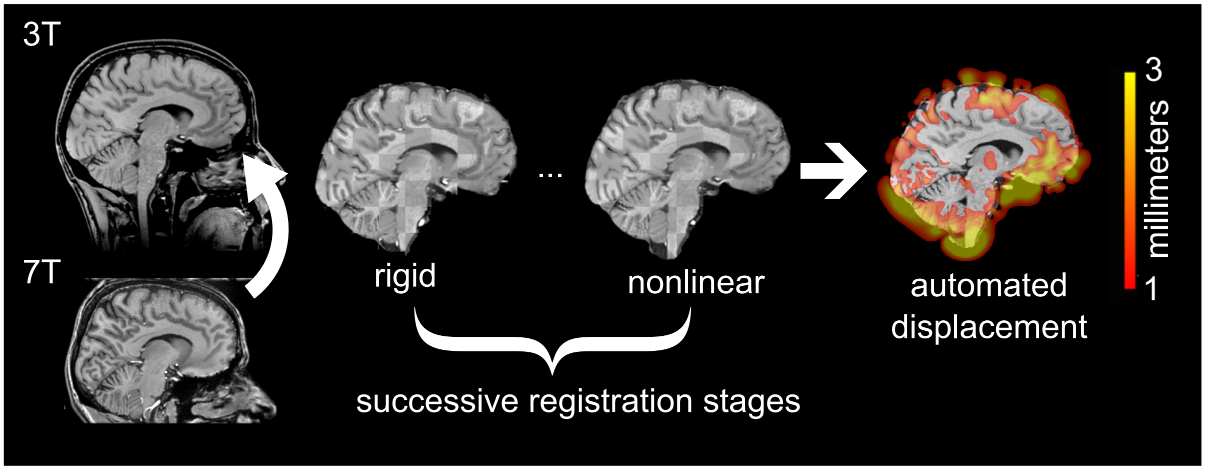

Figure 4.1: Workflow for the quantification of local geometric distortion in a single subject at ultra-high field. The leftmost images represent 3T and 7T images of the same subject in native space at the best equivalent sagittal slice. Qualitatively, the 7T image is more block-shaped than the equivalent 3T image. Checkerboard visualization reveals areas of registration mismatch after rigid and nonlinear registration stages (affine stage omitted from figure). Finally, we quantify local displacement in millimeters overlaid on the 3T image space using the nonlinear deformation field.

4.2 Materials and Methods

4.2.1 Participants and MRI Acquisition Protocol

22 participants (mean age 30.8 ± 9.2 years; 14 female) were scanned on both 3T and 7T imagers at Robarts Research Institute (London, ON, Canada) between 2010 and 2013 (time between scans: 78.2 ± 217.8 days; range: 0-633 days; 12 of 22 participants with scans on the same day). Informed consent was obtained.

All subjects were scanned using a 3T MRI scanner (GE Discovery MR750). A T1-weighted (T1w) 3T image was acquired as part of a DESPOT1-HIFI protocol using a 32-channel head coil [Deoni et al., 2007, Deoni et al., 2005, Deoni et al., 2003] with a receiver bandwidth of 19.23 kHz. The DESPOT1-HIFI technique permits rapid high-resolution quantitative T1 mapping extracted from spoiled gradient recall (SPGR) echo images acquired at two different flip angles (4°/18°) with other parameters remaining the same: TR = 8.36 ms, TE = 3.71 ms, matrix = 220 x 220, slice thickness = 1 mm, resolution = 1 mm isotropic. The T1w image acquired with a flip angle of 18° was used for all further morphometric comparisons between 7T and 3T. Ultra-high field data were acquired on a 7T imager (Agilent, Santa Clara, CA, USA/Siemens, Erlangen, Germany) using a 16-channel transmit-receive head coil array with a receiver bandwidth of 50 kHz. A T1-weighted MPRAGE sequence was acquired (TR = 8.1 ms, TE = 2.8 ms, TI = 650 ms, flip angle = 11°, matrix = 256 x 512 x 172, resolution = 1 mm isotropic, scan time = 5:42 min). Both 3T and 7T datasets were acquired as sagittal source 3D with the readout direction being superior-inferior and the phase-encode direction being anterior-posterior with respect to the brain anatomy.

4.2.2 Data Processing

Intensity non-uniformities of both 7T and 3T T1 images were corrected using retrospective bias field correction by N4 [Sled et al., 1998, Tustison et al., 2010]. The Brain Extraction Tool (BET) as implemented in FSL was used for brain masking (fractional intensity threshold = 0.4). At 7T, bias field correction was performed a second time due to evidence of residual intensity non-uniformity [Boyes et al., 2008, Seiger et al., 2015, Tardif et al., 2010].

An image-processing pipeline was developed to iteratively align a source to a target T1w image. The 3T T1w image was considered the target for registration. The source volume (7T) was registered iteratively to the target volume (3T) first using rigid body (6 degrees-of-freedom or DOF) and affine (12 DOF) registration via block-based matching [Ourselin et al., 2001], followed by nonlinear registration using a free-form deformation algorithm implemented in the NiftyReg package using default parameters [1] [Modat et al., 2010]. The combined linear and nonlinear transformations were concatenated and applied to the source volume, with the result being a 7T T1 image resampled to 3T space at 1 mm isotropic resolution. For group analysis, transformations were computed from 3T to MNI152 space using the same iterative process of rigid to affine to nonlinear registration.

4.2.3 Voxel-Level Metrics

The computed deformation field was converted to a 1 mm isotropic displacement field for each subject providing an estimate of the displacement of a voxel at 7T to the best corresponding local voxel at 3T after nonlinear registration. Euclidean distance was computed from the displacement vector at each voxel location as a quantitative estimate of local geometric distortion, which we have called automated displacement for consistency. Voxel-wise scalar displacements in the standard Cartesian directions were also stored so that we could determine which x, y or z contributed to the local displacement value. In order to evaluate the principal x, y or z component of displacement at each voxel, we used two different metrics: maximum component and relative index. The maximum component was computed by calculating the maximum x, y or z component. The relative index was calculated by normalizing the displacement in each component by the sum of displacements (x + y + z).

The image isocenter coordinates were propagated from the 7T and 3T origins (world coordinates: 0,0,0) to the MNI152 reference space using the previously computed transformations. The relationship between distance from isocenter and local displacement was plotted on a bivariate histogram across all voxels and subjects.

For group analysis, the scalar automated displacement and component maps were transformed into MNI152 space using the previously computed transformations from 3T to standard space. Mean automated displacement was calculated as a summary measure for all included subjects. To evaluate the effect of the position of the 7T image isocenter on distortion, we computed correlation maps between the x, y, and z components of the isocenter with corresponding voxel estimates of automated displacement.

Scalar displacement and correlation maps for each subject were imported into R (version 3.2.4) for statistical processing. At each voxel within the reference brain mask, we considered any statistically significant displacement more than 1 voxel (1 mm at 3T) to be clinically significant, and thus tested the null hypothesis that voxel-wise displacement was less than 1 mm. Non-parametric Wilcoxon rank sum testing was used for statistical analysis. Multiple comparisons correction was performed using the false-discovery rate (FDR) controlling for an adjusted

---

[1] https://sourceforge.net/projects/niftyreg/; git version hash key 83d8d1182ed4c227ce4764f1fdab3b1797eecd8d downloaded and compiled January 13, 2016

p-value (q-value < 0.025). The FDR-corrected q maps were converted to binary masks, which were then applied to the effect size maps and overlaid on the reference atlas for visualization.

4.2.4 Region-of-Interest Analysis

Region-of-interest (ROI) analysis was performed using the Harvard-Oxford (Desikan et al., 2006; 113 regions) and ATAG subcortical [Keuken et al., 2013] atlases in MNI space. Since the ATAG atlas is probabilistic, we used binarized ROIs after thresholding for voxels with ≥ 10% likelihood of the corresponding label. In addition, a lobar atlas was derived from the Harvard-Oxford atlas by classifying each of the 113 regions into frontal, parietal, occipital, temporal, insular, and subcortical regions (6 per hemisphere; 12 regions). Regional differences in geometric distortion were summarized using two measures: mean displacement (average automated displacement among all voxels in the ROI) and maximum displacement (average displacement after taking maximum automated displacement at each voxel in the ROI). As in the voxel-wise analysis, the null hypothesis of less than 1 mm (1 voxel) of displacement was tested non-parametrically. Multiple comparisons correction was performed for all ROIs (137 total) separate from the voxel-wise analysis using an FDR of q < 0.025. The regional effect of isocenter position was summarized using mean x, y, and z correlation in each ROI (137 x 3 = 411 total comparisons) also corrected using the same FDR.

4.2.5 Validation

Quality of image preprocessing and registration were evaluated by visual inspection (JCL, TYZ) of all subject data by examining correspondence between anatomical features in images as overlays in 3D Slicer [Fedorov et al., 2012]. Quantitative validation was performed by manual fiducial placement on both 7T and 3T datasets, also in 3D Slicer. Twenty subjects had five midline fiducials using a previously published protocol [Duchin et al., 2012], and five subjects had 75 fiducials. The midline fiducial locations were the following:

1. Anterior commissure
2. Posterior commissure
3. Midpoint of the cerebral aqueduct
4. Midpoint of the optic chiasm
5. Midpoint of the infundibulum

Five randomly chosen subjects had a total of 75 fiducials placed (5 midline, 60 whole brain, 10 in highly displaced areas). For the whole brain fiducials, 30 were placed in each hemisphere with the rater choosing salient 3D neuroanatomical locations that could be identified on the cortical surface and sulci. An additional 10 fiducials were chosen based on regions identified as highly displaced, in other words, voxels located in areas of increased displacement identified by overlaying our automated method on the subject's 3T image.

Each fiducial was placed by two raters (JCL, TYZ) on the 7T image after initial placement at 3T for each subject. After several weeks, the fiducials were independently placed a second time at 7T by a single rater (TYZ). The Euclidean distance was used to estimate landmark placement error between corresponding landmarks at 7T by the same rater to estimate intra-rater reliability, and between corresponding landmarks on the average fiducial location for TYZ and the corresponding landmark placed by JCL to estimate inter-rater reliability. All fiducials were also classified into categories: midline (5 landmarks previously described), lobar (temporal, occipital, parietal, frontal, insular), subcortical, and highly displaced.

The mean 7T fiducial location between all three manual ratings (TYZ x 2, JCL x 1) was used for all subsequent evaluations of registration quality between 7T and 3T images. The mean 7T fiducial locations were spatially aligned into 3T space iteratively using the transformations calculated in Section 4.2.2 on Data Processing. The Euclidean distance between the aligned 7T fiducial location and the corresponding 3T fiducial estimated registration error for each stage. The fiducial registration error after rigid body and affine registration steps provided an estimate of geometric distortion as calculated manually, which we call manual displacement. We evaluated our candidate automated displacement measure against manual displacement using Pearson correlation and a Bland-Altman plot for agreement [Bland and Altman, 1986]. To determine if there was a significant difference with registration steps, we performed a two-tailed Wilcoxon rank sum test between all combinations of fiducial categories and registration steps (14 fiducial categories, 3 x registration steps = 42 comparisons). These results were adjusted using the false-discovery rate (FDR) controlling for an adjusted p-value (q-value < 0.025) [Genovese et al., 2002].

4.2.6 Effect of Gradient Distortion Correction

Data analyzed as part of the study were acquired prior to the scanner upgrade from an Agilent 7T to a Siemens 7T. As a result, post hoc gradient distortion correction was not available for evaluation. We prospectively scanned a single subject at 7T and 3T using best equivalent MP2RAGE sequences at 0.8 mm resolution [Marques et al., 2010]. At 7T, the MP2RAGE protocol was as follows: TR = 6.0 s, TE = 2.19 ms, matrix = 208 x 320 x 320, resolution = 0.8

mm isotropic, scan time = 9:36 min). At 3T, the protocol was: TR = 5.0 s, TE = 3.51 ms, matrix = 208 x 320 x 320, resolution = 0.8 mm isotropic, scan time = 8:27 min). Both uncorrected and distortion corrected datasets were acquired and processed through our automated framework as described in Section 4.2.2. The density maps of automated displacements within the masked brain were plotted and compared. The corresponding displacement maps with and without correction were visually assessed. Finally, ROI analysis was performed and percent change due to correction was calculated as the difference between corrected and uncorrected displacement divided by uncorrected displacement.

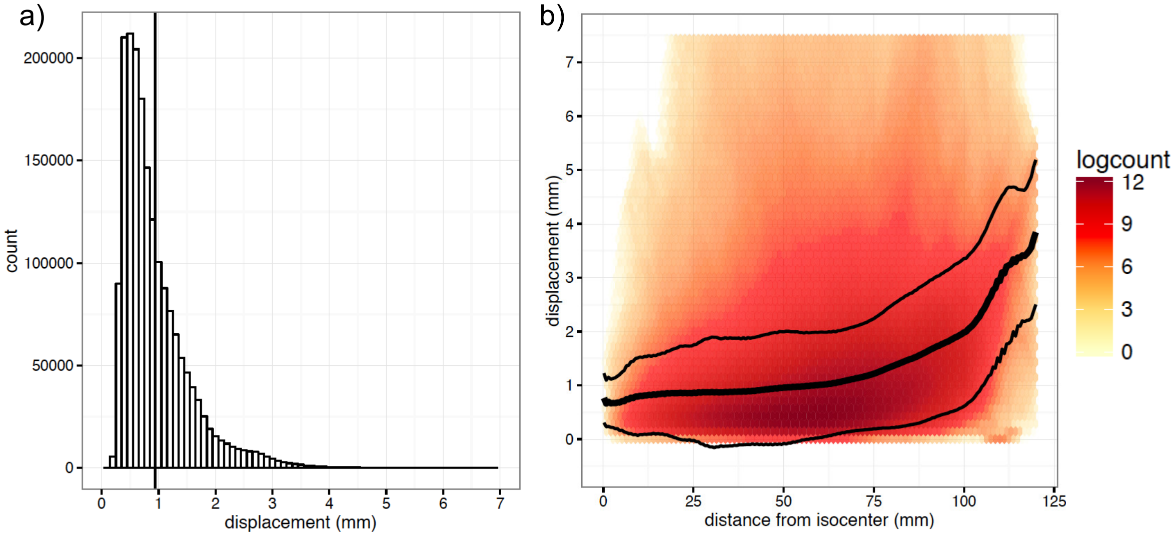

Figure 4.2: The histogram of mean automated displacements within the masked brain is shown in (a). Since automated displacement is derived from the Euclidean distance between points, all are greater than 0 mm. The histogram has a right skew deviation. The vertical line shows the mean of 0.94 mm. Local voxel displacement is demonstrated to increase with distance from the 7T image isocenter (b). Voxels across all subjects in the study were binned in a 2D histogram (heatmap) according to displacement and distance from isocenter (log-scaled). Mean (thick line) and standard deviation (thin lines) are shown. Mean automated displacement is demonstrated to increase beyond 1 mm at 80 mm.

4.3 Results

4.3.1 General Findings

Nonlinear registration, but not linear registration alone, qualitatively improved our ability to structurally align 7T and 3T images for the same subject (Figure 4.1). As shown in Figure 4.2a, automated displacement was always greater than zero, showed right skew deviation, and did not meet statistical criteria for normality (Anderson-Darling test, p-value < 0.00). Given these observations, the non-parametric Wilcoxon rank sum test was used for statistical analysis. We performed one-tailed hypothesis testing with the null hypothesis of displacement < 1 mm, as only locations with more than 1 mm (or voxel) of displacement were considered clinically significant. Statistically significant displacements in the opposite direction (i.e., close to zero mm) were not considered clinically meaningful and thus the lower tail was excluded from analysis.

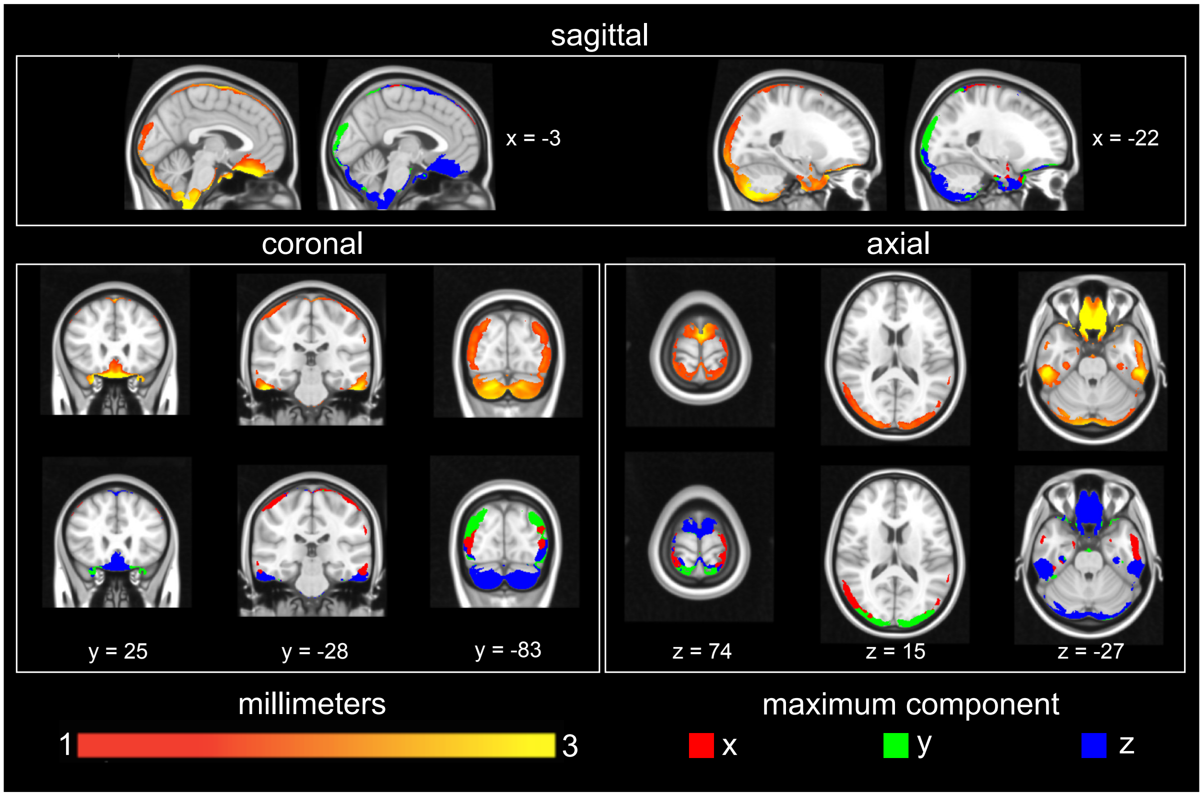

Figure 4.3: Selected images from displacement maps computed for group analysis are overlaid on the MNI152 template with slice references in world coordinates. All voxels shown are significant after controlling for multiple comparisons using FDR ($q < 0.025$). Each displacement map has a corresponding image showing an overlay of the maximum x, y or z component shown in red, green or blue, respectively, for all significant regions. The main component found was in the z-direction in 56.84%, followed by the x-direction in 22.51%, and finally the y-direction in 20.64%.

4.3.2 Identification and Characterization of Local Distortion

By extracting local metrics of displacement from the deformation field, we were able to identify local voxels systematically affected by geometric distortion at ultra-high field, quantified in millimeters. Selected images are shown for a single subject (Figure 4.1) and on group analysis

(Figure 4.3). Overall, 13.2% of voxels within the brain mask showed statistically significant displacement greater than 1 mm. Voxel-wise analysis identified significant distortions bilaterally on the floor of the anterior and middle fossae in the orbitofrontal cortex, mesial temporal poles, fusiform and temporal-occipital gyri, posterior inferior temporal gyri, and in the occipital/suboccipital regions. The maximum component of displacement was in the x direction at 42.60%, followed by the longitudinal direction (z) at 37.31%, and finally in the y direction at 20.01%. Using the relative index, the contribution in the x component was 35.00%, z component was 34.87%, and y component was 30.12%. When analyzing only those voxels identified as significantly displaced after adjustment, the maximum component was predominantly in the longitudinal direction (z component) at 56.84%, followed by the x component at 22.51%, and finally the y component at 20.65% (Figure 4.3). The relative index also shifted to be first in the z component at 40.31%, followed by the y component at 31.18%, and finally the x component 28.52%. We correlated voxel-wise displacement with the x, y, z positions of the 7T image isocenter and found that the superior parietal region was negatively correlated and the suboccipital was positively correlated with z position (Figure 4.4). Regions close to air-filled sinuses were not significantly correlated with isocenter position.

4.3.3 Distortion Increases with Isocenter Distance

Geometric distortions increased with distance from the image isocenter to over 1 mm at 80 mm distance from the isocenter (Figure 4.2b). The 7T isocenter location in our dataset was $x = -1.91 \pm 2.67$ mm, $y = 2.27 \pm 7.41$ mm, and $z = 3.41 \pm 12.98$ mm, and the 3T isocenter location was $x = 3.17 \pm 3.80$ mm, $y = -21.11 \pm 5.72$ mm, $z = -16.04 \pm 9.53$ mm in MNI152 world coordinates. The mean distance between 7T and 3T isocenters was 33.18 mm ± 12.54 mm (differences in each component: $x = -5.08 \pm 4.26$, $y = 23.38 \pm 8.47$, $z = 19.45 \pm 14.99$).

4.3.4 Region-of-Interest Analysis

Regional effects of from geometric distortion are summarized in Tables 4.1-4.3. After adjustment for multiple comparisons, no lobar ROIs were statistically significant, although there was a trend towards significance in the average voxel-wise displacement in the left occipital and temporal lobes (Table 4.1). Maximum displacements were noted to be highest in bilateral frontal, temporal, and occipital lobes, observed to be 7-8 mm, 4-6 mm, and 4-5 mm respectively, on average across subjects. Using the full Harvard-Oxford atlas, 17 of 113 regions, or 15.0%, met thresholds of statistical significance after FDR correction ($q < 0.025$) (Table 4.2; full table available in Appendix Section B.1). Regions identified were: bilateral temporal poles, left anterior middle temporal gyrus, bilateral posterior inferior temporal gyri, bilateral

Table 4.1: Mean and maximum displacements in millimeters for ROIs part of the lobar and ATAG subcortical atlases.

region	side	atlas	mean	stdev	V	p-value	q-value	max	max stdev
Left Red Nucleus	left	ATAG	1.02	0.53	111	0.69	1.00	1.69	0.98
Left Substantia Nigra	left	ATAG	0.86	0.39	76	0.95	1.00	1.52	0.67
Left Subthalamic Nucleus	left	ATAG	1.05	0.59	108	0.73	1.00	1.48	0.79
Left Striatum	left	ATAG	0.59	0.14	0	1.00	1.00	2.41	0.99
Left Globus Pallidus Externus	left	ATAG	0.48	0.15	0	1.00	1.00	1.33	0.66
Left Globus Pallidus Internus	left	ATAG	0.55	0.21	2	1.00	1.00	1.19	0.55
Right Red Nucleus	right	ATAG	1.03	0.40	131	0.45	1.00	1.71	0.72
Right Substantia Nigra	right	ATAG	0.78	0.30	31	1.00	1.00	1.48	0.80
Right Subthalamic Nucleus	right	ATAG	0.98	0.53	99	0.81	1.00	1.44	0.70
Right Striatum	right	ATAG	0.60	0.19	3	1.00	1.00	2.38	0.91
Right Globus Pallidus Externus	right	ATAG	0.50	0.22	2	1.00	1.00	1.31	0.81
Right Globus Pallidus Internus	right	ATAG	0.50	0.24	6	1.00	1.00	1.10	0.72
Left Frontal	left	lobar	0.91	0.12	30	1.00	1.00	7.69	1.19
Left Parietal	left	lobar	0.81	0.11	4	1.00	1.00	3.46	0.73
Left Occipital	left	lobar	1.15	0.26	197	0.01	0.08	4.62	1.83
Left Temporal	left	lobar	1.11	0.21	195	0.01	0.09	5.99	1.53
Left Insular	left	lobar	0.61	0.10	0	1.00	1.00	1.80	0.30
Left Subcortical	left	lobar	0.70	0.22	11	1.00	1.00	2.61	1.10
Right Frontal	right	lobar	0.89	0.11	24	1.00	1.00	8.07	1.71
Right Parietal	right	lobar	0.76	0.11	1	1.00	1.00	3.56	0.79
Right Occipital	right	lobar	1.07	0.17	166	0.10	0.50	4.24	0.94
Right Temporal	right	lobar	1.04	0.12	169	0.09	0.43	5.75	0.96
Right Insular	right	lobar	0.66	0.13	1	1.00	1.00	2.07	0.62
Right Subcortical	right	lobar	0.75	0.24	25	1.00	1.00	2.94	0.98

V represents the Wilcoxon rank sum statistic, p-value is unadjusted, and q-value is FDR adjusted. None of the regions met thresholds for statistical significance after FDR correction at a rate of q-value < 0.025.

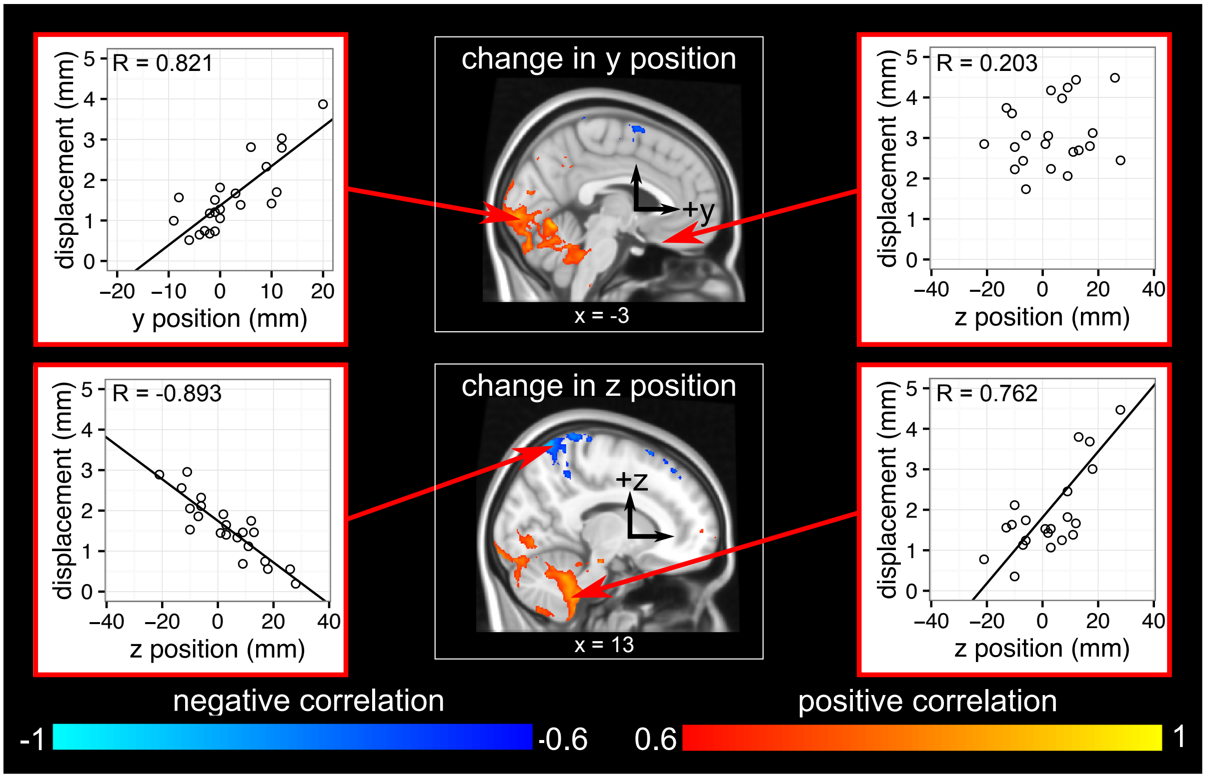

Figure 4.4: The effect of 7T isocenter position on local distortion. Correlation maps of isocenter position against displacement are overlaid on selected sagittal images on the MNI152 template with corresponding world coordinates. All voxels shown are significant after controlling for multiple comparisons using FDR ($q < 0.025$). The top and bottom images show regions with statistically significant correlation with the y and z isocenter positions, respectively. Red arrows point to corresponding voxel locations where local automated displacement is plotted against isocenter position. The perpendicular black arrows mark the location of the in-plane isocenter in MNI152 space. Positive correlation is observed with a more anterior (increasing y) and superior (increasing z) position. Negative correlation is observed with a more inferior (decreasing z) isocenter position. Note that there is no significant correlation in a region of the orbitofrontal cortex shown to have high displacement in Figure 4.3, a region known to be prone to susceptibility effects.

inferior lateral occipital cortex, bilateral frontal medial cortex, bilateral subcallosal cortex, bilateral anterior parahippocampal gyri, bilateral anterior temporal fusiform cortex, and bilateral occipital poles. None of the subcortical regions defined on the ATAG subcortical atlas were significantly displaced. Maximum displacements around common stereotactic targets, including the substantia nigra and subthalamic nucleus, were 1-2 mm on average across subjects. The bilateral striatum ROIs, which were the largest subcortical structures in the ATAG atlas, showed the highest maximum displacement in the 2-3 mm range.

Twenty-two regions were identified that demonstrated significant correlations of isocenter position with local displacement as shown in Table 4.3 (for the complete table, see Table S2 in Appendix Section B.1). Most significant correlations were related to the y or z components

Table 4.2: Mean and maximum displacements in millimeters for ROIs from the Harvard-Oxford atlas meeting thresholds for statistical significance.

region	side	mean	stdev	V	max	max stdev	
Left Temporal Pole	left	1.18	0.28	217	5.16	1.57	*
Right Temporal Pole	right	1.17	0.24	213	4.87	1.50	*
Left Middle Temporal Gyrus Anterior	left	1.54	0.67	228	3.58	1.34	*
Left Inferior Temporal Gyrus Posterior	left	1.73	0.36	252	5.34	0.84	*
Right Inferior Temporal Gyrus Posterior	right	1.56	0.34	253	5.05	0.82	*
Left Lateral Occipital Cortex Inferior	left	1.31	0.26	248	3.62	1.32	*
Right Lateral Occipital Cortex Inferior	right	1.28	0.18	253	3.45	0.57	*
Left Frontal Medial Cortex	left	1.75	0.59	251	5.68	1.12	*
Right Frontal Medial Cortex	right	1.84	0.56	253	5.77	0.94	*
Left Subcallosal Cortex	left	1.72	0.33	252	6.87	0.67	*
Right Subcallosal Cortex	right	1.80	0.38	253	6.87	0.62	*
Left Parahippocampal Gyrus Anterior	left	1.51	0.88	244	3.84	1.89	*
Right Parahippocampal Gyrus Anterior	right	1.40	0.35	249	4.00	1.27	*
Left Temporal Fusiform Cortex Anterior	left	1.62	0.85	247	3.77	1.85	*
Right Temporal Fusiform Cortex Anterior	right	1.59	0.57	247	3.52	1.13	*
Left Occipital Pole	left	1.64	0.65	248	4.33	1.95	*
Right Occipital Pole	right	1.55	0.46	252	4.01	1.08	*

V represents the Wilcoxon rank sum statistic, p-value is unadjusted, and q-value is FDR adjusted. * All 13 regions shown met thresholds for statistical significance after FDR correction at a rate of $q < 0.025$. For the full table, please see Appendix Section B.1.

Table 4.3: Correlation of displacements with change in position of image isocenter for regions meeting thresholds for statistical significance.

region	side	atlas	component	corr	
Right Subcallosal Cortex	right	HarvardOxford	x	-0.675	*
Left Occipital	left	lobar	y	0.848	*
Right Occipital	right	lobar	y	0.767	*
Left Inferior Frontal Gyrus Pars Opercularis	left	HarvardOxford	y	0.71	*
Left Intracalcarine Cortex	left	HarvardOxford	y	0.696	*
Right Intracalcarine Cortex	right	HarvardOxford	y	0.716	*
Left Lingual Gyrus	left	HarvardOxford	y	0.832	*
Right Lingual Gyrus	right	HarvardOxford	y	0.802	*
Left Occipital Fusiform Gyrus	left	HarvardOxford	y	0.772	*
Right Occipital Fusiform Gyrus	right	HarvardOxford	y	0.795	*
Left Supracalcarine Cortex	left	HarvardOxford	y	0.646	*
Right Supracalcarine Cortex	right	HarvardOxford	y	0.795	*
Left Occipital Pole	left	HarvardOxford	y	0.837	*
Right Occipital Pole	right	HarvardOxford	y	0.85	*
Right Parietal	right	lobar	z	-0.724	*
Right Postcentral Gyrus	right	HarvardOxford	z	-0.79	*
Right Superior Parietal Lobule	right	HarvardOxford	z	-0.869	*
Left Intracalcarine Cortex	left	HarvardOxford	z	0.68	*
Right Parahippocampal Gyrus Posterior	right	HarvardOxford	z	0.669	*
Left Lingual Gyrus	left	HarvardOxford	z	0.7	*
Right Lingual Gyrus	right	HarvardOxford	z	0.688	*
Right Occipital Fusiform Gyrus	right	HarvardOxford	z	0.695	*

The corr values represent the correlation of the corresponding x, y, or z component of the 7T image isocenter with mean automated displacement in that region-of-interest, p-value is unadjusted, and q-value is FDR adjusted at a rate of $q < 0.025$. * 22 regions met thresholds for statistical significance after FDR correction. For the full table, please see Appendix Section B.1.

of the isocenter, except for the right subcallosal cortex which correlated with x. At the lobar level, bilateral occipital and right parietal regions were correlated with isocenter position. At the sub-lobar level, regions identified as correlating with the y position of isocenter were: left pars opercularis, bilateral intracalcarine cortex, bilateral lingual gyri, bilateral occipital fusiform gyri, bilateral supracalcarine cortex, and bilateral occipital poles. With z position, the following regions were identified: right postcentral gyrus, right superior parietal lobule, left intracalcarine cortex, right parahippocampal gyrus posterior, bilateral lingual gyrus, and right occipital fusiform gyrus.

4.3.5 Validation

Our results were validated using manual fiducial placement on 5 subjects. Successive stages of registration from rigid body to affine to nonlinear registration resulted in mean fiducial error changes from 1.09 ± 0.77 to 0.98 ± 0.69 to 0.98 ± 0.67 mm, respectively. Trends toward improvements in fiducial registration error were generally observed with successive stages of registration in Table 4.4. However, after adjusting p-values for multiple comparisons, only the fiducial registration error in the optic chiasm landmark reached statistical significance comparing rigid to nonlinear registration (1.61 ± 0.59 to 0.88 ± 0.44; q-value < 0.01).

Intra-rater reliability was 0.86 ± 0.35 mm. Inter-rater reliability was 1.14 ± 0.77 mm. Our automated method demonstrated excellent correlation (R = 0.8755, p-value < 0.00) and agreement on Bland-Altman plotting (Figure 4.5) with manual displacement.

4.3.6 Effect of Gradient Distortion Correction

We compared the results using our automated framework with and without vendor-provided gradient distortion correction in a single subject (Figure 4.6 and Table S3 in Appendix Section B.1). The percentage of voxels with displacement greater than 1 mm dropped from 31.9% without correction to 20.4% with correction. The mean whole brain displacement decreased from 0.548 mm to 0.472 mm—a 13.8% reduction in distortion. The density plot was left-shifted with a narrower right-sided tail suggesting fewer geometric outliers. We have included Table S3 (Appendix Section B.1) summarizing the trend of improvements across ROIs, with particularly large reductions in the bilateral parietal and occipital lobes (up to almost 60% reduction in displacements).

Table 4.4: Fiducial registration error (in mm) with successive registration steps in different categories.

region	rigid	stdev	affine	stdev	nlin	stdev	
total	1.09	0.77	0.98	0.69	0.98	0.67	
temporal	0.96	0.61	0.85	0.62	0.94	0.71	
occipital	1.26	1.13	1.02	0.83	0.78	0.42	
parietal	1.22	0.77	1.02	0.61	0.96	0.62	
frontal	0.91	0.45	0.76	0.37	0.86	0.52	
insular	0.91	0.58	0.80	0.48	0.67	0.43	
subcortical	0.91	0.53	0.84	0.52	0.88	0.51	
midline total	0.99	0.55	0.88	0.43	0.86	0.47	
AC	0.80	0.45	0.66	0.38	0.66	0.39	
PC	0.55	0.22	0.59	0.25	0.60	0.24	
midpoint of aqueduct	0.89	0.39	1.03	0.46	1.07	0.47	
optic chiasm	1.61	0.59	1.19	0.46	0.88	0.44	*
midpoint of infundibulum	1.11	0.42	0.95	0.24	1.08	0.57	
displacement	1.86	1.28	1.88	1.00	1.67	0.83	

Fiducial registration error was assessed for rigid body, affine (12-parameter), and nonlinear registration steps. Fiducials classified as displacement represent selected locations that were chosen retrospectively at areas identified as displaced using the automated method. All interactions were assessed using Wilcoxon rank sum statistics (i.e. two-tailed test for fiducial error with rigid versus affine, rigid versus nonlinear, and affine versus nonlinear registration). * Only one test (rigid versus nonlinear registration for the optic chiasm) met thresholds for statistical significance after FDR correction (q-value < 0.01).

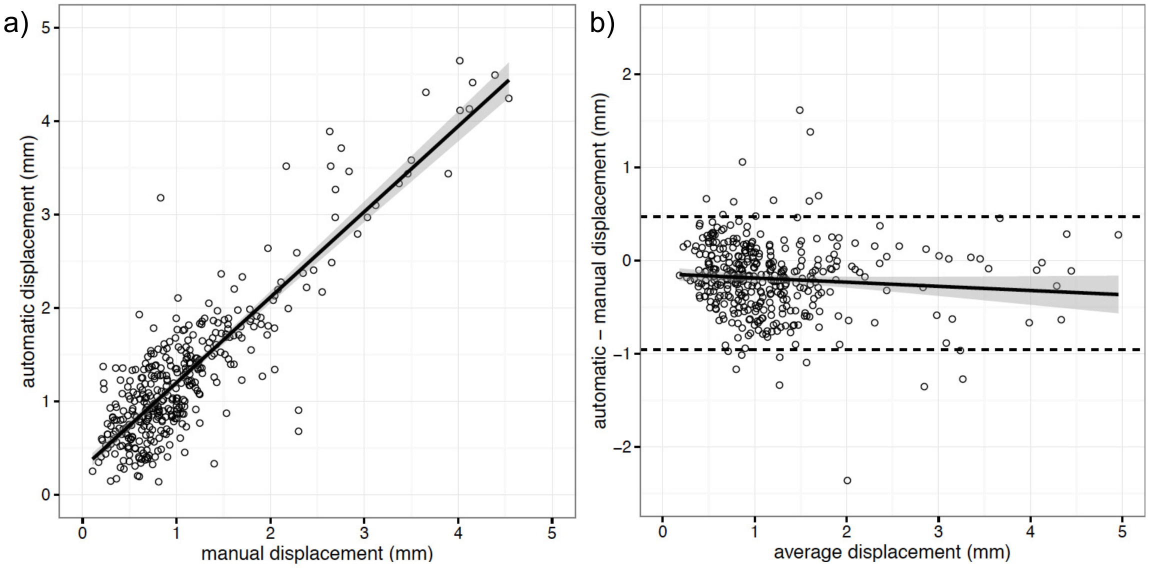

Figure 4.5: (a) Plot of automated displacement against gold-standard manual displacement demonstrated good correlation (R = 0.8755, p-value < 0.00). (b) Bland-Altman plotting reveals that automated displacement slightly underestimates manual displacement (mean = -0.193 mm) with good agreement between manual and automated measures. Gray error bands represent 95% confidence intervals.

4.4 Discussion

The principal results of this study can be summarized as follows. Focal areas of geometric distortion in higher fields can be identified automatically from the deformation field used in nonlinear registration to images acquired at lower fields. We evaluated our automated method on a T1-weighted MRI dataset, the MRI sequence predominantly used as an anatomical reference for structural and functional studies. Distortions were increased at tissue interfaces, particularly the floor of the middle and anterior fossae, but also in the occipital/suboccipital region (Figure 4.1 and 4.3; Table 4.2). Distortions were also increased with distance from the image isocenter to over 1 mm at 80 mm distance from the isocenter (Figure 4.2b). Distortions were correlated with the image isocenter location, particularly in the parietal, occipital, and suboccipital regions, but generally not at tissue interfaces (Figure 4.4; Table 4.3). Traditional deep brain surgery targets including the STN and GPi were minimally displaced (Table 4.1). Geometric distortion correction resulted in a mean reduction in distortion of 13.8%. Finally, our automated framework compared favorably to manual fiducial placement (Figure 4.5). Moving forward, our methodology can be used to evaluate other 7T protocols, including T2-weighted [Kwon et al., 2012], susceptibility-weighted [Abosch et al., 2010, Chandran et al., 2016, Schäfer et al., 2012], and T1 inversion recovery images [Sudhyadhom et al., 2009, Tour-

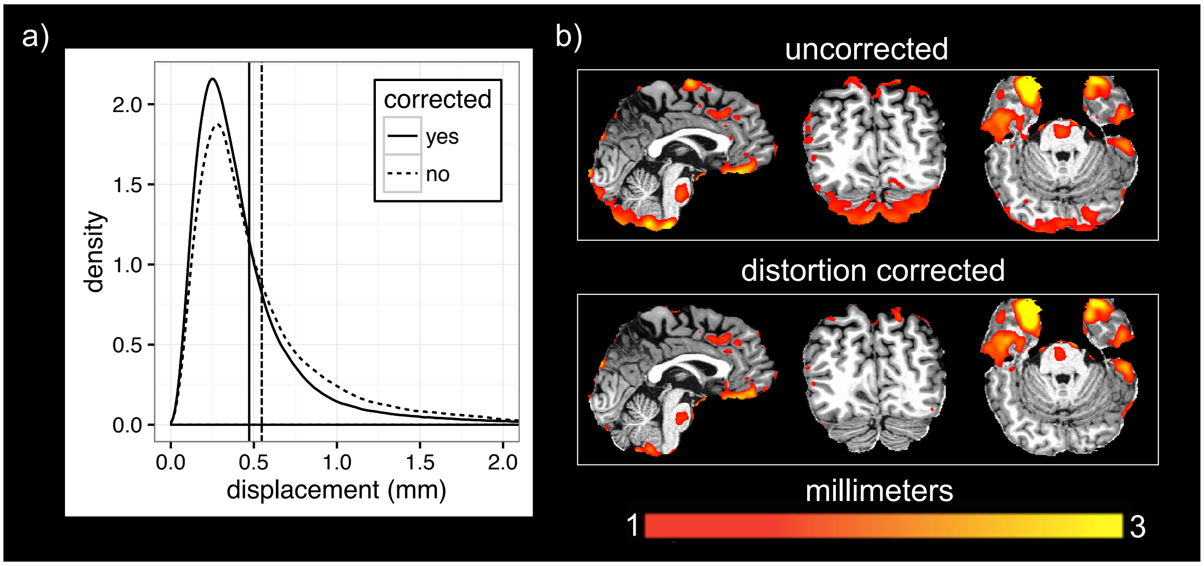

Figure 4.6: The effect of vendor-provided gradient distortion correction on local displacement in a single subject. A density map of automated displacements within the masked brain with (solid line) and without (dashed line) distortion correction applied (a). The mean displacement is decreased from 0.548 mm to 0.472 mm with distortion correction (a percent reduction of 13.8%). Automated displacement maps are overlaid on the subject's own 3T structural scan (b). Decreased displacement is visualized throughout the scan particularly in the suboccipital region. Distortions identified near air-filled sinuses (floor of the middle fossa and orbitofrontal cortex) remain.

dias et al., 2014].

Phantom validation represents an important paradigm for the calibration of MRI scanners and the assessment of geometric distortion. In a phantom comprised of regularly spaced acrylic rods mounted on an epoxy-based skull base, Cho and colleagues showed sub-millimeter accuracy between manually placed fiducials at 7T and on CT [Cho et al., 2010]. Using a proprietary phantom, Dammann et al. [Dammann et al., 2011] found hardware-related geometric distortion generally smaller than 1 mm within a range of 80 mm from the magnet isocenter, consistent with our own observations (Figure 4.2b), except in a T2-weighted sequence. However, results have been inconsistent with other studies suggesting more severe distortions in the several millimeter range [Littmann et al., 2006, Neumann et al., 2015, Watanabe et al., 2006]. Another practical point is that some of the commonly used MRI phantoms [Fonov et al., 2010] do not fit within the field-of-view in head-specific gradient coils. Finally, phantom validation captures gradient nonlinearities [Fonov et al., 2010], but would not be able to capture physiological distortion resulting from magnetic susceptibility at tissue interfaces that are subject-specific.

In vivo studies are better able to evaluate physiological distortion not captured using MRI phantoms. One of the early studies looking at the feasibility of 7T for stereotaxy analyzed subjects scanned at both 1.5T and 7T [Duchin et al., 2012]. Using manual segmentation, the authors observed that fiducials placed in central brain regions were minimally distorted, except for the optic chiasm and infundibulum landmarks abutting the anterior fossa, as we have also confirmed (Figure 4.1, Table 4.3). By dividing the MRI volume into 9 block-shaped regions arranged about the image isocenter, they demonstrated larger distortions proximal to air-filled cavities (inferior frontally). Our methodology expands on the original work by Duchin and colleagues by providing an automated framework that compared favorably with gold-standard manual measures in terms of both correlation and agreement (Figure 4.5). Our own observations are compatible with their work (Figure 4.1 and 4.3; Table 4.2), while providing additional neuroanatomical detail about focal regions of spatial uncertainty at the voxel-wise and regional scales that can be examined prospectively in patient-specific datasets (Figure 4.3; Table 4.1-4.2). Given the known linear increase in magnetic susceptibility with increasing B_0, we would expect over 2x increase in susceptibility artifact from 3T to 7T for an equivalent MRI sequence. When isolating the contribution of distortion in the main Cartesian directions, we found that voxels identified as significantly distorted had a predominant z-axis deviation in 56.84% of voxels, which may result from B_0-related distortions, consistent with prior work [Neumann et al., 2015, Watanabe et al., 2006].

Geometric distortion can be corrected using a number of different methods. One common technique is to apply spherical harmonics correction based on gradient coil geometry, derived from the design parameters of the coil itself. Langlois et al. demonstrated that applying spherical harmonics correction alone decreased error to the sub-millimeter range in a phantom study at 1.5T [Langlois et al., 1999]. It remains unclear how much spherical harmonics correction improves geometric inhomogeneity at ultra-high field. A recent study observed that applying vendor-provided spherical harmonics correction resulted in higher stereotactic error than without, raising the potential concern that inappropriate use of these algorithms can worsen geometric accuracy [Neumann et al., 2015]. When the spherical harmonics information is not directly available, post hoc phantom-based correction has been found to improve geometric accuracy and reproducibility in multi-site datasets [Jovicich et al., 2006]. However, the estimates on the percent variability accounted for by phantom-based correction are broad, ranging from 17-90% depending on the study [Caramanos et al., 2010, Fonov et al., 2010, Jovicich et al., 2006]. Altogether, there remains no gold-standard geometric distortion correction algorithm. In a single dataset with and without gradient correction, we demonstrated a promising mean reduction of 13.8% in our distortion estimate with reductions up to 60% in the occipital lobes (Figure 4.6 and Table S3). The only exceptions were in regions close to air-filled cavities—where the main cause of distortion is likely related to B_0 susceptibility rather than gradient inhomogeneity. A complementary approach for B_0-related distortion correction has recently gained attention as a preprocessing step in the Human Connectome Project (HCP)

[Glasser et al., 2013, van der Kouwe et al., 2008]. The acquired B_0 field map is scaled by the readout dwell time, and used as a distortion field. This methodology, called field map (or readout) correction has been traditionally applied to echo planar images [Jezzard and Balaban, 1995], but more recently in the HCP, has been used to correct high-resolution structural MR images [Glasser et al., 2013] with the presumption that correction with a low-resolution map is still accurate because B_0 inhomogeneity is smoothly varying. Qualitative improvements with B_0 field map correction have been demonstrated, but one possible application of our pipeline is to better quantify the impact of field map correction on residual distortion in gradient-corrected images. Overall, the framework described in this manuscript can be applied generally to evaluate the effect of different correction methods more systematically.

No significant local displacement in the ATAG subcortical atlas was observed, which included STN and GPi regions (Table 4.1). Most of the midline fiducials were minimally displaced, except for the optic chiasm, which was displaced at 1.61 ± 0.59 mm with rigid registration alone, improving significantly with nonlinear registration (Table 4.4). Consistent with prior literature, this landmark is likely prone to distortion from magnetic susceptibility at the floor of the anterior fossa proximal to similarly affected inferior frontal regions in our automated analysis (Figure 4.3, Table 4.2), and supported by previous work [Duchin et al., 2012].

Our results demonstrate that local displacement increased with distance from the image isocenter with greater than 1 mm of displacement on average beyond 80 mm (Figure 4.2b). Furthermore, the data are not normally distributed, and researchers and clinicians should be aware of geometric inaccuracies in these outlier regions, particularly with critical applications like stereotactic surgery. In particular, we found that inferior frontal, parasagittal, and occipital cortices were distorted. While these regions are outside traditional zones for neurosurgical intervention, the number of putative neuromodulation targets continues to grow, and one of the more well-studied targets for refractory depression, the subgenual or subcallosal cingulate cortex [Johansen-Berg et al., 2008, Lozano et al., 2008], lies within a region of high distortion (Figure 4.3, Table 4.2). Previous studies have shown that variability in the location of the image isocenter can have an effect on study-related morphometric measures [Caramanos et al., 2010, Jovicich et al., 2006]. While the variability in isocenter placement at both 3T and 7T is quite high in our study, particularly in the z-direction, these results are similar to findings in multi-site structural MRI studies [Jovicich et al., 2006]. By correlating the position of the isocenter with local displacement, we identified the superior parietal region and suboccipital regions as being particularly prone to isocenter displacement. Regions close to air-filled sinuses were not affected in the same way thus suggesting B_0 may be the likely reason for distortion in these regions. Finally, isocenter discrepancies also highlight important differences between 7T and 3T imagers that result in large differences in isocenter location. At 3T, the isocenter is typically lower in the z direction with a lower standard deviation since externally, we are aiming for the nasion. At 7T, the magnet and coil are at the extreme end of the table, and thus, we are more limited in our ability to use external landmarks like the nasion for more consistent isocenter placement. Overall, in order to limit large geometric inaccuracies including gradient distortions, our results suggest that a researcher interested in a particular region should place it as close to the 7T isocenter as possible.

There are several limitations to our work. Our workflow requires nonlinear registration of participant data acquired from a target image at ultra-high field to a reference image at lower-field (in this case, 3T). We have assumed that the 3T dataset is relatively free of geometric inhomogeneity, even though distortion is known to exist at lower fields [Caramanos et al., 2010, Jovicich et al., 2006]. Despite this, recent clinical studies have suggested a comparable safety profile using 3T MR-based images for surgical interventions compared with 1.5T [Cheng et al., 2014, Houshmand et al., 2014]. Certain special precautions including the use of high receiver bandwidth and vendor-provided gradient distortion correction techniques can help to ensure 3T images are geometrically more accurate. Computed tomography (CT) data, which were unavailable for this cohort of subjects, can be considered a gold-standard for geometric evaluation. However, the lack of tissue contrast could result in difficulties with nonlinear registration with MRI. A recent systematic review established that CT/MRI fusion is not trivial with most studies reporting over 1 mm of registration error [Geevarghese et al., 2016, Thani et al., 2011]. Variability in the image isocenter may also be an important confound in our dataset, although our results are similar to data from multi-center anatomical trials [Jovicich et al., 2006]. It is possible that distortion near air-filled sinuses may be an artifact of degraded image quality in these regions [Tardif et al., 2015] rather than true distortion, but nevertheless, the algorithm captures the potential spatial uncertainty in these regions which should be accounted for in neuroimaging studies and surgical planning. Finally, while our project describes focal estimates of geometric distortion at a voxel-level, these results are specific to the scanner and sequence assessed, as well as the gradient coil used.

4.5 Conclusions

Our automated framework quantifies, in millimeters, the extent of geometric distortion resulting from ultra-high field structural MRI at the group and subject levels. These results have important implications for evaluating patient-specific local spatial uncertainty. We have demonstrated that our method quantifies voxel-wise distortion and in addition, can help characterize the source of inhomogeneity by observing interactions of our measure with isocenter location and gradient distortion correction methods. Our results point to the need for caution if using ultra-high field MRI for purposes where morphological accuracy is critical, including stereotactic interventions, as well as the need for scanner and sequence-specific calibration of geometric inhomogeneity. We confirmed that our automated method compared favorably with manual fiducial displacement, thus permitting prospective evaluation of the effect of MRI sequences, putative correction algorithms, and scanner modifications on geometric distortion.

Chapter 5

Direct visualization and characterization of the human zona incerta and surrounding regions

This chapter is work being prepared for submission.

- Lau, J. C., Parrent, A. G., Xiao, Y., Gilmore, G. G., Demarco, J., MacDougall, K. W., Currie, C., Peters, T. M., & Khan, A. R. (2019). Direct visualization and characterization of the human zona incerta and surrounding regions.

5.1 Introduction

The zona incerta (ZI) is a small but diffuse structure in the deep brain first identified by Auguste Forel in 1877, famously described as "an immensely confusing area about which nothing can be said" [Forel, 1877]. Forel appreciated that the ZI consisted of gray matter located between the external medullary lamina of the thalamus and the corpus Luysi (subthalamic nucleus; STN) of otherwise "indefinite" description. It is particularly telling that Forel found the ZI so difficult to describe given his crucial role in the careful delineation of surrounding fibre tracts still often referred to eponymously as the fields of Forel [Gallay et al., 2008]. Since its original description, much has been learned about the ZI and its surrounds although robust *in vivo* visualization has remained elusive.

The anatomical boundaries of the ZI have generally been described in the context of its more discrete neighbours rather than based on any consistent feature of the region itself. Packed in a small area between the ventral thalamus, STN, and lateral red nucleus (RN), the ZI is situated at a complex junction of major white matter pathways including the cerebellothalamic, pallidothalamic, medial lemniscal, and corticospinal tracts. Along its dorsal, ventral, and medial borders, the ZI is surrounded by the fasciculus thalamicus (ft; also known as the H1 field of Forel), the fasciculus lenticularis (fl; also known as the H2 field of Forel), and the H field, which is a convergence of the fl and the ansa lenticularis (al), respectively [Nieuwenhuys et al., 2007, Gallay et al., 2008]. The rostral ZI (rZI) is continuous with the reticular nucleus of the thalamus laterally and with the lateral hypothalamus anteromedially. The caudal ZI (cZI) is laterally bounded by the STN and posterior limb of the internal capsule. To date, most of the details regarding the region are the result of meticulous study of carefully prepared post-mortem specimens [Schaltenbrand and Wahren, 1977, Morel, 2007, Gallay et al., 2008].

Cytoarchitectonic and myeloarchitectonic studies have identified the ZI as a nuclear complex consisting of loosely arranged neurons of heterogeneous morphology with a diverse immunohistochemical profile [Nieuwenhuys et al., 2007]. In Golgi preparations of the ZI, two main neuronal classes have been identified: principal cells and interneurons [Ma et al., 1997]. Gene expression studies have revealed a common embryological origin along with the reticular nucleus of the thalamus and pregeniculate nucleus of the ventral diencephalon, specifically the prethalamic (prosomere 3) segment, which predominantly contains gabaergic neurons [Watson et al., 2014]. Through immunohistochemical analysis in experimental animals, a general pattern of at least four component ZI sectors has emerged in the rostral, dorsal, ventral, and caudal directions [Mitrofanis, 2005]. Tract-tracing studies have identified extensive and often bilateral connections between the ZI and the cortex, subcortex, and spinal cord [Mitrofanis, 2005, Watson et al., 2014]. At least five functional subsectors within the ZI have been suggested: auditory, limbic, motor, somatosensory, and visual. However, unlike other nearby structures like the STN, no robust immunohistochemical biomarker has been described for the ZI proper.

The diversity of chemical expression and widespread connections suggest an important modulatory role of the zona incerta in regulating brain function. The zona incerta forms extensive inhibitory connections with spinothalamic relay nuclei in experimental animals, and thus may play an important role in modulating neuropathic pain and the somatosensory system [Masri et al., 2009, Truini et al., 2013]. In a perhaps related manner, the rostral ZI is believed to provide inhibitory control over the thalamus during sleep [Llinás and Jahnsen, 1982, Watson et al., 2014], which may also relate to its perceived role in modulating consciousness [Power et al., 1999, Power and Mitrofanis, 1999, Mitrofanis, 2005, Giacino et al., 2014].

In humans, the most well-studied role of the zona incerta is as a putative target for neuromodulatory therapy transmitted either within the caudal zona incerta (cZI) or its vicinity, which has been observed to be highly effective for the treatment of essential tremor [Hariz and Blomstedt, 2017]. These investigations began in the 1960s with leucotomy (selective white matter ablation) treatments [Spiegel and Wycis, 1954, Wertheimer et al., 1960, Spiegel et al., 1962, Spiegel et al., 1964, Mundinger, 1965, Bertrand et al., 1969, Velasco et al., 1975], but as technologies improved, electrical stimulation to these regions has also been demonstrated to be effective [Mohadjer et al., 1990, Velasco et al., 2001, Nowacki et al., 2018, Velasco et al., 1972, Plaha et al., 2006, Blomstedt et al., 2010, Fiechter et al., 2017]. Yet because of poor direct visualization, controversy has remained as to whether the therapeutic effect is derived from modulation of the cell bodies in the cZI, wayward connections such as the cerebellothalamic tracts (also known as the prelemniscal radiations or raprl) [Velasco et al., 1972, Castro et al., 2015] or some combination of both [Blomstedt et al., 2010]. Given the ambiguity and high functional density of the region, some prefer to consider the stereotactic target more broadly as the posterior subthalamic area (PSA) [Hariz and Blomstedt, 2017, Blomstedt et al., 2018, Nowacki et al., 2018]. Targeting of the region relies on identification of the PSA indirectly relative to the adjacent subthalamic nucleus (STN) and red nucleus (RN), which are visible on T2-weighted scans [Blomstedt et al., 2010] (see Section 5.2.6 for more details).

The increased inherent signal resulting from increasing magnetic field strength has presented an opportunity to visualize brain structures that have not been seen at lower field

Table 5.1: MRI sequence details.

Sequence		TE (ms)	TR (ms)	TI	Flip Angle (^{o})	Matrix Size	PAT*	Averages	Resolution	Acquisition Time (min:sec)
MP2RAGE	3D	2.73	6000	800/2700	4/5	342x342x224	3	1	0.7x0.7x0.7	10:14
SA2RAGE	3D	0.81	2400	45/1800	4/11	128x128x64	2	1	1.9x1.9x2.1	2:28
SPACE	3D	398	4000	NA	variable	320x320x224	3	1.6	0.7x0.7x0.7	10:28

* PAT = parallel acquisition technique (acceleration factor)

strengths [Marques and Norris, 2017]. By exploiting T2-related tissue properties, ultra-high magnetic field (7 Tesla; 7T) MRI has enabled direct visualization of many deep brain nuclei with increased resolution and signal-to-noise ratio (SNR) including the red nucleus, substantia nigra, and subthalamic nucleus [Schäfer et al., 2012, Keuken et al., 2013, Plantinga et al., 2018], known to be rich in iron [Zecca et al., 2004, Haacke et al., 2005]. Paralleling these successes, previous attempts at direct visualization of the zona incerta have focussed on the use of T2-based contrast, with purported identification of the rZI, but not the cZI [Kerl et al., 2013]. In this study, we report that by employing high-resolution quantitative T1 mapping at 7-Tesla, robust visualization of the zona incerta is now possible *in vivo* along the entire rostrocaudal axis, enabling comprehensive anatomical characterization of this previously obscure deep brain region.

5.2 Materials and Methods

5.2.1 Participant and image acquisition details

We recruited 32 cognitively intact, healthy participants (46.2 ± 13.5 years; median: 48 years; range: 20-70 years; 12 female and 20 male; right-handed). This study was approved by the Western University Health Sciences Research Ethics Board. All subjects signed a written consent form to participate. The imaging studies were performed in a 7-Tesla head-only scanner (Siemens Magnetom; Siemens Healthcare GmbH, Erlangen, Germany) at the Western University Centre for Functional and Metabolic Mapping (CFMM). An 8-channel parallel transmit/32-receive channel coil was used [Gilbert et al., 2011]. After localization and preparatory sequences, each subject underwent a 3D MP2RAGE [Marques et al., 2010], 3D SA2RAGE [Eggenschwiler et al., 2012], and 3D optimized fast-spin echo (T2 SPACE) acquisitions (see Table 5.1).

5.2.2 Image pre-processing and template creation

Upon completion of an MRI scan session, the images were pushed to a DICOM server (dcm4che; `https://www.dcm4che.org`) with automatic data standardization and conversion to the Brain

Imaging Data Structure (BIDS) [Gorgolewski et al., 2016] using the autobids platform (`https://github.com/khanlab/autobids`) deployed on a high-performance compute cluster. Autobids utilizes scanner-specific heuristics enabled by heudiconv (`https://github.com/nipy/heudiconv`) preconfigured and validated on multiparametric 7T MRI sequences for DICOM to nifti conversion using dcm2niix [Li et al., 2016] and organization into BIDS.

All individual MRI sequences were corrected for gradient nonlinearities using 3D distortion correction [Glasser et al., 2013, Lau et al., 2018a] prior to further processing. The objective of individual preprocessing steps was to adequately prepare the individual MRI sequences for quantitative image analysis and also linear alignment with the subject's T1-weighted structural MRI scan containerized as BIDS apps [Gorgolewski et al., 2017]. The outputs of the preprocessing steps were visually assessed for quality (JL).

5.2.3 Pre-processing: MP2RAGE

As part of the MP2RAGE acquisition, two different images were created at separate inversions. Using a lookup table, these inversion images were used to create synthetic quantitative T1 maps devoid of proton density contrast, reception field bias, and first order transmit field inhomogeneity. Minimal pre-processing was necessary except for using the B_1 field map (SA2RAGE) sequence to correct for intensity inhomogeneity [Eggenschwiler et al., 2012]; specifically, no post hoc intensity nonuniformity correction was employed. This SA2RAGE-corrected T1 map was used for quantitative analysis. The T1w image was used as a reference image for rigid-body alignment of the T2SPACE scan.

5.2.4 Pre-processing: T2SPACE

Raw images from the scanner were observed to have significant intensity inhomogeneities. The bias fields were corrected using an initial nonuniformity correction step with N4 [Sled et al., 1998, Tustison et al., 2010] enabling more accurate registration of the T1w image (and associated brain mask) to T2w. A synthetic T1-T2w fusion image was created by multiplying the T1w by the T2w image [Xiao et al., 2014] and re-estimating the intensity inhomogeneity again with N4. The original T2w image was denoised using the adaptive non-local means method [Manjón et al., 2010] and the obtained inhomogeneity estimation was applied to the denoised image resulting in a final preprocessed T2w image in the scanner space. Rigid registration to the T1w scan was re-estimated using the preprocessed image. Final preprocessed images included both a T2w volume in the original scanner space as well as one resampled into the T1w structural space. The process was bootstrapped once after creating an initial T2w template (see Section 5.2.5 Template Creation) and using the template for histogram-based intensity normalization. Note that because of the combination of post hoc bias field correction and intensity normalization necessary to produce more homogeneous images, the per voxel values of the T2SPACE images are not directly comparable between scans in a quantitative manner. This processing pipeline has been released and containerized as a BIDS app (`https://github.com/khanlab/prepT2space/`).

5.2.5 Template creation

The antsMultivariateTemplateCreation2 pipeline was used for multimodal (T1,T2) template creation [Avants et al., 2011]. A corresponding T2w template (in T1w space) was created after propagating the participant T2w images to T1w template space using the relevant transformations produced using prepT2space. An initial template was created using rigid body alignment of each participant's T1w scan to the MNI2009bAsym template (0.5 mm isotropic resolution) [Fonov et al., 2009]. Over a series of 10 subsequent bootstrapped iterations, the deformable registration was refined (shrink factors: 12x6x4x2x1; smoothing factors: 6x3x2x1x0vox; max iterations: 100x100x70x50x10; transformation model: Greedy SyN; similarity metric: cross-correlation). Using the derived affine and nonlinear transforms, the individual sequences (T1map and T2) were transformed and resampled using trilinear interpolation into the template space. Mean intensity images were generated for each parametric sequence. The log Jacobian was computed, providing an estimate of local deformation required to transform each participant into the template space. The scripts for template creation have been archived for reference (`https://github.com/jclauneuro/snsx32/`). Spatial correspondence was quantified using a recently described anatomical fiducial (AFID) placement protocol by three trained raters who placed 32 AFIDs on the original scanner space for the T1w images using 3D Slicer [Fedorov et al., 2012], so that anatomical fiducial localization error (AFLE; Euclidean distance between point placements) could be calculated. This permitted the computation of residual AFID registration error (AFRE) to be calculated across these same features [Lau et al., 2018b] (RRID:SCR_016623) to quantify the accuracy of template creation, which is the subject of Chapter 3.

5.2.6 Region-of-interest segmentation

The zona incerta, subthalamic nucleus, and substantia nigra were segmented using the 10th iteration T1 and T2 combined template using ITK-SNAP version 3.6.0. Each rater segmented the regions twice, with sessions spaced more than two weeks apart. A representative template segmentation was derived by averaging all segmented ROIs and thresholding by majority voting (> 50%) – this was considered the “gold” standard. Three raters segmented the RN and STN twice using the T2 image (JD, JL, YX). The pZI, rZI, cZI, raprl, and the ft were segmented twice by two raters (GG, JL) using the T1 map image. To our knowledge, the ZI has not been previously segmented from *in vivo* images. As such, two stereotactic neurosurgeons (AP, KM) were consulted throughout the ZI segmentation process: first, after the initial segmentations by the lead author (JL); second, after identifying critical boundaries of the ZI particularly rostrally; and finally, to review the final consensus segmentation. Several histological human brain atlases were used as references [Schaltenbrand and Wahren, 1977, Morel, 2007, Hawrylycz et al., 2012].

The rostral ZI presented some challenges to accurate identification, not for lack of contrast, but due to difficulty with determining its relationship with the fl and ft. On closer review, we speculate that the fl actually runs through the rostral portion of the ZI. We provide labels for the ZI as a whole, and provide separate labels for the dorsal rZI, vZI, interposed fl, and cZI. The lateral aspect of the central portion of the ZI (between rostral and caudal ends) was too thin to segment along its entire length even at 7T.

5.2.7 Stereotactic target localization

Target locations in the bilateral posterior subthalamic area were placed according to the placement scheme of Nowacki and colleagues [Nowacki et al., 2018] (Figure 5.3). This scheme relies on anatomical targeting based on axial T2-weighted images after performing an initial AC-PC transformation with placement at the center of each commissure. This target involves the identification of three different lines: a horizontal line drawn along the equator of the RN identified on the axial slice of maximal diameter, an oblique line drawn along the long-axis of the STN, and finally, an oblique line perpendicular to the long-axis of the STN intersecting the lateral border of the RN at its equator. The placements were reviewed via consensus with two neurosurgeons who practice stereotactic neurosurgery (AP, KM). Optimal target location was also investigated prospectively in a patient with essential tremor who had undergone cZI implantation with adequate long-term follow-up and Essential Tremor Rating Scale (ETRS) recorded.

5.3 Results

5.3.1 Template Creation

Mean AFLE after quality control was 0.91 ± 0.69 mm. Visual inspection of AFIDs revealed good spatial correspondence as well as evidence of good anatomical detail in subcortical struc-

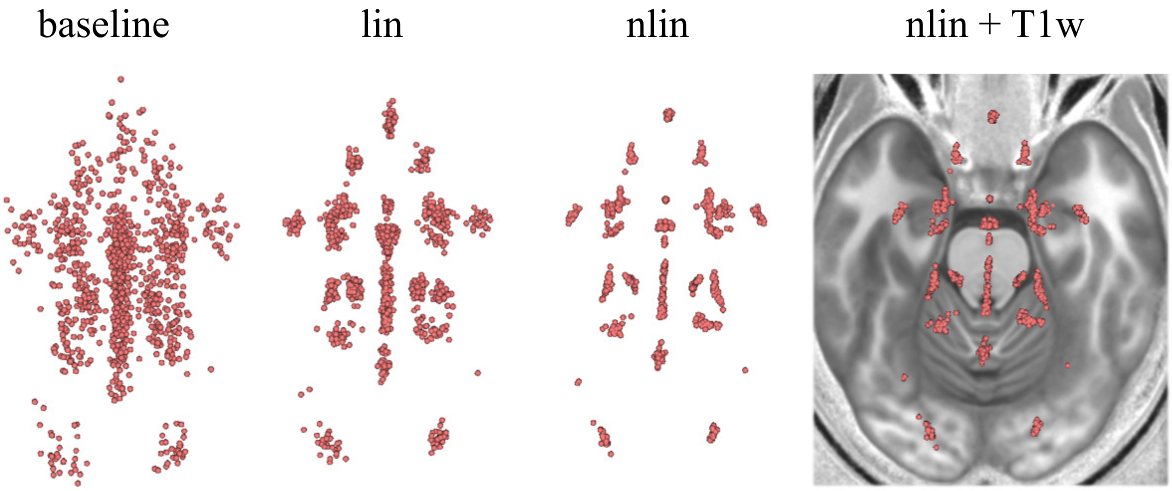

Figure 5.1: Visual inspection of AFIDs revealed good convergence with successive template generation steps showing the baseline correspondence between images followed by the linear only template and finally the combined (linear and nonlinear) template after 10 iterations of template building. The information here is corroborated in Tables 5.2 and 5.3.

tures of the final template (Figure 5.1). Mean AFRE decreased globally across all AFID points with registration complexity improving from 29.62 ± 11.58 mm at baseline to 3.47 ± 1.62 mm after linear registration and to 2.80 ± 0.90 mm after deformable registration (one iteration). Further increases were noted with successive iterations of template generation to 2.06 ± 0.92 mm after 4 iterations to 1.27 ± 1.02 mm after 10 iterations. Mean AFRE improved to a limit of 2.82 ± 1.47 mm with linear registration alone with little improvement beyond 6 iterations, while improvements were noted up to 10 iterations with deformable registration (see Table 5.3 and Figure 5.1).

Several AFID features were particularly difficult to register, with registration errors higher than the expected manual anatomical fiducial localization error. In particular, we identified several features with more than 6 mm of registration error: the lateral mesencephalic sulci, temporal horns, and origins of the indusium griseum bilaterally (Figure 5.1 and Table 5.3).

5.3.2 Direct visualization and segmentation of the zona incerta region

We pooled submillimetric (0.7 mm isotropic) *in vivo* 7T MRI data from cognitively intact participants to characterize the human ZI in relation to surrounding structures of the subthalamic region with a specific focus on longitudinal (T1) relaxometry. After windowing to a threshold of between 1000-2000 ms, the contrasts from T1 mapping within the ventral thalamus and subthalamic region were strikingly similar to classical Nissl staining (Figure 5.1) with white matter generally darker stained relative to gray matter. This permitted facile identification of

Table 5.2: Improvement in linear and nonlinear AFRE with multiple iterations of template creation.

iteration	lin AFRE	nlin AFRE
0	29.88 ± 11.75 (61.50)	29.88 ± 11.75 (61.50)
1	3.47 ± 1.62 (10.01)	2.87 ± 0.94 (8.58)
2	3.31 ± 1.57 (9.95)	2.61 ± 0.95 (8.59)
3	3.15 ± 1.53 (9.79)	2.37 ± 0.95 (8.44)
4	3.04 ± 1.50 (9.66)	2.12 ± 0.96 (8.39)
5	2.94 ± 1.47 (9.52)	1.90 ± 0.97 (8.11)
6	2.86 ± 1.45 (9.38)	1.71 ± 1.00 (8.05)
7	2.80 ± 1.43 (9.33)	1.53 ± 1.04 (8.05)
8	2.79 ± 1.44 (9.18)	1.41 ± 1.05 (7.88)
9	2.73 ± 1.37 (9.19)	1.34 ± 1.08 (7.81)
10	2.82 ± 1.47 (9.23)	1.33 ± 1.09 (7.84)

AFRE values summarized as: mean ± standard deviation (max value)

the zona incerta and surrounding structures in reference to a number of classic and modern atlases [Schaltenbrand and Wahren, 1977, Morel, 2007, Hawrylycz et al., 2012, Mai et al., 2015].

The ZI could be visualized along its entire rostrocaudal axis and was distinct from the surrounding white matter tracts, specifically the external medullary lamina of the ventral thalamus, fasciculus thalamicus (ft), and fasciculus lenticularis (fl). Regions of high T1 signal were identified both superior and inferior to the fl which we believe represent distinct dorsal and ventral components of the rZI. Interestingly, the ventral component which we observed has been obscurely named on the classic Schaltenbrand atlas, where it is unnamed on select coronal sections (Figure 2.1b; Coronal: +2.0 mm), and ambiguously named on relevant sagittal sections. The labelling is no clearer in modern atlases with some atlases preferring to incorporate this label as a protrusion of the lateral hypothalamus. Caudally, the cZI was clearly distinct from nearby gray matter nuclei including the STN and RN (Figure 2.1b; Coronal: -7.0 mm). Furthermore, we identified a distinct hypointense region within the posterior subthalamic area, anterior to the cZI and anterolateral to the RN coinciding with the fct (aka raprl), previously only identified on histological sections (Figure 2.1b; Coronal: -7.0 mm; Axial: -3.5 mm).

Segmentation of the ZI and nearby RN and STN enabled visualization of the spatial relationship between these structures as three-dimensional models (Figure 5.2). We also provided segmentations of the cZI separately as well as the relevant portions of the ft and fct. Based on our analysis, we estimate that the ZI proper spans ~ 15 mm along its main axis, ~ 5 mm in the medial-to-lateral direction, and varying in height from thinner than 0.5 mm along its lateral boundary to as thick as ~ 5 mm in the cZI. The volume of the ZI proper was 219.5 mm^3 on the left and 211.5 mm^3 on the right. The cZI volume was 63.8 mm^3 on the left and 65.9 mm^3

Table 5.3: AFRE summarized for the final template used in this study (10th iteration).

AFID	Description	Mean AFRE
01	AC	0.41 ± 0.20 (1.05)
02	PC	0.47 ± 0.29 (1.56)
03	infracollicular sulcus	0.69 ± 0.21 (1.19)
04	PMJ	0.93 ± 0.63 (2.86)
05	superior interpeduncular fossa	0.70 ± 0.29 (1.26)
06	R superior LMS	1.11 ± 0.67 (2.93)
07	L superior LMS	1.00 ± 0.54 (2.41)
08	R inferior LMS	1.35 ± 1.23 (6.81)
09	L inferior LMS	1.56 ± 1.30 (6.13)
10	culmen	2.16 ± 1.08 (5.40)
11	intermammillary sulcus	0.80 ± 0.44 (1.99)
12	R MB	0.64 ± 0.36 (1.60)
13	L MB	0.59 ± 0.38 (1.81)
14	pineal gland	1.66 ± 0.93 (4.19)
15	R LV at AC	2.11 ± 1.42 (5.28)
16	L LV at AC	1.90 ± 1.37 (5.48)
17	R LV at PC	2.84 ± 1.90 (8.15)
18	L LV at PC	2.37 ± 1.57 (6.53)
19	genu of CC	1.28 ± 0.74 (3.52)
20	splenium	0.94 ± 0.53 (2.47)
21	R AL temporal horn	1.98 ± 1.31 (5.25)
22	L AL temporal horn	1.92 ± 1.06 (4.97)
23	R superior AM temporal horn	1.72 ± 1.36 (6.41)
24	L superior AM temporal horn	1.41 ± 0.85 (3.92)
25	R inferior AM temporal horn	2.29 ± 1.26 (5.17)
26	L inferior AM temporal horn	1.86 ± 0.99 (5.44)
27	R indusium griseum origin	2.07 ± 1.44 (4.70)
28	L indusium griseum origin	2.04 ± 1.67 (7.84)
29	R ventral occipital horn	2.44 ± 4.11 (24.49)
30	L ventral occipital horn	3.85 ± 5.05 (22.42)
31	R olfactory sulcal fundus	1.43 ± 1.02 (4.05)
32	L olfactory sulcal fundus	1.60 ± 1.10 (6.10)

AFRE values summarized as: mean ± standard deviation (max value)

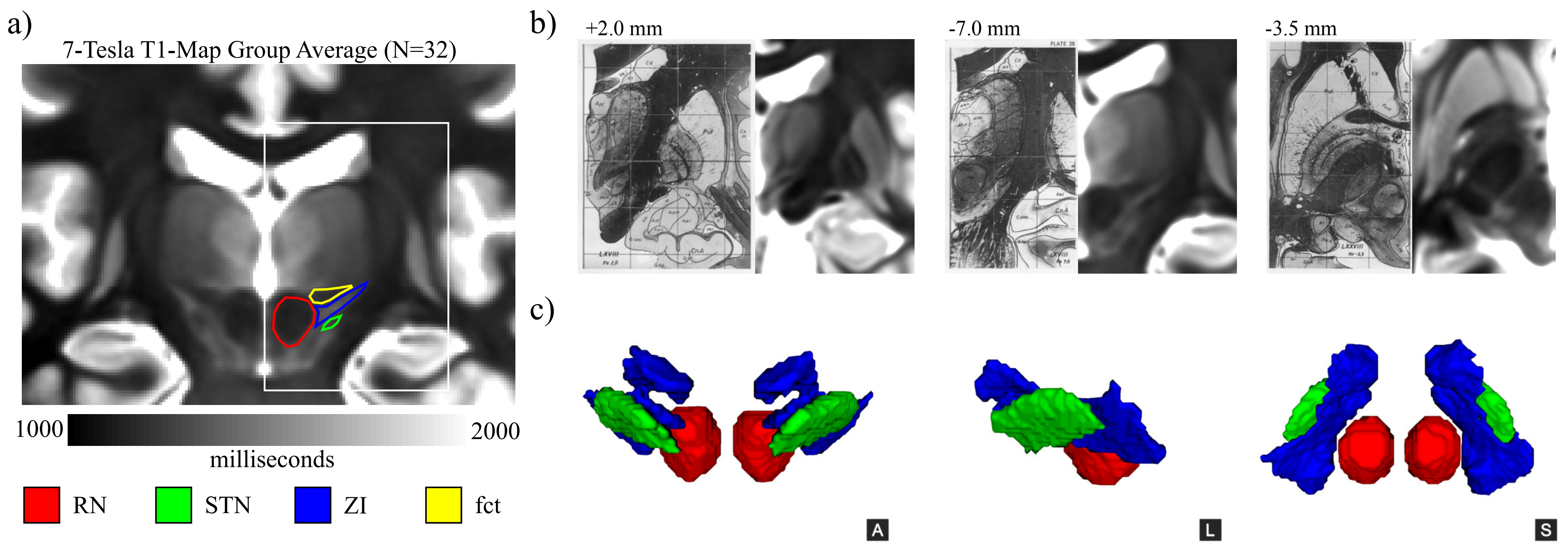

Figure 5.2: Study data demonstrating that the ZI (blue) and surrounding structures can be robustly delineated *in vivo* using 7T MP2RAGE data (a). Actual image values relate to inherent tissue properties; thus thresholding to a set window (1000-2000 ms) in MP2RAGE is actually meaningful in comparison to traditional weighted images. The striking similarity between a histological atlas [Schaltenbrand and Wahren, 1977] and *in vivo* study data is demonstrated in several select slices (+2.0 and -7.0 mm relative to the anterior commissure in the coronal plane; -3.5 mm relative to the axial plane) (b). Visualization of the models of the RN, STN, and ZI in group average space (c).

Table 5.4: Summary of T1 values, volume, centroids of key structures of the ZI region.

		ZI	cZI	fct	RN	STN
T1 (ms)	left	1329.1 +/- 111.4	1361.5 +/- 63.9	1192.2 +/- 39.6	1169.2 +/- 36.5	1115.6 +/- 65.4
	right	1315.3 +/- 107.2	1339.5 +/- 59.9	1184.4 +/- 36.6	1163.7 +/- 34.8	1128.6 +/- 47.5
volume (mm^3)	left	219.5	63.75	162.5	324.2	168.5
	right	211.5	65.88	161.5	337.5	163.6
AC-PC Coordinates	left	(9.1,2.5,2.6)	(12.3,8.7,4.9)	(10.4,5.1,1.5)	(4.4,6.5,5.9)	(9.7,0.3,3.4)
	right	(-9.7,2.6,2.3)	(-13.0,9.0,4.0)	(-10.2,5.2,1.7)	(-4.6,6.4,5.8)	(-10.3,0.4,3.2)

on the right. Regarding relevant nearby white matter regions, the fct was ~ 4-5 mm along its longest axis, representing 1-3 voxels if relying on DTI alone compared to 5-7 voxels with the MP2RAGE protocol with a total volume of 162.5 mm^3 on the left and 162.5 mm^3 on the right. Note that this is similar in size to the STN in most reported studies (e.g. [Xiao et al., 2014]).

5.3.3 Tissue properties of the zona incerta region

The mean T1 relaxometry values and volumes for the bilateral red nucleus, subthalamic nucleus, and zona incerta structures are provided in Table 5.4. The zona incerta appears prominent as a hyperintense region located in the subthalamic region with T1 values generally in the 1300-1500 ms range with similar relaxometry parameters to cortex (see Table 1.1), providing in vivo support that the ZI represents a distinct gray matter region.

5.3.4 Deep brain stimulation of the caudal zona incerta

T1 values, volumes, and centroid locations are summarized in Table 5.4. We found sufficient contrast (contrast-to-noise ratio = 2.7-4.3) to allow separation of the cZI and fct, which has important implications for more precise targeting within the PSA. We discovered that the T2-based indirect method for targeting described was closer to the fct than the cZI centroid (3.6 vs 5.4 mm) in both our template and also the active contact location in a patient with excellent post-operative outcome for essential tremor (Essential Tremor Rating Scale improvement by 60% total and by 80% for hand tremor and function).

5.4 Discussion

The present study demonstrates that robust visualization of the zona incerta region is possible using high-resolution quantitative T1 mapping. We report the first precise delineation of the zona incerta region *in vivo* providing estimates of the morphology (volume, dimensions) and

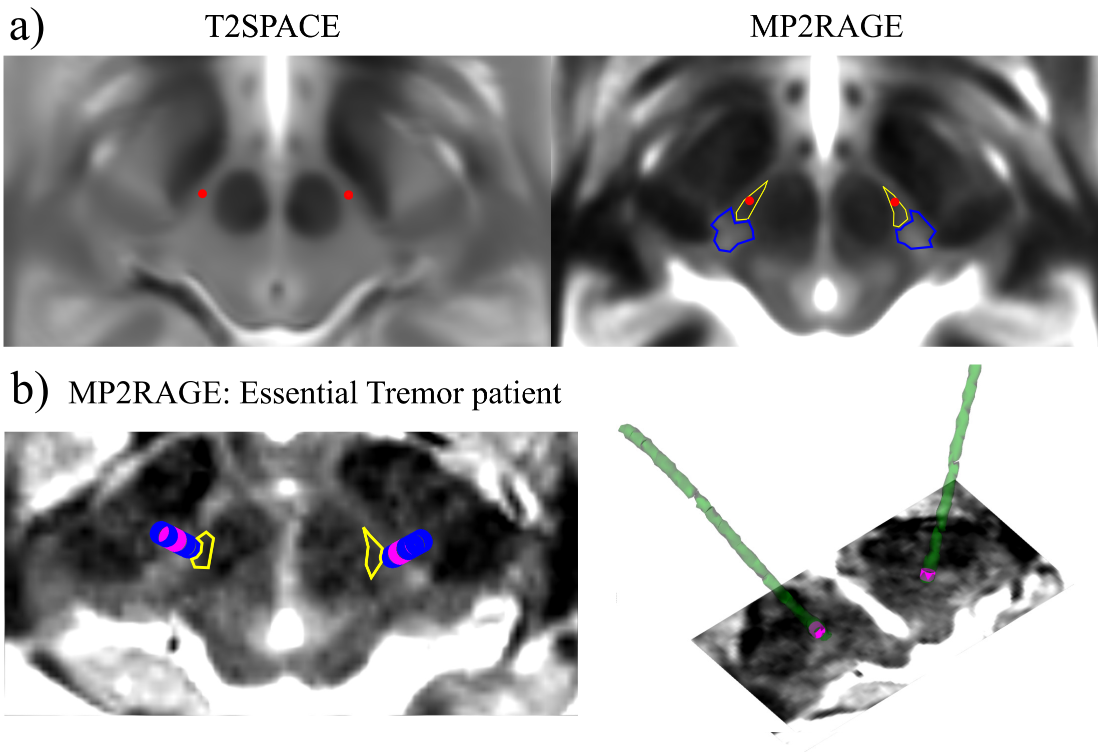

Figure 5.3: Study data demonstrates that the optimal target for essential tremor patients is likely the fasciculus thalamicus (fct) rather than the caudal zona incerta. Representative axial slices of the upper mesencephalon in the study group average space depicting T2 and MP2RAGE contrasts (a). The stereotactic target for essential tremor as described by Nowacki [8] is shown as a red dot within the posterior subthalamic area based on the relative location of the STN and RN in T2 images. The same target is superimposed onto the MP2RAGE average with outlines of the fct and cZI in yellow and blue respectively (a). Note that while no contrast can separate the fct from the cZI in the T2 image, the two can be visualized separately in the corresponding MP2RAGE map with the target lying within the fct region. The optimal stimulation electrode for a patient with essential tremor is shown in pink (b) as well as the relative location of the zona incerta and fct (yellow).

longitudinal relaxation-based properties of the region. Furthermore, we have identified a region of the rostral ZI inferior to the thalamic fasciculus, which to our knowledge has not previously been labeled on histological atlases of the human brain (Figure 5.2) we believe this represents the ventral rZI. Due to the striking similarity in tissue contrast with classic post-mortem Nissl staining, we were able to segment the fct (raprl) as a substructure within the posterior subthalamic area separate from the cZI. By exploiting the signal advantages of ultra-high field MRI and template averaging, we demonstrated that the zona incerta is visible *in vivo*, determined that this nuclear region can be decoupled from surrounding fibre pathways, and were able to employ this methodology for prospective identification of the active stimulation location for deep brain stimulation.

Efforts at visualizing small structures of the deep brain using high-field MRI have mostly focussed on transverse relaxation properties (i.e. T2- and T2* shortening) due to the well-documented iron-rich, and thus paramagnetic contrast produced by many subcortical nuclei [Zecca et al., 2004, Haacke et al., 2005]. Increasing the strength of the main magnetic field (B_0) results in an at least linear increase in SNR, a three- to four- fold increase compared to conventional clinical 1.5 Tesla MRI, along with significantly higher resolution. Visualization at high fields has led to more robust imaging of small structures including the STN and SN using T2-based contrast mechanisms [Keuken et al., 2013]. Others have attempted to visualize the ZI using T2 contrast, yet the region has remained elusive except for one study purporting to show that the rZI is visible, but which we show here is actually the fasciculus lenticularis (Figure 5.4). Instead, protocols for stereotactic targeting of the cZI have relied on the relative visibility of the surrounding red nucleus and STN, which can be used to infer the location of the stereotactic target within the PSA. Overall the poor visualization of ZI on T2 contrast suggests that this region is not a strong generator of T2 contrast.

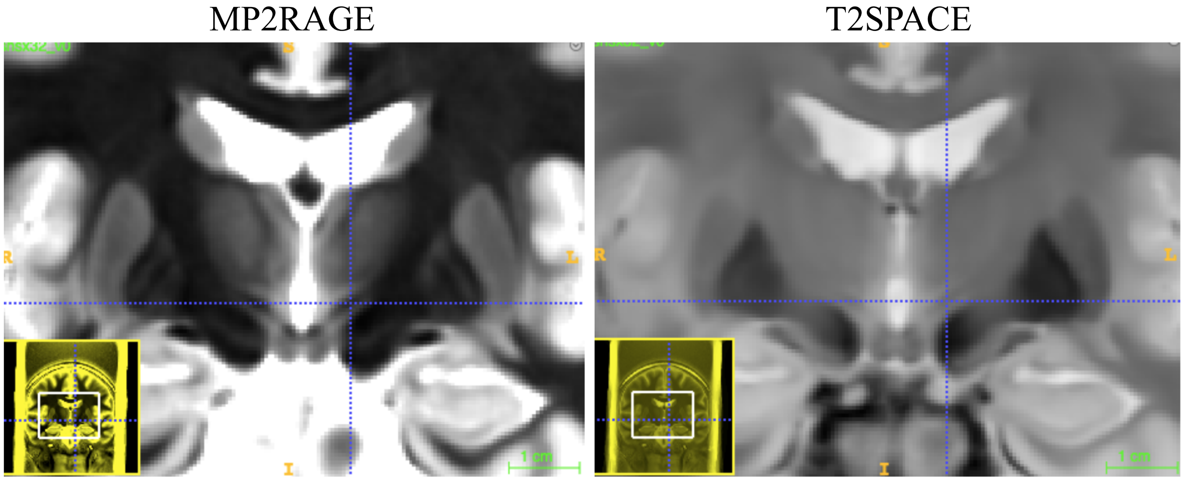

Figure 5.4: The crosshair is placed on the location identified by [Kerl et al., 2013] as the rostral ZI but overlaid on our joint MP2RAGE and T2SPACE templates. The corresponding location on the the MP2RAGE (T1 map) sequence demonstrates that this feature is actually hypointense on T1 map suggestive of white matter and thus represents the fasciculus lenticularis rather than the rZI. See Figure 5.2b for the corresponding labels in a histological reference space.

In the present study, we focus on longitudinal (T1) rather than T2 relaxation properties of the ZI, to demonstrate its salience, and propose its use as a robust *in vivo* biomarker for delineating structures in the region. T1 relaxation times increase in a field-dependent manner, as does the dispersion between brain tissue types [Rooney et al., 2007], which have the effect of improving contrast between tissue types at 7T. This advantage has been exploited to parcellate thalamic nuclei [Tourdias et al., 2014] and investigate cortical laminae [Trampel et al., 2017].

Surgical planning and *in vivo* histology have been considered as important potential applications of the MP2RAGE sequence since its initial development [Marques et al., 2010, Marques and Gruetter, 2013]. Using this method, we demonstrate that the ZI can also be visualized along its entire rostrocaudal axis using this MRI-based tissue property (Figure 5.2). Furthermore, we found sufficient difference in T1-related tissue parameters to allows separation of the cZI from nearby white matter tracts, including the fct of the posterior subthalamic area and the ft and other components of the fields of Forel in the rZI. Rostrally, this permitted more complete characterization of the relationship between the fl and rZI, which we believe divides the rZI into dorsal and ventral components, which have been described in immunohistochemical analysis of experimental animals [Mitrofanis, 2005, Watson et al., 2014] and in at least one human brain atlas [Mai et al., 2015]. Although the increase in T1 tissue values with field strength has been perceived as a disadvantage due to increased scan time, our experience demonstrates that sufficient resolution and contrast can be attained with a scan time of just over 10 minutes (Figure 5.2; Table 5.1) with an additional 2 minute sequence for on scanner B_1 inhomogeneity correction [Eggenschwiler et al., 2012].

Since the boundaries of the ZI have not previously been well-defined in three dimensions, we elected to perform consensus segmentations using group averaging as a strategy to further boost the SNR for accurate delineation of these structures from our 7T data. Our interpretation of the boundaries of the zona incerta using *in vivo* sequences was based on meticulous comparison with annotations of the zona incerta from classical and modern histological atlases [Schaltenbrand and Wahren, 1977, Morel, 2007, Hawrylycz et al., 2012, Mai et al., 2015]. Our technique compares favorably with classic post-mortem atlases for mesoscale morphometric analysis due to our ability to pool structural information from a set of 32 participants and also circumvent the challenges of histological processing that can result in tissue shrinkage, deformation, and tears. While errors in registration may result in errors in segmentation of the individual subjects, we were able to confirm adequate spatial correspondence by using visual quality control and also by determining that fiducial registration error was in the millimetric range (Table 5.2 and Figure 5.1). Our high-resolution template creation approach allowed for the pooling of data from multiple participants (N=32) into a single reference space allowing us to better account for intersubject variability compared to histological atlas creation, which is also prone to tissue deformations [Morel, 2007]. Due to the complexity of this structure, future efforts will involve further clarifying the exact boundaries of the rostral ZI through a combination of detailed histological analysis and population studies of the region.

Based on our analysis, T1 maps appear to represent an optimal quantitative contrast by which to visualize the zona incerta region. As already mentioned, there is very close correspondence in intensity between our *in vivo* T1 maps with Nissl staining [Schaltenbrand and

Wahren, 1977, Weiskopf et al., 2015]. However, the correspondence with histology is not strictly one-to-one, noting that the RN and STN appear hypointense on T1 maps despite being largely gray matter regions in the current study (Table 5.4; Figure 5.2) as well as in work from other groups (e.g. [Keuken et al., 2017]). We believe that the relatively low T1 map contrast in these regions is related to the density of myelinated tracts travelling within these nuclear regions. In the ZI region, which is relatively sparsely nucleated, the traversing white matter tracts seem to occur at specific spatial clusters (ft and raprl). Multiparametric approaches may help further characterize underlying tissue properties. We have found the multicontrast approach (both T1 and T2) helpful for establishing that a region previously identified as the rZI [Kerl et al., 2013] actually represents the fl (Figure 5.4). Unfortunately, due to limitations in our T2 protocol, we could not investigate the T2 values quantitatively (see Methods).

Our analysis demonstrates that there is sufficient signal and contrast within the PSA region to allow separation of the cZI from the fct and ml (see Table 5.4). We discovered that commonly used T2-based indirect anatomical target and optimal stimulation locations were closer to the fct than the cZI centroid. These findings are in line with other work suggesting that a proportion of benefit is derived from stimulation of wayward white matter tracts in the fct (raprl) [Spiegel et al., 1964, Mundinger, 1965, Velasco et al., 1972, Mohadjer et al., 1990, Blomstedt et al., 2010, Blomstedt et al., 2018], and also concordant with recent studies employing diffusion tensor imaging (DTI) [Fiechter et al., 2017, Dallapiazza et al., 2018, Velasco et al., 2018]. Compared to DTI-based measures, high-field T1 mapping has higher SNR, is less prone to image distortions, and is acquired at inherently higher resolution (0.7 mm compared to 2-3 mm isotropic). We have determined that the dimensions of the fct within the PSA is $\sim$ 4-5 mm along its longest axis, representing 1-3 voxels if relying on DTI alone compared to 5-7 voxels using our MP2RAGE protocol. Nowacki and colleagues have previously suggested that the DRTT (dentatorubrothalamic tract within raprl) is the key area within the PSA for targeting [Fiechter et al., 2017]. However, their analysis of the active contact location suggests that the most efficient stimulation location was further away (1.84 ± 1.24 mm) from the DRTT than the least efficient stimulation location (0.92 ± 1.21 mm) – although this did not meet thresholds of statistical significance [Nowacki et al., 2018].

Radiofrequency inhomogeneity is a well-known problem with increasing magnetic field strength biasing the interpretation of T1 maps since stronger RF pulses are required for excitation and detection leading to more pronounced intensity bias in the images [Rooney et al., 2007] (Fig1). The MP2RAGE sequence used in this study was designed to be a self bias-field correcting sequence free of PD and T2* weighting, RF receiver field bias, and low-order RF transmit field bias [Marques et al., 2010]. In this study, we also acquired an additional low-resolution B_1 mapping protocol, SA2RAGE [Eggenschwiler et al., 2012], as a means to detect

Table 5.5: Comparison between MP2RAGE sequence used in this study and that used by [Forstmann et al., 2014].

Sequence		TE (ms)	TR (ms)	TI	Flip Angle (^{o})	Matrix Size	PAT*	Averages	Resolution	Acquisition Time (min:sec)
Current Study	3D	2.73	6000	800/2700	4/5	342x342x224	3	1	0.7x0.7x0.7	10:14
Forstmann 2014	3D	2.45	5000	900/2750	4/11	320x320x240	2	1	0.7x0.7x0.7	10:57

* PAT = parallel acquisition technique (acceleration factor)

and subsequently correct the transmit inhomogeneity. Finally, and perhaps most importantly, our acquisitions benefited from the use of parallel transmission of RF pulses using a multiple channel approach [Gilbert et al., 2011], a hardware-based approach for achieving better intensity homogeneity. This combination of hardware and software calibrations has helped to improve the quality and homogeneity of our 7T T1 map acquisitions enabling more robust identification and characterization of the ZI and surrounding region.

Some discrepancy was noted when comparing values reported by others who have investigated the subthalamic region using MP2RAGE-based T1 mapping [Forstmann et al., 2014, Keuken et al., 2017]. In particular, our values tended to be $\sim$ 100-200 ms shorter within the STN and SN. More perplexing was that we also noted some difference in age-related trends using our ROIs. Several factors may account for the discrepancies between our studies. Beyond inter-scanner variability in hardware (e.g. our use of parallel transmission) and our use of SA2RAGE-based correct (see the paragraph above), inter-protocol variability has been reported [Stikov et al., 2015]. In addition, there were some differences in acquisition parameters (Table 5.5), which unfortunately due to assumptions about mono-exponential longitudinal relaxation in the MP2RAGE implementation can introduce additional sequence-dependent measurement variability [Rioux et al., 2016]. These factors all lead the T1 value measurements to tend to be more precise than accurate, contributing to inter-site differences. For ROI segmentation, Forstmann et al. performed meticulous labelling of the STN and SN for every subject by two raters, a highly manually intensive process [Forstmann et al., 2014]. Our approach, instead, relied on careful delineation of the ROIs in reference space, with propagation error quantified to $\sim$ 1 mm using a recently described metric for estimating registration accuracy between template and subject scans [Lau et al., 2019] (see Chapter 3). Perhaps the most important difference relates to the Forstmann group's choice to use "conjunction masks" as the choice of ROI (that is the intersection between the labels of two raters as the choice of ROI). This approach ensures that summary measures are obtained for voxel regions confidently within the structure of interest, thus preventing boundary effects such as the impact of changes in surrounding structures; but on the other hand, underestimates the volume of the structures (e.g. the STN sizes reported by Forstmann and colleagues tended to be lower $\sim$ 50 mm^3 than those reported by other groups). In the future, these data can be pooled into larger multisite analyses with standardized workflows that will better clarify our findings on a larger scale.

Our findings add to the growing body of knowledge that the optimal DBS target within the posterior subthalamic area is at the anterior boundary of the cZI abutting or directly within the fasciculus cerebellothalamicus [Herrington et al., 2016]. This suggests that direct targeting of the white matter, in other words connection-based targeting, may be central to efficacy, which is increasingly being recognized for the treatment of tremor [Akram et al., 2018] and other disorders [Horn et al., 2017b, Horn et al., 2017c]. Our approach using T1 mapping for visualizing relevant WM tracts (fct, al, ft, fl) is in contrast to more common methods using diffusion-based imaging. In regards to human *in vivo* studies, DTI studies have mostly focussed on connections between larger cortical and subcortical structures since achieving high resolution (submillimetric) images in clinically feasible timeframes for DTI remains a challenge. There is also increasing acknowledgement that connectivity-based methods are prone to producing false-positive tracts [Maier-Hein et al., 2017]. An additional advantage of using T1 mapping is that the images can simultaneously be used as a baseline structural scan and furthermore employed to identify the target, eliminating the need for an image fusion step, which can introduce error.

5.5 Conclusions

We demonstrate using ultra-high field MRI and template averaging that the zona incerta is visible *in vivo* in control and patient datasets. In addition, we determined that this nuclear region can be decoupled from surrounding fibre pathways. Due to the striking similarity in tissue contrast with classic post-mortem Nissl staining, we were able to segment the fasciculus cerebellothalamicus as a substructure within the posterior subthalamic area separate from the caudal ZI. Furthermore, we identified a region of the rostral ZI inferior to the thalamic fasciculus, which to our knowledge has not previously been labeled on histological atlases of the human brain, and which we believe represents the ventral rZI described in experimental animals [Mitrofanis, 2005]. This work enables high-resolution *in vivo* visualization of a region previously only seen on histology, paving the way for patient-specific optimization and characterization of stereotactic targets.

Chapter 6

Conclusions and Future Directions

The work in this thesis has explored ways in which ultra-high field magnetic resonance imaging can be integrated into the practice of stereotactic neurosurgery. The unique contributions can be summarized as follows:

- Chapter 2: For the first time, an ultra-high field MRI template is integrated into the surgical workflow to assist with surgical planning for deep brain stimulation surgery cases.
- Chapter 3: A novel anatomical fiducial placement protocol is developed, validated, and used prospectively to quantify the limits of template-assisted surgical planning.
- Chapter 4: A novel morphometry workflow is employed to characterize local geometric distortion in ultra-high field MR images identifying systematic regions with higher geometric uncertainty, which should be taken into account if using high-field imaging for surgical planning.
- Chapter 5: A number of important stereotactic targets (i.e. the zona incerta and fasciculus thalamicus) are directly visualized and characterized for the first time *in vivo* at high resolution using T1 mapping methods at ultra-high field.

By identifying the limits of atlas- and template-assisted stereotactic planning, characterizing regional biases of spatial uncertainty, and identifying anatomical targets not prreviously visible *in vivo*, this work paves the way for patient-specific surgical planning using ultra-high field MRI.

6.1 The Limits of Image-Based Targeting

Proof-of-principle evidence for template-assisted surgical planning for deep brain stimulation surgery is provided in Chapter 2. By employing deformable (nonlinear) registration methods, this represents a reasonable technique where patient imaging is inadequate, i.e. when only standard field MRI is available and where clinical imaging is subpar (motion artifact, etc.). In Section 3.3.3, the geometric limits of template-assisted registration with patient datasets were explored, demonstrating that with current state-of-the-art deformable registration methods, errors in point-based registration were present even beyond the limits of localization error. This analysis revealed misregistrations on the order of 1.80 ± 2.09 mm and as high as over 30 mm. These results provide evidence that standard deformable registration methods remain insufficiently accurate for the purposes of stereotactic neurosurgery, and also suggest that high-quality patient-specific imaging may be a welcome alternative.

While using patient-specific imaging avoids the problem encountered with template registration where two images with different anatomical features are matched, geometric distortion in images, particularly with an increase to high-field may present some issues. Several sources for geometric distortion issues have been highlighted in Chapter 4. In a dataset of subjects scanned at ultra-high field and standard field, we were able to characterize the location of these spatial biases. These B_0-related issues tended to occur at air-tissue boundaries such as the floor of the middle fossa. Fortunately, the work in this thesis has determined that the areas of the deep brain which are the putative targets for the majority of stereotactic procedures are relatively protected from these effects paving the way for the use of patient specific 7T imaging. These results are not necessarily generalizable to other scanners given the unique combination of hardware. However, the framework used that employs voxel-wise morphometric analysis can be used by other groups. Also in the future, other specific sources of distortion that are sequence-specific, i.e. Maxwell distortions, should be explored.

Despite advances in resolution for patient imaging and well-optimized distortion correction methods, other factors, that may be limiting the ability to accurately target these small brain structures, become more important. In the neurosurgical literature, the term *application accuracy* is used to describe the multifactorial nature of this problem in the surgical environment. That is, targeting error is influenced by many different variables from the quality of preoperative imaging, image fusion, the quality of fixation of the frame or pins to the head, to the limits of physical accuracy of the devices being employed to perform targeting [Maciunas et al., 1994, Grunert et al., 2003, Henderson et al., 2004, Shamir et al., 2011]. It has been perceived that the physical or mechanical accuracy of current physical frames is on the order of 1-2 mm. Recent evidence suggests some modest improvement in targeting accuracy (to 1-1.5 mm error) with modern robotic devices for stereotactic targeting [Cardinale et al., 2013]. While worth mentioning, this thesis has focussed on optimizing the image-based aspects of the application accuracy problem.

6.2 Multiparametric Imaging for Stereotactic Neurosurgery

The latter part of this thesis has focussed on using T1 mapping for visualizing small structures in the deep brain. Integration with other quantitative MRI-based parameters would provide richer multi-contrast information that could be used to better delineate between different local tissue types. For example, other acquisition types that characterize local magnetic properties using multi-echo acquisitions and associated post-processing methods (R2* and quantitative susceptibility mapping), and local diffusion-related properties such as mean diffusivity (MD) and fractional anisotropy (FA) have been demonstrated to be beneficial for surgical planning.

These different imaging methods reflect to different extents underlying biological features related to molecular-level content (water, iron, myelin, gray matter) and organization (anistropy, etc.).

Over the past few years, connectomic approaches that focus on the connections between regions to optimizing neuromodulation sites has become increasingly popular [Fox et al., 2014]. These methods focus on using diffusion-based or functional MRI-based sequences to determine coherence or connectivity based on DBS lead locations. For Parkinson's disease, these studies have focussed on large tract connections to cortex and their association with lead location [Vanegas-Arroyave et al., 2016, Akram et al., 2017, Horn et al., 2017b, Horn et al., 2017c]. However, despite convergence of evidence from multiple groups, these methods have recently been discovered to be prone to false-positive results [Maier-Hein et al., 2017]. Ultimately, the approach taken in this thesis, particularly with increasingly higher resolution imaging, should be considered complementary to these endeavours enabling accurate localization of smaller tracts and structures for integration into connectivity analyses.

6.3 "Asleep" Deep Brain Stimulation Surgery

Over the last several years, a number of groups have shifted to "asleep" DBS surgery–that is, advocating for direct image-based directing using pre-operative imaging with intraoperative verification with the patient under general anaesthesia [Hyam et al., 2015, Chen et al., 2016, Brodsky et al., 2017]. To date, all the existing asleep DBS protocols have relied on imaging at standard magnetic field strengths. Overall, good success has been documented, although a recent meta-analysis suggests that patients who were awake during surgery suffered from fewer stimulation-related side effects than those performed asleep [Ho et al., 2017]. This has been corroborated in a recent single center study demonstrating improved outcomes in awake versus asleep patients [Blasberg et al., 2018]. Another recent retrospective study observed that while image-based targeting was appropriate in the vast majority of cases, in 20% of cases the imaging-based target proved to be suboptimal [Lozano et al., 2018]. Still, others continue to advocate for MER recordings with recent evidence demonstrating that multiple MER tracks are more beneficial than the use of a single track [Bjerknes et al., 2018]. These recent findings all point to the need for caution and that other adjuncts, whether microelectrode recording or better imaging (see Chapter 5), may help to facilitate improved clinical benefit in patients undergoing stereotactic neurosurgery. In the future, 7T imaging for *in vivo* visualization and direct targeting of brain structures for DBS may eliminate the need for awake surgery enabling personalized therapy where DBS target selection is guided by high-quality, patient-specific imaging.

Microelectrode recording during surgery has been central to the origins of stereotaxy and the discovery of targets for DBS implantation, and yet there has been a clear shift with improving imaging towards making this technique obsolete. With improving imaging, the number of trajectories to be explored may be decreased, which should help mitigate any risk of complications to the patient and decrease overall operating room time. So what becomes of MER in the future? There is no doubt about the role of MER for neuroscientific study, but will it remain important in specific circumstances for clinical decision-making? These discussions are mostly beyond the limits of the presented work. However, my belief is that MER will not disappear and will continue to be an important component of functional neurosurgery. However, the importance of single neuron activity in clinical practice will shift from its use for localization to processing of these signals for decoding more complex behaviours and activities, including its use in brain-computer interfaces.

6.4 Innovations in Stereotaxy

Functional neurosurgery is an exciting subspecialty within neurosurgery with many new technological developments over the past several decades. Directional leads and the possibility of current steering allow for some tolerance to targeting error by allowing “sculpting” of the field of stimulation. MRI-guided laser ablation has become a valid treatment option for temporal lobe epilepsy [Willie et al., 2014, Gross et al., 2018]. Closed loop deep brain stimulation devices now allow for responsive treatment based on specific brain signals [Morrell, 2011, Herron et al., 2016]. Optogenetic [Gradinaru et al., 2010] and chemogenetic [Roth, 2016] modulation have come to the forefront as tools in neuroscience. Initial safety trials have at least demonstrated short-term safety of gene therapy in human subjects [LeWitt et al., 2011]. Robotic devices are enabling more and more accurate stereotactic placement [Cardinale et al., 2013]. All these developments can be aided by more accurate image-based targeting.

6.5 Conclusions

To conclude, the question of target selection not only for classic indications like Parkinson’s disease and Essential Tremor but the growing number of indications remains an unsolved problem. Determining the exact location of the most effective target that maximizes benefit while minimizing side effects or complications will be greatly assisted by having access to higher-resolution *in vivo* brain imaging, facilitated by higher field imaging. With the recent approval of specific ultra-high field scanner configurations by the FDA, more groups are investing in this technology, and accelerations in developments in this growing field are to be anticipated over the next decade. The opportunity to pool ultra-high field data across multiple centers will also enable generalizability of the findings in this thesis.

Appendices

Appendix A

Chapter 3 Supplementary Material

A.1 Phase 1: Supplementary Material

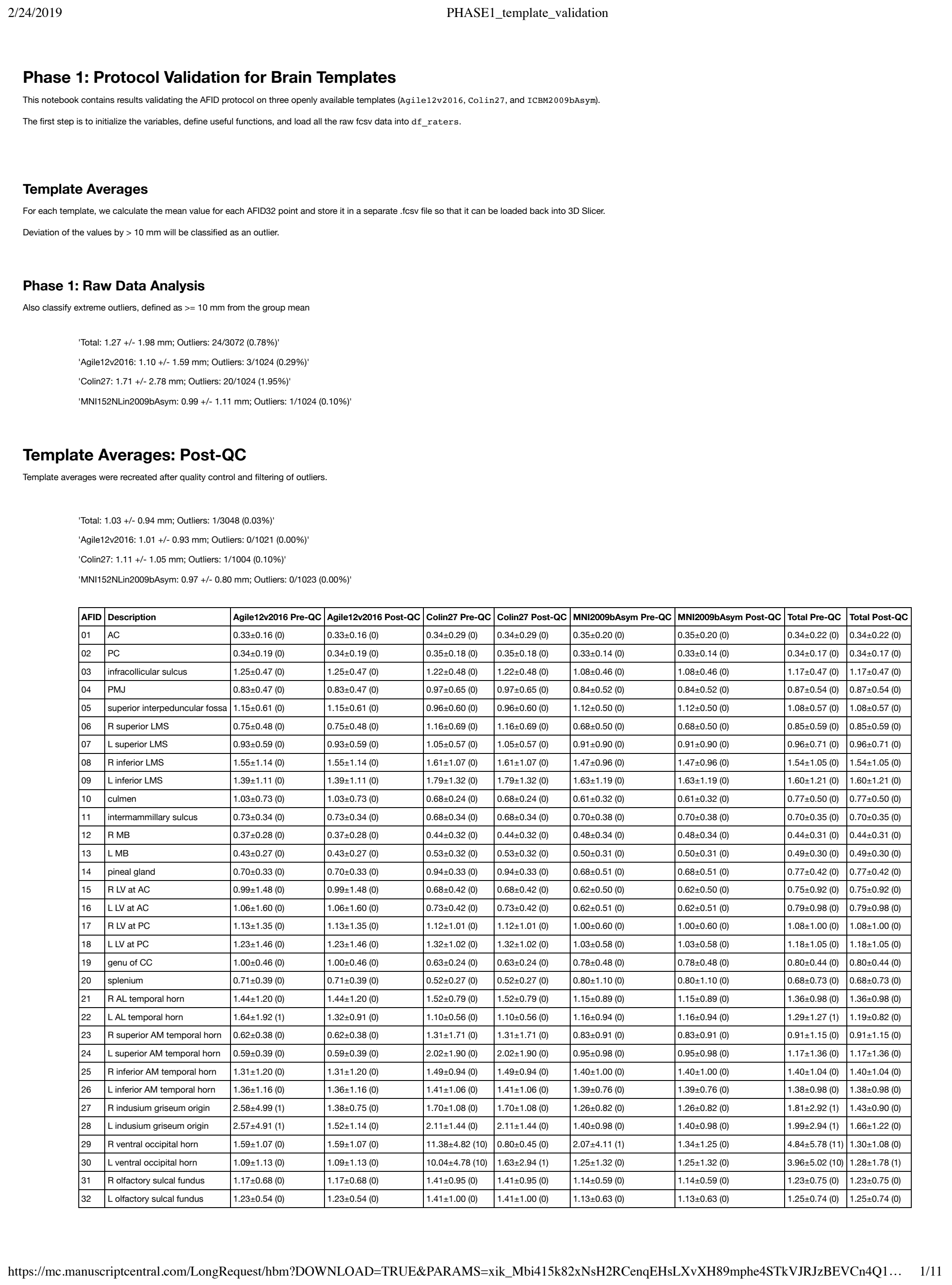

2/24/2019 PHASE1_template_validation

Phase 1: Protocol Validation for Brain Templates

This notebook contains results validating the AFID protocol on three openly available templates (`Agile12v2016`, `Colin27`, and `ICBM2009bAsym`).

The first step is to initialize the variables, define useful functions, and load all the raw fcsv data into `df_raters`.

Template Averages

For each template, we calculate the mean value for each AFID32 point and store it in a separate .fcsv file so that it can be loaded back into 3D Slicer.

Deviation of the values by > 10 mm will be classified as an outlier.

Phase 1: Raw Data Analysis

Also classify extreme outliers, defined as >= 10 mm from the group mean

```
'Total: 1.27 +/- 1.98 mm; Outliers: 24/3072 (0.78%)'

'Agile12v2016: 1.10 +/- 1.59 mm; Outliers: 3/1024 (0.29%)'

'Colin27: 1.71 +/- 2.78 mm; Outliers: 20/1024 (1.95%)'

'MNI152NLin2009bAsym: 0.99 +/- 1.11 mm; Outliers: 1/1024 (0.10%)'
```

Template Averages: Post-QC

Template averages were recreated after quality control and filtering of outliers.

```
'Total: 1.03 +/- 0.94 mm; Outliers: 1/3048 (0.03%)'

'Agile12v2016: 1.01 +/- 0.93 mm; Outliers: 0/1021 (0.00%)'

'Colin27: 1.11 +/- 1.05 mm; Outliers: 1/1004 (0.10%)'

'MNI152NLin2009bAsym: 0.97 +/- 0.80 mm; Outliers: 0/1023 (0.00%)'
```

AFID	Description	Agile12v2016 Pre-QC	Agile12v2016 Post-QC	Colin27 Pre-QC	Colin27 Post-QC	MNI2009bAsym Pre-QC	MNI2009bAsym Post-QC	Total Pre-QC	Total Post-QC
01	AC	0.33±0.16 (0)	0.33±0.16 (0)	0.34±0.29 (0)	0.34±0.29 (0)	0.35±0.20 (0)	0.35±0.20 (0)	0.34±0.22 (0)	0.34±0.22 (0)
02	PC	0.34±0.19 (0)	0.34±0.19 (0)	0.35±0.18 (0)	0.35±0.18 (0)	0.33±0.14 (0)	0.33±0.14 (0)	0.34±0.17 (0)	0.34±0.17 (0)
03	infracollicular sulcus	1.25±0.47 (0)	1.25±0.47 (0)	1.22±0.48 (0)	1.22±0.48 (0)	1.08±0.46 (0)	1.08±0.46 (0)	1.17±0.47 (0)	1.17±0.47 (0)
04	PMJ	0.83±0.47 (0)	0.83±0.47 (0)	0.97±0.65 (0)	0.97±0.65 (0)	0.84±0.52 (0)	0.84±0.52 (0)	0.87±0.54 (0)	0.87±0.54 (0)
05	superior interpeduncular fossa	1.15±0.61 (0)	1.15±0.61 (0)	0.96±0.60 (0)	0.96±0.60 (0)	1.12±0.50 (0)	1.12±0.50 (0)	1.08±0.57 (0)	1.08±0.57 (0)
06	R superior LMS	0.75±0.48 (0)	0.75±0.48 (0)	1.16±0.69 (0)	1.16±0.69 (0)	0.68±0.50 (0)	0.68±0.50 (0)	0.85±0.59 (0)	0.85±0.59 (0)
07	L superior LMS	0.93±0.59 (0)	0.93±0.59 (0)	1.05±0.57 (0)	1.05±0.57 (0)	0.91±0.90 (0)	0.91±0.90 (0)	0.96±0.71 (0)	0.96±0.71 (0)
08	R inferior LMS	1.55±1.14 (0)	1.55±1.14 (0)	1.61±1.07 (0)	1.61±1.07 (0)	1.47±0.96 (0)	1.47±0.96 (0)	1.54±1.05 (0)	1.54±1.05 (0)
09	L inferior LMS	1.39±1.11 (0)	1.39±1.11 (0)	1.79±1.32 (0)	1.79±1.32 (0)	1.63±1.19 (0)	1.63±1.19 (0)	1.60±1.21 (0)	1.60±1.21 (0)
10	culmen	1.03±0.73 (0)	1.03±0.73 (0)	0.68±0.24 (0)	0.68±0.24 (0)	0.61±0.32 (0)	0.61±0.32 (0)	0.77±0.50 (0)	0.77±0.50 (0)
11	intermammillary sulcus	0.73±0.34 (0)	0.73±0.34 (0)	0.68±0.34 (0)	0.68±0.34 (0)	0.70±0.38 (0)	0.70±0.38 (0)	0.70±0.35 (0)	0.70±0.35 (0)
12	R MB	0.37±0.28 (0)	0.37±0.28 (0)	0.44±0.32 (0)	0.44±0.32 (0)	0.48±0.34 (0)	0.48±0.34 (0)	0.44±0.31 (0)	0.44±0.31 (0)
13	L MB	0.43±0.27 (0)	0.43±0.27 (0)	0.53±0.32 (0)	0.53±0.32 (0)	0.50±0.31 (0)	0.50±0.31 (0)	0.49±0.30 (0)	0.49±0.30 (0)
14	pineal gland	0.70±0.33 (0)	0.70±0.33 (0)	0.94±0.33 (0)	0.94±0.33 (0)	0.68±0.51 (0)	0.68±0.51 (0)	0.77±0.42 (0)	0.77±0.42 (0)
15	R LV at AC	0.99±1.48 (0)	0.99±1.48 (0)	0.68±0.42 (0)	0.68±0.42 (0)	0.62±0.50 (0)	0.62±0.50 (0)	0.75±0.92 (0)	0.75±0.92 (0)
16	L LV at AC	1.06±1.60 (0)	1.06±1.60 (0)	0.73±0.42 (0)	0.73±0.42 (0)	0.62±0.51 (0)	0.62±0.51 (0)	0.79±0.98 (0)	0.79±0.98 (0)
17	R LV at PC	1.13±1.35 (0)	1.13±1.35 (0)	1.12±1.01 (0)	1.12±1.01 (0)	1.00±0.60 (0)	1.00±0.60 (0)	1.08±1.00 (0)	1.08±1.00 (0)
18	L LV at PC	1.23±1.46 (0)	1.23±1.46 (0)	1.32±1.02 (0)	1.32±1.02 (0)	1.03±0.58 (0)	1.03±0.58 (0)	1.18±1.05 (0)	1.18±1.05 (0)
19	genu of CC	1.00±0.46 (0)	1.00±0.46 (0)	0.63±0.24 (0)	0.63±0.24 (0)	0.78±0.48 (0)	0.78±0.48 (0)	0.80±0.44 (0)	0.80±0.44 (0)
20	splenium	0.71±0.39 (0)	0.71±0.39 (0)	0.52±0.27 (0)	0.52±0.27 (0)	0.80±1.10 (0)	0.80±1.10 (0)	0.68±0.73 (0)	0.68±0.73 (0)
21	R AL temporal horn	1.44±1.20 (0)	1.44±1.20 (0)	1.52±0.79 (0)	1.52±0.79 (0)	1.15±0.89 (0)	1.15±0.89 (0)	1.36±0.98 (0)	1.36±0.98 (0)
22	L AL temporal horn	1.64±1.92 (1)	1.32±0.91 (0)	1.10±0.56 (0)	1.10±0.56 (0)	1.16±0.94 (0)	1.16±0.94 (0)	1.29±1.27 (1)	1.19±0.82 (0)
23	R superior AM temporal horn	0.62±0.38 (0)	0.62±0.38 (0)	1.31±1.71 (0)	1.31±1.71 (0)	0.83±0.91 (0)	0.83±0.91 (0)	0.91±1.15 (0)	0.91±1.15 (0)
24	L superior AM temporal horn	0.59±0.39 (0)	0.59±0.39 (0)	2.02±1.90 (0)	2.02±1.90 (0)	0.95±0.98 (0)	0.95±0.98 (0)	1.17±1.36 (0)	1.17±1.36 (0)
25	R inferior AM temporal horn	1.31±1.20 (0)	1.31±1.20 (0)	1.49±0.94 (0)	1.49±0.94 (0)	1.40±1.00 (0)	1.40±1.00 (0)	1.40±1.04 (0)	1.40±1.04 (0)
26	L inferior AM temporal horn	1.36±1.16 (0)	1.36±1.16 (0)	1.41±1.06 (0)	1.41±1.06 (0)	1.39±0.76 (0)	1.39±0.76 (0)	1.38±0.98 (0)	1.38±0.98 (0)
27	R indusium griseum origin	2.58±4.99 (1)	1.38±0.75 (0)	1.70±1.08 (0)	1.70±1.08 (0)	1.26±0.82 (0)	1.26±0.82 (0)	1.81±2.92 (1)	1.43±0.90 (0)
28	L indusium griseum origin	2.57±4.91 (1)	1.52±1.14 (0)	2.11±1.44 (0)	2.11±1.44 (0)	1.40±0.98 (0)	1.40±0.98 (0)	1.99±2.94 (1)	1.66±1.22 (0)
29	R ventral occipital horn	1.59±1.07 (0)	1.59±1.07 (0)	11.38±4.82 (10)	0.80±0.45 (0)	2.07±4.11 (1)	1.34±1.25 (0)	4.84±5.78 (11)	1.30±1.08 (0)
30	L ventral occipital horn	1.09±1.13 (0)	1.09±1.13 (0)	10.04±4.78 (10)	1.63±2.94 (1)	1.25±1.32 (0)	1.25±1.32 (0)	3.96±5.02 (10)	1.28±1.78 (1)
31	R olfactory sulcal fundus	1.17±0.68 (0)	1.17±0.68 (0)	1.41±0.95 (0)	1.41±0.95 (0)	1.14±0.59 (0)	1.14±0.59 (0)	1.23±0.75 (0)	1.23±0.75 (0)
32	L olfactory sulcal fundus	1.23±0.54 (0)	1.23±0.54 (0)	1.41±1.00 (0)	1.41±1.00 (0)	1.13±0.63 (0)	1.13±0.63 (0)	1.25±0.74 (0)	1.25±0.74 (0)

https://mc.manuscriptcentral.com/LongRequest/hbm?DOWNLOAD=TRUE&PARAMS=xik_Mbi415k82xNsH2RCenqEHsLXvXH89mphe4STkVJRJzBEVCn4Q1… 1/11

Demographics of Raters

Details regarding experience, etc.

rater_id	imaging_exp	neuro_exp	slicer_exp	description
Rater01	24	24	24	undergrad_student
Rater02	0	0	0	medical_student
Rater03	8	0	8	undergrad_student
Rater04	24	6	0	grad_student
Rater05	0	24	0	grad_student
Rater06	24	12	12	grad_student
Rater07	12	48	12	grad_student
Rater08	0	0	0	undergrad_student

'Imaging Experience: 11.5 +/- 11.2 months (Range: 0.0-24.0)'

'Neuroanatomy Experience: 14.2 +/- 17.0 months (Range: 0.0-48.0)'

'3D Slicer Experience: 7.0 +/- 8.8 months (Range: 0.0-24.0)'

Secondary Analyses

We first evaluated whether there was any evidence of learning across sessions (excluding session 0 which was completed as part of a group tutorial). There were negative trends in the mean AFLE with increasing session number but these did not meet thresholds of statistical analysis. The first column is the effect, second column is the associated p-value.

(Intercept)	1.090	0.0000
session	-0.024	0.1141

Did specific raters demonstrate any learning?

Because of the trends, we explored further to determine whether any specific raters demonstrated any learning. After multiple comparisons correction, only two raters demonstrated statistically significant change with session number. Rater #4 was observed to start at a baseline increased rating error in the first session (1.64 mm) but demonstrated a decrease in AFLE with session number improving by 0.1-0.2 mm per session based on the linear model (statistically significant improvement). On the contrary, Rater #2 who started with an intercept of 0.59 mm (better than the average) showed worsening of rater error with time.

rater	(Intercept)	pval_(Intercept)	session	pval_session	pval_session_adjusted	pval_session_significant
1	0.78	0	0.02	0.5644	0.6450	FALSE
2	0.59	0	0.12	0.0001	0.0009	TRUE
3	1.30	0	-0.06	0.1624	0.2783	FALSE
4	1.64	0	-0.17	0.0002	0.0009	TRUE
5	1.05	0	0.04	0.2881	0.3841	FALSE
6	1.08	0	-0.04	0.1739	0.2783	FALSE
7	0.84	0	0.02	0.7086	0.7086	FALSE
8	1.45	0	-0.12	0.0210	0.0560	FALSE

Did AFLE improve for specific AFIDs?

We wanted to see if specific AFIDs tended to improve with more training (i.e. more sessions). This analysis did not survive multiple comparisons analysis.

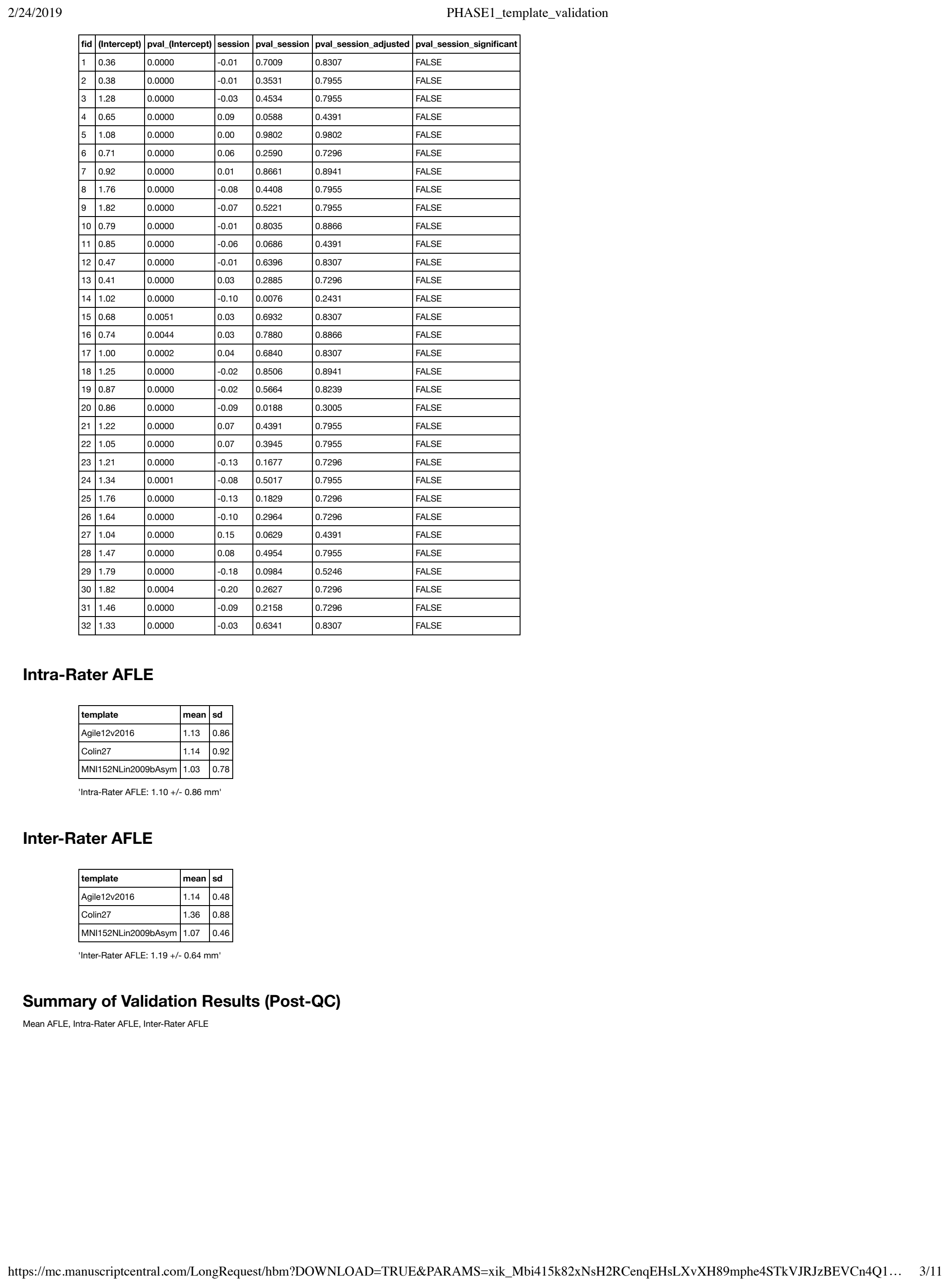

2/24/2019 PHASE1_template_validation

fid	(Intercept)	pval_(Intercept)	session	pval_session	pval_session_adjusted	pval_session_significant
1	0.36	0.0000	-0.01	0.7009	0.8307	FALSE
2	0.38	0.0000	-0.01	0.3531	0.7955	FALSE
3	1.28	0.0000	-0.03	0.4534	0.7955	FALSE
4	0.65	0.0000	0.09	0.0588	0.4391	FALSE
5	1.08	0.0000	0.00	0.9802	0.9802	FALSE
6	0.71	0.0000	0.06	0.2590	0.7296	FALSE
7	0.92	0.0000	0.01	0.8661	0.8941	FALSE
8	1.76	0.0000	-0.08	0.4408	0.7955	FALSE
9	1.82	0.0000	-0.07	0.5221	0.7955	FALSE
10	0.79	0.0000	-0.01	0.8035	0.8866	FALSE
11	0.85	0.0000	-0.06	0.0686	0.4391	FALSE
12	0.47	0.0000	-0.01	0.6396	0.8307	FALSE
13	0.41	0.0000	0.03	0.2885	0.7296	FALSE
14	1.02	0.0000	-0.10	0.0076	0.2431	FALSE
15	0.68	0.0051	0.03	0.6932	0.8307	FALSE
16	0.74	0.0044	0.03	0.7880	0.8866	FALSE
17	1.00	0.0002	0.04	0.6840	0.8307	FALSE
18	1.25	0.0000	-0.02	0.8506	0.8941	FALSE
19	0.87	0.0000	-0.02	0.5664	0.8239	FALSE
20	0.86	0.0000	-0.09	0.0188	0.3005	FALSE
21	1.22	0.0000	0.07	0.4391	0.7955	FALSE
22	1.05	0.0000	0.07	0.3945	0.7955	FALSE
23	1.21	0.0000	-0.13	0.1677	0.7296	FALSE
24	1.34	0.0001	-0.08	0.5017	0.7955	FALSE
25	1.76	0.0000	-0.13	0.1829	0.7296	FALSE
26	1.64	0.0000	-0.10	0.2964	0.7296	FALSE
27	1.04	0.0000	0.15	0.0629	0.4391	FALSE
28	1.47	0.0000	0.08	0.4954	0.7955	FALSE
29	1.79	0.0000	-0.18	0.0984	0.5246	FALSE
30	1.82	0.0004	-0.20	0.2627	0.7296	FALSE
31	1.46	0.0000	-0.09	0.2158	0.7296	FALSE
32	1.33	0.0000	-0.03	0.6341	0.8307	FALSE

Intra-Rater AFLE

template	mean	sd
Agile12v2016	1.13	0.86
Colin27	1.14	0.92
MNI152NLin2009bAsym	1.03	0.78

'Intra-Rater AFLE: 1.10 +/- 0.86 mm'

Inter-Rater AFLE

template	mean	sd
Agile12v2016	1.14	0.48
Colin27	1.36	0.88
MNI152NLin2009bAsym	1.07	0.46

'Inter-Rater AFLE: 1.19 +/- 0.64 mm'

Summary of Validation Results (Post-QC)

Mean AFLE, Intra-Rater AFLE, Inter-Rater AFLE

https://mc.manuscriptcentral.com/LongRequest/hbm?DOWNLOAD=TRUE&PARAMS=xik_Mbi415k82xNsH2RCenqEHsLXvXH89mphe4STkVJRJzBEVCn4Q1… 3/11

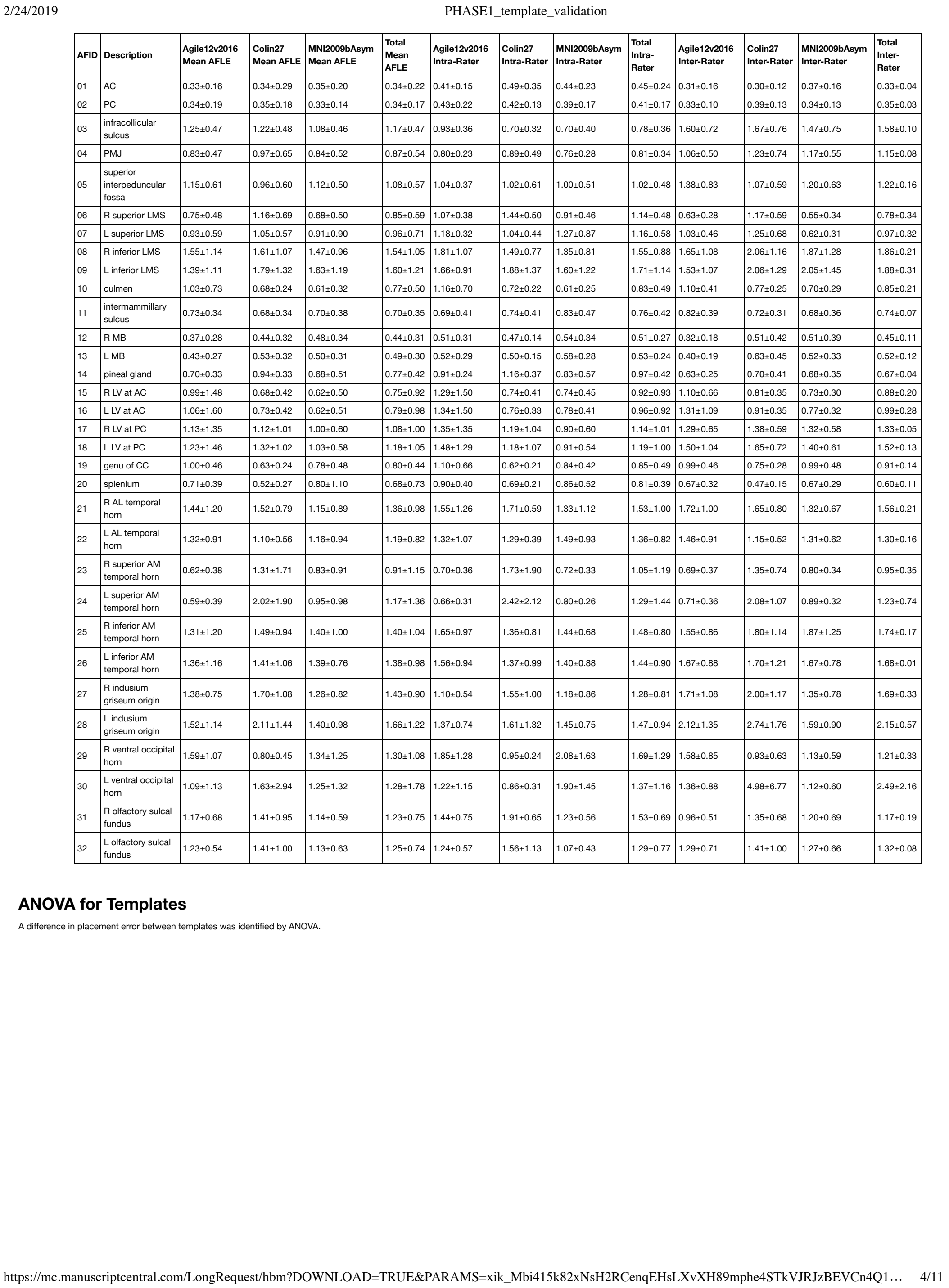

2/24/2019 PHASE1_template_validation

AFID	Description	Agile12v2016 Mean AFLE	Colin27 Mean AFLE	MNI2009bAsym Mean AFLE	Total Mean AFLE	Agile12v2016 Intra-Rater	Colin27 Intra-Rater	MNI2009bAsym Intra-Rater	Total Intra-Rater	Agile12v2016 Inter-Rater	Colin27 Inter-Rater	MNI2009bAsym Inter-Rater	Total Inter-Rater
01	AC	0.33±0.16	0.34±0.29	0.35±0.20	0.34±0.22	0.41±0.15	0.49±0.35	0.44±0.23	0.45±0.24	0.31±0.16	0.30±0.12	0.37±0.16	0.33±0.04
02	PC	0.34±0.19	0.35±0.18	0.33±0.14	0.34±0.17	0.43±0.22	0.42±0.13	0.39±0.17	0.41±0.17	0.33±0.10	0.39±0.13	0.34±0.13	0.35±0.03
03	infracollicular sulcus	1.25±0.47	1.22±0.48	1.08±0.46	1.17±0.47	0.93±0.36	0.70±0.32	0.70±0.40	0.78±0.36	1.60±0.72	1.67±0.76	1.47±0.75	1.58±0.10
04	PMJ	0.83±0.47	0.97±0.65	0.84±0.52	0.87±0.54	0.80±0.23	0.89±0.49	0.76±0.28	0.81±0.34	1.06±0.50	1.23±0.74	1.17±0.55	1.15±0.08
05	superior interpeduncular fossa	1.15±0.61	0.96±0.60	1.12±0.50	1.08±0.57	1.04±0.37	1.02±0.61	1.00±0.51	1.02±0.48	1.38±0.83	1.07±0.59	1.20±0.63	1.22±0.16
06	R superior LMS	0.75±0.48	1.16±0.69	0.68±0.50	0.85±0.59	1.07±0.38	1.44±0.50	0.91±0.46	1.14±0.48	0.63±0.28	1.17±0.59	0.55±0.34	0.78±0.34
07	L superior LMS	0.93±0.59	1.05±0.57	0.91±0.90	0.96±0.71	1.18±0.32	1.04±0.44	1.27±0.87	1.16±0.58	1.03±0.46	1.25±0.68	0.62±0.31	0.97±0.32
08	R inferior LMS	1.55±1.14	1.61±1.07	1.47±0.96	1.54±1.05	1.81±1.07	1.49±0.77	1.35±0.81	1.55±0.88	1.65±1.08	2.06±1.16	1.87±1.28	1.86±0.21
09	L inferior LMS	1.39±1.11	1.79±1.32	1.63±1.19	1.60±1.21	1.66±0.91	1.88±1.37	1.60±1.22	1.71±1.14	1.53±1.07	2.06±1.29	2.05±1.45	1.88±0.31
10	culmen	1.03±0.73	0.68±0.24	0.61±0.32	0.77±0.50	1.16±0.70	0.72±0.22	0.61±0.25	0.83±0.49	1.10±0.41	0.77±0.25	0.70±0.29	0.85±0.21
11	intermammillary sulcus	0.73±0.34	0.68±0.34	0.70±0.38	0.70±0.35	0.69±0.41	0.74±0.41	0.83±0.47	0.76±0.42	0.82±0.39	0.72±0.31	0.68±0.36	0.74±0.07
12	R MB	0.37±0.28	0.44±0.32	0.48±0.34	0.44±0.31	0.51±0.31	0.47±0.14	0.54±0.34	0.51±0.27	0.32±0.18	0.51±0.42	0.51±0.39	0.45±0.11
13	L MB	0.43±0.27	0.53±0.32	0.50±0.31	0.49±0.30	0.52±0.29	0.50±0.15	0.58±0.28	0.53±0.24	0.40±0.19	0.63±0.45	0.52±0.33	0.52±0.12
14	pineal gland	0.70±0.33	0.94±0.33	0.68±0.51	0.77±0.42	0.91±0.24	1.16±0.37	0.83±0.57	0.97±0.42	0.63±0.25	0.70±0.41	0.68±0.35	0.67±0.04
15	R LV at AC	0.99±1.48	0.68±0.42	0.62±0.50	0.75±0.92	1.29±1.50	0.74±0.41	0.74±0.45	0.92±0.93	1.10±0.66	0.81±0.35	0.73±0.30	0.88±0.20
16	L LV at AC	1.06±1.60	0.73±0.42	0.62±0.51	0.79±0.98	1.34±1.50	0.76±0.33	0.78±0.41	0.96±0.92	1.31±1.09	0.91±0.35	0.77±0.32	0.99±0.28
17	R LV at PC	1.13±1.35	1.12±1.01	1.00±0.60	1.08±1.00	1.35±1.35	1.19±1.04	0.90±0.60	1.14±1.01	1.29±0.65	1.38±0.59	1.32±0.58	1.33±0.05
18	L LV at PC	1.23±1.46	1.32±1.02	1.03±0.58	1.18±1.05	1.48±1.29	1.18±1.07	0.91±0.54	1.19±1.00	1.50±1.04	1.65±0.72	1.40±0.61	1.52±0.13
19	genu of CC	1.00±0.46	0.63±0.24	0.78±0.48	0.80±0.44	1.10±0.66	0.62±0.21	0.84±0.42	0.85±0.49	0.99±0.46	0.75±0.28	0.99±0.48	0.91±0.14
20	splenium	0.71±0.39	0.52±0.27	0.80±1.10	0.68±0.73	0.90±0.40	0.69±0.21	0.86±0.52	0.81±0.39	0.67±0.32	0.47±0.15	0.67±0.29	0.60±0.11
21	R AL temporal horn	1.44±1.20	1.52±0.79	1.15±0.89	1.36±0.98	1.55±1.26	1.71±0.59	1.33±1.12	1.53±1.00	1.72±1.00	1.65±0.80	1.32±0.67	1.56±0.21
22	L AL temporal horn	1.32±0.91	1.10±0.56	1.16±0.94	1.19±0.82	1.32±1.07	1.29±0.39	1.49±0.93	1.36±0.82	1.46±0.91	1.15±0.52	1.31±0.62	1.30±0.16
23	R superior AM temporal horn	0.62±0.38	1.31±1.71	0.83±0.91	0.91±1.15	0.70±0.36	1.73±1.90	0.72±0.33	1.05±1.19	0.69±0.37	1.35±0.74	0.80±0.34	0.95±0.35
24	L superior AM temporal horn	0.59±0.39	2.02±1.90	0.95±0.98	1.17±1.36	0.66±0.31	2.42±2.12	0.80±0.26	1.29±1.44	0.71±0.36	2.08±1.07	0.89±0.32	1.23±0.74
25	R inferior AM temporal horn	1.31±1.20	1.49±0.94	1.40±1.00	1.40±1.04	1.65±0.97	1.36±0.81	1.44±0.68	1.48±0.80	1.55±0.86	1.80±1.14	1.87±1.25	1.74±0.17
26	L inferior AM temporal horn	1.36±1.16	1.41±1.06	1.39±0.76	1.38±0.98	1.56±0.94	1.37±0.99	1.40±0.88	1.44±0.90	1.67±0.88	1.70±1.21	1.67±0.78	1.68±0.01
27	R indusium griseum origin	1.38±0.75	1.70±1.08	1.26±0.82	1.43±0.90	1.10±0.54	1.55±1.00	1.18±0.86	1.28±0.81	1.71±1.08	2.00±1.17	1.35±0.78	1.69±0.33
28	L indusium griseum origin	1.52±1.14	2.11±1.44	1.40±0.98	1.66±1.22	1.37±0.74	1.61±1.32	1.45±0.75	1.47±0.94	2.12±1.35	2.74±1.76	1.59±0.90	2.15±0.57
29	R ventral occipital horn	1.59±1.07	0.80±0.45	1.34±1.25	1.30±1.08	1.85±1.28	0.95±0.24	2.08±1.63	1.69±1.29	1.58±0.85	0.93±0.63	1.13±0.59	1.21±0.33
30	L ventral occipital horn	1.09±1.13	1.63±2.94	1.25±1.32	1.28±1.78	1.22±1.15	0.86±0.31	1.90±1.45	1.37±1.16	1.36±0.88	4.98±6.77	1.12±0.60	2.49±2.16
31	R olfactory sulcal fundus	1.17±0.68	1.41±0.95	1.14±0.59	1.23±0.75	1.44±0.75	1.91±0.65	1.23±0.56	1.53±0.69	0.96±0.51	1.35±0.68	1.20±0.69	1.17±0.19
32	L olfactory sulcal fundus	1.23±0.54	1.41±1.00	1.13±0.63	1.25±0.74	1.24±0.57	1.56±1.13	1.07±0.43	1.29±0.77	1.29±0.71	1.41±1.00	1.27±0.66	1.32±0.08

ANOVA for Templates

A difference in placement error between templates was identified by ANOVA.

https://mc.manuscriptcentral.com/LongRequest/hbm?DOWNLOAD=TRUE&PARAMS=xik_Mbi415k82xNsH2RCenqEHsLXvXH89mphe4STkVJRJzBEVCn4Q1… 4/11

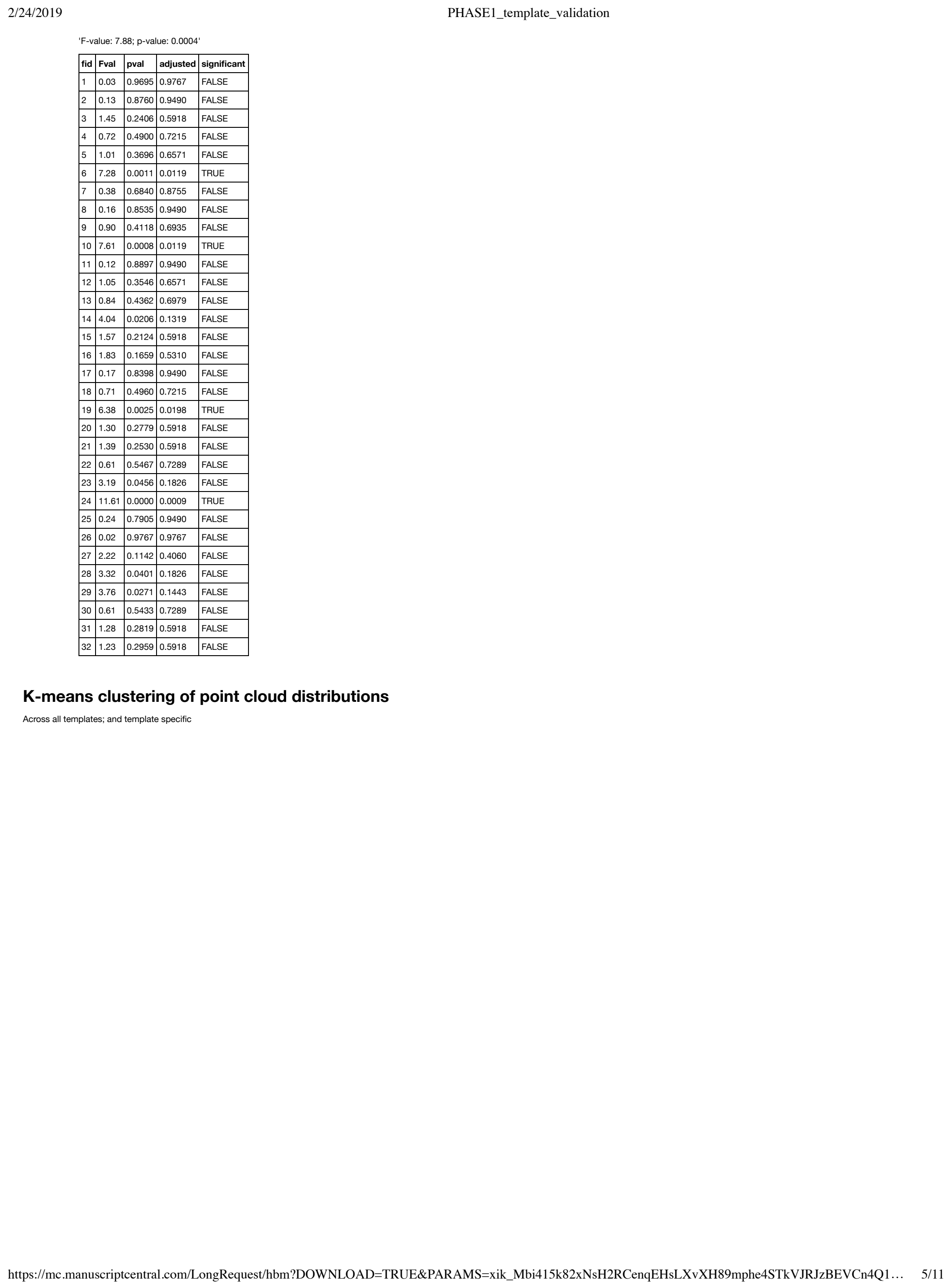

'F-value: 7.88; p-value: 0.0004'

fid	Fval	pval	adjusted	significant
1	0.03	0.9695	0.9767	FALSE
2	0.13	0.8760	0.9490	FALSE
3	1.45	0.2406	0.5918	FALSE
4	0.72	0.4900	0.7215	FALSE
5	1.01	0.3696	0.6571	FALSE
6	7.28	0.0011	0.0119	TRUE
7	0.38	0.6840	0.8755	FALSE
8	0.16	0.8535	0.9490	FALSE
9	0.90	0.4118	0.6935	FALSE
10	7.61	0.0008	0.0119	TRUE
11	0.12	0.8897	0.9490	FALSE
12	1.05	0.3546	0.6571	FALSE
13	0.84	0.4362	0.6979	FALSE
14	4.04	0.0206	0.1319	FALSE
15	1.57	0.2124	0.5918	FALSE
16	1.83	0.1659	0.5310	FALSE
17	0.17	0.8398	0.9490	FALSE
18	0.71	0.4960	0.7215	FALSE
19	6.38	0.0025	0.0198	TRUE
20	1.30	0.2779	0.5918	FALSE
21	1.39	0.2530	0.5918	FALSE
22	0.61	0.5467	0.7289	FALSE
23	3.19	0.0456	0.1826	FALSE
24	11.61	0.0000	0.0009	TRUE
25	0.24	0.7905	0.9490	FALSE
26	0.02	0.9767	0.9767	FALSE
27	2.22	0.1142	0.4060	FALSE
28	3.32	0.0401	0.1826	FALSE
29	3.76	0.0271	0.1443	FALSE
30	0.61	0.5433	0.7289	FALSE
31	1.28	0.2819	0.5918	FALSE
32	1.23	0.2959	0.5918	FALSE

K-means clustering of point cloud distributions

Across all templates; and template specific

2/24/2019 PHASE1_template_validation

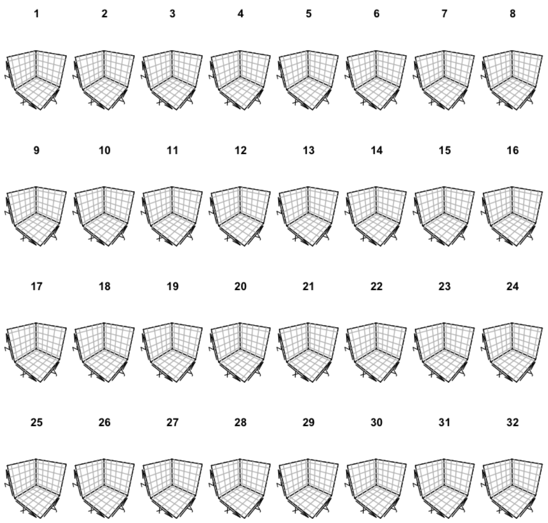

Agile12v2016 only

https://mc.manuscriptcentral.com/LongRequest/hbm?DOWNLOAD=TRUE&PARAMS=xik_Mbi415k82xNsH2RCenqEHsLXvXH89mphe4STkVJRJzBEVCn4Q1… 6/11

2/24/2019 PHASE1_template_validation

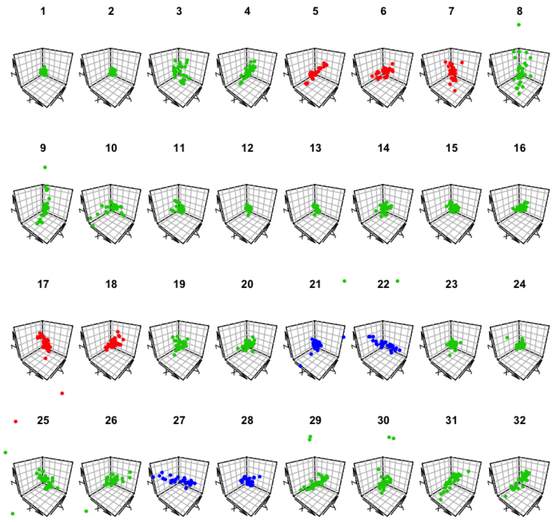

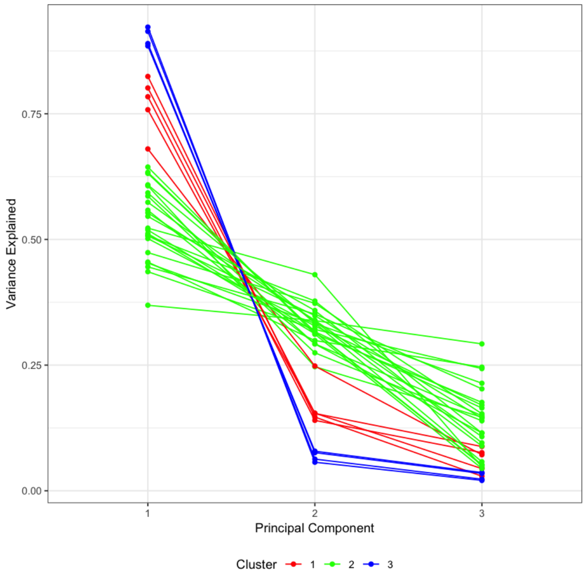

Colin27 only

https://mc.manuscriptcentral.com/LongRequest/hbm?DOWNLOAD=TRUE&PARAMS=xik_Mbi415k82xNsH2RCenqEHsLXvXH89mphe4STkVJRJzBEVCn4Q1… 7/11

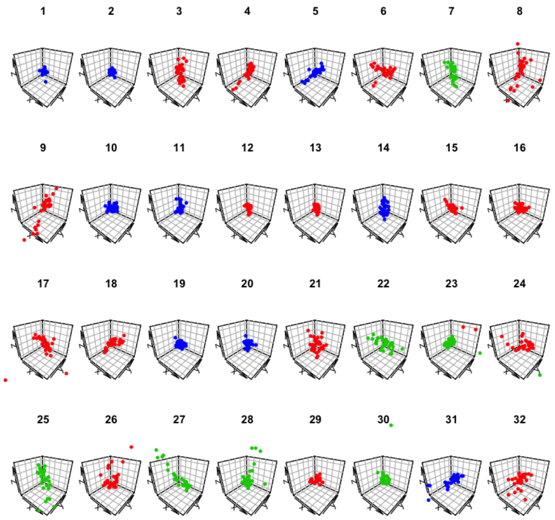

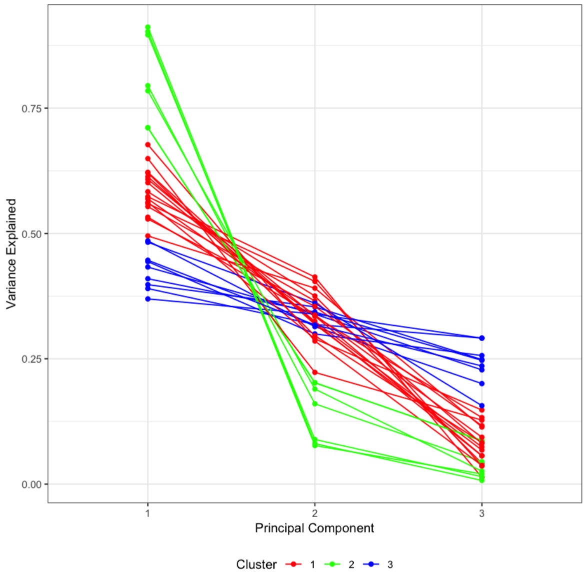

MNI152NLin2009bAsym Only

2/24/2019 PHASE1_template_validation

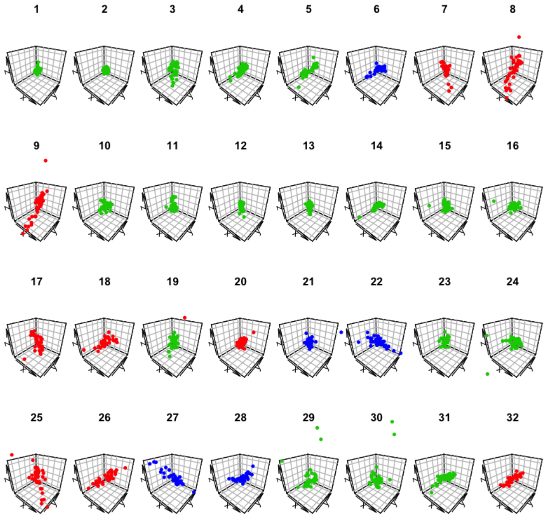

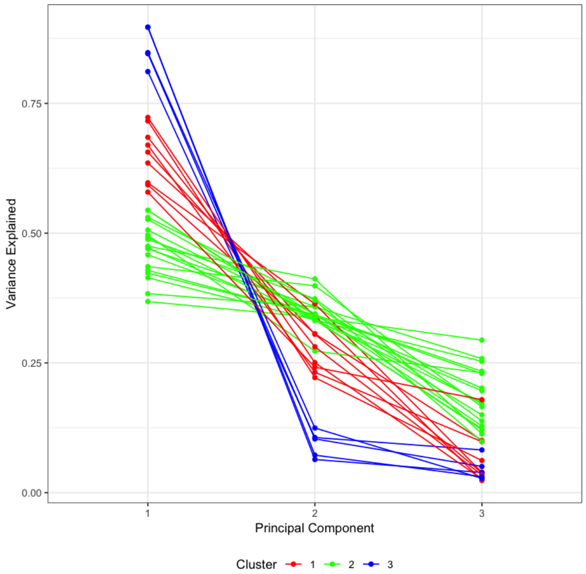

All templates combined

https://mc.manuscriptcentral.com/LongRequest/hbm?DOWNLOAD=TRUE&PARAMS=xik_Mbi415k82xNsH2RCenqEHsLXvXH89mphe4STkVJRJzBEVCn4Q1… 9/11

2/24/2019 PHASE1_template_validation

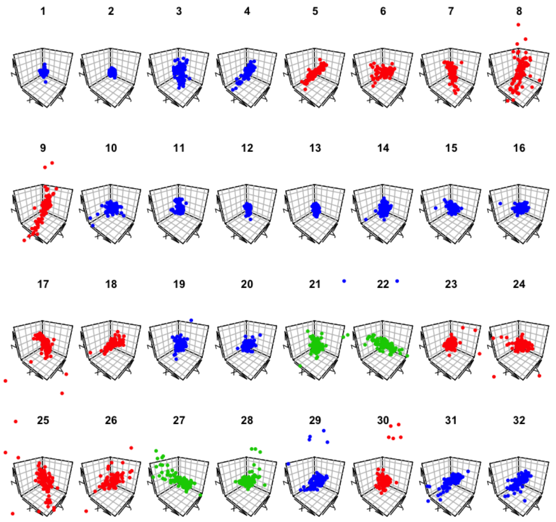

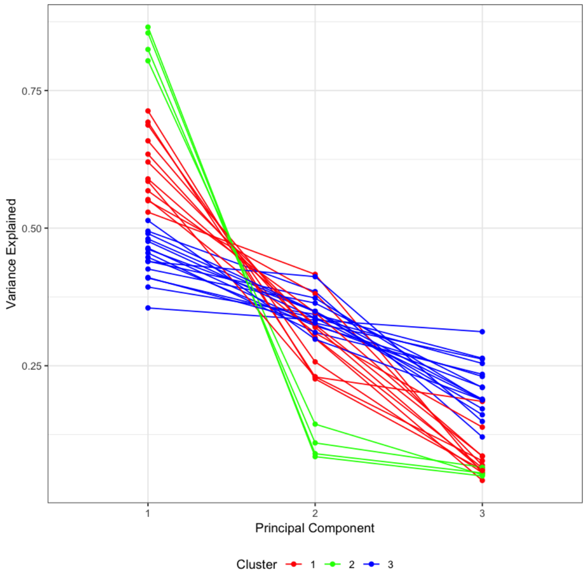

https://mc.manuscriptcentral.com/LongRequest/hbm?DOWNLOAD=TRUE&PARAMS=xik_Mbi415k82xNsH2RCenqEHsLXvXH89mphe4STkVJRJzBEVCn4Q… 10/11

2/24/2019 PHASE1_template_validation

```
R version 3.5.1 (2018-07-02)
Platform: x86_64-apple-darwin14.5.0 (64-bit)
Running under: macOS High Sierra 10.13.2

Matrix products: default
BLAS: /System/Library/Frameworks/Accelerate.framework/Versions/A/Frameworks/vecLib.framework/Versions/A/libBLAS.dylib
LAPACK: /System/Library/Frameworks/Accelerate.framework/Versions/A/Frameworks/vecLib.framework/Versions/A/libLAPACK.dylib

locale:
[1] en_CA.UTF-8/en_CA.UTF-8/en_CA.UTF-8/C/en_CA.UTF-8/en_CA.UTF-8

attached base packages:
[1] stats     graphics  grDevices utils     datasets  methods   base

other attached packages:
[1] plot3D_1.1.1   ggplot2_3.0.0  reshape2_1.4.3 digest_0.6.16  plyr_1.8.4

loaded via a namespace (and not attached):
 [1] Rcpp_0.12.17     compiler_3.5.1   pillar_1.3.0     bindr_0.1.1
 [5] base64enc_0.1-3  tools_3.5.1      uuid_0.1-2       jsonlite_1.5
 [9] evaluate_0.11    tibble_1.4.2     gtable_0.2.0     pkgconfig_2.0.2
[13] rlang_0.2.1      IRdisplay_0.5.0  IRkernel_0.8.12  bindrcpp_0.2.2
[17] repr_0.15.0      withr_2.1.2      stringr_1.3.1    dplyr_0.7.6
[21] grid_3.5.1       tidyselect_0.2.4 glue_1.3.0       R6_2.2.2
[25] pbdZMQ_0.3-3     purrr_0.2.5      magrittr_1.5     scales_1.0.0
[29] htmltools_0.3.6  misc3d_0.8-4     assertthat_0.2.0 colorspace_1.3-2
[33] labeling_0.3     stringi_1.2.4    lazyeval_0.2.1   munsell_0.5.0
[37] crayon_1.3.4
```

https://mc.manuscriptcentral.com/LongRequest/hbm?DOWNLOAD=TRUE&PARAMS=xik_Mbi415k82xNsH2RCenqEHsLXvXH89mphe4STkVJRJzBEVCn4Q… 11/11

A.2 Phase 2: Supplementary Material

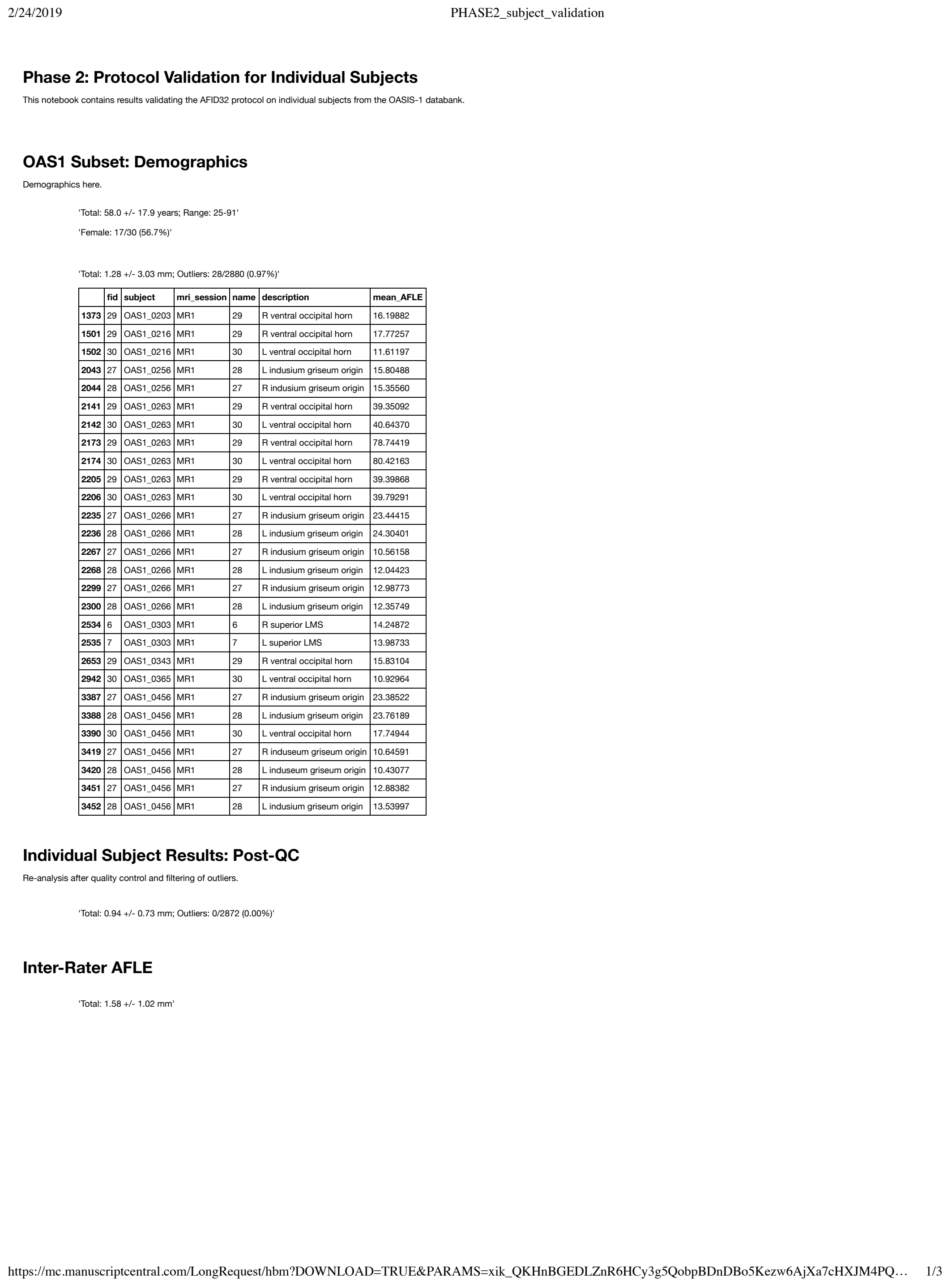

2/24/2019 PHASE2_subject_validation

Phase 2: Protocol Validation for Individual Subjects

This notebook contains results validating the AFID32 protocol on individual subjects from the OASIS-1 databank.

OAS1 Subset: Demographics

Demographics here.

'Total: 58.0 +/- 17.9 years; Range: 25-91'

'Female: 17/30 (56.7%)'

'Total: 1.28 +/- 3.03 mm; Outliers: 28/2880 (0.97%)'

	fid	subject	mri_session	name	description	mean_AFLE
1373	29	OAS1_0203	MR1	29	R ventral occipital horn	16.19882
1501	29	OAS1_0216	MR1	29	R ventral occipital horn	17.77257
1502	30	OAS1_0216	MR1	30	L ventral occipital horn	11.61197
2043	27	OAS1_0256	MR1	28	L indusium griseum origin	15.80488
2044	28	OAS1_0256	MR1	27	R indusium griseum origin	15.35560
2141	29	OAS1_0263	MR1	29	R ventral occipital horn	39.35092
2142	30	OAS1_0263	MR1	30	L ventral occipital horn	40.64370
2173	29	OAS1_0263	MR1	29	R ventral occipital horn	78.74419
2174	30	OAS1_0263	MR1	30	L ventral occipital horn	80.42163
2205	29	OAS1_0263	MR1	29	R ventral occipital horn	39.39868
2206	30	OAS1_0263	MR1	30	L ventral occipital horn	39.79291
2235	27	OAS1_0266	MR1	27	R indusium griseum origin	23.44415
2236	28	OAS1_0266	MR1	28	L indusium griseum origin	24.30401
2267	27	OAS1_0266	MR1	27	R indusium griseum origin	10.56158
2268	28	OAS1_0266	MR1	28	L indusium griseum origin	12.04423
2299	27	OAS1_0266	MR1	27	R indusium griseum origin	12.98773
2300	28	OAS1_0266	MR1	28	L indusium griseum origin	12.35749
2534	6	OAS1_0303	MR1	6	R superior LMS	14.24872
2535	7	OAS1_0303	MR1	7	L superior LMS	13.98733
2653	29	OAS1_0343	MR1	29	R ventral occipital horn	15.83104
2942	30	OAS1_0365	MR1	30	L ventral occipital horn	10.92964
3387	27	OAS1_0456	MR1	27	R indusium griseum origin	23.38522
3388	28	OAS1_0456	MR1	28	L indusium griseum origin	23.76189
3390	30	OAS1_0456	MR1	30	L ventral occipital horn	17.74944
3419	27	OAS1_0456	MR1	27	R induseum griseum origin	10.64591
3420	28	OAS1_0456	MR1	28	L induseum griseum origin	10.43077
3451	27	OAS1_0456	MR1	27	R indusium griseum origin	12.88382
3452	28	OAS1_0456	MR1	28	L indusium griseum origin	13.53997

Individual Subject Results: Post-QC

Re-analysis after quality control and filtering of outliers.

'Total: 0.94 +/- 0.73 mm; Outliers: 0/2872 (0.00%)'

Inter-Rater AFLE

'Total: 1.58 +/- 1.02 mm'

https://mc.manuscriptcentral.com/LongRequest/hbm?DOWNLOAD=TRUE&PARAMS=xik_QKHnBGEDLZnR6HCy3g5QobpBDnDBo5Kezw6AjXa7cHXJM4PQ… 1/3

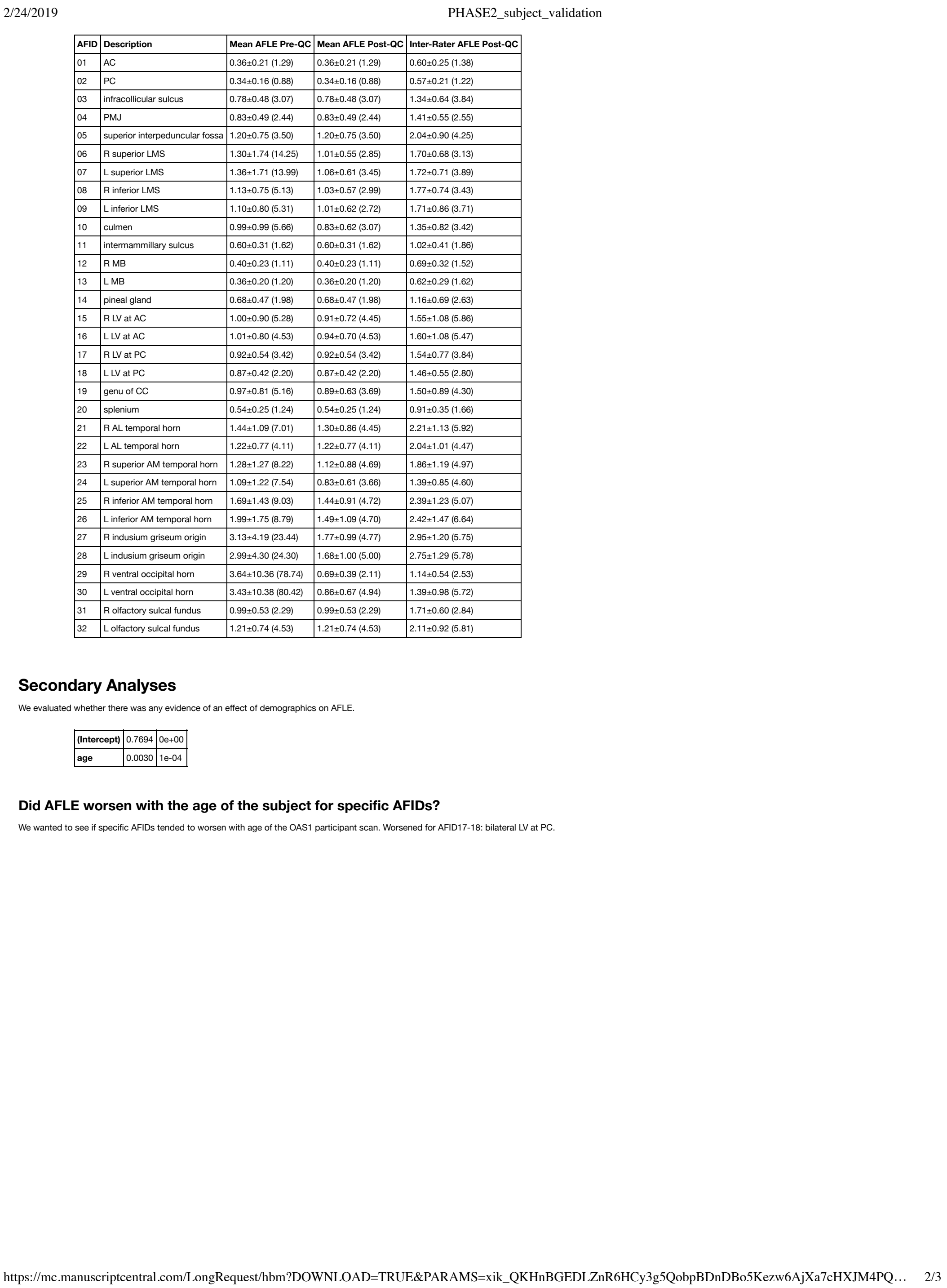

AFID	Description	Mean AFLE Pre-QC	Mean AFLE Post-QC	Inter-Rater AFLE Post-QC
01	AC	0.36±0.21 (1.29)	0.36±0.21 (1.29)	0.60±0.25 (1.38)
02	PC	0.34±0.16 (0.88)	0.34±0.16 (0.88)	0.57±0.21 (1.22)
03	infracollicular sulcus	0.78±0.48 (3.07)	0.78±0.48 (3.07)	1.34±0.64 (3.84)
04	PMJ	0.83±0.49 (2.44)	0.83±0.49 (2.44)	1.41±0.55 (2.55)
05	superior interpeduncular fossa	1.20±0.75 (3.50)	1.20±0.75 (3.50)	2.04±0.90 (4.25)
06	R superior LMS	1.30±1.74 (14.25)	1.01±0.55 (2.85)	1.70±0.68 (3.13)
07	L superior LMS	1.36±1.71 (13.99)	1.06±0.61 (3.45)	1.72±0.71 (3.89)
08	R inferior LMS	1.13±0.75 (5.13)	1.03±0.57 (2.99)	1.77±0.74 (3.43)
09	L inferior LMS	1.10±0.80 (5.31)	1.01±0.62 (2.72)	1.71±0.86 (3.71)
10	culmen	0.99±0.99 (5.66)	0.83±0.62 (3.07)	1.35±0.82 (3.42)
11	intermammillary sulcus	0.60±0.31 (1.62)	0.60±0.31 (1.62)	1.02±0.41 (1.86)
12	R MB	0.40±0.23 (1.11)	0.40±0.23 (1.11)	0.69±0.32 (1.52)
13	L MB	0.36±0.20 (1.20)	0.36±0.20 (1.20)	0.62±0.29 (1.62)
14	pineal gland	0.68±0.47 (1.98)	0.68±0.47 (1.98)	1.16±0.69 (2.63)
15	R LV at AC	1.00±0.90 (5.28)	0.91±0.72 (4.45)	1.55±1.08 (5.86)
16	L LV at AC	1.01±0.80 (4.53)	0.94±0.70 (4.53)	1.60±1.08 (5.47)
17	R LV at PC	0.92±0.54 (3.42)	0.92±0.54 (3.42)	1.54±0.77 (3.84)
18	L LV at PC	0.87±0.42 (2.20)	0.87±0.42 (2.20)	1.46±0.55 (2.80)
19	genu of CC	0.97±0.81 (5.16)	0.89±0.63 (3.69)	1.50±0.89 (4.30)
20	splenium	0.54±0.25 (1.24)	0.54±0.25 (1.24)	0.91±0.35 (1.66)
21	R AL temporal horn	1.44±1.09 (7.01)	1.30±0.86 (4.45)	2.21±1.13 (5.92)
22	L AL temporal horn	1.22±0.77 (4.11)	1.22±0.77 (4.11)	2.04±1.01 (4.47)
23	R superior AM temporal horn	1.28±1.27 (8.22)	1.12±0.88 (4.69)	1.86±1.19 (4.97)
24	L superior AM temporal horn	1.09±1.22 (7.54)	0.83±0.61 (3.66)	1.39±0.85 (4.60)
25	R inferior AM temporal horn	1.69±1.43 (9.03)	1.44±0.91 (4.72)	2.39±1.23 (5.07)
26	L inferior AM temporal horn	1.99±1.75 (8.79)	1.49±1.09 (4.70)	2.42±1.47 (6.64)
27	R indusium griseum origin	3.13±4.19 (23.44)	1.77±0.99 (4.77)	2.95±1.20 (5.75)
28	L indusium griseum origin	2.99±4.30 (24.30)	1.68±1.00 (5.00)	2.75±1.29 (5.78)
29	R ventral occipital horn	3.64±10.36 (78.74)	0.69±0.39 (2.11)	1.14±0.54 (2.53)
30	L ventral occipital horn	3.43±10.38 (80.42)	0.86±0.67 (4.94)	1.39±0.98 (5.72)
31	R olfactory sulcal fundus	0.99±0.53 (2.29)	0.99±0.53 (2.29)	1.71±0.60 (2.84)
32	L olfactory sulcal fundus	1.21±0.74 (4.53)	1.21±0.74 (4.53)	2.11±0.92 (5.81)

Secondary Analyses

We evaluated whether there was any evidence of an effect of demographics on AFLE.

(Intercept)	0.7694	0e+00
age	0.0030	1e-04

Did AFLE worsen with the age of the subject for specific AFIDs?

We wanted to see if specific AFIDs tended to worsen with age of the OAS1 participant scan. Worsened for AFID17-18: bilateral LV at PC.

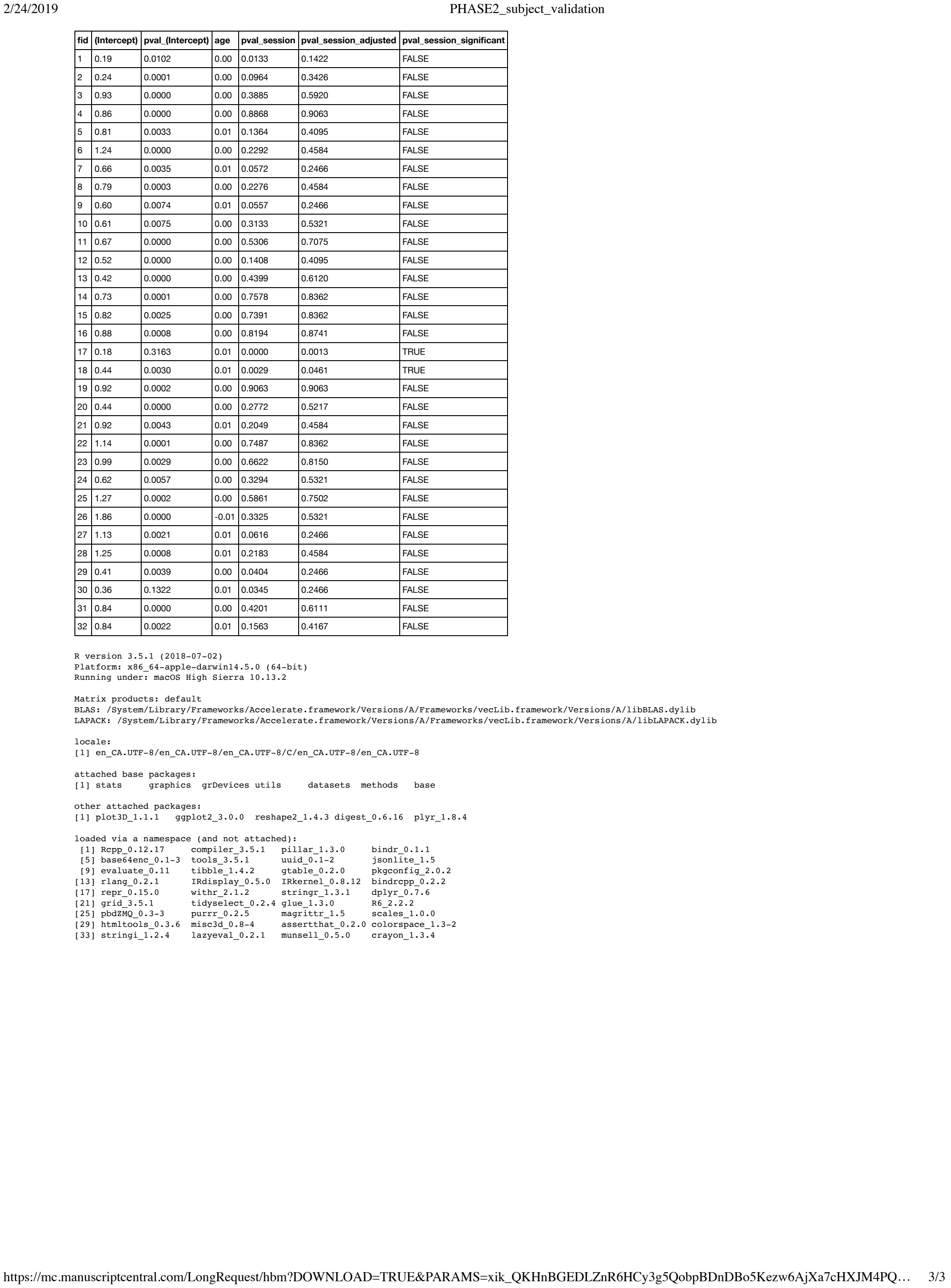

2/24/2019 PHASE2_subject_validation

fid	(Intercept)	pval_(Intercept)	age	pval_session	pval_session_adjusted	pval_session_significant
1	0.19	0.0102	0.00	0.0133	0.1422	FALSE
2	0.24	0.0001	0.00	0.0964	0.3426	FALSE
3	0.93	0.0000	0.00	0.3885	0.5920	FALSE
4	0.86	0.0000	0.00	0.8868	0.9063	FALSE
5	0.81	0.0033	0.01	0.1364	0.4095	FALSE
6	1.24	0.0000	0.00	0.2292	0.4584	FALSE
7	0.66	0.0035	0.01	0.0572	0.2466	FALSE
8	0.79	0.0003	0.00	0.2276	0.4584	FALSE
9	0.60	0.0074	0.01	0.0557	0.2466	FALSE
10	0.61	0.0075	0.00	0.3133	0.5321	FALSE
11	0.67	0.0000	0.00	0.5306	0.7075	FALSE
12	0.52	0.0000	0.00	0.1408	0.4095	FALSE
13	0.42	0.0000	0.00	0.4399	0.6120	FALSE
14	0.73	0.0001	0.00	0.7578	0.8362	FALSE
15	0.82	0.0025	0.00	0.7391	0.8362	FALSE
16	0.88	0.0008	0.00	0.8194	0.8741	FALSE
17	0.18	0.3163	0.01	0.0000	0.0013	TRUE
18	0.44	0.0030	0.01	0.0029	0.0461	TRUE
19	0.92	0.0002	0.00	0.9063	0.9063	FALSE
20	0.44	0.0000	0.00	0.2772	0.5217	FALSE
21	0.92	0.0043	0.01	0.2049	0.4584	FALSE
22	1.14	0.0001	0.00	0.7487	0.8362	FALSE
23	0.99	0.0029	0.00	0.6622	0.8150	FALSE
24	0.62	0.0057	0.00	0.3294	0.5321	FALSE
25	1.27	0.0002	0.00	0.5861	0.7502	FALSE
26	1.86	0.0000	-0.01	0.3325	0.5321	FALSE
27	1.13	0.0021	0.01	0.0616	0.2466	FALSE
28	1.25	0.0008	0.01	0.2183	0.4584	FALSE
29	0.41	0.0039	0.00	0.0404	0.2466	FALSE
30	0.36	0.1322	0.01	0.0345	0.2466	FALSE
31	0.84	0.0000	0.00	0.4201	0.6111	FALSE
32	0.84	0.0022	0.01	0.1563	0.4167	FALSE

```
R version 3.5.1 (2018-07-02)
Platform: x86_64-apple-darwin14.5.0 (64-bit)
Running under: macOS High Sierra 10.13.2

Matrix products: default
BLAS: /System/Library/Frameworks/Accelerate.framework/Versions/A/Frameworks/vecLib.framework/Versions/A/libBLAS.dylib
LAPACK: /System/Library/Frameworks/Accelerate.framework/Versions/A/Frameworks/vecLib.framework/Versions/A/libLAPACK.dylib

locale:
[1] en_CA.UTF-8/en_CA.UTF-8/en_CA.UTF-8/C/en_CA.UTF-8/en_CA.UTF-8

attached base packages:
[1] stats     graphics  grDevices utils     datasets  methods   base

other attached packages:
[1] plot3D_1.1.1   ggplot2_3.0.0  reshape2_1.4.3 digest_0.6.16  plyr_1.8.4

loaded via a namespace (and not attached):
 [1] Rcpp_0.12.17     compiler_3.5.1   pillar_1.3.0     bindr_0.1.1
 [5] base64enc_0.1-3  tools_3.5.1      uuid_0.1-2       jsonlite_1.5
 [9] evaluate_0.11    tibble_1.4.2     gtable_0.2.0     pkgconfig_2.0.2
[13] rlang_0.2.1      IRdisplay_0.5.0  IRkernel_0.8.12  bindrcpp_0.2.2
[17] repr_0.15.0      withr_2.1.2      stringr_1.3.1    dplyr_0.7.6
[21] grid_3.5.1       tidyselect_0.2.4 glue_1.3.0       R6_2.2.2
[25] pbdZMQ_0.3-3     purrr_0.2.5      magrittr_1.5     scales_1.0.0
[29] htmltools_0.3.6  misc3d_0.8-4     assertthat_0.2.0 colorspace_1.3-2
[33] stringi_1.2.4    lazyeval_0.2.1   munsell_0.5.0    crayon_1.3.4
```

https://mc.manuscriptcentral.com/LongRequest/hbm?DOWNLOAD=TRUE&PARAMS=xik_QKHnBGEDLZnR6HCy3g5QobpBDnDBo5Kezw6AjXa7cHXJM4PQ… 3/3

A.3 Phase 3: Supplementary Material

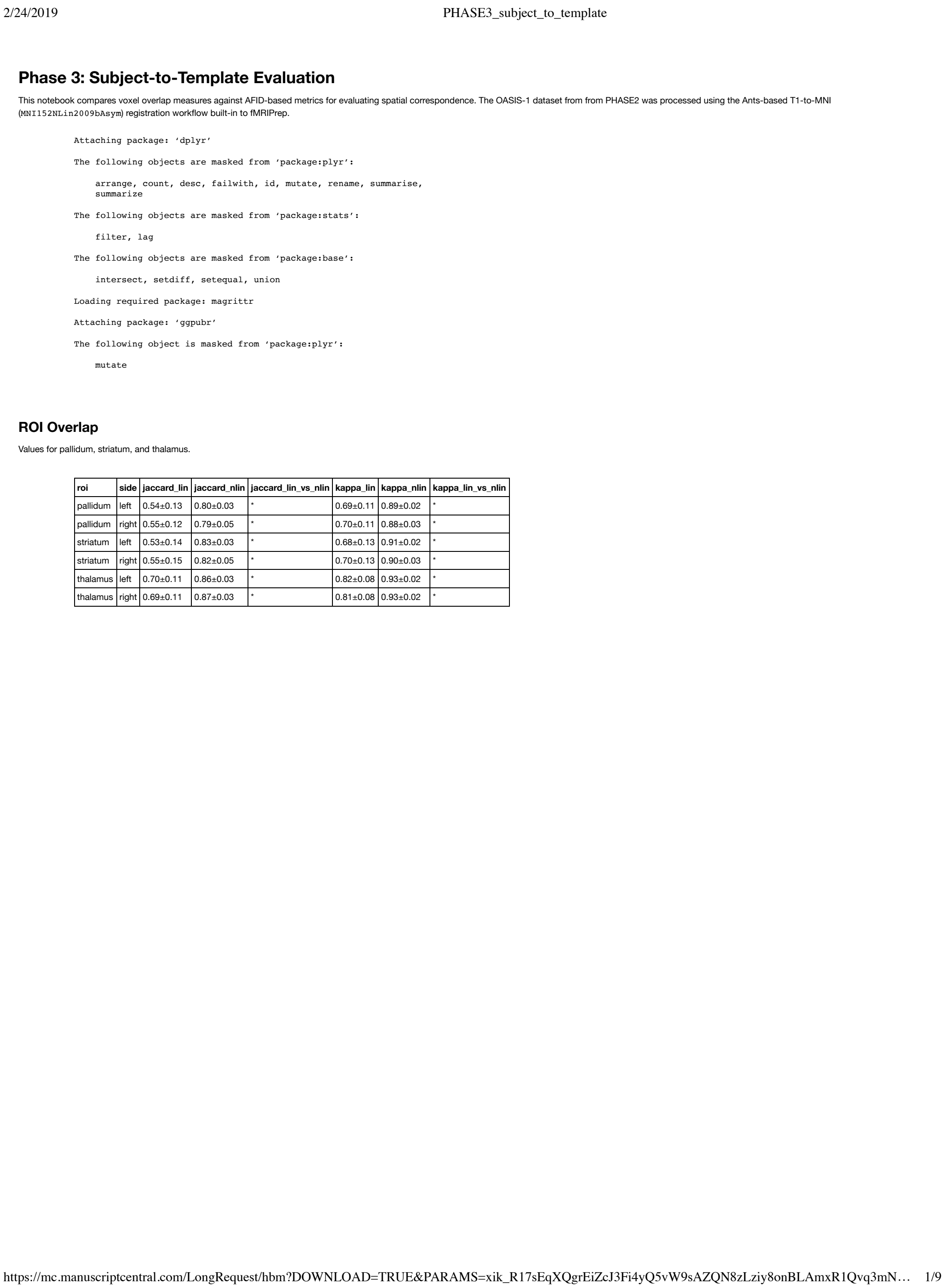

Phase 3: Subject-to-Template Evaluation

This notebook compares voxel overlap measures against AFID-based metrics for evaluating spatial correspondence. The OASIS-1 dataset from from PHASE2 was processed using the Ants-based T1-to-MNI (`MNI152NLin2009bAsym`) registration workflow built-in to fMRIPrep.

```
Attaching package: ‘dplyr’

The following objects are masked from ‘package:plyr’:

    arrange, count, desc, failwith, id, mutate, rename, summarise,
    summarize

The following objects are masked from ‘package:stats’:

    filter, lag

The following objects are masked from ‘package:base’:

    intersect, setdiff, setequal, union

Loading required package: magrittr

Attaching package: ‘ggpubr’

The following object is masked from ‘package:plyr’:

    mutate
```

ROI Overlap

Values for pallidum, striatum, and thalamus.

roi	side	jaccard_lin	jaccard_nlin	jaccard_lin_vs_nlin	kappa_lin	kappa_nlin	kappa_lin_vs_nlin
pallidum	left	0.54±0.13	0.80±0.03	*	0.69±0.11	0.89±0.02	*
pallidum	right	0.55±0.12	0.79±0.05	*	0.70±0.11	0.88±0.03	*
striatum	left	0.53±0.14	0.83±0.03	*	0.68±0.13	0.91±0.02	*
striatum	right	0.55±0.15	0.82±0.05	*	0.70±0.13	0.90±0.03	*
thalamus	left	0.70±0.11	0.86±0.03	*	0.82±0.08	0.93±0.02	*
thalamus	right	0.69±0.11	0.87±0.03	*	0.81±0.08	0.93±0.02	*

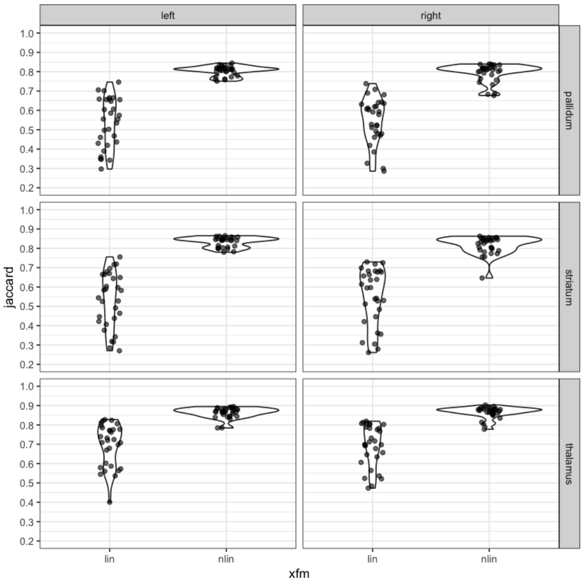

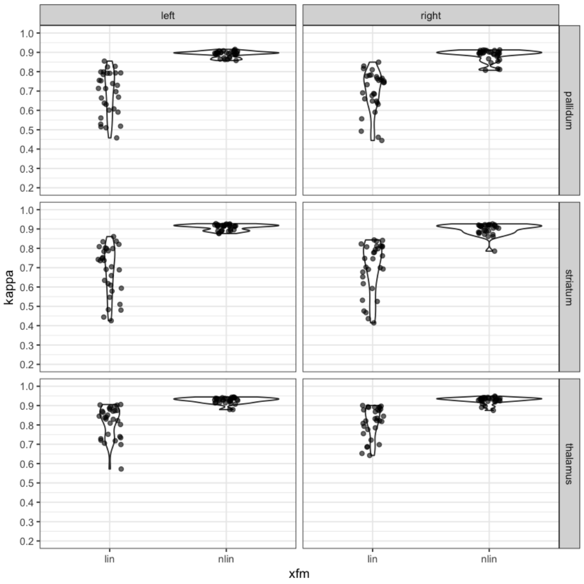

AFRE

Anatomical FRE is evaluated here as a metric for looking at the spatial correspondence between images. Here they are summarized globally, for each AFID, and for each subject. Qualitatively, the ventricles are misaligned for OAS1_0109 which accounts for the maximally error observed in this analysis of > 30 mm AFRE.

Nonlinear Transform Results

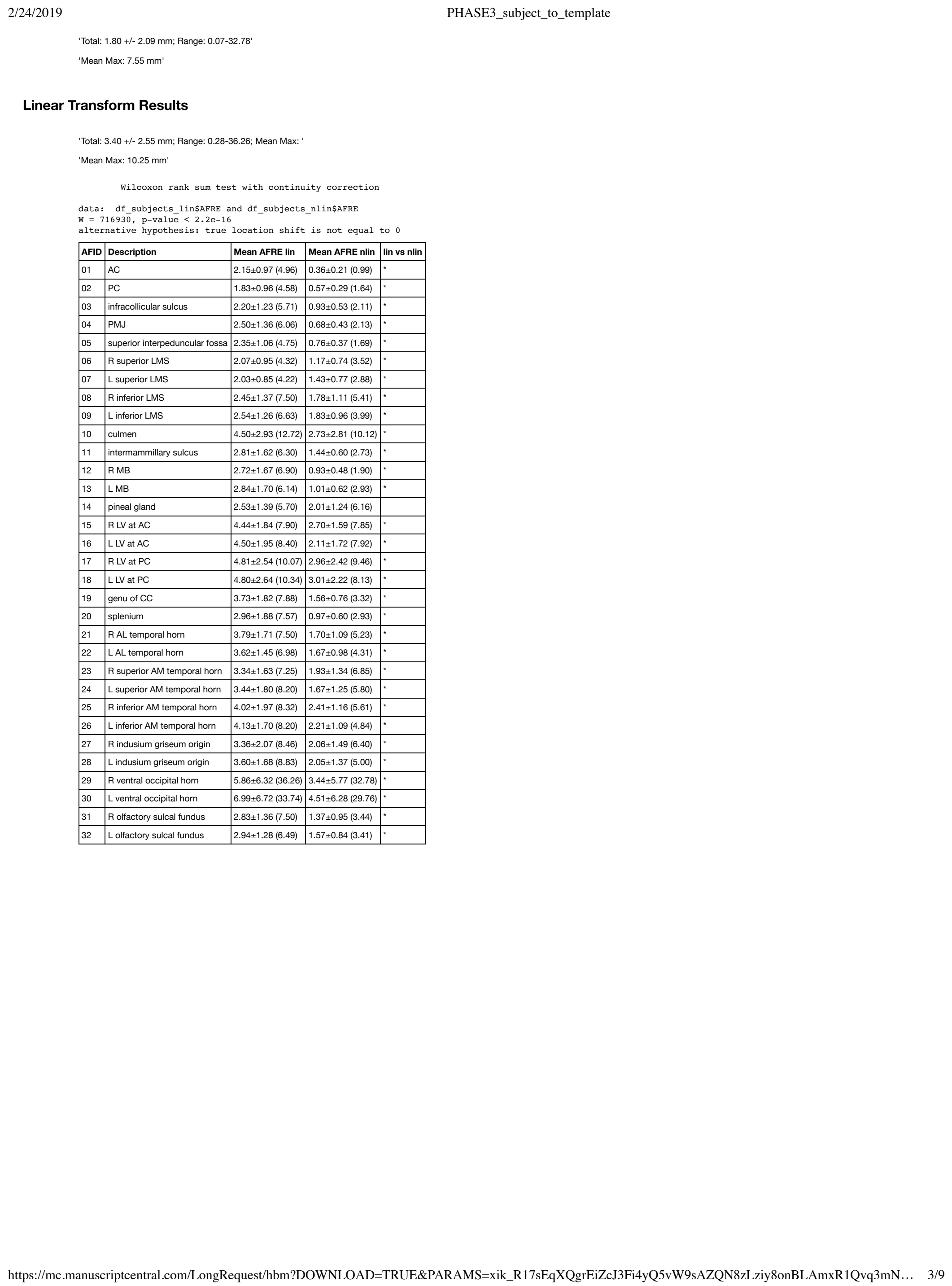

2/24/2019 PHASE3_subject_to_template

'Total: 1.80 +/- 2.09 mm; Range: 0.07-32.78'

'Mean Max: 7.55 mm'

Linear Transform Results

'Total: 3.40 +/- 2.55 mm; Range: 0.28-36.26; Mean Max: '

'Mean Max: 10.25 mm'

```
        Wilcoxon rank sum test with continuity correction

data:  df_subjects_lin$AFRE and df_subjects_nlin$AFRE
W = 716930, p-value < 2.2e-16
alternative hypothesis: true location shift is not equal to 0
```

AFID	Description	Mean AFRE lin	Mean AFRE nlin	lin vs nlin
01	AC	2.15±0.97 (4.96)	0.36±0.21 (0.99)	*
02	PC	1.83±0.96 (4.58)	0.57±0.29 (1.64)	*
03	infracollicular sulcus	2.20±1.23 (5.71)	0.93±0.53 (2.11)	*
04	PMJ	2.50±1.36 (6.06)	0.68±0.43 (2.13)	*
05	superior interpeduncular fossa	2.35±1.06 (4.75)	0.76±0.37 (1.69)	*
06	R superior LMS	2.07±0.95 (4.32)	1.17±0.74 (3.52)	*
07	L superior LMS	2.03±0.85 (4.22)	1.43±0.77 (2.88)	*
08	R inferior LMS	2.45±1.37 (7.50)	1.78±1.11 (5.41)	*
09	L inferior LMS	2.54±1.26 (6.63)	1.83±0.96 (3.99)	*
10	culmen	4.50±2.93 (12.72)	2.73±2.81 (10.12)	*
11	intermammillary sulcus	2.81±1.62 (6.30)	1.44±0.60 (2.73)	*
12	R MB	2.72±1.67 (6.90)	0.93±0.48 (1.90)	*
13	L MB	2.84±1.70 (6.14)	1.01±0.62 (2.93)	*
14	pineal gland	2.53±1.39 (5.70)	2.01±1.24 (6.16)	
15	R LV at AC	4.44±1.84 (7.90)	2.70±1.59 (7.85)	*
16	L LV at AC	4.50±1.95 (8.40)	2.11±1.72 (7.92)	*
17	R LV at PC	4.81±2.54 (10.07)	2.96±2.42 (9.46)	*
18	L LV at PC	4.80±2.64 (10.34)	3.01±2.22 (8.13)	*
19	genu of CC	3.73±1.82 (7.88)	1.56±0.76 (3.32)	*
20	splenium	2.96±1.88 (7.57)	0.97±0.60 (2.93)	*
21	R AL temporal horn	3.79±1.71 (7.50)	1.70±1.09 (5.23)	*
22	L AL temporal horn	3.62±1.45 (6.98)	1.67±0.98 (4.31)	*
23	R superior AM temporal horn	3.34±1.63 (7.25)	1.93±1.34 (6.85)	*
24	L superior AM temporal horn	3.44±1.80 (8.20)	1.67±1.25 (5.80)	*
25	R inferior AM temporal horn	4.02±1.97 (8.32)	2.41±1.16 (5.61)	*
26	L inferior AM temporal horn	4.13±1.70 (8.20)	2.21±1.09 (4.84)	*
27	R indusium griseum origin	3.36±2.07 (8.46)	2.06±1.49 (6.40)	*
28	L indusium griseum origin	3.60±1.68 (8.83)	2.05±1.37 (5.00)	*
29	R ventral occipital horn	5.86±6.32 (36.26)	3.44±5.77 (32.78)	*
30	L ventral occipital horn	6.99±6.72 (33.74)	4.51±6.28 (29.76)	*
31	R olfactory sulcal fundus	2.83±1.36 (7.50)	1.37±0.95 (3.44)	*
32	L olfactory sulcal fundus	2.94±1.28 (6.49)	1.57±0.84 (3.41)	*

https://mc.manuscriptcentral.com/LongRequest/hbm?DOWNLOAD=TRUE&PARAMS=xik_R17sEqXQgrEiZcJ3Fi4yQ5vW9sAZQN8zLziy8onBLAmxR1Qvq3mN… 3/9

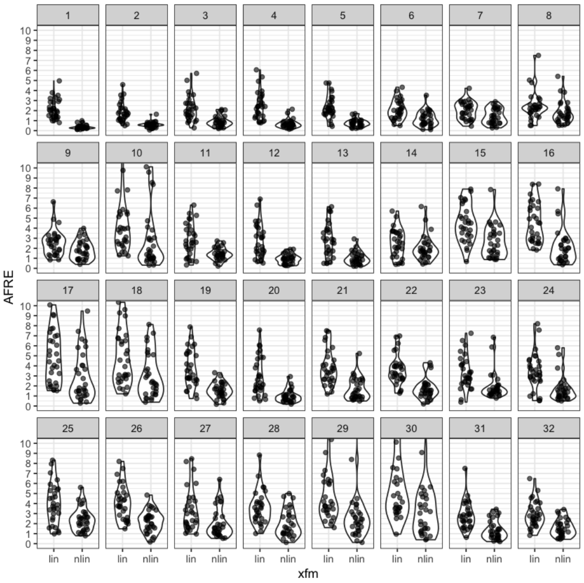

Subject level analysis of lin versus nlin

Revealed 3 subjects where mean AFRE was not statistically different. However, individual afids demonstrated high AFRE.

One subject appeared to be well registered with linear registration alone. The other two had extreme registration errors (over 8 mm AFRE).

subject	AFRE_lin	AFRE_nlin	AFRE_qval_significant
OAS1_0010	4.44±2.06 (11.19)	1.82±1.25 (5.61)	*
OAS1_0086	3.19±1.41 (6.40)	1.33±1.14 (5.66)	*
OAS1_0101	3.10±2.22 (8.83)	2.46±2.14 (8.36)	
OAS1_0109	4.86±8.12 (36.26)	3.89±7.34 (32.78)	
OAS1_0114	3.31±2.03 (8.32)	1.52±1.21 (5.88)	*
OAS1_0117	4.08±2.15 (9.76)	1.74±1.81 (10.12)	*
OAS1_0145	2.33±1.69 (7.57)	1.27±1.45 (6.85)	*
OAS1_0177	2.84±1.78 (7.06)	1.54±0.82 (2.83)	*
OAS1_0180	4.08±2.20 (10.13)	2.52±1.69 (6.45)	*
OAS1_0188	3.35±1.80 (9.08)	1.65±1.21 (5.08)	*
OAS1_0200	2.56±1.45 (7.88)	1.47±0.96 (4.84)	*
OAS1_0203	3.78±3.89 (23.96)	2.46±3.89 (22.40)	*
OAS1_0216	2.19±1.61 (7.58)	1.73±1.02 (4.48)	
OAS1_0239	2.89±2.03 (11.68)	1.56±1.63 (8.55)	*
OAS1_0249	3.34±1.65 (8.53)	1.63±1.08 (4.66)	*
OAS1_0255	3.48±1.77 (6.68)	1.29±0.75 (3.16)	*
OAS1_0256	4.16±2.00 (7.90)	1.52±0.97 (3.56)	*
OAS1_0263	3.97±2.36 (10.34)	1.29±0.96 (3.96)	*
OAS1_0266	3.67±1.18 (7.50)	1.60±1.22 (6.16)	*
OAS1_0274	2.90±1.87 (7.73)	1.99±2.34 (8.13)	*
OAS1_0284	3.90±2.59 (13.41)	1.84±1.85 (8.39)	*
OAS1_0303	2.70±1.23 (5.41)	1.47±0.85 (4.03)	*
OAS1_0343	3.32±1.69 (7.95)	2.43±1.95 (9.46)	*
OAS1_0345	2.31±1.30 (6.16)	1.57±1.10 (4.11)	*
OAS1_0357	2.58±1.61 (7.43)	1.47±1.35 (5.30)	*
OAS1_0365	4.18±2.07 (9.61)	1.65±1.35 (6.50)	*
OAS1_0371	2.64±1.31 (6.92)	1.33±0.82 (3.81)	*
OAS1_0395	3.27±1.96 (11.14)	1.68±1.28 (6.68)	*
OAS1_0398	3.85±3.04 (12.40)	1.81±1.80 (9.09)	*
OAS1_0456	4.64±2.73 (12.72)	2.42±2.01 (9.59)	*

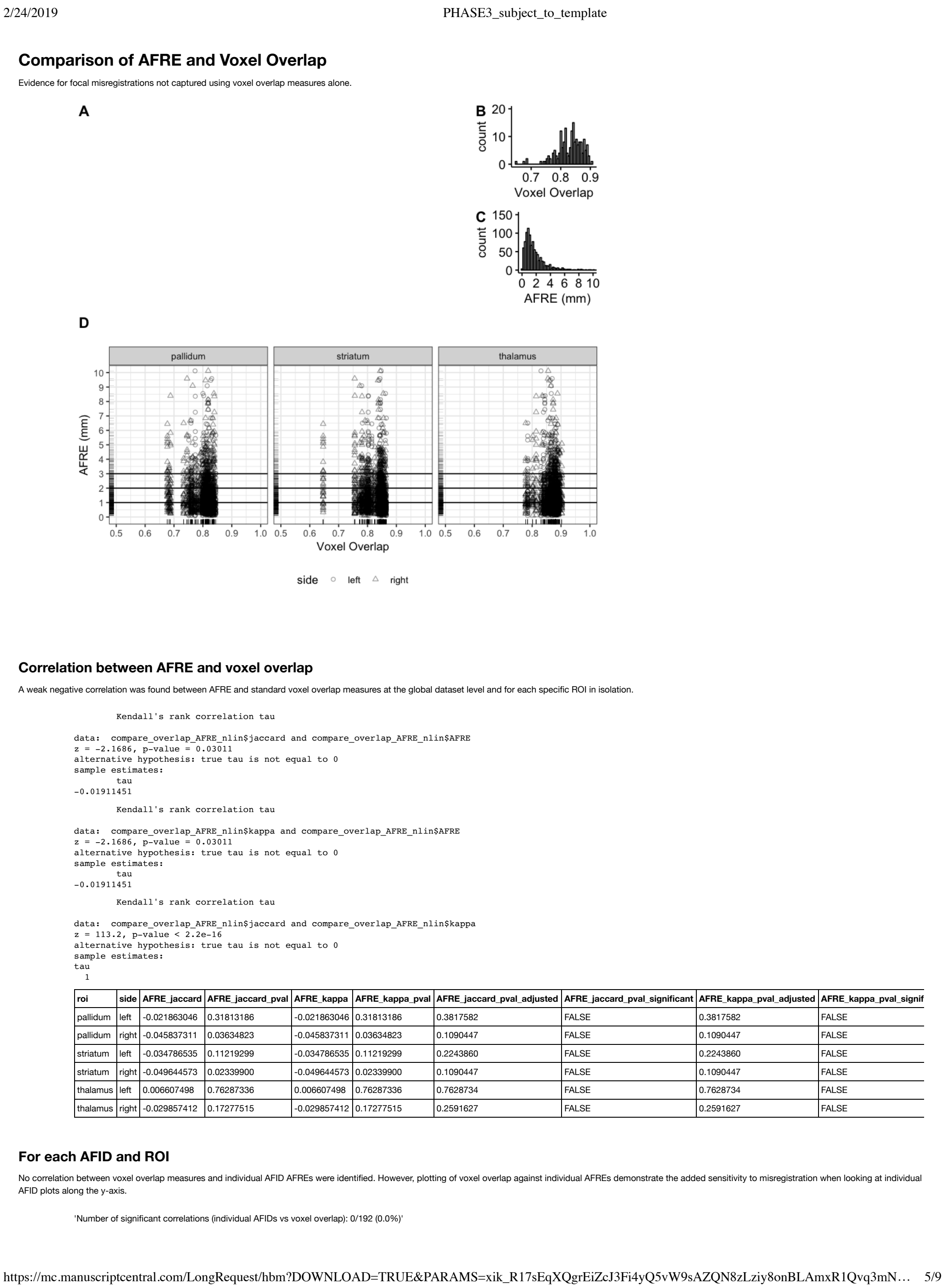

2/24/2019 PHASE3_subject_to_template

Comparison of AFRE and Voxel Overlap

Evidence for focal misregistrations not captured using voxel overlap measures alone.

Correlation between AFRE and voxel overlap

A weak negative correlation was found between AFRE and standard voxel overlap measures at the global dataset level and for each specific ROI in isolation.

```
        Kendall's rank correlation tau

data:  compare_overlap_AFRE_nlin$jaccard and compare_overlap_AFRE_nlin$AFRE
z = -2.1686, p-value = 0.03011
alternative hypothesis: true tau is not equal to 0
sample estimates:
        tau
-0.01911451

        Kendall's rank correlation tau

data:  compare_overlap_AFRE_nlin$kappa and compare_overlap_AFRE_nlin$AFRE
z = -2.1686, p-value = 0.03011
alternative hypothesis: true tau is not equal to 0
sample estimates:
        tau
-0.01911451

        Kendall's rank correlation tau

data:  compare_overlap_AFRE_nlin$jaccard and compare_overlap_AFRE_nlin$kappa
z = 113.2, p-value < 2.2e-16
alternative hypothesis: true tau is not equal to 0
sample estimates:
tau
  1
```

roi	side	AFRE_jaccard	AFRE_jaccard_pval	AFRE_kappa	AFRE_kappa_pval	AFRE_jaccard_pval_adjusted	AFRE_jaccard_pval_significant	AFRE_kappa_pval_adjusted	AFRE_kappa_pval_signif
pallidum	left	-0.021863046	0.31813186	-0.021863046	0.31813186	0.3817582	FALSE	0.3817582	FALSE
pallidum	right	-0.045837311	0.03634823	-0.045837311	0.03634823	0.1090447	FALSE	0.1090447	FALSE
striatum	left	-0.034786535	0.11219299	-0.034786535	0.11219299	0.2243860	FALSE	0.2243860	FALSE
striatum	right	-0.049644573	0.02339900	-0.049644573	0.02339900	0.1090447	FALSE	0.1090447	FALSE
thalamus	left	0.006607498	0.76287336	0.006607498	0.76287336	0.7628734	FALSE	0.7628734	FALSE
thalamus	right	-0.029857412	0.17277515	-0.029857412	0.17277515	0.2591627	FALSE	0.2591627	FALSE

For each AFID and ROI

No correlation between voxel overlap measures and individual AFID AFREs were identified. However, plotting of voxel overlap against individual AFREs demonstrate the added sensitivity to misregistration when looking at individual AFID plots along the y-axis.

'Number of significant correlations (individual AFIDs vs voxel overlap): 0/192 (0.0%)'

https://mc.manuscriptcentral.com/LongRequest/hbm?DOWNLOAD=TRUE&PARAMS=xik_R17sEqXQgrEiZcJ3Fi4yQ5vW9sAZQN8zLziy8onBLAmxR1Qvq3mN… 5/9

Pallidum

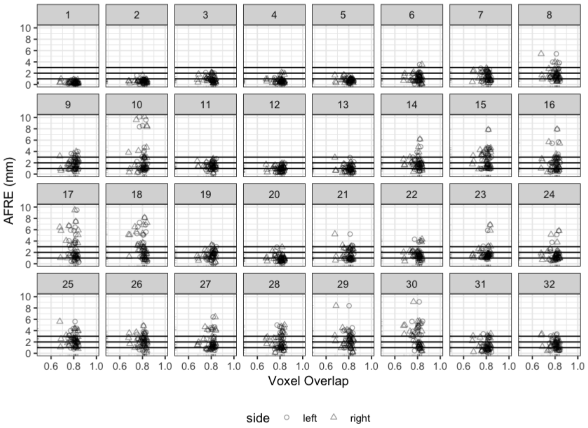

Striatum

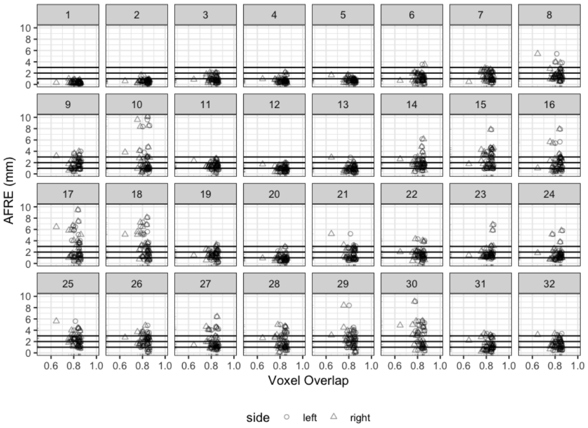

Thalamus

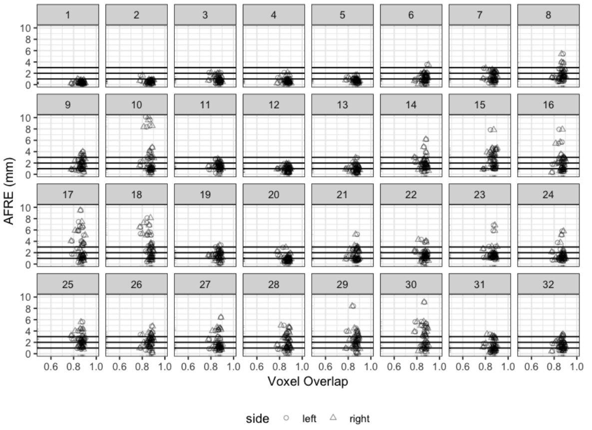

AFLE versus AFRE

In this section, we examine whether AFLE and AFRE are correlated and establish a baseline for when AFRE should be considered beyond placement-related (AFLE) error. The first vertical line is the mean AFLE for OASIS-1 subjects. Second is 1 s.d., third is 2 s.d.

A positive correlation between AFLE and AFRE was found to be statistically significant although the actual effect size of the correlation was small.

```
'Num Outlier AFIDs (> 2 s.d. above mean AFLE): 135/960 (14.06%)'

'Num Unique Outlier AFIDs (> 2 s.d. above mean AFLE): 22/32 (68.75%)'

        Kendall's rank correlation tau

data:  AFLE_vs_AFRE$AFRE and AFLE_vs_AFRE$mean_AFLE
z = 6.9796, p-value = 2.959e-12
alternative hypothesis: true tau is not equal to 0
sample estimates:
      tau
0.1504519
```

2/24/2019 PHASE3_subject_to_template

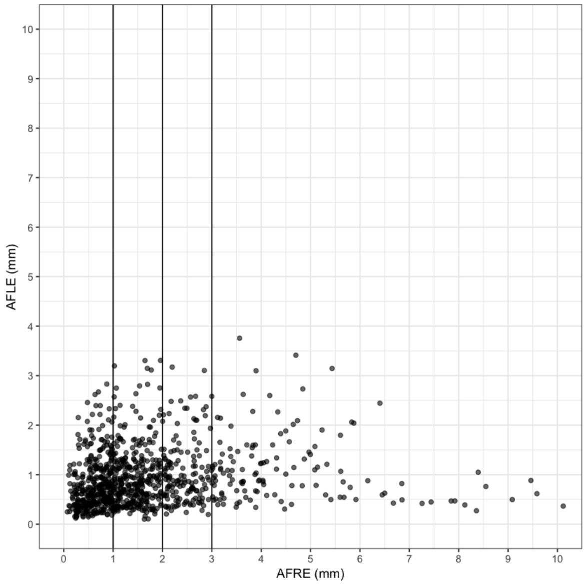

Secondary Analyses

We evaluated whether there was any evidence of an effect of demographics (e.g. age of the participants being registered) on AFRE. Age resulted in a global AFRE change of 0.0075 mm/year (i.e. a small but statistically significant effect). No specific AFIDs were found to contribute to this age-related AFRE change after multiple comparisons correction.

(Intercept)	2.1635	0.0000
age	0.0075	0.0191

https://mc.manuscriptcentral.com/LongRequest/hbm?DOWNLOAD=TRUE&PARAMS=xik_R17sEqXQgrEiZcJ3Fi4yQ5vW9sAZQN8zLziy8onBLAmxR1Qvq3mN… 8/9

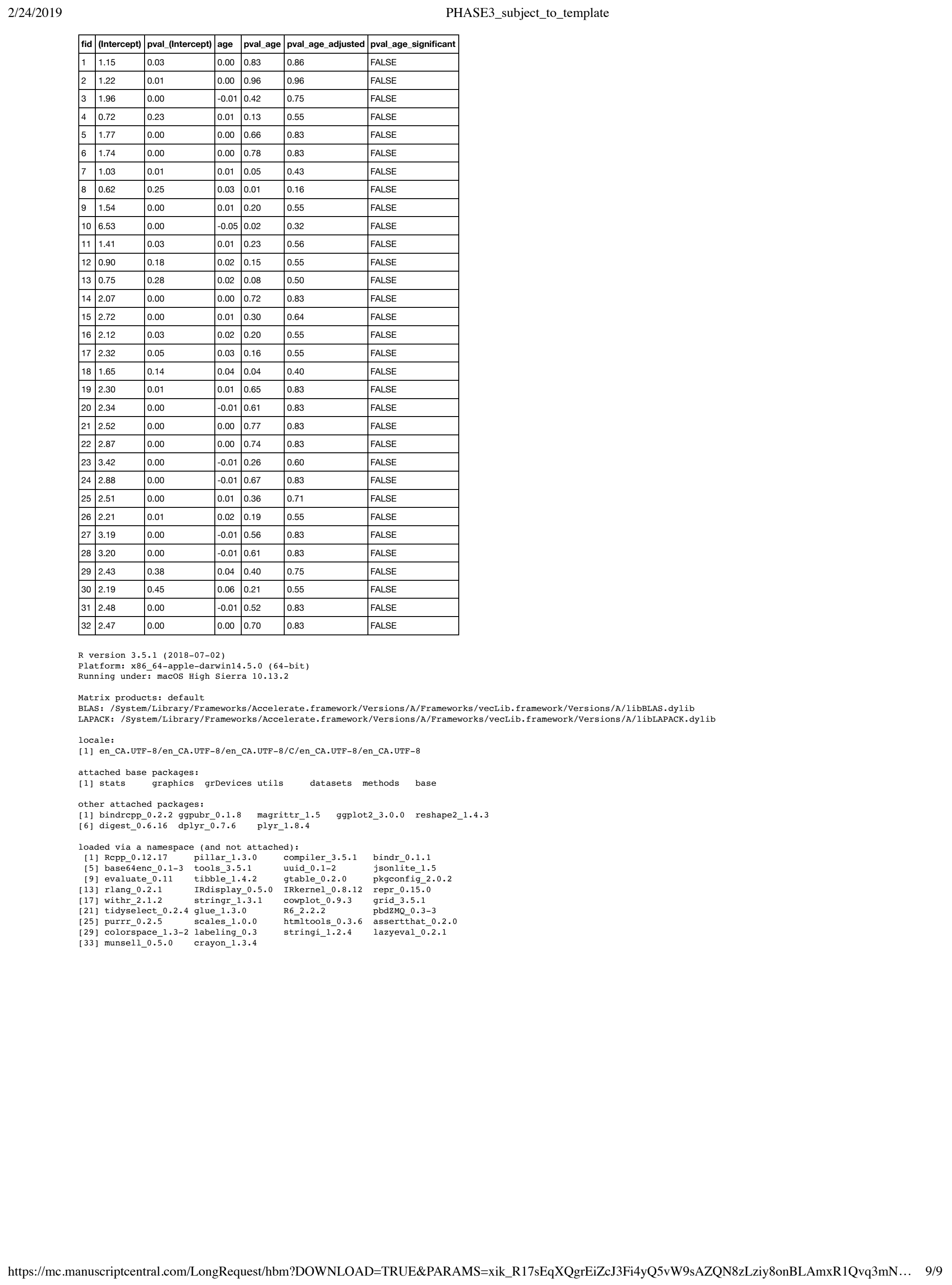

2/24/2019 PHASE3_subject_to_template

fid	(Intercept)	pval_(Intercept)	age	pval_age	pval_age_adjusted	pval_age_significant
1	1.15	0.03	0.00	0.83	0.86	FALSE
2	1.22	0.01	0.00	0.96	0.96	FALSE
3	1.96	0.00	-0.01	0.42	0.75	FALSE
4	0.72	0.23	0.01	0.13	0.55	FALSE
5	1.77	0.00	0.00	0.66	0.83	FALSE
6	1.74	0.00	0.00	0.78	0.83	FALSE
7	1.03	0.01	0.01	0.05	0.43	FALSE
8	0.62	0.25	0.03	0.01	0.16	FALSE
9	1.54	0.00	0.01	0.20	0.55	FALSE
10	6.53	0.00	-0.05	0.02	0.32	FALSE
11	1.41	0.03	0.01	0.23	0.56	FALSE
12	0.90	0.18	0.02	0.15	0.55	FALSE
13	0.75	0.28	0.02	0.08	0.50	FALSE
14	2.07	0.00	0.00	0.72	0.83	FALSE
15	2.72	0.00	0.01	0.30	0.64	FALSE
16	2.12	0.03	0.02	0.20	0.55	FALSE
17	2.32	0.05	0.03	0.16	0.55	FALSE
18	1.65	0.14	0.04	0.04	0.40	FALSE
19	2.30	0.01	0.01	0.65	0.83	FALSE
20	2.34	0.00	-0.01	0.61	0.83	FALSE
21	2.52	0.00	0.00	0.77	0.83	FALSE
22	2.87	0.00	0.00	0.74	0.83	FALSE
23	3.42	0.00	-0.01	0.26	0.60	FALSE
24	2.88	0.00	-0.01	0.67	0.83	FALSE
25	2.51	0.00	0.01	0.36	0.71	FALSE
26	2.21	0.01	0.02	0.19	0.55	FALSE
27	3.19	0.00	-0.01	0.56	0.83	FALSE
28	3.20	0.00	-0.01	0.61	0.83	FALSE
29	2.43	0.38	0.04	0.40	0.75	FALSE
30	2.19	0.45	0.06	0.21	0.55	FALSE
31	2.48	0.00	-0.01	0.52	0.83	FALSE
32	2.47	0.00	0.00	0.70	0.83	FALSE

```
R version 3.5.1 (2018-07-02)
Platform: x86_64-apple-darwin14.5.0 (64-bit)
Running under: macOS High Sierra 10.13.2

Matrix products: default
BLAS: /System/Library/Frameworks/Accelerate.framework/Versions/A/Frameworks/vecLib.framework/Versions/A/libBLAS.dylib
LAPACK: /System/Library/Frameworks/Accelerate.framework/Versions/A/Frameworks/vecLib.framework/Versions/A/libLAPACK.dylib

locale:
[1] en_CA.UTF-8/en_CA.UTF-8/en_CA.UTF-8/C/en_CA.UTF-8/en_CA.UTF-8

attached base packages:
[1] stats     graphics  grDevices utils     datasets  methods   base

other attached packages:
[1] bindrcpp_0.2.2 ggpubr_0.1.8   magrittr_1.5   ggplot2_3.0.0  reshape2_1.4.3
[6] digest_0.6.16  dplyr_0.7.6    plyr_1.8.4

loaded via a namespace (and not attached):
 [1] Rcpp_0.12.17     pillar_1.3.0     compiler_3.5.1   bindr_0.1.1
 [5] base64enc_0.1-3  tools_3.5.1      uuid_0.1-2       jsonlite_1.5
 [9] evaluate_0.11    tibble_1.4.2     gtable_0.2.0     pkgconfig_2.0.2
[13] rlang_0.2.1      IRdisplay_0.5.0  IRkernel_0.8.12  repr_0.15.0
[17] withr_2.1.2      stringr_1.3.1    cowplot_0.9.3    grid_3.5.1
[21] tidyselect_0.2.4 glue_1.3.0       R6_2.2.2         pbdZMQ_0.3-3
[25] purrr_0.2.5      scales_1.0.0     htmltools_0.3.6  assertthat_0.2.0
[29] colorspace_1.3-2 labeling_0.3     stringi_1.2.4    lazyeval_0.2.1
[33] munsell_0.5.0    crayon_1.3.4
```

https://mc.manuscriptcentral.com/LongRequest/hbm?DOWNLOAD=TRUE&PARAMS=xik_R17sEqXQgrEiZcJ3Fi4yQ5vW9sAZQN8zLziy8onBLAmxR1Qvq3mN… 9/9

A.4 Phase 4: Supplementary Material

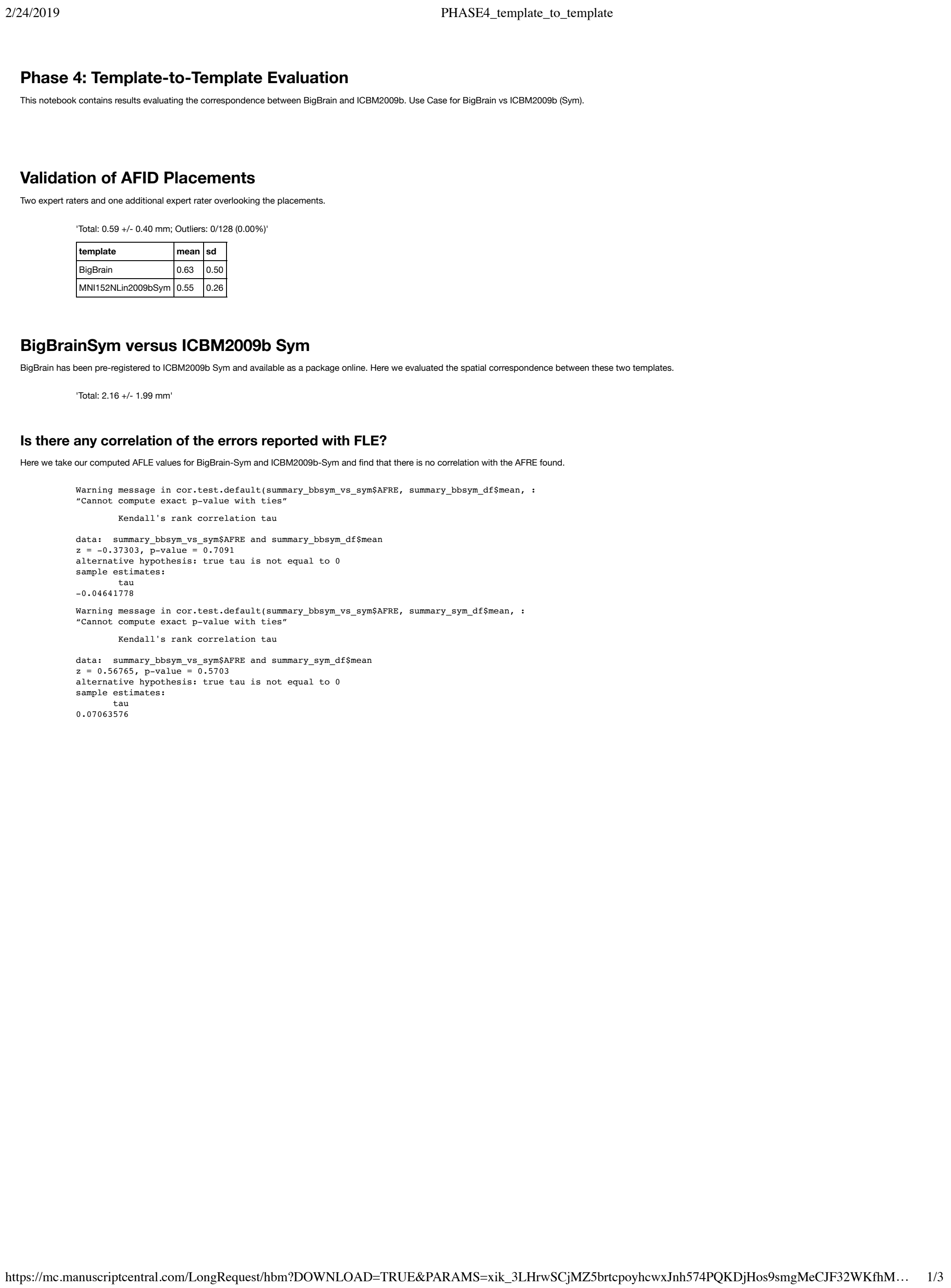

2/24/2019 PHASE4_template_to_template

Phase 4: Template-to-Template Evaluation

This notebook contains results evaluating the correspondence between BigBrain and ICBM2009b. Use Case for BigBrain vs ICBM2009b (Sym).

Validation of AFID Placements

Two expert raters and one additional expert rater overlooking the placements.

```
'Total: 0.59 +/- 0.40 mm; Outliers: 0/128 (0.00%)'
```

template	mean	sd
BigBrain	0.63	0.50
MNI152NLin2009bSym	0.55	0.26

BigBrainSym versus ICBM2009b Sym

BigBrain has been pre-registered to ICBM2009b Sym and available as a package online. Here we evaluated the spatial correspondence between these two templates.

```
'Total: 2.16 +/- 1.99 mm'
```

Is there any correlation of the errors reported with FLE?

Here we take our computed AFLE values for BigBrain-Sym and ICBM2009b-Sym and find that there is no correlation with the AFRE found.

```
Warning message in cor.test.default(summary_bbsym_vs_sym$AFRE, summary_bbsym_df$mean, :
“Cannot compute exact p-value with ties”

        Kendall's rank correlation tau

data:  summary_bbsym_vs_sym$AFRE and summary_bbsym_df$mean
z = -0.37303, p-value = 0.7091
alternative hypothesis: true tau is not equal to 0
sample estimates:
        tau
-0.04641778

Warning message in cor.test.default(summary_bbsym_vs_sym$AFRE, summary_sym_df$mean, :
“Cannot compute exact p-value with ties”

        Kendall's rank correlation tau

data:  summary_bbsym_vs_sym$AFRE and summary_sym_df$mean
z = 0.56765, p-value = 0.5703
alternative hypothesis: true tau is not equal to 0
sample estimates:
       tau
0.07063576
```

https://mc.manuscriptcentral.com/LongRequest/hbm?DOWNLOAD=TRUE&PARAMS=xik_3LHrwSCjMZ5brtcpoyhcwxJnh574PQKDjHos9smgMeCJF32WKfhM… 1/3

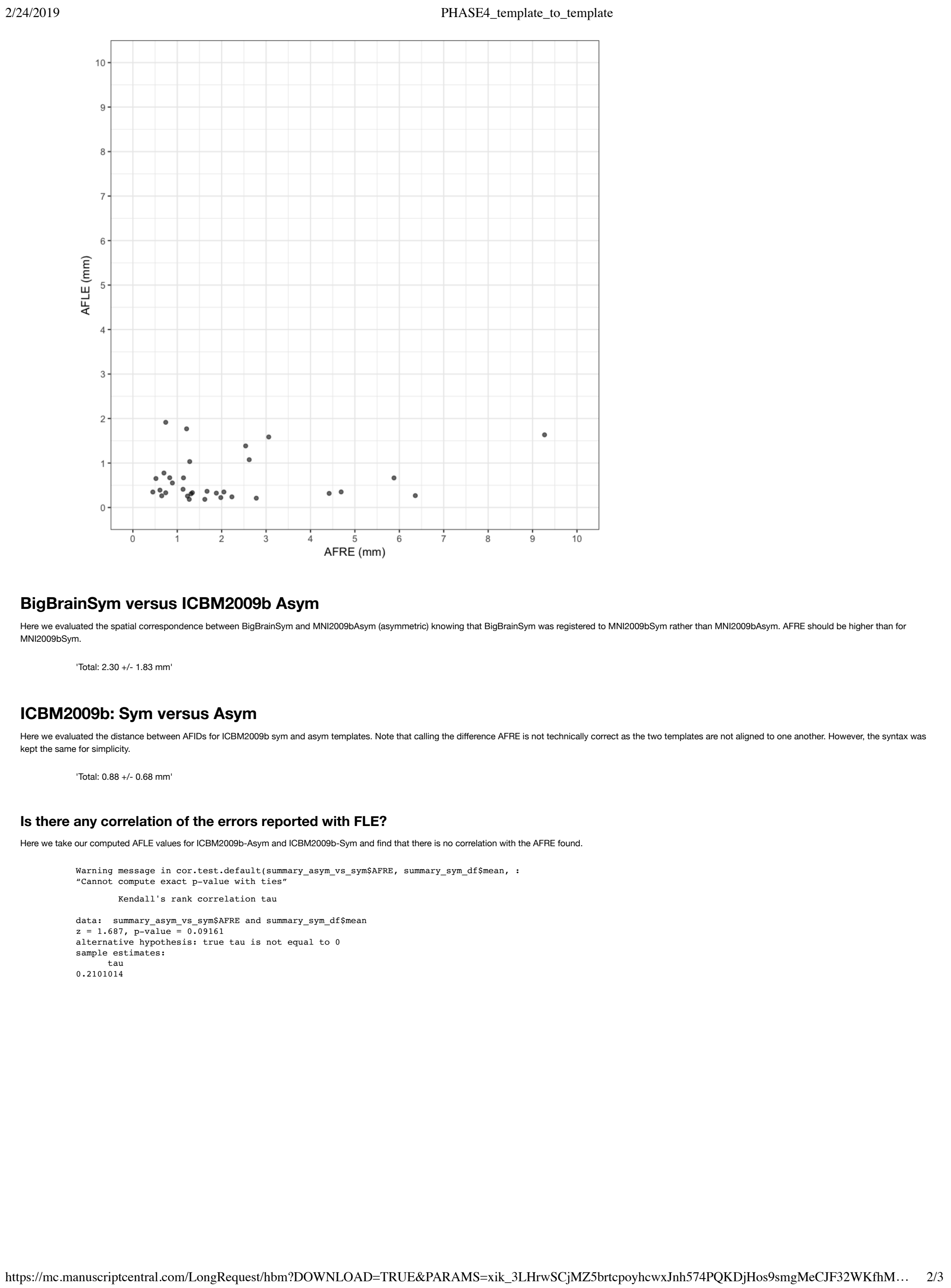

2/24/2019 PHASE4_template_to_template

BigBrainSym versus ICBM2009b Asym

Here we evaluated the spatial correspondence between BigBrainSym and MNI2009bAsym (asymmetric) knowing that BigBrainSym was registered to MNI2009bSym rather than MNI2009bAsym. AFRE should be higher than for MNI2009bSym.

```
'Total: 2.30 +/- 1.83 mm'
```

ICBM2009b: Sym versus Asym

Here we evaluated the distance between AFIDs for ICBM2009b sym and asym templates. Note that calling the difference AFRE is not technically correct as the two templates are not aligned to one another. However, the syntax was kept the same for simplicity.

```
'Total: 0.88 +/- 0.68 mm'
```

Is there any correlation of the errors reported with FLE?

Here we take our computed AFLE values for ICBM2009b-Asym and ICBM2009b-Sym and find that there is no correlation with the AFRE found.

```
Warning message in cor.test.default(summary_asym_vs_sym$AFRE, summary_sym_df$mean, :
“Cannot compute exact p-value with ties”

	Kendall's rank correlation tau

data:  summary_asym_vs_sym$AFRE and summary_sym_df$mean
z = 1.687, p-value = 0.09161
alternative hypothesis: true tau is not equal to 0
sample estimates:
      tau 
0.2101014 
```

https://mc.manuscriptcentral.com/LongRequest/hbm?DOWNLOAD=TRUE&PARAMS=xik_3LHrwSCjMZ5brtcpoyhcwxJnh574PQKDjHos9smgMeCJF32WKfhM… 2/3

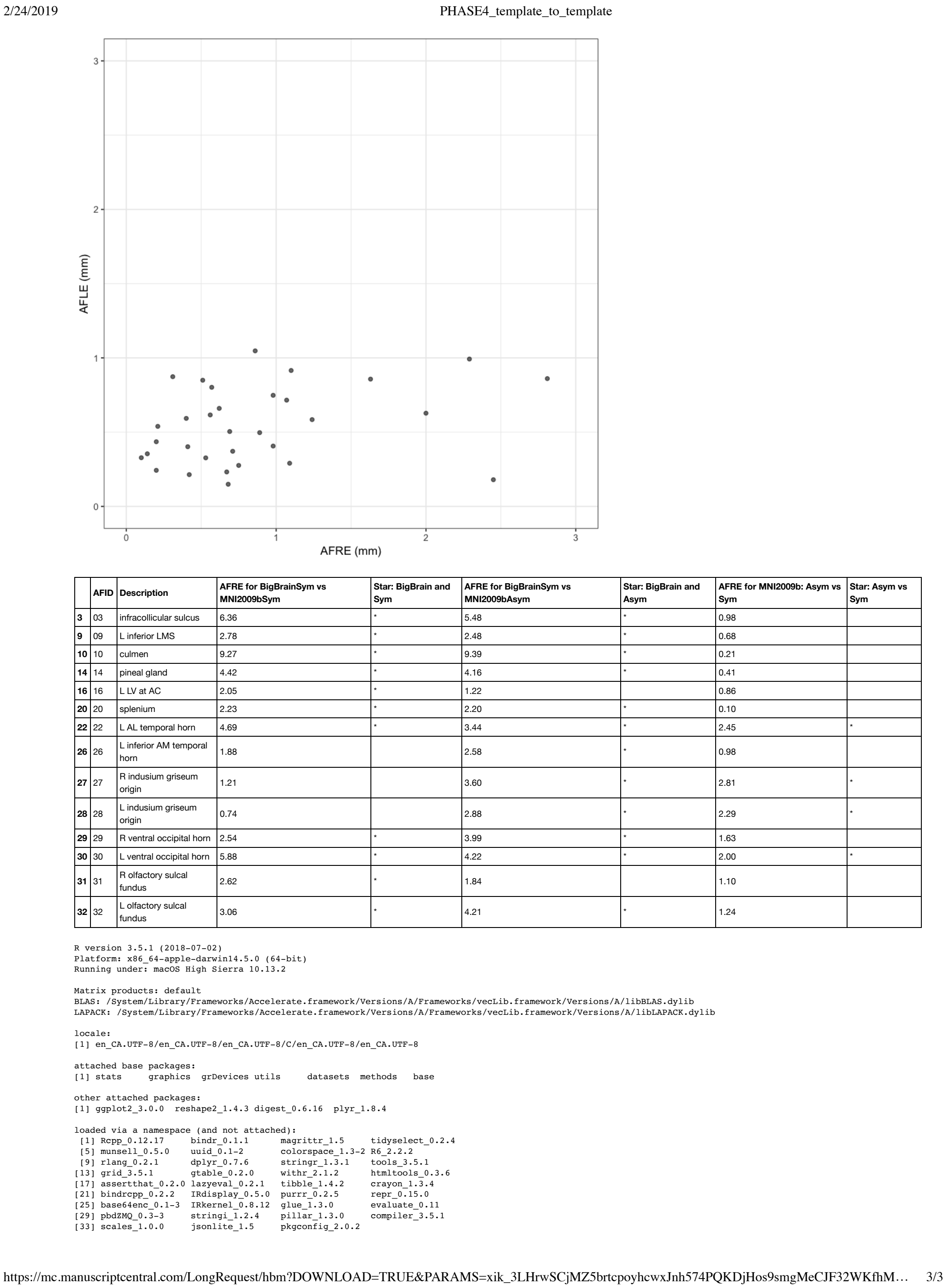

2/24/2019 PHASE4_template_to_template

	AFID	Description	AFRE for BigBrainSym vs MNI2009bSym	Star: BigBrain and Sym	AFRE for BigBrainSym vs MNI2009bAsym	Star: BigBrain and Asym	AFRE for MNI2009b: Asym vs Sym	Star: Asym vs Sym
3	03	infracollicular sulcus	6.36	*	5.48	*	0.98	
9	09	L inferior LMS	2.78	*	2.48	*	0.68	
10	10	culmen	9.27	*	9.39	*	0.21	
14	14	pineal gland	4.42	*	4.16	*	0.41	
16	16	L LV at AC	2.05	*	1.22		0.86	
20	20	splenium	2.23	*	2.20	*	0.10	
22	22	L AL temporal horn	4.69	*	3.44	*	2.45	*
26	26	L inferior AM temporal horn	1.88		2.58	*	0.98	
27	27	R indusium griseum origin	1.21		3.60	*	2.81	*
28	28	L indusium griseum origin	0.74		2.88	*	2.29	*
29	29	R ventral occipital horn	2.54	*	3.99	*	1.63	
30	30	L ventral occipital horn	5.88	*	4.22	*	2.00	*
31	31	R olfactory sulcal fundus	2.62	*	1.84		1.10	
32	32	L olfactory sulcal fundus	3.06	*	4.21	*	1.24	

```
R version 3.5.1 (2018-07-02)
Platform: x86_64-apple-darwin14.5.0 (64-bit)
Running under: macOS High Sierra 10.13.2

Matrix products: default
BLAS: /System/Library/Frameworks/Accelerate.framework/Versions/A/Frameworks/vecLib.framework/Versions/A/libBLAS.dylib
LAPACK: /System/Library/Frameworks/Accelerate.framework/Versions/A/Frameworks/vecLib.framework/Versions/A/libLAPACK.dylib

locale:
[1] en_CA.UTF-8/en_CA.UTF-8/en_CA.UTF-8/C/en_CA.UTF-8/en_CA.UTF-8

attached base packages:
[1] stats     graphics  grDevices utils     datasets  methods   base

other attached packages:
[1] ggplot2_3.0.0  reshape2_1.4.3 digest_0.6.16  plyr_1.8.4

loaded via a namespace (and not attached):
 [1] Rcpp_0.12.17     bindr_0.1.1      magrittr_1.5     tidyselect_0.2.4
 [5] munsell_0.5.0    uuid_0.1-2       colorspace_1.3-2 R6_2.2.2
 [9] rlang_0.2.1      dplyr_0.7.6      stringr_1.3.1    tools_3.5.1
[13] grid_3.5.1       gtable_0.2.0     withr_2.1.2      htmltools_0.3.6
[17] assertthat_0.2.0 lazyeval_0.2.1   tibble_1.4.2     crayon_1.3.4
[21] bindrcpp_0.2.2   IRdisplay_0.5.0  purrr_0.2.5      repr_0.15.0
[25] base64enc_0.1-3  IRkernel_0.8.12  glue_1.3.0       evaluate_0.11
[29] pbdZMQ_0.3-3     stringi_1.2.4    pillar_1.3.0     compiler_3.5.1
[33] scales_1.0.0     jsonlite_1.5     pkgconfig_2.0.2
```

https://mc.manuscriptcentral.com/LongRequest/hbm?DOWNLOAD=TRUE&PARAMS=xik_3LHrwSCjMZ5brtcpoyhcwxJnh574PQKDjHos9smgMeCJF32WKfhM… 3/3

Appendix B

Chapter 4 Supplementary Material

B.1 Supplementary Tables

region	side	atlas	mean	stdev	V	*p*-value	*q*-value	max	max stdev
Left Red Nucleus	left	ATAG	1.02	0.53	111	0.69492	1.00000	1.69	0.98
Left Substantia Nigra	left	ATAG	0.86	0.39	76	0.95079	1.00000	1.52	0.67
Left Subthalamic Nucleus	left	ATAG	1.05	0.59	108	0.72770	1.00000	1.48	0.79
Left Striatum	left	ATAG	0.59	0.14	0	1.00000	1.00000	2.41	0.99
Left Globus Pallidus Externus	left	ATAG	0.48	0.15	0	1.00000	1.00000	1.33	0.66
Left Globus Pallidus Internus	left	ATAG	0.55	0.21	2	1.00000	1.00000	1.19	0.55
Right Red Nucleus	right	ATAG	1.03	0.40	131	0.44937	1.00000	1.71	0.72
Right Substantia Nigra	right	ATAG	0.78	0.30	31	0.99953	1.00000	1.48	0.80
Right Subthalamic Nucleus	right	ATAG	0.98	0.53	99	0.81473	1.00000	1.44	0.70
Right Striatum	right	ATAG	0.60	0.19	3	1.00000	1.00000	2.38	0.91
Right Globus Pallidus Externus	right	ATAG	0.50	0.22	2	1.00000	1.00000	1.31	0.81
Right Globus Pallidus Internus	right	ATAG	0.50	0.24	6	1.00000	1.00000	1.10	0.72
Left Frontal	left	lobar	0.91	0.12	30	0.99960	1.00000	7.69	1.19
Left Parietal	left	lobar	0.81	0.11	4	1.00000	1.00000	3.46	0.73
Left Occipital	left	lobar	1.15	0.26	197	0.01043	0.07938	4.62	1.83
Left Temporal	left	lobar	1.11	0.21	195	0.01257	0.08610	5.99	1.53
Left Insular	left	lobar	0.61	0.10	0	1.00000	1.00000	1.80	0.30
Left Subcortical	left	lobar	0.70	0.22	11	0.99999	1.00000	2.61	1.10
Right Frontal	right	lobar	0.89	0.11	24	0.99985	1.00000	8.07	1.71
Right Parietal	right	lobar	0.76	0.11	1	1.00000	1.00000	3.56	0.79
Right Occipital	right	lobar	1.07	0.17	166	0.10496	0.49586	4.24	0.94
Right Temporal	right	lobar	1.04	0.12	169	0.08810	0.43104	5.75	0.96
Right Insular	right	lobar	0.66	0.13	1	1.00000	1.00000	2.07	0.62
Right Subcortical	right	lobar	0.75	0.24	25	0.99982	1.00000	2.94	0.98
Left Lateral Ventricle	left	HarvardOxford	0.37	0.05	0	1.00000	1.00000	1.33	0.42
Left Thalamus	left	HarvardOxford	0.86	0.41	63	0.98206	1.00000	2.45	1.11
Left Caudate	left	HarvardOxford	0.64	0.25	8	1.00000	1.00000	1.81	0.58
Left Putamen	left	HarvardOxford	0.57	0.12	0	1.00000	1.00000	1.95	0.72
Left Pallidum	left	HarvardOxford	0.51	0.18	1	1.00000	1.00000	1.44	0.71
Brainstem	NA	HarvardOxford	1.31	0.64	179	0.04587	0.25135	7.50	1.93
Left Hippocampus	left	HarvardOxford	0.72	0.20	11	0.99999	1.00000	3.09	1.78
Left Amygdala	left	HarvardOxford	1.14	0.49	131	0.44937	1.00000	3.23	1.86
Left Accumbens	left	HarvardOxford	0.93	0.40	79	0.93966	1.00000	1.95	1.04
Right Lateral Ventricle	right	HarvardOxford	0.39	0.08	0	1.00000	1.00000	1.33	0.46
Right Thalamus	right	HarvardOxford	0.99	0.41	113	0.67218	1.00000	2.74	1.10
Right Caudate	right	HarvardOxford	0.60	0.18	1	1.00000	1.00000	1.63	0.53
Right Putamen	right	HarvardOxford	0.59	0.26	13	0.99998	1.00000	1.96	0.95

Right Pallidum	right	HarvardOxford	0.51	0.25	8	1.00000	1.00000	1.35	0.82	
Right Hippocampus	right	HarvardOxford	0.67	0.16	1	1.00000	1.00000	2.50	0.89	
Right Amygdala	right	HarvardOxford	1.07	0.54	107	0.73824	1.00000	2.72	1.23	
Right Accumbens	right	HarvardOxford	0.82	0.39	51	0.99426	1.00000	1.79	0.94	
Left Frontal Pole	left	HarvardOxford	0.91	0.24	43	0.99766	1.00000	6.92	1.62	
Right Frontal Pole	right	HarvardOxford	0.91	0.12	41	0.99816	1.00000	7.49	2.02	
Left Insular Cortex	left	HarvardOxford	0.61	0.10	0	1.00000	1.00000	1.80	0.30	
Right Insular Cortex	right	HarvardOxford	0.66	0.13	1	1.00000	1.00000	2.07	0.62	
Left Superior Frontal Gyrus	left	HarvardOxford	1.06	0.32	143	0.30508	1.00000	4.38	1.25	
Right Superior Frontal Gyrus	right	HarvardOxford	1.01	0.36	114	0.66057	1.00000	4.36	1.29	
Left Middle Frontal Gyrus	left	HarvardOxford	0.73	0.12	0	1.00000	1.00000	2.59	0.52	
Right Middle Frontal Gyrus	right	HarvardOxford	0.67	0.13	0	1.00000	1.00000	2.31	0.49	
Left Inferior Frontal Gyrus Pars Triangularis	left	HarvardOxford	0.85	0.25	51	0.99426	1.00000	2.30	0.65	
Right Inferior Frontal Gyrus Pars Triangularis	right	HarvardOxford	0.81	0.24	34	0.99927	1.00000	2.29	0.75	
Left Inferior Frontal Gyrus Pars Opercularis	left	HarvardOxford	0.81	0.28	43	0.99766	1.00000	2.32	0.69	
Right Inferior Frontal Gyrus Pars Opercularis	right	HarvardOxford	0.71	0.17	9	0.99999	1.00000	1.95	0.48	
Left Precentral Gyrus	left	HarvardOxford	0.87	0.12	15	0.99997	1.00000	3.95	1.04	
Right Precentral Gyrus	right	HarvardOxford	0.83	0.12	8	1.00000	1.00000	3.85	0.87	
Left Temporal Pole	left	HarvardOxford	1.18	0.28	217	0.00110	0.00940	5.16	1.57	*
Right Temporal Pole	right	HarvardOxford	1.17	0.24	213	0.00184	0.01479	4.87	1.50	*
Left Superior Temporal Gyrus Anterior	left	HarvardOxford	0.89	0.42	57	0.98957	1.00000	2.41	0.97	
Right Superior Temporal Gyrus Anterior	right	HarvardOxford	0.87	0.22	56	0.99052	1.00000	2.26	0.55	
Left Superior Temporal Gyrus Posterior	left	HarvardOxford	0.88	0.23	66	0.97692	1.00000	2.13	0.60	
Right Superior Temporal Gyrus Posterior	right	HarvardOxford	0.87	0.27	57	0.98957	1.00000	2.22	0.78	
Left Middle Temporal Gyrus Anterior	left	HarvardOxford	1.54	0.67	228	0.00021	0.00196	3.58	1.34	*
Right Middle Temporal Gyrus Anterior	right	HarvardOxford	1.13	0.42	155	0.18527	0.79317	2.83	0.84	
Left Middle Temporal Gyrus Posterior	left	HarvardOxford	1.16	0.29	196	0.01146	0.08262	3.73	0.94	
Right Middle Temporal Gyrus Posterior	right	HarvardOxford	1.02	0.28	138	0.36309	1.00000	3.17	0.84	
Left Middle Temporal Gyrus TemporoOccipital	left	HarvardOxford	1.11	0.27	174	0.06444	0.32697	2.99	0.53	
Right Middle Temporal Gyrus TemporoOccipital	right	HarvardOxford	1.05	0.31	140	0.33943	1.00000	3.02	0.83	
Left Inferior Temporal Gyrus Anterior	left	HarvardOxford	1.30	0.53	190	0.01954	0.12166	3.29	1.35	
Right Inferior Temporal Gyrus Anterior	right	HarvardOxford	1.08	0.29	161	0.13781	0.60905	2.79	0.62	
Left Inferior Temporal Gyrus Posterior	left	HarvardOxford	1.73	0.36	252	0.00000	0.00001	5.34	0.84	*
Right Inferior Temporal Gyrus Posterior	right	HarvardOxford	1.56	0.34	253	0.00000	0.00001	5.05	0.82	*
Left Inferior Temporal Gyrus TemporoOccipital	left	HarvardOxford	1.09	0.32	136	0.38726	1.00000	3.50	1.15	
Right Inferior Temporal Gyrus TemporoOccipital	right	HarvardOxford	1.08	0.17	186	0.02712	0.15483	3.82	0.85	
Left Postcentral Gyrus	left	HarvardOxford	0.90	0.15	44	0.99736	1.00000	3.03	0.67	
Right Postcentral Gyrus	right	HarvardOxford	0.87	0.18	41	0.99816	1.00000	3.30	0.88	

Left Superior Parietal Lobule	left	HarvardOxford	0.88	0.26	72	0.96311	1.00000	2.32	0.54	
Right Superior Parietal Lobule	right	HarvardOxford	0.91	0.32	86	0.90651	1.00000	2.55	0.67	
Left Supramarginal Gyrus Anterior	left	HarvardOxford	0.89	0.18	51	0.99426	1.00000	2.41	0.54	
Right Supramarginal Gyrus Anterior	right	HarvardOxford	0.82	0.17	19	0.99994	1.00000	2.31	0.56	
Left Supramarginal Gyrus Posterior	left	HarvardOxford	1.00	0.21	122	0.56320	1.00000	2.70	0.54	
Right Supramarginal Gyrus Posterior	right	HarvardOxford	0.87	0.14	20	0.99993	1.00000	2.55	0.48	
Left Angular Gyrus	left	HarvardOxford	1.01	0.23	136	0.38726	1.00000	2.75	0.62	
Right Angular Gyrus	right	HarvardOxford	0.96	0.23	96	0.83956	1.00000	2.84	0.51	
Left Lateral Occipital Cortex Superior	left	HarvardOxford	1.10	0.23	186	0.02712	0.15483	3.37	0.57	
Right Lateral Occipital Cortex Superior	right	HarvardOxford	1.07	0.23	174	0.06444	0.32697	3.28	0.61	
Left Lateral Occipital Cortex Inferior	left	HarvardOxford	1.31	0.26	248	0.00000	0.00003	3.62	1.32	*
Right Lateral Occipital Cortex Inferior	right	HarvardOxford	1.28	0.18	253	0.00000	0.00001	3.45	0.57	*
Left Intracalcarine Cortex	left	HarvardOxford	0.65	0.27	13	0.99998	1.00000	1.77	0.61	
Right Intracalcarine Cortex	right	HarvardOxford	0.53	0.23	3	1.00000	1.00000	1.51	0.59	
Left Frontal Medial Cortex	left	HarvardOxford	1.75	0.59	251	0.00000	0.00001	5.68	1.12	*
Right Frontal Medial Cortex	right	HarvardOxford	1.84	0.56	253	0.00000	0.00001	5.77	0.94	*
Left Juxtapositional Lobule Cortex (formerly SMA)	left	HarvardOxford	1.05	0.43	128	0.48731	1.00000	3.97	1.40	
Right Juxtapositional Lobule Cortex (formerly SMA)	right	HarvardOxford	1.05	0.53	116	0.63691	1.00000	3.82	1.49	
Left Subcallosal Cortex	left	HarvardOxford	1.72	0.33	252	0.00000	0.00001	6.87	0.67	*
Right Subcallosal Cortex	right	HarvardOxford	1.80	0.38	253	0.00000	0.00001	6.87	0.62	*
Left Paracingulate Gyrus	left	HarvardOxford	0.73	0.27	27	0.99975	1.00000	2.63	1.09	
Right Paracingulate Gyrus	right	HarvardOxford	0.73	0.22	17	0.99996	1.00000	2.54	0.95	
Left Cingulate Gyrus Anterior	left	HarvardOxford	0.65	0.15	1	1.00000	1.00000	2.12	0.79	
Right Cingulate Gyrus Anterior	right	HarvardOxford	0.70	0.20	11	0.99999	1.00000	2.41	0.93	
Left Cingulate Gyrus Posterior	left	HarvardOxford	0.52	0.11	0	1.00000	1.00000	1.75	0.32	
Right Cingulate Gyrus Posterior	right	HarvardOxford	0.54	0.19	1	1.00000	1.00000	1.83	0.51	
Left Precuneus Cortex	left	HarvardOxford	0.63	0.12	0	1.00000	1.00000	2.80	0.92	
Right Precuneus Cortex	right	HarvardOxford	0.54	0.09	0	1.00000	1.00000	2.53	0.55	
Left Cuneal Cortex	left	HarvardOxford	0.84	0.23	38	0.99875	1.00000	2.51	0.82	
Right Cuneal Cortex	right	HarvardOxford	0.71	0.18	2	1.00000	1.00000	2.29	0.80	
Left Frontal Orbital Cortex	left	HarvardOxford	1.10	0.22	191	0.01794	0.11702	6.20	1.50	
Right Frontal Orbital Cortex	right	HarvardOxford	1.08	0.27	150	0.23139	0.96061	6.74	2.16	
Left Parahippocampal Gyrus Anterior	left	HarvardOxford	1.51	0.88	244	0.00001	0.00008	3.84	1.89	*
Right Parahippocampal Gyrus Anterior	right	HarvardOxford	1.40	0.35	249	0.00000	0.00003	4.00	1.27	*
Left Parahippocampal Gyrus Posterior	left	HarvardOxford	0.80	0.23	33	0.99937	1.00000	2.24	0.52	
Right Parahippocampal Gyrus Posterior	right	HarvardOxford	0.76	0.13	4	1.00000	1.00000	2.10	0.31	
Left Lingual Gyrus	left	HarvardOxford	0.70	0.26	17	0.99996	1.00000	2.63	1.38	
Right Lingual Gyrus	right	HarvardOxford	0.63	0.20	4	1.00000	1.00000	2.28	0.90	

Left Temporal Fusiform Cortex Anterior	left	HarvardOxford	1.62	0.85	247	0.00000	0.00004	3.77	1.85	*
Right Temporal Fusiform Cortex Anterior	right	HarvardOxford	1.59	0.57	247	0.00000	0.00004	3.52	1.13	*
Left Temporal Fusiform Cortex Posterior	left	HarvardOxford	1.04	0.31	125	0.52537	1.00000	3.58	1.15	
Right Temporal Fusiform Cortex Posterior	right	HarvardOxford	1.08	0.25	164	0.11738	0.53604	3.49	0.60	
Left Temporal Fusiform Cortex TemporoOccipital	left	HarvardOxford	0.64	0.23	8	1.00000	1.00000	2.04	0.89	
Right Temporal Fusiform Cortex TemporoOccipital	right	HarvardOxford	0.65	0.21	6	1.00000	1.00000	2.53	0.77	
Left Occipital Fusiform Gyrus	left	HarvardOxford	1.03	0.57	104	0.76861	1.00000	2.92	1.71	
Right Occipital Fusiform Gyrus	right	HarvardOxford	0.83	0.42	68	0.97288	1.00000	2.56	1.07	
Left Frontal Operculum Cortex	left	HarvardOxford	0.61	0.14	0	1.00000	1.00000	1.71	0.54	
Right Frontal Operculum Cortex	right	HarvardOxford	0.55	0.15	0	1.00000	1.00000	1.46	0.41	
Left Central Opercular Cortex	left	HarvardOxford	0.61	0.15	0	1.00000	1.00000	1.91	0.48	
Right Central Opercular Cortex	right	HarvardOxford	0.57	0.13	0	1.00000	1.00000	1.71	0.45	
Left Parietal Operculum Cortex	left	HarvardOxford	0.55	0.12	0	1.00000	1.00000	1.64	0.37	
Right Parietal Operculum Cortex	right	HarvardOxford	0.53	0.11	0	1.00000	1.00000	1.70	0.48	
Left Planum Polare	left	HarvardOxford	0.65	0.14	0	1.00000	1.00000	1.67	0.49	
Right Planum Polare	right	HarvardOxford	0.79	0.25	31	0.99953	1.00000	1.78	0.44	
Left Heschl Gyrus	left	HarvardOxford	0.62	0.26	21	0.99991	1.00000	1.53	0.42	
Right Heschl Gyrus	right	HarvardOxford	0.68	0.21	6	1.00000	1.00000	1.64	0.49	
Left Planum Temporale	left	HarvardOxford	0.65	0.16	1	1.00000	1.00000	1.87	0.43	
Right Planum Temporale	right	HarvardOxford	0.63	0.13	0	1.00000	1.00000	1.72	0.46	
Left Supracalcarine Cortex	left	HarvardOxford	0.59	0.21	3	1.00000	1.00000	1.53	0.52	
Right Supracalcarine Cortex	right	HarvardOxford	0.49	0.17	1	1.00000	1.00000	1.15	0.36	
Left Occipital Pole	left	HarvardOxford	1.64	0.65	248	0.00000	0.00003	4.33	1.95	*
Right Occipital Pole	right	HarvardOxford	1.55	0.46	252	0.00000	0.00001	4.01	1.08	*

V represents the Wilcoxon rank sum statistic, p-value is unadjusted, and q-value is FDR adjusted. * 13 regions met thresholds for statistical significance after FDR correction at a rate of $q < 0.025$.

Appendix C

Ethics Approvals

C.1 Retrospective images for deep brain stimulation surgery.

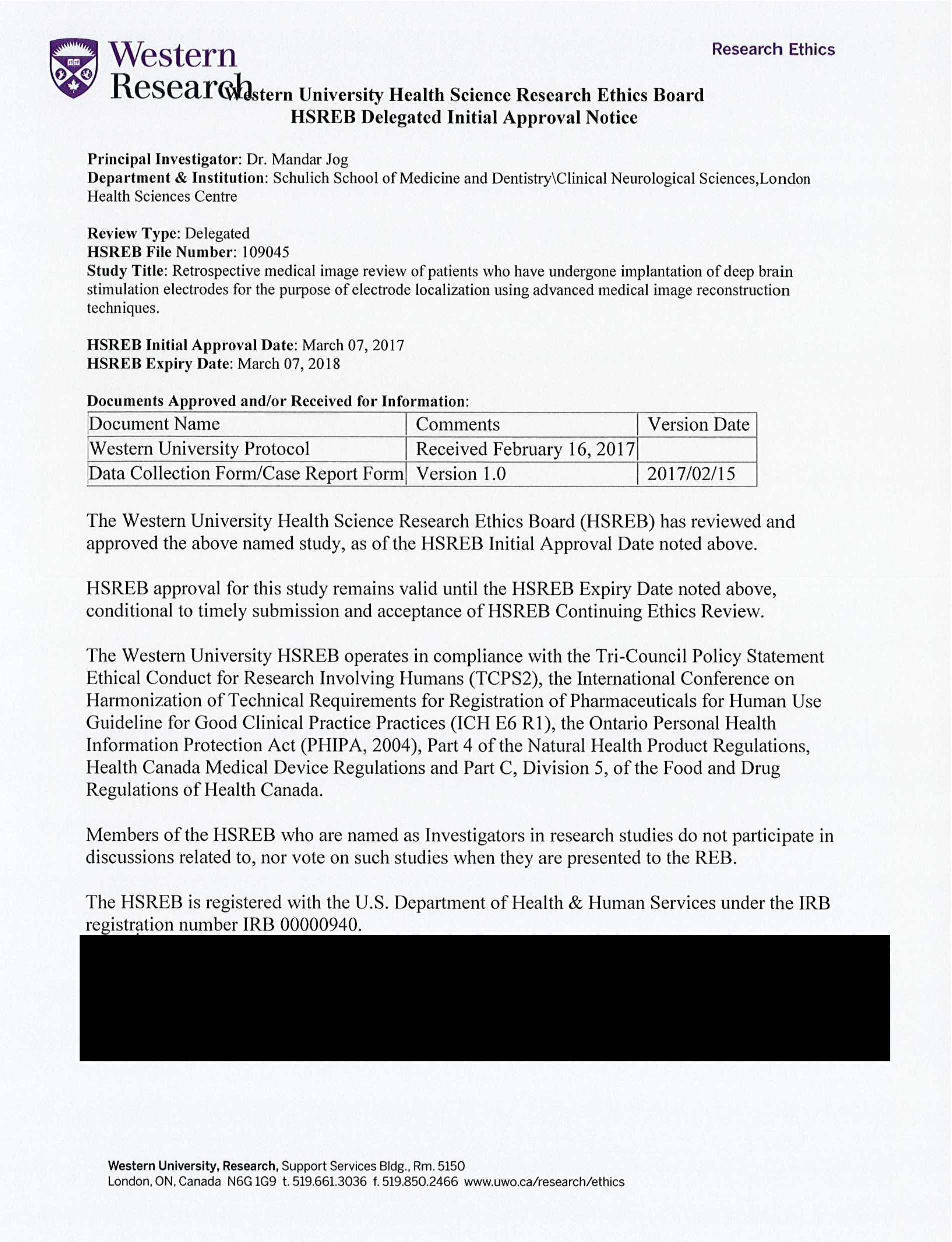

Western Research

Research Ethics

Western University Health Science Research Ethics Board
HSREB Delegated Initial Approval Notice

Principal Investigator: Dr. Mandar Jog
Department & Institution: Schulich School of Medicine and Dentistry\Clinical Neurological Sciences,London Health Sciences Centre

Review Type: Delegated
HSREB File Number: 109045
Study Title: Retrospective medical image review of patients who have undergone implantation of deep brain stimulation electrodes for the purpose of electrode localization using advanced medical image reconstruction techniques.

HSREB Initial Approval Date: March 07, 2017
HSREB Expiry Date: March 07, 2018

Documents Approved and/or Received for Information:

Document Name	Comments	Version Date
Western University Protocol	Received February 16, 2017	
Data Collection Form/Case Report Form	Version 1.0	2017/02/15

The Western University Health Science Research Ethics Board (HSREB) has reviewed and approved the above named study, as of the HSREB Initial Approval Date noted above.

HSREB approval for this study remains valid until the HSREB Expiry Date noted above, conditional to timely submission and acceptance of HSREB Continuing Ethics Review.

The Western University HSREB operates in compliance with the Tri-Council Policy Statement Ethical Conduct for Research Involving Humans (TCPS2), the International Conference on Harmonization of Technical Requirements for Registration of Pharmaceuticals for Human Use Guideline for Good Clinical Practice Practices (ICH E6 R1), the Ontario Personal Health Information Protection Act (PHIPA, 2004), Part 4 of the Natural Health Product Regulations, Health Canada Medical Device Regulations and Part C, Division 5, of the Food and Drug Regulations of Health Canada.

Members of the HSREB who are named as Investigators in research studies do not participate in discussions related to, nor vote on such studies when they are presented to the REB.

The HSREB is registered with the U.S. Department of Health & Human Services under the IRB registration number IRB 00000940.

[redacted]

Western University, Research, Support Services Bldg., Rm. 5150
London, ON, Canada N6G 1G9 t. 519.661.3036 f. 519.850.2466 www.uwo.ca/research/ethics

C.2 7T images for geometric distortion study.

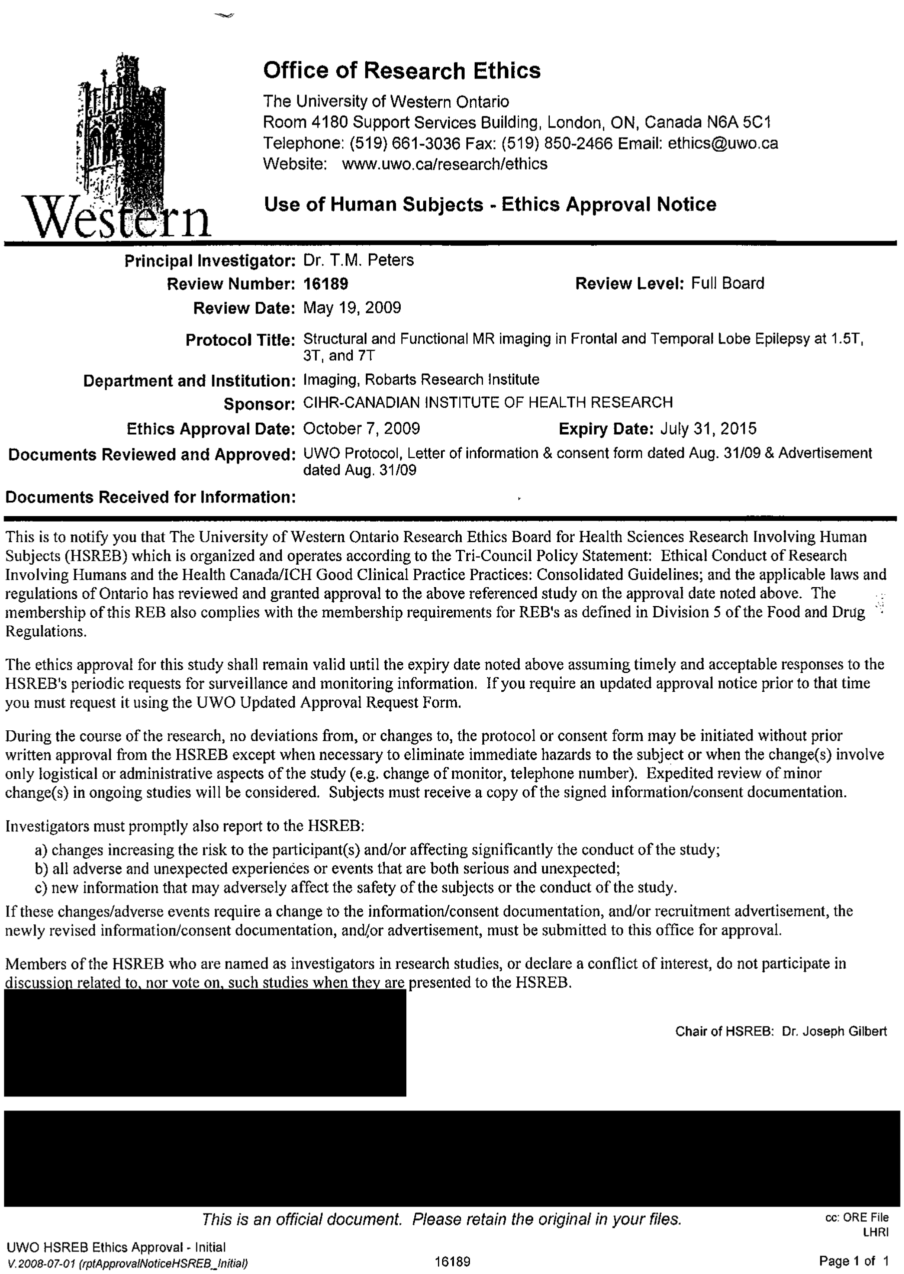

Western

Office of Research Ethics

The University of Western Ontario
Room 4180 Support Services Building, London, ON, Canada N6A 5C1
Telephone: (519) 661-3036 Fax: (519) 850-2466 Email: ethics@uwo.ca
Website: www.uwo.ca/research/ethics

Use of Human Subjects - Ethics Approval Notice

Principal Investigator: Dr. T.M. Peters
Review Number: **16189** **Review Level:** Full Board
Review Date: May 19, 2009
Protocol Title: Structural and Functional MR imaging in Frontal and Temporal Lobe Epilepsy at 1.5T, 3T, and 7T
Department and Institution: Imaging, Robarts Research Institute
Sponsor: CIHR-CANADIAN INSTITUTE OF HEALTH RESEARCH
Ethics Approval Date: October 7, 2009 **Expiry Date:** July 31, 2015
Documents Reviewed and Approved: UWO Protocol, Letter of information & consent form dated Aug. 31/09 & Advertisement dated Aug. 31/09
Documents Received for Information:

This is to notify you that The University of Western Ontario Research Ethics Board for Health Sciences Research Involving Human Subjects (HSREB) which is organized and operates according to the Tri-Council Policy Statement: Ethical Conduct of Research Involving Humans and the Health Canada/ICH Good Clinical Practice Practices: Consolidated Guidelines; and the applicable laws and regulations of Ontario has reviewed and granted approval to the above referenced study on the approval date noted above. The membership of this REB also complies with the membership requirements for REB's as defined in Division 5 of the Food and Drug Regulations.

The ethics approval for this study shall remain valid until the expiry date noted above assuming timely and acceptable responses to the HSREB's periodic requests for surveillance and monitoring information. If you require an updated approval notice prior to that time you must request it using the UWO Updated Approval Request Form.

During the course of the research, no deviations from, or changes to, the protocol or consent form may be initiated without prior written approval from the HSREB except when necessary to eliminate immediate hazards to the subject or when the change(s) involve only logistical or administrative aspects of the study (e.g. change of monitor, telephone number). Expedited review of minor change(s) in ongoing studies will be considered. Subjects must receive a copy of the signed information/consent documentation.

Investigators must promptly also report to the HSREB:

a) changes increasing the risk to the participant(s) and/or affecting significantly the conduct of the study;
b) all adverse and unexpected experiences or events that are both serious and unexpected;
c) new information that may adversely affect the safety of the subjects or the conduct of the study.

If these changes/adverse events require a change to the information/consent documentation, and/or recruitment advertisement, the newly revised information/consent documentation, and/or advertisement, must be submitted to this office for approval.

Members of the HSREB who are named as investigators in research studies, or declare a conflict of interest, do not participate in discussion related to, nor vote on, such studies when they are presented to the HSREB.

[redacted]

Chair of HSREB: Dr. Joseph Gilbert

[redacted]

This is an official document. Please retain the original in your files.

cc: ORE File
LHRI

UWO HSREB Ethics Approval - Initial
V.2008-07-01 (rptApprovalNoticeHSREB_Initial)
16189
Page 1 of 1

C.3 Prospective 7T stereotaxy study.

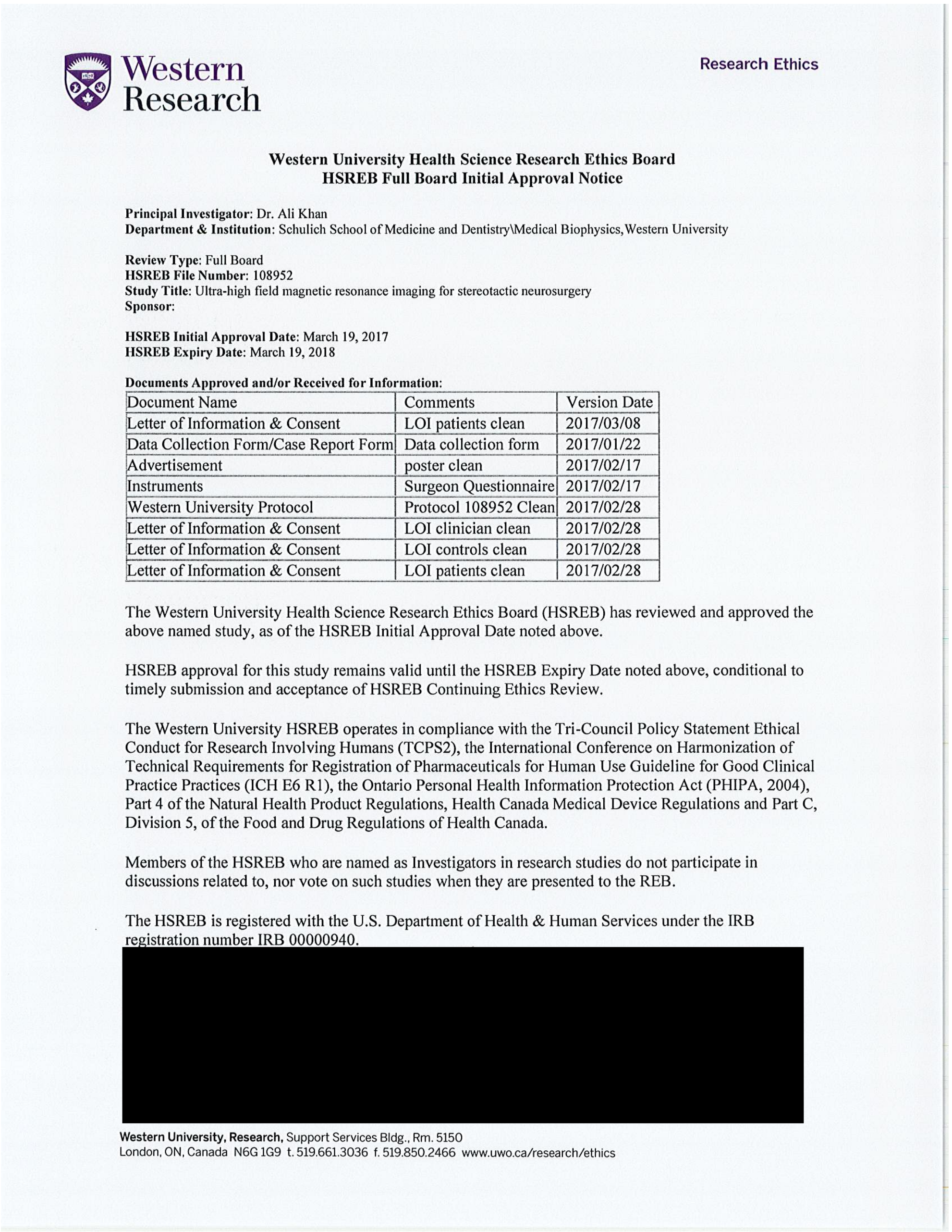

Western
Research

Research Ethics

Western University Health Science Research Ethics Board
HSREB Full Board Initial Approval Notice

Principal Investigator: Dr. Ali Khan
Department & Institution: Schulich School of Medicine and Dentistry\Medical Biophysics,Western University

Review Type: Full Board
HSREB File Number: 108952
Study Title: Ultra-high field magnetic resonance imaging for stereotactic neurosurgery
Sponsor:

HSREB Initial Approval Date: March 19, 2017
HSREB Expiry Date: March 19, 2018

Documents Approved and/or Received for Information:

Document Name	Comments	Version Date
Letter of Information & Consent	LOI patients clean	2017/03/08
Data Collection Form/Case Report Form	Data collection form	2017/01/22
Advertisement	poster clean	2017/02/17
Instruments	Surgeon Questionnaire	2017/02/17
Western University Protocol	Protocol 108952 Clean	2017/02/28
Letter of Information & Consent	LOI clinician clean	2017/02/28
Letter of Information & Consent	LOI controls clean	2017/02/28
Letter of Information & Consent	LOI patients clean	2017/02/28

The Western University Health Science Research Ethics Board (HSREB) has reviewed and approved the above named study, as of the HSREB Initial Approval Date noted above.

HSREB approval for this study remains valid until the HSREB Expiry Date noted above, conditional to timely submission and acceptance of HSREB Continuing Ethics Review.

The Western University HSREB operates in compliance with the Tri-Council Policy Statement Ethical Conduct for Research Involving Humans (TCPS2), the International Conference on Harmonization of Technical Requirements for Registration of Pharmaceuticals for Human Use Guideline for Good Clinical Practice Practices (ICH E6 R1), the Ontario Personal Health Information Protection Act (PHIPA, 2004), Part 4 of the Natural Health Product Regulations, Health Canada Medical Device Regulations and Part C, Division 5, of the Food and Drug Regulations of Health Canada.

Members of the HSREB who are named as Investigators in research studies do not participate in discussions related to, nor vote on such studies when they are presented to the REB.

The HSREB is registered with the U.S. Department of Health & Human Services under the IRB registration number IRB 00000940.

[redacted]

Western University, Research, Support Services Bldg., Rm. 5150
London, ON, Canada N6G 1G9 t. 519.661.3036 f. 519.850.2466 www.uwo.ca/research/ethics

Appendix D

Copyright Transfers and Reprint Permissions

Reprint permissions for the following accepted articles which I have primarily authored have been obtained:

- Chapter 2: Lau, J. C., MacDougall, K. W., Arango, M. F., Peters, T. M., Parrent, A. G., & Khan, A. R. (2017). Ultra-High Field Template-Assisted Target Selection for Deep Brain Stimulation Surgery. World Neurosurgery, 103, 531–537.
- Chapter 4: Lau, J. C., Khan, A. R., Zeng, T. Y., MacDougall, K. W., Parrent, A. G., & Peters, T. M. (2018). Quantification of local geometric distortion in structural magnetic resonance images: Application to ultra-high fields. NeuroImage, 168, 141–151.

Inquiries into copyright permission were made for figures in Chapter 1 for the following:

- [Rooney et al., 2007]: See the included Copyright Transfer note.
- [Gallay et al., 2008]: This article is Open Access.

All other material is under sole ownership by the author, including bioRxiv pre-prints, and articles currently under submission or revision.

D.1 Copyright for [Rooney et al., 2007]

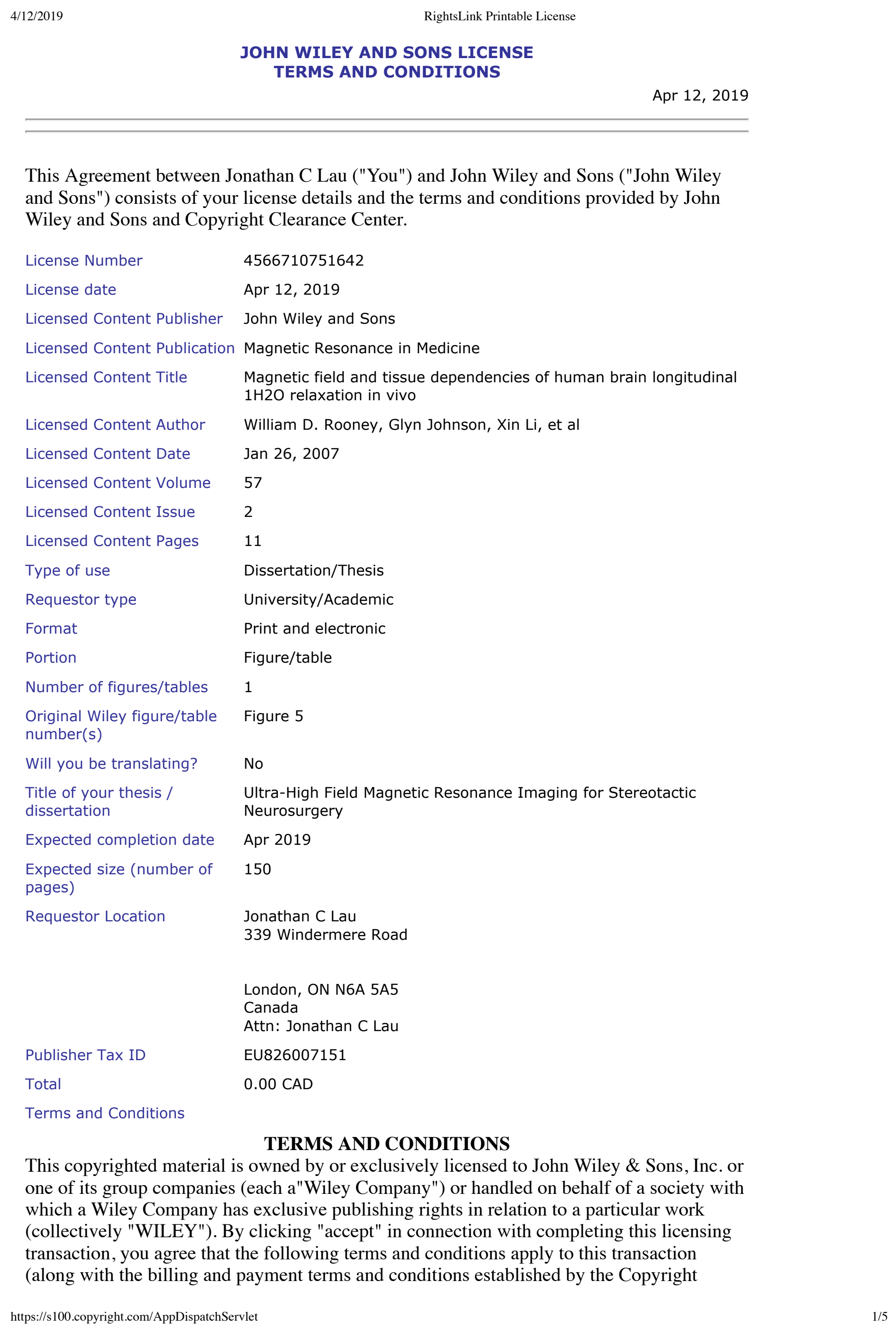

JOHN WILEY AND SONS LICENSE
TERMS AND CONDITIONS

Apr 12, 2019

This Agreement between Jonathan C Lau ("You") and John Wiley and Sons ("John Wiley and Sons") consists of your license details and the terms and conditions provided by John Wiley and Sons and Copyright Clearance Center.

License Number	4566710751642
License date	Apr 12, 2019
Licensed Content Publisher	John Wiley and Sons
Licensed Content Publication	Magnetic Resonance in Medicine
Licensed Content Title	Magnetic field and tissue dependencies of human brain longitudinal 1H2O relaxation in vivo
Licensed Content Author	William D. Rooney, Glyn Johnson, Xin Li, et al
Licensed Content Date	Jan 26, 2007
Licensed Content Volume	57
Licensed Content Issue	2
Licensed Content Pages	11
Type of use	Dissertation/Thesis
Requestor type	University/Academic
Format	Print and electronic
Portion	Figure/table
Number of figures/tables	1
Original Wiley figure/table number(s)	Figure 5
Will you be translating?	No
Title of your thesis / dissertation	Ultra-High Field Magnetic Resonance Imaging for Stereotactic Neurosurgery
Expected completion date	Apr 2019
Expected size (number of pages)	150
Requestor Location	Jonathan C Lau 339 Windermere Road London, ON N6A 5A5 Canada Attn: Jonathan C Lau
Publisher Tax ID	EU826007151
Total	0.00 CAD
Terms and Conditions	

TERMS AND CONDITIONS

This copyrighted material is owned by or exclusively licensed to John Wiley & Sons, Inc. or one of its group companies (each a"Wiley Company") or handled on behalf of a society with which a Wiley Company has exclusive publishing rights in relation to a particular work (collectively "WILEY"). By clicking "accept" in connection with completing this licensing transaction, you agree that the following terms and conditions apply to this transaction (along with the billing and payment terms and conditions established by the Copyright

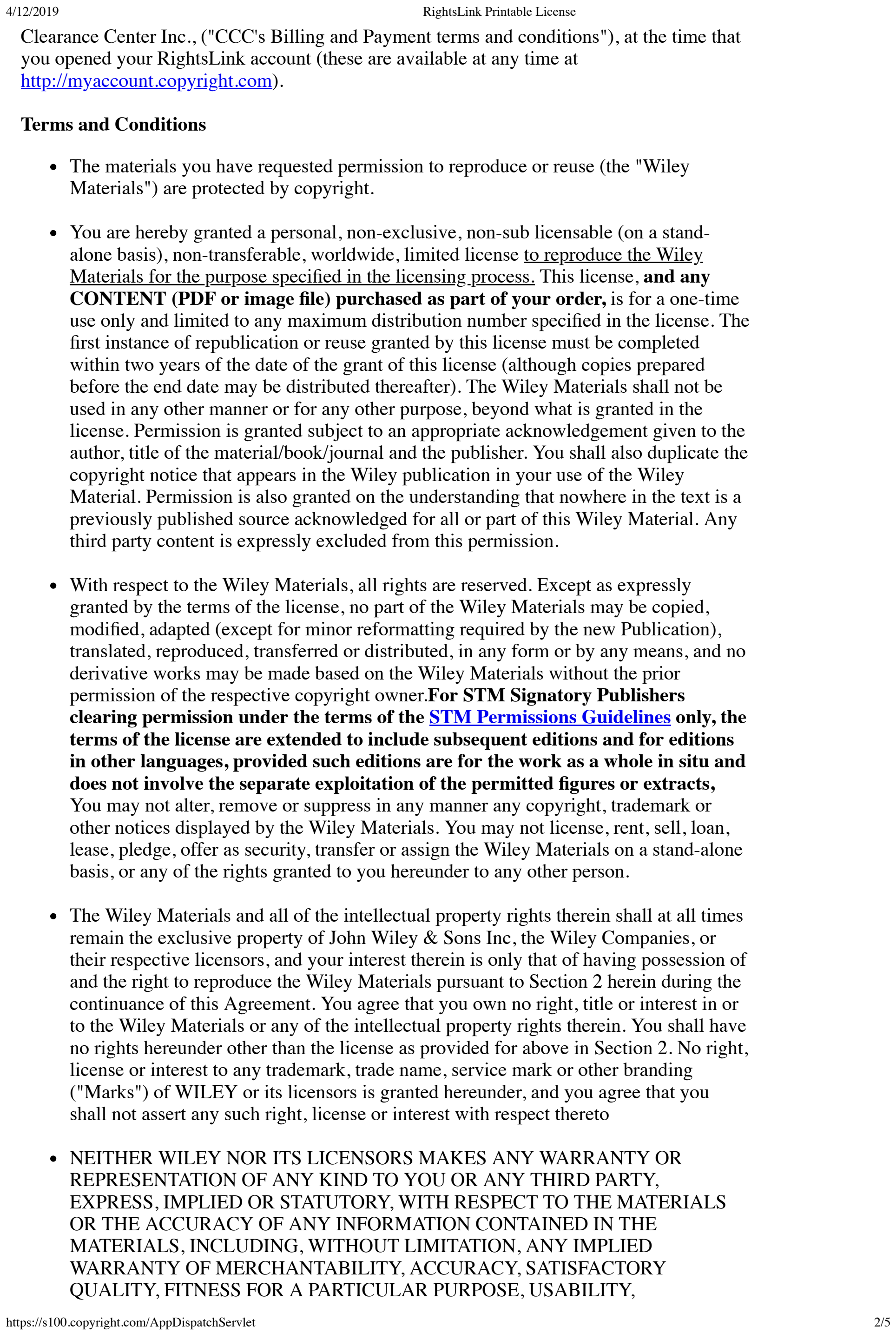

Clearance Center Inc., ("CCC's Billing and Payment terms and conditions"), at the time that you opened your RightsLink account (these are available at any time at http://myaccount.copyright.com).

Terms and Conditions

- The materials you have requested permission to reproduce or reuse (the "Wiley Materials") are protected by copyright.

- You are hereby granted a personal, non-exclusive, non-sub licensable (on a stand-alone basis), non-transferable, worldwide, limited license to reproduce the Wiley Materials for the purpose specified in the licensing process. This license, **and any CONTENT (PDF or image file) purchased as part of your order,** is for a one-time use only and limited to any maximum distribution number specified in the license. The first instance of republication or reuse granted by this license must be completed within two years of the date of the grant of this license (although copies prepared before the end date may be distributed thereafter). The Wiley Materials shall not be used in any other manner or for any other purpose, beyond what is granted in the license. Permission is granted subject to an appropriate acknowledgement given to the author, title of the material/book/journal and the publisher. You shall also duplicate the copyright notice that appears in the Wiley publication in your use of the Wiley Material. Permission is also granted on the understanding that nowhere in the text is a previously published source acknowledged for all or part of this Wiley Material. Any third party content is expressly excluded from this permission.

- With respect to the Wiley Materials, all rights are reserved. Except as expressly granted by the terms of the license, no part of the Wiley Materials may be copied, modified, adapted (except for minor reformatting required by the new Publication), translated, reproduced, transferred or distributed, in any form or by any means, and no derivative works may be made based on the Wiley Materials without the prior permission of the respective copyright owner.**For STM Signatory Publishers clearing permission under the terms of the STM Permissions Guidelines only, the terms of the license are extended to include subsequent editions and for editions in other languages, provided such editions are for the work as a whole in situ and does not involve the separate exploitation of the permitted figures or extracts,** You may not alter, remove or suppress in any manner any copyright, trademark or other notices displayed by the Wiley Materials. You may not license, rent, sell, loan, lease, pledge, offer as security, transfer or assign the Wiley Materials on a stand-alone basis, or any of the rights granted to you hereunder to any other person.

- The Wiley Materials and all of the intellectual property rights therein shall at all times remain the exclusive property of John Wiley & Sons Inc, the Wiley Companies, or their respective licensors, and your interest therein is only that of having possession of and the right to reproduce the Wiley Materials pursuant to Section 2 herein during the continuance of this Agreement. You agree that you own no right, title or interest in or to the Wiley Materials or any of the intellectual property rights therein. You shall have no rights hereunder other than the license as provided for above in Section 2. No right, license or interest to any trademark, trade name, service mark or other branding ("Marks") of WILEY or its licensors is granted hereunder, and you agree that you shall not assert any such right, license or interest with respect thereto

- NEITHER WILEY NOR ITS LICENSORS MAKES ANY WARRANTY OR REPRESENTATION OF ANY KIND TO YOU OR ANY THIRD PARTY, EXPRESS, IMPLIED OR STATUTORY, WITH RESPECT TO THE MATERIALS OR THE ACCURACY OF ANY INFORMATION CONTAINED IN THE MATERIALS, INCLUDING, WITHOUT LIMITATION, ANY IMPLIED WARRANTY OF MERCHANTABILITY, ACCURACY, SATISFACTORY QUALITY, FITNESS FOR A PARTICULAR PURPOSE, USABILITY,

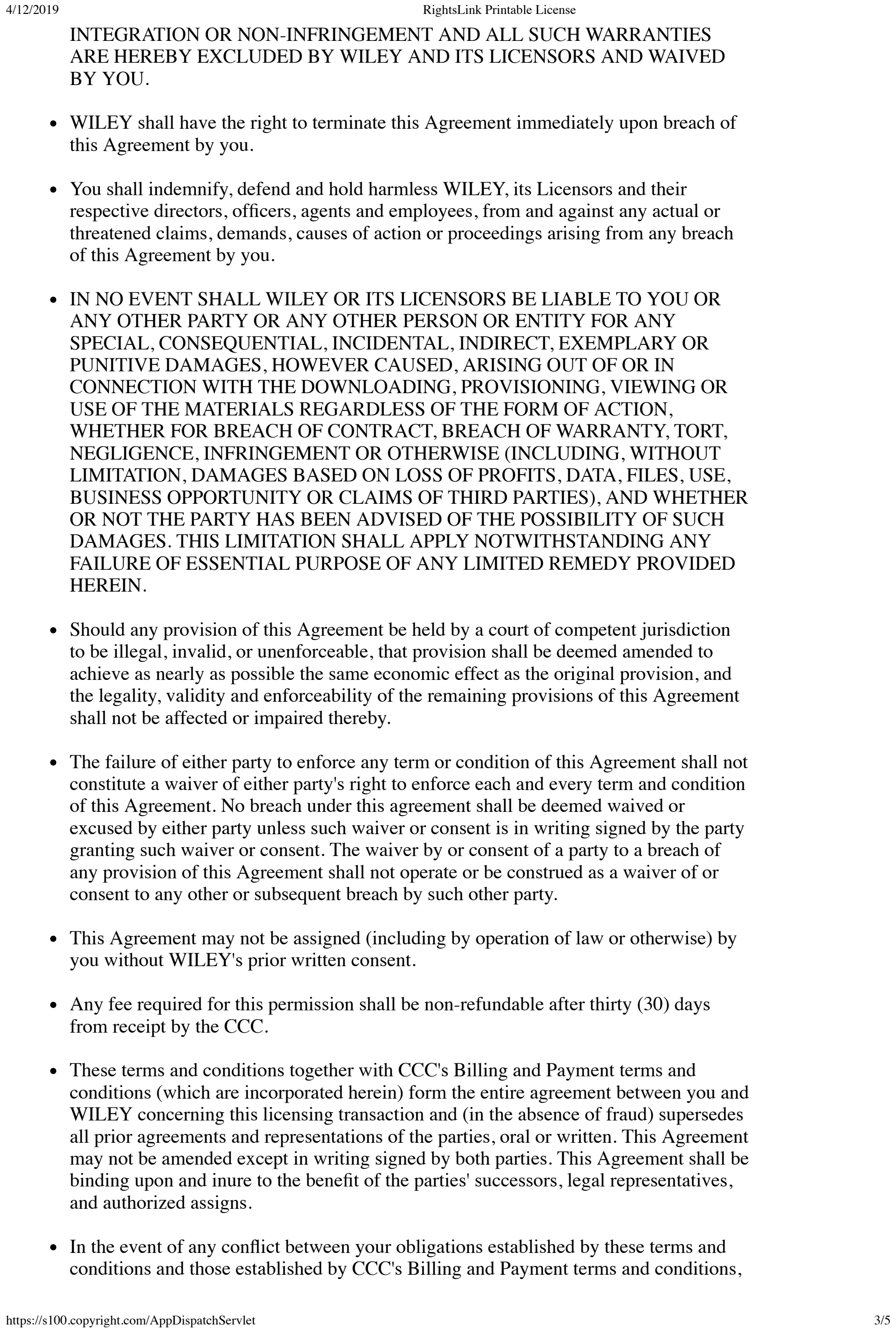

INTEGRATION OR NON-INFRINGEMENT AND ALL SUCH WARRANTIES ARE HEREBY EXCLUDED BY WILEY AND ITS LICENSORS AND WAIVED BY YOU.

- WILEY shall have the right to terminate this Agreement immediately upon breach of this Agreement by you.

- You shall indemnify, defend and hold harmless WILEY, its Licensors and their respective directors, officers, agents and employees, from and against any actual or threatened claims, demands, causes of action or proceedings arising from any breach of this Agreement by you.

- IN NO EVENT SHALL WILEY OR ITS LICENSORS BE LIABLE TO YOU OR ANY OTHER PARTY OR ANY OTHER PERSON OR ENTITY FOR ANY SPECIAL, CONSEQUENTIAL, INCIDENTAL, INDIRECT, EXEMPLARY OR PUNITIVE DAMAGES, HOWEVER CAUSED, ARISING OUT OF OR IN CONNECTION WITH THE DOWNLOADING, PROVISIONING, VIEWING OR USE OF THE MATERIALS REGARDLESS OF THE FORM OF ACTION, WHETHER FOR BREACH OF CONTRACT, BREACH OF WARRANTY, TORT, NEGLIGENCE, INFRINGEMENT OR OTHERWISE (INCLUDING, WITHOUT LIMITATION, DAMAGES BASED ON LOSS OF PROFITS, DATA, FILES, USE, BUSINESS OPPORTUNITY OR CLAIMS OF THIRD PARTIES), AND WHETHER OR NOT THE PARTY HAS BEEN ADVISED OF THE POSSIBILITY OF SUCH DAMAGES. THIS LIMITATION SHALL APPLY NOTWITHSTANDING ANY FAILURE OF ESSENTIAL PURPOSE OF ANY LIMITED REMEDY PROVIDED HEREIN.

- Should any provision of this Agreement be held by a court of competent jurisdiction to be illegal, invalid, or unenforceable, that provision shall be deemed amended to achieve as nearly as possible the same economic effect as the original provision, and the legality, validity and enforceability of the remaining provisions of this Agreement shall not be affected or impaired thereby.

- The failure of either party to enforce any term or condition of this Agreement shall not constitute a waiver of either party's right to enforce each and every term and condition of this Agreement. No breach under this agreement shall be deemed waived or excused by either party unless such waiver or consent is in writing signed by the party granting such waiver or consent. The waiver by or consent of a party to a breach of any provision of this Agreement shall not operate or be construed as a waiver of or consent to any other or subsequent breach by such other party.

- This Agreement may not be assigned (including by operation of law or otherwise) by you without WILEY's prior written consent.

- Any fee required for this permission shall be non-refundable after thirty (30) days from receipt by the CCC.

- These terms and conditions together with CCC's Billing and Payment terms and conditions (which are incorporated herein) form the entire agreement between you and WILEY concerning this licensing transaction and (in the absence of fraud) supersedes all prior agreements and representations of the parties, oral or written. This Agreement may not be amended except in writing signed by both parties. This Agreement shall be binding upon and inure to the benefit of the parties' successors, legal representatives, and authorized assigns.

- In the event of any conflict between your obligations established by these terms and conditions and those established by CCC's Billing and Payment terms and conditions,

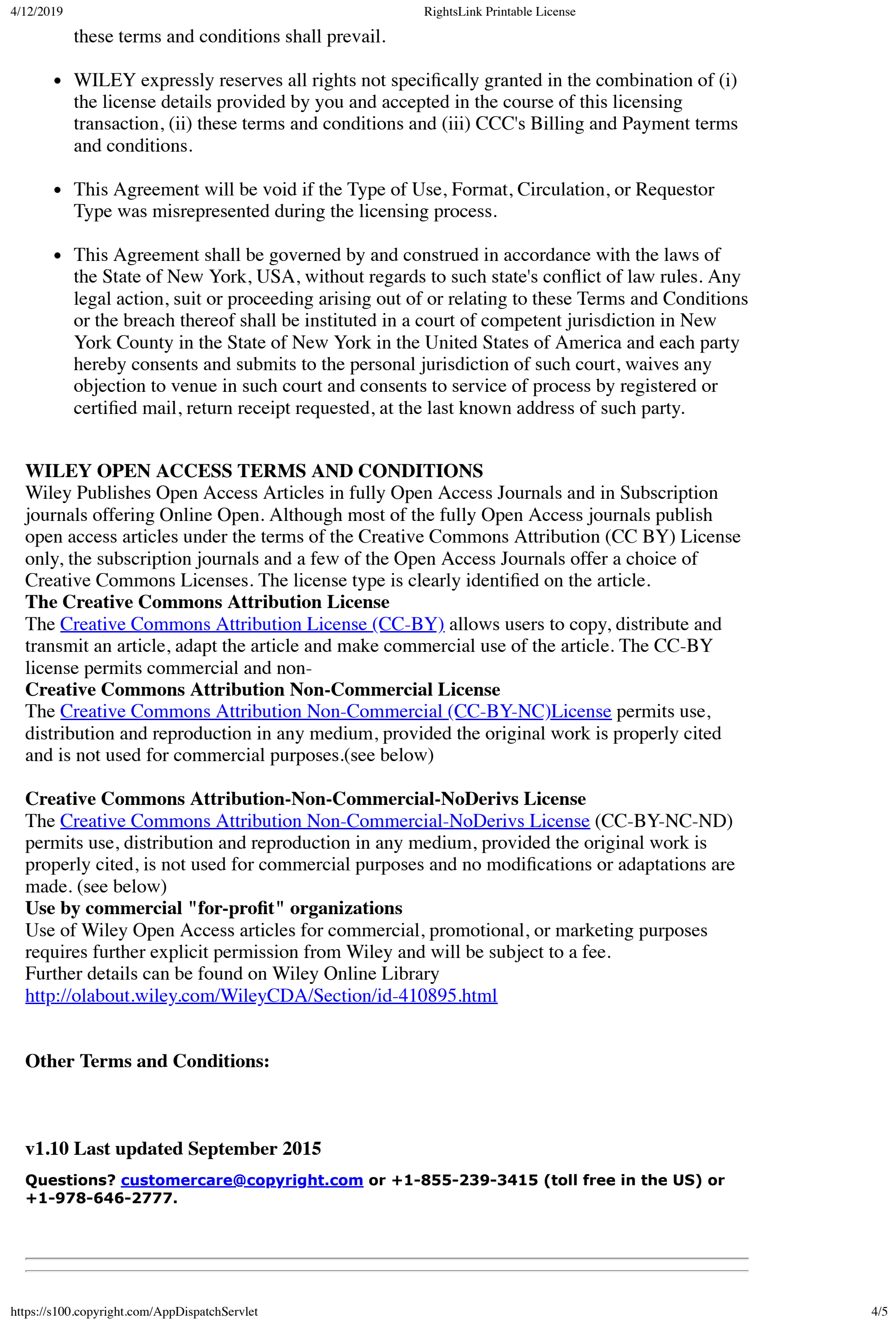

these terms and conditions shall prevail.

- WILEY expressly reserves all rights not specifically granted in the combination of (i) the license details provided by you and accepted in the course of this licensing transaction, (ii) these terms and conditions and (iii) CCC's Billing and Payment terms and conditions.

- This Agreement will be void if the Type of Use, Format, Circulation, or Requestor Type was misrepresented during the licensing process.

- This Agreement shall be governed by and construed in accordance with the laws of the State of New York, USA, without regards to such state's conflict of law rules. Any legal action, suit or proceeding arising out of or relating to these Terms and Conditions or the breach thereof shall be instituted in a court of competent jurisdiction in New York County in the State of New York in the United States of America and each party hereby consents and submits to the personal jurisdiction of such court, waives any objection to venue in such court and consents to service of process by registered or certified mail, return receipt requested, at the last known address of such party.

WILEY OPEN ACCESS TERMS AND CONDITIONS
Wiley Publishes Open Access Articles in fully Open Access Journals and in Subscription journals offering Online Open. Although most of the fully Open Access journals publish open access articles under the terms of the Creative Commons Attribution (CC BY) License only, the subscription journals and a few of the Open Access Journals offer a choice of Creative Commons Licenses. The license type is clearly identified on the article.

The Creative Commons Attribution License
The Creative Commons Attribution License (CC-BY) allows users to copy, distribute and transmit an article, adapt the article and make commercial use of the article. The CC-BY license permits commercial and non-

Creative Commons Attribution Non-Commercial License
The Creative Commons Attribution Non-Commercial (CC-BY-NC)License permits use, distribution and reproduction in any medium, provided the original work is properly cited and is not used for commercial purposes.(see below)

Creative Commons Attribution-Non-Commercial-NoDerivs License
The Creative Commons Attribution Non-Commercial-NoDerivs License (CC-BY-NC-ND) permits use, distribution and reproduction in any medium, provided the original work is properly cited, is not used for commercial purposes and no modifications or adaptations are made. (see below)

Use by commercial "for-profit" organizations
Use of Wiley Open Access articles for commercial, promotional, or marketing purposes requires further explicit permission from Wiley and will be subject to a fee.
Further details can be found on Wiley Online Library
http://olabout.wiley.com/WileyCDA/Section/id-410895.html

Other Terms and Conditions:

v1.10 Last updated September 2015

Questions? customercare@copyright.com or +1-855-239-3415 (toll free in the US) or +1-978-646-2777.

4/12/2019 RightsLink Printable License

https://s100.copyright.com/AppDispatchServlet 5/5

Bibliography

[Abosch et al., 2013] Abosch, A., Timmermann, L., Bartley, S., Rietkerk, H. G., Whiting, D., Connolly, P. J., Lanctin, D., and Hariz, M. I. (2013). An international survey of deep brain stimulation procedural steps. *Stereotactic and Functional Neurosurgery*, 91(1):1–11.

[Abosch et al., 2010] Abosch, A., Yacoub, E., Ugurbil, K., and Harel, N. (2010). An Assessment of Current Brain Targets for Deep Brain Stimulation Surgery With Susceptibility-Weighted Imaging at 7 Tesla. *Neurosurgery*, 67(6):1745–1756.

[Accolla et al., 2016] Accolla, E. A., Herrojo Ruiz, M., Horn, A., Schneider, G.-H., Schmitz-Hübsch, T., Draganski, B., and Kühn, A. A. (2016). Brain networks modulated by subthalamic nucleus deep brain stimulation. *Brain*, 139(9):2503–2515.

[Akram et al., 2018] Akram, H., Dayal, V., Mahlknecht, P., Georgiev, D., Hyam, J., Foltynie, T., Limousin, P., De Vita, E., Jahanshahi, M., Ashburner, J., Behrens, T., Hariz, M., and Zrinzo, L. (2018). Connectivity derived thalamic segmentation in deep brain stimulation for tremor. *NeuroImage: Clinical*, 18(December 2017):130–142.

[Akram et al., 2017] Akram, H., Sotiropoulos, S. N., Jbabdi, S., Georgiev, D., Mahlknecht, P., Hyam, J., Foltynie, T., Limousin, P., De Vita, E., Jahanshahi, M., Hariz, M., Ashburner, J., Behrens, T., and Zrinzo, L. (2017). Subthalamic deep brain stimulation sweet spots and hyperdirect cortical connectivity in Parkinson's disease. *NeuroImage*, 158(July):332–345.

[Amunts et al., 2014] Amunts, K., Hawrylycz, M. J., Van Essen, D. C., Van Horn, J. D., Harel, N., Poline, J. B., De Martino, F., Bjaalie, J. G., Dehaene-Lambertz, G., Dehaene, S., Valdes-Sosa, P., Thirion, B., Zilles, K., Hill, S. L., Abrams, M. B., Tass, P. a., Vanduffel, W., Evans, a. C., and Eickhoff, S. B. (2014). Interoperable atlases of the human brain. *NeuroImage*, 99:525–532.

[Amunts et al., 2013] Amunts, K., Lepage, C., Borgeat, L., Mohlberg, H., Dickscheid, T., Rousseau, M.-É., Bludau, S., Bazin, P.-L., Lewis, L. B., Oros-Peusquens, A.-M., Shah, N. J., Lippert, T., Zilles, K., and Evans, A. C. (2013). BigBrain: an ultrahigh-resolution 3D human brain model. *Science (New York, N.Y.)*, 340(6139):1472–5.

[Anderson et al., 2004] Anderson, T., Hu, B., Pittman, Q., and Kiss, Z. H. T. (2004). Mechanisms of deep brain stimulation: An intracellular study in rat thalamus. *Journal of Physiology*, 559(1):301–313.

[Andy et al., 1963] Andy, O. J., Jurko, M. F., and Sias, F. R. (1963). Subthalamotomy in Treatment of Parkinsonian Tremor. *Journal of Neurosurgery*, pages 860–870.

[Åström et al., 2010] Åström, M., Tripoliti, E., Hariz, M. I., Zrinzo, L. U., Martinez-Torres, I., Limousin, P., and Wårdell, K. (2010). Patient-specific model-based investigation of speech intelligibility and movement during deep brain stimulation. *Stereotactic and Functional Neurosurgery*, 88(4):224–233.

[Avants et al., 2008] Avants, B. B., Epstein, C. L., Grossman, M., and Gee, J. C. (2008). Symmetric diffeomorphic image registration with cross-correlation: Evaluating automated labeling of elderly and neurodegenerative brain. *Medical Image Analysis*, 12(1):26–41.

[Avants et al., 2011] Avants, B. B., Tustison, N. J., Song, G., Cook, P. A., Klein, A., and Gee, J. C. (2011). A reproducible evaluation of ANTs similarity metric performance in brain image registration. *NeuroImage*, 54(3):2033–2044.

[Bancaud et al., 1965] Bancaud, J., Talairach, J., and Bonis, A. (1965). *La stereo-electroencephalographie dans l'epilepsie.* Masson, Paris, France.

[Benabid et al., 1994] Benabid, A., Pollak, P., Gross, C., Hoffmann, D., Benazzouz, A., Gao, D., Laurent, A., Gentil, M., and Perret, J. (1994). Acute and Long-Term Effects of Subthalamic Nucleus Stimulation in Parkinson's Disease. *Stereotactic and Functional Neurosurgery*, 62(1-4):76–84.

[Benabid et al., 1991] Benabid, A., Pollak, P., Hoffmann, D., Gervason, C., Hommel, M., Perret, J., de Rougemont, J., and Gao, D. (1991). Long-term suppression of tremor by chronic stimulation of the ventral intermediate thalamic nucleus. *The Lancet*, 337(8738):403–406.

[Benabid et al., 1988] Benabid, A., Pollak, P., Louveau, A., Henry, S., and de Rougemont, J. (1988). Combined (Thalamotomy and Stimulation) Stereotactic Surgery of the VIM Thalamic Nucleus for Bilateral Parkinson Disease. *Stereotactic and Functional Neurosurgery*, 50(1-6):344–346.

[Benabid et al., 1996] Benabid, A. L., Pollak, P., Gao, D., Hoffmann, D., Limousin, P., Gay, E., Payen, I., and Benazzouz, A. (1996). Chronic electrical stimulation of the ventralis intermedius nucleus of the thalamus as a treatment of movement disorders. *Journal of Neurosurgery*, 84(2):203–214.

[Bergman et al., 1990] Bergman, H., Wichmann, T., and DeLong, M. (1990). Reversal of experimental parkinsonism by lesions of the subthalamic nucleus. *Science*, 249(4975):1436–1438.

[Bertrand et al., 1969] Bertrand, C., Hardy, J., Molina-Negro, P., and Martínez, N. (1969). Optimum physiological target for the arrest of tremor. In *Third Symposium on Parkinson's Disease*, pages 251–259. Livingstone, Edinburgh.

[Besl et al., 1992] Besl, P. P. J., Mckay, N. D., and McKay, H. (1992). A method for registration of 3-D shapes. *IEEE Transactions on Pattern Analysis and Machine Intelligence*, 14(2):239–256.

[Bjerknes et al., 2018] Bjerknes, S., Toft, M., Konglund, A. E., Pham, U., Waage, T. R., Pedersen, L., Skjelland, M., Haraldsen, I., Andersson, S., Dietrichs, E., and Skogseid, I. M. (2018). Multiple Microelectrode Recordings in STN-DBS Surgery for Parkinson's Disease: A Randomized Study. *Movement Disorders Clinical Practice*, 5(3):296–305.

[Bland and Altman, 1986] Bland, J. and Altman, D. (1986). Statistical methods for assessing agreement between two methods of clinical measurement. *Lancet*, 1(8476):307–310.

[Blasberg et al., 2018] Blasberg, F., Wojtecki, L., Elben, S., Slotty, P. J., Vesper, J., Schnitzler, A., and Groiss, S. J. (2018). Comparison of Awake vs. Asleep Surgery for Subthalamic Deep Brain Stimulation in Parkinson's Disease. *Neuromodulation*, 2018.

[Bloch, 1946] Bloch, F. (1946). Nuclear Induction. *Physical Review*, 70(7-8):460–474.

[Blomstedt et al., 2007] Blomstedt, P., Olivecrona, M., Sailer, A., and Hariz, M. I. (2007). Dittmar and the history of stereotaxy; or rats, rabbits, and references. *Neurosurgery*, 60(1):198–201.

[Blomstedt et al., 2010] Blomstedt, P., Sandvik, U., and Tisch, S. (2010). Deep brain stimulation in the posterior subthalamic area in the treatment of essential tremor. *Movement Disorders*, 25(10):1350–1356.

[Blomstedt et al., 2018] Blomstedt, P., Stenmark Persson, R., Hariz, G.-M., Linder, J., Fredricks, A., Häggström, B., Philipsson, J., Forsgren, L., and Hariz, M. (2018). Deep brain stimulation in the caudal zona incerta versus best medical treatment in patients with Parkinson's disease: a randomised blinded evaluation. *Journal of Neurology, Neurosurgery & Psychiatry*, pages jnnp–2017–317219.

[Bookstein, 1997] Bookstein, F. (1997). Landmark methods for forms without landmarks: morphometrics of group differences in outline shape. *Med Image Anal*, 1(3):225–243.

[Boyes et al., 2008] Boyes, R. G., Gunter, J. L., Frost, C., Janke, A. L., Yeatman, T., Hill, D. L. G., Bernstein, M. A., Thompson, P. M., Weiner, M. W., Schuff, N., Alexander, G. E., Killiany, R. J., DeCarli, C., Jack, C. R., and Fox, N. C. (2008). Intensity non-uniformity correction using N3 on 3-T scanners with multichannel phased array coils. *NeuroImage*, 39(4):1752–1762.

[Brett et al., 2002] Brett, M., Johnsrude, I. S., and Owen, A. M. (2002). The problem of functional localization in the human brain. *Nature reviews. Neuroscience*, 3(3):243–9.

[Brodsky et al., 2017] Brodsky, M. A., Anderson, S., Murchison, C., Seier, M., Wilhelm, J., Vederman, A., and Burchiel, K. J. (2017). Clinical outcomes of asleep vs awake deep brain stimulation for Parkinson disease. *Neurology*, page 10.1212/WNL.0000000000004630.

[Caramanos et al., 2010] Caramanos, Z., Fonov, V. S., Francis, S. J., Narayanan, S., Pike, G. B., Collins, D. L., and Arnold, D. L. (2010). Gradient distortions in MRI: Characterizing and correcting for their effects on SIENA-generated measures of brain volume change. *NeuroImage*, 49(2):1601–1611.

[Cardinale et al., 2013] Cardinale, F., Cossu, M., Castana, L., Casaceli, G., Schiariti, M. P., Miserocchi, A., Fuschillo, D., Moscato, A., Caborni, C., Arnulfo, G., and Lo Russo, G. (2013). Stereoelectroencephalography: Surgical methodology, safety, and stereotactic application accuracy in 500 procedures. *Neurosurgery*, 72(3):353–366.

[Castro et al., 2015] Castro, G., Carrillo-Ruiz, J. D., Salcido, V., Soto, J., García-Gomar, G., Velasco, A. L., and Velasco, F. (2015). Optimizing Prelemniscal Radiations as a Target for Motor Symptoms in Parkinson's Disease Treatment. *Stereotactic and Functional Neurosurgery*, 93(4):282–291.

[Chakravarty et al., 2009] Chakravarty, M. M., Broadbent, S., Rosa-Neto, P., Lambert, C. M., and Collins, D. L. (2009). Design, construction, and validation of an MRI-compatible vibrotactile stimulator intended for clinical use. *Journal of Neuroscience Methods*, 184(1):129–135.

[Chakravarty et al., 2008] Chakravarty, M. M., Sadikot, A. F., Germann, J., Bertrand, G., and Collins, D. L. (2008). Towards a validation of atlas warping techniques. *Medical Image Analysis*, 12(6):713–726.

[Chandran et al., 2016] Chandran, A. S., Bynevelt, M., and Lind, C. R. P. (2016). Magnetic resonance imaging of the subthalamic nucleus for deep brain stimulation. *Journal of Neurosurgery*, 124(January):96–105.

[Chen et al., 2016] Chen, T., Mirzadeh, Z., Chapple, K., Lambert, M., and Ponce, F. A. (2016). Complication rates, lengths of stay, and readmission rates in "awake" and "asleep" deep brain simulation. *Journal of Neurosurgery*, pages 1–10.

[Cheng et al., 2014] Cheng, C.-H., Huang, H.-M., Lin, H.-L., and Chiou, S.-M. (2014). 1.5T versus 3T MRI for targeting subthalamic nucleus for deep brain stimulation. *British Journal of Neurosurgery*, 28(4):467–470.

[Cho et al., 2010] Cho, Z.-H., Min, H.-K., Oh, S.-H., Han, J.-Y., Park, C.-W., Chi, J.-G., Kim, Y.-B., Paek, S. H., Lozano, A. M., and Lee, K. H. (2010). Direct visualization of deep brain stimulation targets in Parkinson disease with the use of 7-tesla magnetic resonance imaging. *Journal of Neurosurgery*, 113(3):639–647.

[Collins et al., 1994] Collins, D. L., Neelin, P., Peters, T. M., and Evans, A. C. (1994). Automatic 3D intersubject registration of MR volumetric data in standardized Talairach space. *Journal of computer assisted tomography*, 18(2):192–205.

[Cooper, 1960] Cooper, I. (1960). Results of 1,000 consecutive basal ganglia operations for Parkinsonism. *Annals of Internal Medicine*, 52(3):483.

[Cooper, 1953] Cooper, I. S. (1953). Ligation of the anterior choroidal artery for involuntary movements; parkinsonism. *The Psychiatric quarterly*, 27(2):317–9.

[Dale et al., 1999] Dale, A., Fischl, B., and Sereno, M. (1999). Cortical surface-based analysis. I. Segmentation and surface reconstruction. *Neuroimage*, 9(2):179–194.

[Dallapiazza et al., 2018] Dallapiazza, R. F., Lee, D. J., De Vloo, P., Fomenko, A., Hamani, C., Hodaie, M., Kalia, S. K., Fasano, A., and Lozano, A. M. (2018). Outcomes from stereotactic surgery for essential tremor. *Journal of Neurology, Neurosurgery & Psychiatry*, pages jnnp–2018–318240.

[Dammann et al., 2011] Dammann, P., Kraff, O., Wrede, K. H., Ozkan, N., Orzada, S., Mueller, O. M., Sandalcioglu, I. E., Sure, U., Gizewski, E. R., Ladd, M. E., and Gasser, T. (2011). Evaluation of Hardware-related Geometrical Distortion in Structural MRI at 7 Tesla for Image-guided Applications in Neurosurgery. *Academic Radiology*, 18(7):910–916.

[Dandy, 1918] Dandy, W. E. (1918). Ventriculography following the injection of air into the cerebral ventricles. *Annals of surgery*, 68(1):5–11.

[Dandy, 1946] Dandy, W. E. (1946). The location of the conscious center in the brain; the corpus striatum. *Bulletin of the Johns Hopkins Hospital*, 79:34–58.

[Delong and Wichmann, 2012] Delong, M. and Wichmann, T. (2012). Deep brain stimulation for movement and other neurologic disorders. *Annals of the New York Academy of Sciences*, 1265(1):1–8.

[DeLong, 1990] DeLong, M. R. (1990). Primate models of movement disorders of basal ganglia origin. *Trends in Neurosciences*, 13(7):281–285.

[Deoni et al., 2007] Deoni, S., Rutt, B., Parrent, A., and Peters, T. (2007). Segmentation of thalamic nuclei using a modified k-means clustering algorithm and high-resolution quantitative magnetic resonance imaging at 1.5 T. *NeuroImage*, 34(1):117–126.

[Deoni et al., 2008] Deoni, S. C., Williams, S. C., Jezzard, P., Suckling, J., Murphy, D. G., and Jones, D. K. (2008). Standardized structural magnetic resonance imaging in multicentre studies using quantitative T1 and T2 imaging at 1.5 T. *NeuroImage*, 40(2):662–671.

[Deoni et al., 2005] Deoni, S. C. L., Peters, T. M., and Rutt, B. K. (2005). High-resolution T1 and T2 mapping of the brain in a clinically acceptable time with DESPOT1 and DESPOT2. *Magnetic Resonance in Medicine*, 53(1):237–241.

[Deoni et al., 2003] Deoni, S. C. L., Rutt, B. K., and Peters, T. M. (2003). Rapid combined T1 and T2 mapping using gradient recalled acquisition in the steady state. *Magnetic Resonance in Medicine*, 49(3):515–526.

[Deuschl et al., 2006] Deuschl, G., Schade-Brittinger, C., Krack, P., Volkmann, J., Schäfer, H., Bötzel, K., Daniels, C., Deutschländer, A., Dillmann, U., Eisner, W., Gruber, D., Hamel, W., Herzog, J., Hilker, R., Klebe, S., Kloß, M., Koy, J., Krause, M., Kupsch, A., Lorenz, D., Lorenzl, S., Mehdorn, H. M., Moringlane, J. R., Oertel, W., Pinsker, M. O., Reichmann, H., Reuß, A., Schneider, G.-H., Schnitzler, A., Steude, U., Sturm, V., Timmermann, L., Tronnier, V., Trottenberg, T., Wojtecki, L., Wolf, E., Poewe, W., Voges, J., and German Parkinson Study Group, N. S. (2006). A Randomized Trial of Deep-Brain Stimulation for Parkinson's Disease. *New England Journal of Medicine*, 355(9):896–908.

[Doby, 1992] Doby, T. (1992). Cerebral angiography and Egas Moniz. *American Journal of Roentgenology*, 159(2):364–364.

[Duchin et al., 2012] Duchin, Y., Abosch, A., Yacoub, E., Sapiro, G., and Harel, N. (2012). Feasibility of using ultra-high field (7 T) MRI for clinical surgical targeting. *PloS one*, 7(5):e37328.

[Eggenschwiler et al., 2012] Eggenschwiler, F., Kober, T., Magill, A. W., Gruetter, R., and Marques, J. P. (2012). SA2RAGE: A new sequence for fast B1 +-mapping. *Magnetic Resonance in Medicine*, 67(6):1609–1619.

[Eickhoff et al., 2009] Eickhoff, S. B., Laird, A. R., Grefkes, C., Wang, L. E., Zilles, K., and Fox, P. T. (2009). Coordinate-based activation likelihood estimation meta-analysis of neuroimaging data: A random-effects approach based on empirical estimates of spatial uncertainty. *Human Brain Mapping*, 30(9):2907–2926.

[Ernst and Anderson, 1966] Ernst, R. R. and Anderson, W. A. (1966). Application of fourier transform spectroscopy to magnetic resonance. *Review of Scientific Instruments*, 37(1):93–102.

[Ernst et al., 1987] Ernst, R. R., Bodenhausen, G., and Wokaun, A. (1987). *Principles of Nuclear Magnetic Resonance in One and Two Dimensions*. Clarendon Press, Oxford.

[Esteban et al., 2018] Esteban, O., Markiewicz, C. J., Blair, R. W., Moodie, C. A., Ayse, I., Erramuzpe, A., Kent, J. D., Goncalves, M., Dupre, E., Snyder, M., Oya, H., Ghosh, S. S., Wright, J., Durnez, J., Poldrack, R. A., and Gorgolewski, K. J. (2018). FMRIPrep : a robust preprocessing pipeline for functional MRI. 5:1–20.

[Evans et al., 1992] Evans, A., Marrett, S., Neelin, P., Collins, L., Worsley, K., Dai, W., Milot, S., Meyer, E., and Bub, D. (1992). Anatomical mapping of functional activation in stereotactic coordinate space. *Neuroimage*, 1(1):43–53.

[Evans et al., 2012] Evans, A. C., Janke, A. L., Collins, D. L., and Baillet, S. (2012). Brain templates and atlases. *NeuroImage*, 62(2):911–922.

[Ewert et al., 2019] Ewert, S., Horn, A., Finkel, F., Li, N., Kühn, A. A., and Herrington, T. M. (2019). Optimization and comparative evaluation of nonlinear deformation algorithms for atlas-based segmentation of DBS target nuclei. *NeuroImage*, 184(August 2018):586–598.

[Fedorov et al., 2012] Fedorov, A., Beichel, R., Kalpathy-Cramer, J., Finet, J., Fillion-Robin, J. C., Pujol, S., Bauer, C., Jennings, D., Fennessy, F., Sonka, M., Buatti, J., Aylward, S., Miller, J. V., Pieper, S., and Kikinis, R. (2012). 3D Slicer as an image computing platform for the Quantitative Imaging Network. *Magnetic Resonance Imaging*, 30(9):1323–1341.

[Feigin et al., 2017] Feigin, V. L., Abajobir, A. A., Abate, K. H., Abd-Allah, F., Abdulle, A. M., Abera, S. F., Abyu, G. Y., Ahmed, M. B., Aichour, A. N., Aichour, I., Aichour, M. T. E., Akinyemi, R. O., Alabed, S., Al-Raddadi, R., Alvis-Guzman, N., Amare, A. T., Ansari, H., Anwari, P., Ärnlöv, J., Asayesh, H., Asgedom, S. W., Atey, T. M., Avila-Burgos, L., Frinel, E., Avokpaho, G. A., Barac, A., Barboza, M., Barker-Collo, S. L., Bärnighausen, T., Bedi, N., Beghi, E., Bennett, D. A., Bensenor, I. M., Berhane, A., Betsu, B. D., Bhaumik, S., Birlik, S. M., Biryukov, S., Boneya, D. J., Bulto, L. N. B., Carabin, H., Casey, D., Castañeda-Orjuela, C. A., Catalá-López, F., Chen, H., Chitheer, A. A., Chowdhury, R., Christensen, H., Dandona, L., Dandona, R., de Veber, G. A., Dharmaratne, S. D., Do, H. P., Dokova, K., Dorsey, E. R., Ellenbogen, R. G., Eskandarieh, S., Farvid, M. S., Fereshtehnejad, S.-M., Fischer, F., Foreman, K. J., Geleijnse, J. M., Gillum, R. F., Giussani, G., Gona, P. N., Goulart, A. C., Gugnani, H. C., Gupta, R., Gupta, R., Hamadeh, R. R., Hambisa, M., Hankey, G. J., Hareri, H. A., Havmoeller, R., Hay, S. I., Heydarpour, P., Hotez, P. J., Jakovljevic, M. M. B., Javanbakht, M., Jeemon, P., Jonas, J. B., Kalkonde, Y., Kandel, A., Karch, A., Kasaeian, A., Kastor, A., Keiyoro, P. N., Khader, Y. S., Khalil, I. A., Khan, E. A., Khang, Y.-H., Tawfih, A., Khoja, A., Khubchandani, J., Kim, D., Kim, Y. J., Kivimaki, M., Kokubo, Y., Kosen, S., Kravchenko, M., Krishnamurthi, R. V., Defo, B. K., Kumar, G. A., Kumar, R., Kyu, H. H., Larsson, A., Lavados, P. M., Li, Y., Liang, X., Liben, M. L., Lo, W. D., Logroscino, G., Lotufo, P. A., Loy, C. T., Mackay, M. T., El Razek, H. M. A., El Razek, M. M. A., Majeed, A., Malekzadeh, R., Manhertz, T., Mantovani, L. G., Massano, J., Mazidi, M., McAlinden, C., Mehata, S., Mehndiratta, M. M., Memish, Z. A., Mendoza, W., Mengistie, M. A., Mensah, G. A., Meretoja, A., Mezgebe, H. B., Miller, T. R., Mishra, S. R., Ibrahim, N. M., Mohammadi, A., Mohammed, K. E., Mohammed, S., Mokdad, A. H., Moradi-Lakeh, M., Velasquez, I. M., Musa, K. I., Naghavi, M., Ngunjiri, J. W., Nguyen, C. T., Nguyen, G., Le Nguyen, Q., Nguyen, T. H., Nichols, E., Ningrum, D. N. A., Nong, V. M., Norrving, B., Noubiap, J. J. N., Ogbo, F. A., Owolabi, M. O., Pandian, J. D., Petzold, M., Phillips, M. R., Piradov, M. A., Poulton, R. G., Pourmalek, F., Qorbani, M., Rafay, A., Rahman, M., Rahman, M. H., Rai, R. K., Rajsic, S., Ranta, A., Rawaf, S., Renzaho, A. M., Rezai, M. S., Roshandel, G., Rubagotti, E., Sachdev, P., Safiri, S., Sahathevan, R., Sahraian, M. A., Samy, A. M., Santalucia, P., Santos, I. S., Sartorius, B., Satpathy, M., Sawhney, M., Saylan, M. I., Sepanlou, S. G., Shaikh, M. A., Shakir, R., Shamsizadeh, M., Sheth, K. N., Shigematsu, M., Shoman, H., Silva, D. A. S., Smith, M., Sobngwi, E., Sposato, L. A., Stein, D. J., Steiner, T. J., Stovner, L. J., Abdulkader, R. S., EI Szoeke, C., Tabarés-Seisdedos, R., Tanne, D., Theadom, A. M., Thrift, A. G., Tirschwell, D. L., Topor-Madry, R., Tran, B. X., Truelsen, T., Tuem, K. B., Ukwaja, K. N., Uthman, O. A., Varakin, Y. Y., Vasankari, T., Venketasubramanian, N., Vlassov, V. V., Wadilo, F., Wakayo, T., Wallin, M. T., Weiderpass, E., Westerman, R., Wijeratne, T., Wiysonge, C. S., Woldu, M. A., Wolfe, C. D. A., Xavier, D., Xu, G., Yano, Y., Yimam, H. H., Yonemoto, N., Yu, C., Zaidi, Z., El Sayed Zaki, M., Zunt, J. R., Murray, C. J. L., and Vos, T. (2017). Global, regional, and national burden of neurological disorders during 1990–2015: a systematic analysis for the Global Burden of Disease Study 2015. *The Lancet Neurology*.

[Fiechter et al., 2017] Fiechter, M., Nowacki, A., Oertel, M. F., Fichtner, J., Debove, I., Lachenmayer, M. L., Wiest, R., Bassetti, C. L., Raabe, A., Kaelin-Lang, A., Schüpbach, M. W., and Pollo, C. (2017). Deep Brain Stimulation for Tremor: Is There a Common Structure? *Stereotactic and Functional Neurosurgery*, 95(4):243–250.

[Fischl, 2004] Fischl, B. (2004). Automatically Parcellating the Human Cerebral Cortex. *Cerebral Cortex*, 14(1):11–22.

[Fischl, 2012] Fischl, B. (2012). FreeSurfer. *NeuroImage*, 62(2):774–781.

[Fitzpatrick and West, 2001] Fitzpatrick, J. M. and West, J. B. (2001). The distribution of target registration error in rigid-body point-based registration. *IEEE Transactions on Medical Imaging*, 20(9):917–927.

[Fitzpatrick et al., 1998] Fitzpatrick, J. M., West, J. B., and Maurer, C. R. (1998). Predicting error in rigid-body point-based registration. *IEEE transactions on medical imaging*, 17(5):694–702.

[Florence et al., 2016] Florence, G., Sameshima, K., Fonoff, E. T., and Hamani, C. (2016). Deep Brain Stimulation: More Complex than the Inhibition of Cells and Excitation of Fibers. *Neuroscientist*, 22(4):332–345.

[Fonov et al., 2009] Fonov, V., Evans, A., McKinstry, R., Almli, C., and Collins, D. (2009). Unbiased nonlinear average age-appropriate brain templates from birth to adulthood. *NeuroImage*, 47:S102–S102.

[Fonov et al., 2011] Fonov, V., Evans, A. C., Botteron, K., Almli, R. R., McKinstry, R. C., Collins, L. L., and Group", B. D. C. (2011). Unbiased average age-appropriate atlases for pediatric studies. *NeuroImage*, 54(1):313–327.

[Fonov et al., 2010] Fonov, V. S., Janke, A., Caramanos, Z., Arnold, D. L., Narayanan, S., Pike, G. B., and Collins, D. L. (2010). Improved precision in the measurement of longitudinal global and regional volumetric changes via a novel MRI gradient distortion characterization and correction technique. *Lecture Notes in Computer Science*, 6326 LNCS:324–333.

[Forel, 1877] Forel, A. (1877). Untersuchungen über die Haubenregion und ihre oberen Verknüpfungen im Gehirne des Menschen und einiger Säugethiere, mit Beiträgen zu den Methoden der Gehirnuntersuchung. *Archiv für Psychiatrie und Nervenkrankheiten*, 7(3):393–495.

[Forstmann et al., 2014] Forstmann, B. U., Keuken, M. C., Schafer, A., Bazin, P.-l., Alkemade, A., and Turner, R. (2014). Multi-modal ultra-high resolution structural 7-Tesla MRI data repository. *Scientific Data*, 1:140050.

[Fox et al., 2014] Fox, M. D., Buckner, R. L., Liu, H., Chakravarty, M. M., Lozano, A. M., and Pascual-Leone, A. (2014). Resting-state networks link invasive and noninvasive brain stimulation across diverse psychiatric and neurological diseases. *Proceedings of the National Academy of Sciences of the United States of America*, 111(41):E4367–75.

[Gallay et al., 2008] Gallay, M. N., Jeanmonod, D., Liu, J., and Morel, A. (2008). Human pallidothalamic and cerebellothalamic tracts: Anatomical basis for functional stereotactic neurosurgery. *Brain Structure and Function*, 212(6):443–463.

[Geevarghese et al., 2016] Geevarghese, R., Tuura, O. G. R., Lumsden, D. E., Samuel, M., Ashkan, K., Ogorman Tuura, R., Lumsden, D. E., Samuel, M., and Ashkan, K. (2016).

Registration Accuracy of CT/MRI Fusion for Localisation of Deep Brain Stimulation Electrode Position: An Imaging Study and Systematic Review. *Stereotactic and Functional Neurosurgery*, 94(3):159–163.

[Genovese et al., 2002] Genovese, C. R., Lazar, N. A., and Nichols, T. (2002). Thresholding of Statistical Maps in Functional Neuroimaging Using the False Discovery Rate. *NeuroImage*, 15(4):870–878.

[Giacino et al., 2014] Giacino, J. T., Fins, J. J., Laureys, S., and Schiff, N. D. (2014). Disorders of consciousness after acquired brain injury: the state of the science. *Nature reviews. Neurology*, 10(2):99–114.

[Gilbert et al., 2011] Gilbert, K. M., Curtis, A. T., Gati, J. S., Klassen, L. M., and Menon, R. S. (2011). A radiofrequency coil to facilitate B 1 + shimming and parallel imaging acceleration in three dimensions at 7 T. *NMR in Biomedicine*, 24(7):815–823.

[Gildenberg and Krauss, 2009] Gildenberg, P. and Krauss, J. (2009). History of Stereotactic Surgery. In Gildenberg, P., Lozano, A., and Tasker, R., editors, *Textbook of Stereotactic and Functional Neurosurgery*, chapter 1. Springer-Verlag, Berlin, 2nd edition.

[Glasser et al., 2013] Glasser, M. F., Sotiropoulos, S. N., Wilson, J. A., Coalson, T. S., Fischl, B., Andersson, J. L., Xu, J., Jbabdi, S., Webster, M., Polimeni, J. R., Van Essen, D. C., and Jenkinson, M. (2013). The minimal preprocessing pipelines for the Human Connectome Project. *NeuroImage*, 80:105–124.

[Gorgolewski et al., 2017] Gorgolewski, K. J., Alfaro-almagro, F., Auer, T., Bellec, P., Capotă, M., Chakravarty, M. M., Churchill, N. W., Cohen, A. L., Craddock, R. C., Devenyi, G. A., Eklund, A., Esteban, O., Flandin, G., Ghosh, S. S., Guntupalli, J. S., Jenkinson, M., Keshavan, A., Kiar, G., Liem, F., Raamana, P. R., Raffelt, D., Steele, C. J., Quirion, P.-O., Smith, R. E., Strother, S. C., Varoquaux, G., Wang, Y., Yarkoni, T., Poldrack, R. A., Capot, M., Chakravarty, M. M., Churchill, N. W., Cohen, A. L., Craddock, C., Devenyi, G. A., Eklund, A., Esteban, O., Keshavan, A., Kiar, G., Liem, F., Raamana, P. R., Raffelt, D., Steele, C. J., Quirion, P.-O., Smith, R. E., Wang, Y., and Yarkoni, T. (2017). BIDS apps: Improving ease of use, accessibility, and reproducibility of neuroimaging data analysis methods. *PLoS computational biology*, 13(3):e1005209.

[Gorgolewski et al., 2016] Gorgolewski, K. J., Auer, T., Calhoun, V. D., Craddock, R. C., and Das, S. (2016). The brain imaging data structure , a format for organizing and describing outputs of neuroimaging experiments. pages 1–9.

[Gorgolewski and Poldrack, 2016] Gorgolewski, K. J. and Poldrack, R. a. (2016). A practical guide for improving transparency and reproducibility in neuroimaging research. pages 1–13.

[Gorgolewski et al., 2015] Gorgolewski, K. J., Varoquaux, G., Rivera, G., Schwarz, Y., Ghosh, S. S., Maumet, C., Sochat, V. V., Nichols, T. E., Poldrack, R. A., Poline, J.-B., Yarkoni, T., and Margulies, D. S. (2015). NeuroVault.org: a web-based repository for collecting and sharing unthresholded statistical maps of the human brain. *Frontiers in Neuroinformatics*, 9(April):1–9.

[Gradinaru et al., 2010] Gradinaru, V., Zhang, F., Ramakrishnan, C., Mattis, J., Prakash, R., Diester, I., Goshen, I., Thompson, K. R., and Deisseroth, K. (2010). Molecular and Cellular Approaches for Diversifying and Extending Optogenetics. *Cell*, 141(1):154–165.

[Gross et al., 2018] Gross, R. E., Stern, M. A., Willie, J. T., Fasano, R. E., Saindane, A. M., Soares, B. P., Pedersen, N. P., and Drane, D. L. (2018). Stereotactic Laser Amygdalohippocampotomy for Mesial Temporal Lobe Epilepsy. *Annals of Neurology*.

[Grunert et al., 2003] Grunert, P., Darabi, K., Espinosa, J., and Filippi, R. (2003). Computer-aided navigation in neurosurgery. *Neurosurgical Review*, 26(2):73–99.

[Guiot and Brion, 1953] Guiot, G. and Brion, S. (1953). Traitement des mouvements anormaux par la coagulation pallidale. Technique et resultats. *Rev Neurol*, (89):578–580.

[Haacke et al., 2005] Haacke, E. M., Cheng, N. Y., House, M. J., Liu, Q., Neelavalli, J., Ogg, R. J., Khan, A., Ayaz, M., Kirsch, W., and Obenaus, A. (2005). Imaging iron stores in the brain using magnetic resonance imaging. *Magnetic Resonance Imaging*, 23(1):1–25.

[Hacker et al., 2016] Hacker, M. L., Currie, A. D., Molinari, A. L., Turchan, M., Millan, S. M., Heusinkveld, L. E., Roach, J., Konrad, P. E., Davis, T. L., Neimat, J. S., Phibbs, F. T., Hedera, P., Byrne, D. W., and Charles, D. (2016). Subthalamic Nucleus Deep Brain Stimulation May Reduce Medication Costs in Early Stage Parkinson's Disease. *Journal of Parkinson's Disease*, 6(1):125–131.

[Hallett, 2014] Hallett, M. (2014). Tremor: Pathophysiology. *Parkinsonism & Related Disorders*, 20(SUPPL.1):S118–S122.

[Hamani et al., 2004] Hamani, C., Saint-Cyr, J. A., Fraser, J., Kaplitt, M., and Lozano, A. M. (2004). The subthalamic nucleus in the context of movement disorders. *Brain*, 127(1):4–20.

[Hardman et al., 2002] Hardman, C. D., Henderson, J. M., Finkelstein, D. I., Horne, M. K., Paxinos, G., and Halliday, G. M. (2002). Comparison of the basal ganglia in rats, marmosets, macaques, baboons, and humans: Volume and neuronal number for the output, internal relay, and striatal modulating nuclei. *Journal of Comparative Neurology*, 445(3):238–255.

[Hariz, 2017] Hariz, M. (2017). My 25 stimulating years with DBS in Parkinson's disease. *Journal of Parkinson's Disease*, 7:S33–S41.

[Hariz and Blomstedt, 2017] Hariz, M. and Blomstedt, P. (2017). Surgical Management of Tremor. In *Youmans and Winn Neurological Surgery*, chapter 87, pages 602–609. Elsevier Inc., 7th editio edition.

[Hariz et al., 2000] Hariz, M. I., Johansson, F., Shamsgovara, P., Johansson, E., Hariz, G. M., and Fagerlund, M. (2000). Bilateral subthalamic nucleus stimulation in a parkinsonian patient with preoperative deficits in speech and cognition: Persistent improvement in mobility but increased dependency: A case study. *Movement Disorders*, 15(1):136–139.

[Hawrylycz et al., 2012] Hawrylycz, M. J., Lein, E. S., Guillozet-Bongaarts, A. L., Shen, E. H., Ng, L., Miller, J. A., van de Lagemaat, L. N., Smith, K. A., Ebbert, A., Riley, Z. L., Abajian, C., Beckmann, C. F., Bernard, A., Bertagnolli, D., Boe, A. F., Cartagena, P. M., Chakravarty, M. M., Chapin, M., Chong, J., Dalley, R. A., Daly, B. D. D., Dang, C., Datta, S., Dee, N., Dolbeare, T. A., Faber, V., Feng, D., Fowler, D. R., Goldy, J., Gregor, B. W., Haradon, Z., Haynor, D. R., Hohmann, J. G., Horvath, S., Howard, R. E., Jeromin, A., Jochim, J. M., Kinnunen, M., Lau, C., Lazarz, E. T., Lee, C., Lemon, T. A., Li, L., Li, Y., Morris, J. A., Overly, C. C., Parker, P. D., Parry, S. E., Reding, M., Royall, J. J., Schulkin, J., Sequeira, P. A. A., Slaughterbeck, C. R., Smith, S. C., Sodt, A. J., Sunkin, S. M., Swanson, B. E., Vawter, M. P., Williams, D., Wohnoutka, P., Zielke, H. R., Geschwind, D. H., Hof, P. R., Smith, S. M., Koch, C., Grant, S. G., and Jones, A. R. (2012). An anatomically comprehensive atlas of the adult human brain transcriptome. *Nature*, 489(7416):391–399.

[Hellier et al., 2003] Hellier, P., Barillot, C., Corouge, I., Gibaud, B., Le Goualher, G., Collins, D., Evans, A., Malandain, G., Ayache, N., Christensen, G., and Johnson, H. (2003). Retrospective evaluation of intersubject brain registration. *IEEE Transactions on Medical Imaging*, 22(9):1120–1130.

[Henderson et al., 2004] Henderson, J. M., Holloway, K. L., Gaede, S. E., and Rosenow, J. M. (2004). The application accuracy of a skull-mounted trajectory guide system for image-guided functional neurosurgery. *Computer aided surgery : official journal of the International Society for Computer Aided Surgery*, 9(4):155–160.

[Herrington et al., 2016] Herrington, T. M., Cheng, J. J., and Eskandar, E. N. (2016). Mechanisms of deep brain stimulation. *Journal of Neurophysiology*, 115(1):19–38.

[Herron et al., 2016] Herron, J. A., Thompson, M. C., Brown, T., Chizeck, H. J., Ojemann, J. G., and Ko, A. L. (2016). Chronic electrocorticography for sensing movement intention and closed-loop deep brain stimulation with wearable sensors in an essential tremor patient. *Journal of Neurosurgery*, pages 1–8.

[Ho et al., 2017] Ho, A. L., Ali, R., Connolly, I. D., Henderson, J. M., Dhall, R., Stein, S. C., and Halpern, C. H. (2017). Awake versus asleep deep brain stimulation for Parkinson's disease: a critical comparison and meta-analysis. *Journal of Neurology, Neurosurgery & Psychiatry*, pages jnnp–2016–314500.

[Holmes et al., 1998] Holmes, C. J., Hoge, R., Collins, L., Woods, R., Toga, A. W. A., and Evans, A. C. A. (1998). Enhancement of MR Images Using Registration for Signal Averaging. *Journal of Computer Assisted Tomography*, 22(2):324–333.

[Horn et al., 2017a] Horn, A., Kühn, A. A., Merkl, A., Shih, L., Alterman, R., and Fox, M. (2017a). Probabilistic conversion of neurosurgical DBS electrode coordinates into MNI space. *NeuroImage*.

[Horn et al., 2017b] Horn, A., Neumann, W.-J., Degen, K., Schneider, G.-H., and Kühn, A. A. (2017b). Toward an electrophysiological "sweet spot" for deep brain stimulation in the subthalamic nucleus. *Human Brain Mapping*, 38(7).

[Horn et al., 2017c] Horn, A., Reich, M., Vorwerk, J., Li, N., Wenzel, G., Fang, Q., Schmitz-Hübsch, T., Nickl, R., Kupsch, A., Volkmann, J., Kühn, A. A., and Fox, M. D. (2017c). Connectivity Predicts deep brain stimulation outcome in Parkinson disease. *Annals of Neurology*, 82(1):67–78.

[Horsley and Clarke, 1908] Horsley, V. and Clarke, R. H. (1908). The structure and functions of the cerebellum examined by a new method. *Brain*, 31(1):45–124.

[Houdart et al., 1966] Houdart, R., Cophignon, J., and Dondey, M. (1966). Comparaison des effets de lésions stéréotaxiques limitées thalamiques et sous-thalamiques. *Stereotactic and Functional Neurosurgery*, 27(1-3):246–250.

[Houshmand et al., 2014] Houshmand, L., Cummings, K. S., Chou, K. L., and Patil, P. G. (2014). Evaluating indirect subthalamic nucleus targeting with validated 3-tesla magnetic resonance imaging. *Stereotactic and Functional Neurosurgery*, 92(6):337–345.

[Hua and Lenz, 2005] Hua, S. E. and Lenz, F. A. (2005). Posture-Related Oscillations in Human Cerebellar Thalamus in Essential Tremor Are Enabled by Voluntary Motor Circuits. *Journal of Neurophysiology*, 93(1):117–127.

[Hyam et al., 2015] Hyam, J. A., Akram, H., Foltynie, T., Limousin, P., Hariz, M., and Zrinzo, L. (2015). What you see is what you get: Lead location within deep brain structures is accurately depicted by stereotactic magnetic resonance imaging. *Clinical Neurosurgery*, 11(3):412–419.

[Jezzard and Balaban, 1995] Jezzard, P. and Balaban, R. S. (1995). Correction for Geometric Distortion in Echo-Planar Images from B0 Field Variations. *Magnetic Resonance in Medicine*, 34(1):65–73.

[Johansen-Berg et al., 2008] Johansen-Berg, H., Gutman, D., Behrens, T., Matthews, P., Rushworth, M., Katz, E., Lozano, A., and Mayberg, H. (2008). Anatomical connectivity of the subgenual cingulate region targeted with deep brain stimulation for treatment-resistant depression. *Cerebral cortex (New York, N.Y. : 1991)*, 18(6):1374–1383.

[Jovicich et al., 2006] Jovicich, J., Czanner, S., Greve, D., Haley, E., van der Kouwe, A., Gollub, R., Kennedy, D., Schmitt, F., Brown, G., Macfall, J., Fischl, B., and Dale, A. (2006). Reliability in multi-site structural MRI studies: effects of gradient non-linearity correction on phantom and human data. *NeuroImage*, 30(2):436–443.

[Kandel and Shchavinskii, 1973] Kandel, E. I. and Shchavinskii, Y. V. (1973). First stereotaxic apparatus created by Russian scientists in the 19th century. *Biomedical Engineering*, 7(2):121–124.

[Kelly et al., 1986] Kelly, P. J., Kall, B. a., Goerss, S., and Earnest, F. (1986). Computer-assisted stereotaxic laser resection of intra-axial brain neoplasms. *Journal of neurosurgery*, 64(3):427–439.

[Kerl et al., 2013] Kerl, H. U., Gerigk, L., Brockmann, M. a., Huck, S., Al-Zghloul, M., Groden, C., Hauser, T., Nagel, A. M., and Nölte, I. S. (2013). Imaging for deep brain stimulation: The zona incerta at 7 Tesla. *World journal of radiology*, 5(1):5–16.

[Kerl et al., 2012] Kerl, H. U., Gerigk, L., Pechlivanis, I., Al-Zghloul, M., Groden, C., and Nölte, I. S. (2012). The subthalamic nucleus at 7.0 Tesla: evaluation of sequence and orientation for deep-brain stimulation. *Acta Neurochirurgica*, 154(11):2051–2062.

[Keuken et al., 2017] Keuken, M. C., Bazin, P.-L., Backhouse, K., Beekhuizen, S., Himmer, L., Kandola, A., Lafeber, J. J., Prochazkova, L., Trutti, A., Schäfer, A., Turner, R., and Forstmann, B. U. (2017). Effects of aging on T1, T2, and QSM MRI values in the subcortex. *Brain Structure and Function*, 58(12):7250–7.

[Keuken et al., 2013] Keuken, M. C., Bazin, P.-L., Schafer, A., Neumann, J., Turner, R., and Forstmann, B. U. (2013). Ultra-High 7T MRI of Structural Age-Related Changes of the Subthalamic Nucleus. *Journal of Neuroscience*, 33(11):4896–4900.

[Kiss et al., 2002] Kiss, Z. H. T., Mooney, D. M., Renaud, L., and Hu, B. (2002). Neuronal response to local electrical stimulation in rat thalamus: physiological implications for mechanisms of deep brain stimulation. *Neuroscience*, 113(1):137–43.

[Klein et al., 2009] Klein, A., Andersson, J., Ardekani, B. A., Ashburner, J., Avants, B., Chiang, M.-C., Christensen, G. E., Collins, D. L., Gee, J., and Hellier, P. (2009). Evaluation of 14 nonlinear deformation algorithms applied to human brain MRI registration. *NeuroImage*, 46(3):786–802.

[Krack et al., 2002] Krack, P., Fraix, V., Mendes, A., Benabid, A.-L., and Pollak, P. (2002). Postoperative management of subthalamic nucleus stimulation for Parkinson's disease. *Movement disorders : official journal of the Movement Disorder Society*, 17 Suppl 3:S188–S197.

[Krack et al., 1999] Krack, P., Pollak, P., Limousin, P., Benazzouz, A., Deuschl, G., and Benabid, A. L. (1999). From off-period dystonia to peak-dose chorea. The clinical spectrum of varying subthalamic nucleus activity. *Brain*, 122(6):1133–1146.

[Kuhn et al., 2008] Kuhn, A. A., Kempf, F., Brucke, C., Gaynor Doyle, L., Martinez-Torres, I., Pogosyan, A., Trottenberg, T., Kupsch, A., Schneider, G.-H., Hariz, M. I., Vandenberghe, W., Nuttin, B., and Brown, P. (2008). High-Frequency Stimulation of the Subthalamic Nucleus Suppresses Oscillatory Activity in Patients with Parkinson's Disease in Parallel with Improvement in Motor Performance. *Journal of Neuroscience*, 28(24):6165–6173.

[Kwon et al., 2012] Kwon, D.-H., Kim, J.-M., Oh, S.-H., Jeong, H.-J., Park, S.-Y., Oh, E.-S., Chi, J.-G., Kim, Y.-B., Jeon, B. S., and Cho, Z.-H. (2012). Seven-tesla magnetic resonance images of the substantia nigra in Parkinson disease. *Annals of Neurology*, 71(2):267–277.

[Laitinen et al., 1992] Laitinen, L. V., Bergenheim, A. T., and Hariz, M. I. (1992). Leksell's posteroventral pallidotomy in the treatment of Parkinson's disease. *Journal of Neurosurgery*, 76(1):53–61.

[Lambert et al., 2012] Lambert, C., Zrinzo, L., Nagy, Z., Lutti, A., Hariz, M., Foltynie, T., Draganski, B., Ashburner, J., and Frackowiak, R. (2012). Confirmation of functional zones within the human subthalamic nucleus: Patterns of connectivity and sub-parcellation using diffusion weighted imaging. *NeuroImage*, 60(1):83–94.

[Langlois et al., 1999] Langlois, S., Desvignes, M., Constans, J. M., and Revenu, M. (1999). MRI geometric distortion: A simple approach to correcting the effects of non-linear gradient fields. *Journal of Magnetic Resonance Imaging*, 9(6):821–831.

[Lau et al., 2018a] Lau, J. C., Khan, A. R., Zeng, T. Y., MacDougall, K. W., Parrent, A. G., and Peters, T. M. (2018a). Quantification of local geometric distortion in structural magnetic resonance images: Application to ultra-high fields. *NeuroImage*, 168:141–151.

[Lau et al., 2018b] Lau, J. C., Kosteniuk, S. E., Macdonald, D. R., and Megyesi, J. F. (2018b). Image-guided Ommaya reservoir insertion for intraventricular chemotherapy: a retrospective series. *Acta Neurochirurgica*, 160(3):539–544.

[Lau et al., 2019] Lau, J. C., Kosteniuk, S. E., Walker, T., Iansavichene, A., Macdonald, D. R., and Megyesi, J. F. (2019). Operative complications with and without image guidance: A systematic review and meta-analysis of the Ommaya reservoir literature. *World Neurosurgery*, 122:404–414.

[Lau et al., 2017] Lau, J. C., MacDougall, K. W., Arango, M. F., Peters, T. M., Parrent, A. G., and Khan, A. R. (2017). Ultra-High Field Template-Assisted Target Selection for Deep Brain Stimulation Surgery. *World Neurosurgery*, 103:531–537.

[Lauterbur, 1973] Lauterbur, P. C. (1973). Image Formation by Induced Local Interactions: Examples Employing Nuclear Magnetic Resonance. *Nature*, 242(5394):190–191.

[Lees et al., 1977] Lees, A. J., Shaw, K. M., and Stern, G. M. (1977). ”Off period” dystonia and ”on period” choreoathetosis in levodopa-treated patients with Parkinson’s disease. *Lancet*, 2(8046):1034.

[Leksell, 1949] Leksell, L. (1949). A stereotaxic apparatus for intracerebral surgery. *Acta Chirurgica Scandinavica*, 99(3):229–233.

[LeWitt et al., 2011] LeWitt, P. A., Rezai, A. R., Leehey, M. A., Ojemann, S. G., Flaherty, A. W., Eskandar, E. N., Kostyk, S. K., Thomas, K., Sarkar, A., Siddiqui, M. S., Tatter, S. B., Schwalb, J. M., Poston, K. L., Henderson, J. M., Kurlan, R. M., Richard, I. H., Van Meter, L., Sapan, C. V., During, M. J., Kaplitt, M. G., and Feigin, A. (2011). AAV2-GAD gene therapy for advanced Parkinson’s disease: A double-blind, sham-surgery controlled, randomised trial. *The Lancet Neurology*, 10(4):309–319.

[Li et al., 2016] Li, X., Morgan, P. S., Ashburner, J., Smith, J., and Rorden, C. (2016). The first step for neuroimaging data analysis: DICOM to NIfTI conversion. *Journal of Neuroscience Methods*, 264:47–56.

[Limousin et al., 1995] Limousin, P., Pollak, P., Benazzouz, A., Hoffmann, D., Le Bas, J. F., Broussolle, E., Perret, J. E., and Benabid, a. L. (1995). Effect of parkinsonian signs and symptoms of bilateral subthalamic nucleus stimulation. *Lancet*, 345(0140-6736 (Print)):91–95.

[Littmann et al., 2006] Littmann, A., Guehring, J., Buechel, C., and Stiehl, H.-S. (2006). Acquisition-related morphological variability in structural MRI. *Academic radiology*, 13(9):1055–1061.

[Liu et al., 2015] Liu, J., Lee, H. J., Weitz, A. J., Fang, Z., Lin, P., Choy, M., Fisher, R., Pinskiy, V., Tolpygo, A., Mitra, P., Schiff, N., and Lee, J. H. (2015). Frequency-selective control of cortical and subcortical networks by central thalamus. *eLife*, (Cl):1–27.

[Llinás and Jahnsen, 1982] Llinás, R. and Jahnsen, H. (1982). Electrophysiology of mammalian thalamic neurones in vitro. *Nature*, 297(5865):406–408.

[Lozano et al., 2008] Lozano, A. M., Mayberg, H. S., Giacobbe, P., Hamani, C., Craddock, C. C., and Kennedy, S. H. (2008). Subcallosal cingulate gyrus deep brain stimulation for treatment-resistant depression. *Biological psychiatry*, 64(6):461–467.

[Lozano et al., 2018] Lozano, C. S., Ranjan, M., Boutet, A., Xu, D. S., Kucharczyk, W., Fasano, A., and Lozano, A. M. (2018). Imaging alone versus microelectrode recording–guided targeting of the STN in patients with Parkinson's disease. *Journal of Neurosurgery*, pages 1–6.

[Ma et al., 1997] Ma, T. P., Johnson, J. C., and Hoskins, G. A. (1997). Organization of the zona incerta in the macaque: An electron microscopic study. *Anatomical Record*, 249(2):259–275.

[Maciunas et al., 1994] Maciunas, R. J., Galloway, R. L., and Latimer, J. W. (1994). The application accuracy of stereotactic frames. *Neurosurgery*, 35(4):682–685.

[Mai et al., 2015] Mai, J., Majtanik, M., and Paxinos, G. (2015). *Atlas of the Human Brain*. Elsevier, 4th edition.

[Maier-Hein et al., 2017] Maier-Hein, K. H., Neher, P. F., Houde, J.-C., Côté, M.-A., Garyfallidis, E., Zhong, J., Chamberland, M., Yeh, F.-C., Lin, Y.-C., Ji, Q., Reddick, W. E., Glass, J. O., Chen, D. Q., Feng, Y., Gao, C., Wu, Y., Ma, J., Renjie, H., Li, Q., Westin, C.-F., Deslauriers-Gauthier, S., González, J. O. O., Paquette, M., St-Jean, S., Girard, G., Rheault, F., Sidhu, J., Tax, C. M. W., Guo, F., Mesri, H. Y., Dávid, S., Froeling, M., Heemskerk, A. M., Leemans, A., Boré, A., Pinsard, B., Bedetti, C., Desrosiers, M., Brambati, S., Doyon, J., Sarica, A., Vasta, R., Cerasa, A., Quattrone, A., Yeatman, J., Khan, A. R., Hodges, W., Alexander, S., Romascano, D., Barakovic, M., Auría, A., Esteban, O., Lemkaddem, A., Thiran, J.-P., Cetingul, H. E., Odry, B. L., Mailhe, B., Nadar, M. S., Pizzagalli, F., Prasad, G., Villalon-Reina, J. E., Galvis, J., Thompson, P. M., Requejo, F. D. S., Laguna, P. L., Lacerda, L. M., Barrett, R., Dell'Acqua, F., Catani, M., Petit, L., Caruyer, E., Daducci, A., Dyrby, T. B., Holland-Letz, T., Hilgetag, C. C., Stieltjes, B., and Descoteaux, M. (2017).

The challenge of mapping the human connectome based on diffusion tractography. *Nature Communications*, 8(1):1349.

[Mangin et al., 2015] Mangin, J. F., Auzias, G., Coulon, O., Sun, Z. Y., Rivière, D., and Régis, J. (2015). Sulci as Landmarks. *Brain Mapping: An Encyclopedic Reference*, 2(2015):45–52.

[Manjón et al., 2010] Manjón, J. V., Coupé, P., Martí-Bonmatí, L., Collins, D. L., and Robles, M. (2010). Adaptive non-local means denoising of MR images with spatially varying noise levels. *Journal of Magnetic Resonance Imaging*, 31(1):192–203.

[Mansfield, 1977] Mansfield, P. (1977). Multi-planar image formation using. *Journal of Physics C*, 10:55–58.

[Mansfield and Grannell, 1973] Mansfield, P. and Grannell, P. K. (1973). NMR 'diffraction' in solids? *Journal of Physics C: Solid State Physics*, 6.

[Marcus et al., 2010] Marcus, D. S., Fotenos, A. F., Csernansky, J. G., Morris, J. C., and Buckner, R. L. (2010). Open Access Series of Imaging Studies: Longitudinal MRI Data in Nondemented and Demented Older Adults. *Journal of Cognitive Neuroscience*, 22(12):2677–2684.

[Marques and Gruetter, 2013] Marques, J. P. and Gruetter, R. (2013). New Developments and Applications of the MP2RAGE Sequence - Focusing the Contrast and High Spatial Resolution R1 Mapping. *PLoS ONE*, 8(7):e69294.

[Marques et al., 2010] Marques, J. P., Kober, T., Krueger, G., van der Zwaag, W., Van de Moortele, P. F., and Gruetter, R. (2010). MP2RAGE, a self bias-field corrected sequence for improved segmentation and T1-mapping at high field. *NeuroImage*, 49(2):1271–1281.

[Marques and Norris, 2017] Marques, J. P. and Norris, D. G. (2017). How to choose the right MR sequence for your research question at 7 T and above? *NeuroImage*.

[Marsden and Parkes, 1976] Marsden, C. and Parkes, J. (1976). "On-Off" effects in patients with Parkinson's disease on chronic levodopa therapy. *The Lancet*, 307(7954):292–296.

[Masri et al., 2009] Masri, R., Quiton, R. L., Lucas, J. M., Murray, P. D., Thompson, S. M., and Keller, A. (2009). Zona Incerta: A Role in Central Pain. *Journal of Neurophysiology*, 102(1):181–191.

[McRobbie et al., 2003] McRobbie, D. W., Moore, E. A., Graves, M. J., and Prince, M. R. (2003). *MRI: From Picture to Proton*. Cambridge University Press.

[Meyers, 1951a] Meyers, R. (1951a). Dandy's striatal theory of "the center of consciousness"; surgical evidence and logical analysis indicating its improbability. *A.M.A. archives of neurology and psychiatry*, 65(6):659–71.

[Meyers, 1951b] Meyers, R. (1951b). Surgical experiments in the therapy of certain 'extrapyramidal' diseases: a current evaluation. *Acta psychiatrica et neurologica. Supplementum*, 67:1–42.

[Meyerson and Linderoth, 2009] Meyerson, B. and Linderoth, B. (2009). History of Stereotactic Neurosurgery in the Nordic Countries. In Gildenberg, P., Lozano, A., and Tasker, R., editors, *Textbook of Stereotactic and Functional Neurosurgery*. Springer-Verlag, Berlin, Heidelberg, 2nd edition.

[Miocinovic et al., 2006] Miocinovic, S., Parent, M., Butson, C. R., Hahn, P. J., Russo, G. S., Vitek, J. L., and McIntyre, C. C. (2006). Computational Analysis of Subthalamic Nucleus and Lenticular Fasciculus Activation During Therapeutic Deep Brain Stimulation. *Journal of Neurophysiology*, 96(3):1569–1580.

[Mitrofanis, 2005] Mitrofanis, J. (2005). Some certainty for the “zone of uncertainty”? Exploring the function of the zona incerta. *Neuroscience*, 130(1):1–15.

[Modat et al., 2010] Modat, M., Ridgway, G. R., Taylor, Z. A., Lehmann, M., Barnes, J., Hawkes, D. J., Fox, N. C., and Ourselin, S. (2010). Fast free-form deformation using graphics processing units. *Computer Methods and Programs in Biomedicine*, 98(3):278–284.

[Mohadjer et al., 1990] Mohadjer, M., Goerke, H., Milios, E., Etou, A., and Mundinger, F. (1990). Long-term results of stereotaxy in the treatment of essential tremor. *Stereotactic and Functional Neurosurgery*, 54-55(October 1989):125–129.

[Morel, 2007] Morel, A. (2007). *Stereotactic Atlas of the Human Thalamus and Basal Ganglia*. Informa Healthcare, New York.

[Morrell, 2011] Morrell, M. J. (2011). Responsive cortical stimulation for the treatment of medically intractable partial epilepsy. *Neurology*, 77(13):1295–1304.

[Mundinger, 1965] Mundinger, F. (1965). Stereotaxic Interventions on the Zona Incerta Area for Treatment of Extrapyramidal Motor Disturbances and their Results. *Stereotactic and Functional Neurosurgery*, 26(3-5):222–230.

[Narabayashi, 1986] Narabayashi, H. (1986). Tremor: its generating mechanism and treatment. *Handbook of Clinical Neurology*, 5(49):597–607.

[Narabayashi and Okuma, 1953] Narabayashi, H. and Okuma, T. (1953). Procaine-oil blocking of the globus pallidus for the treatment of rigidity and tremor of parkinsonism (preliminary report). *Proceedings of the Japan Academy*.

[Neumann et al., 2015] Neumann, J. O., Giese, H., Biller, A., Nagel, A. M., and Kiening, K. (2015). Spatial Distortion in MRI-Guided Stereotactic Procedures: Evaluation in 1.5-, 3- and 7-Tesla MRI Scanners. *Stereotactic and Functional Neurosurgery*, pages 380–386.

[Niemann and Van Nieuwenhofen, 1999] Niemann, K. and Van Nieuwenhofen, I. (1999). One atlas - three anatomies: Relationships of the Schaltenbrand and Wahren microscopic data. *Acta Neurochirurgica*, 141(10):1025–1038.

[Nieuwenhuys et al., 2007] Nieuwenhuys, R., Voogd, J., and van Huijzen, C. (2007). *The Human Central Nervous System*. Steinkopff, 4th edition.

[Nishimura, 1996] Nishimura, D. G. (1996). *Principles of magnetic resonance imaging*. Stanford University.

[Nowacki et al., 2018] Nowacki, A., Debove, I., Rossi, F., Schlaeppi, J. A., Petermann, K., Wiest, R., Schüpbach, M., and Pollo, C. (2018). Targeting the posterior subthalamic area for essential tremor: proposal for MRI-based anatomical landmarks. *Journal of Neurosurgery*, pages 1–8.

[Okun, 2012] Okun, M. S. (2012). Deep-Brain Stimulation for Parkinson's Disease. *New England Journal of Medicine*, 367(16):1529–1538.

[Ourselin et al., 2001] Ourselin, S., Roche, A., Subsol, G., Pennec, X., and Ayache, N. (2001). Reconstructing a 3D structure from serial histological sections. *Image and Vision Computing*, 19(1-2):25–31.

[Pahwa et al., 2001] Pahwa, R., Lyons, K. E., Wilkinson, S. B., Tröster, A. I., Overman, J., Kieltyka, J., and Koller, W. C. (2001). Comparison of thalamotomy to deep brain stimulation of the thalamus in essential tremor. *Movement Disorders*, 16(1):140–143.

[Pahwa et al., 1999] Pahwa, R., Lyons, K. L., Wilkinson, S. B., Carpenter, M. A., Troster, A. I., Searl, J. P., Overman, J., Pickering, S., and Koller, W. C. (1999). Bilateral thalamic stimulation for the treatment of essential tremor. *Neurology*, 53(7):1447–1447.

[Pallavaram et al., 2008] Pallavaram, S., Yu, H., Spooner, J., D'Haese, P., Bodenheimer, B., Konrad, P., and Dawant, B. M. (2008). Intersurgeon Variability in the Selection of Anterior and Posterior Commissures and Its Potential Effects on Target Localization. *Stereotactic and Functional Neurosurgery*, 86:113–119.

[Parkinson, 2002] Parkinson, J. (2002). An Essay on the Shaking Palsy (Originally published in 1817). *Journal of Neuropsychiatry*, 14(2):223–236.

[Perrot et al., 2011] Perrot, M., Rivière, D., and Mangin, J. F. (2011). Cortical sulci recognition and spatial normalization. *Medical Image Analysis*, 15(4):529–550.

[Peters, 2001] Peters, T. M. (2001). Image-guided surgery: From X-rays to Virtual Reality. *Computer Methods in Biomechanics and Biomedical Engineering*, 4(1):27–57.

[Peters, 2006] Peters, T. M. (2006). Image-guidance for surgical procedures. *Physics in medicine and biology*, 51(14):R505–40.

[Plaha et al., 2006] Plaha, P., Ben-Shlomo, Y., Patel, N. K., and Gill, S. S. (2006). Stimulation of the caudal zona incerta is superior to stimulation of the subthalamic nucleus in improving contralateral parkinsonism. *Brain*, 129(7):1732–1747.

[Plantinga et al., 2018] Plantinga, B. R., Temel, Y., Duchin, Y., Uludağ, K., Patriat, R., Roebroeck, A., Kuijf, M., Jahanshahi, A., ter Haar Romenij, B., Vitek, J., and Harel, N. (2018). Individualized parcellation of the subthalamic nucleus in patients with Parkinson's disease with 7T MRI. *NeuroImage*, 168(September):403–411.

[Poewe, 2009] Poewe, W. (2009). Treatments for Parkinson disease-past achievements and current clinical needs. *Neurology*, 72(7 SUPPL. 2):65–73.

[Pollak et al., 1993] Pollak, P., Benabid, A. L., Gross, C., Gao, D. M., Laurent, A., Benazzouz, A., Hoffmann, D., Gentil, M., and Perret, J. (1993). [Effects of the stimulation of the subthalamic nucleus in Parkinson disease]. *Revue neurologique*, 149(3):175–6.

[Power et al., 1999] Power, B. D., Kolmac, C. I., and Mitrofanis, J. (1999). Evidence for a large projection from the zona incerta to the dorsal thalamus. *Journal of Comparative Neurology*, 404(4):554–565.

[Power and Mitrofanis, 1999] Power, B. D. and Mitrofanis, J. (1999). Specificity of projection among cells of the zona incerta. *Journal of Neurocytology*, 28(6):481–493.

[Purcell et al., 1946] Purcell, E. M., Torrey, H. C., and Pound, R. V. (1946). Resonance Absorption by Nuclear Magnetic Moments in a Solid. *Physical Review*, 69(1-2):37–38.

[Raethjen and Deuschl, 2012] Raethjen, J. and Deuschl, G. (2012). The oscillating central network of essential tremor. *Clinical Neurophysiology*, 123(1):61–64.

[Rioux et al., 2016] Rioux, J. A., Levesque, I. R., and Rutt, B. K. (2016). Biexponential longitudinal relaxation in white matter: Characterization and impact on T1mapping with IR-FSE and MP2RAGE. *Magnetic Resonance in Medicine*, 75(6):2265–2277.

[Roentgen, 1895] Roentgen, W. (1895). Ueber eine neue Art von Strahlen. *Sitzungb d Würzburger Physik-Med Ges Jahrg*, page 132.

[Rolston et al., 2016] Rolston, J. D., Englot, D. J., Starr, P. A., and Larson, P. S. (2016). An unexpectedly high rate of revisions and removals in deep brain stimulation surgery: Analysis of multiple databases. *Parkinsonism & Related Disorders*, 33:10–15.

[Rooney et al., 2007] Rooney, W. D., Johnson, G., Li, X., Cohen, E. R., Kim, S. G., Ugurbil, K., and Springer, C. S. (2007). Magnetic field and tissue dependencies of human brain longitudinal 1H2O relaxation in vivo. *Magnetic Resonance in Medicine*, 57(2):308–318.

[Roth, 2016] Roth, B. L. (2016). DREADDs for Neuroscientists. *Neuron*, 89(4):683–694.

[Sankar and Lozano, 2011] Sankar, T. and Lozano, A. M. (2011). Magnetic Resonance Imaging Distortion in Functional Neurosurgery. *World Neurosurgery*, 75(1):29–31.

[Schäfer et al., 2012] Schäfer, A., Forstmann, B. U., Neumann, J., Wharton, S., Mietke, A., Bowtell, R., and Turner, R. (2012). Direct visualization of the subthalamic nucleus and its iron distribution using high-resolution susceptibility mapping. *Human Brain Mapping*, 33(12):2831–2842.

[Schaltenbrand and Wahren, 1977] Schaltenbrand, G. and Wahren, W. (1977). *Atlas for Stereotaxy of the Human Brain*. Thieme, 2 edition.

[Schuepbach et al., 2013] Schuepbach, W. M. M., Rau, J., Knudsen, K., Volkmann, J., Krack, P., Timmermann, L., Hälbig, T. D., Hesekamp, H., Navarro, S. M., Meier, N., Falk, D., Mehdorn, M., Paschen, S., Maarouf, M., Barbe, M. T., Fink, G. R., Kupsch, A., Gruber, D., Schneider, G.-H., Seigneuret, E., Kistner, A., Chaynes, P., Ory-Magne, F., Brefel Courbon, C., Vesper, J., Schnitzler, A., Wojtecki, L., Houeto, J.-L., Bataille, B., Maltête, D., Damier, P., Raoul, S., Sixel-Doering, F., Hellwig, D., Gharabaghi, A., Krüger, R., Pinsker, M. O., Amtage, F., Régis, J.-M., Witjas, T., Thobois, S., Mertens, P., Kloss, M., Hartmann, A., Oertel, W. H., Post, B., Speelman, H., Agid, Y., Schade-Brittinger, C., and Deuschl, G. (2013). Neurostimulation for Parkinson's disease with early motor complications. *The New England journal of medicine*, 368(7):610–22.

[Schuurman et al., 2000] Schuurman, P. R., Bosch, D. A., Bossuyt, P. M., Bonsel, G. J., van Someren, E. J., de Bie, R. M., Merkus, M. P., and Speelman, J. D. (2000). A Comparison of Continuous Thalamic Stimulation and Thalamotomy for Suppression of Severe Tremor. *New England Journal of Medicine*, 342(7):461–468.

[Seiger et al., 2015] Seiger, R., Hahn, A., Hummer, A., Kranz, G. S., Ganger, S., Kublbock, M., Kraus, C., Sladky, R., Kasper, S., Windischberger, C., and Lanzenberger, R. (2015). Voxel-based morphometry at ultra-high fields. A comparison of 7T and 3T MRI data. *NeuroImage*, 113:207–216.

[Shamir et al., 2011] Shamir, R. R., Joskowicz, L., Spektor, S., and Shoshan, Y. (2011). Target and trajectory clinical application accuracy in neuronavigation. *Neurosurgery*, 68(SUPPL. 1):95–102.

[Shields et al., 2007] Shields, D. C., Gorgulho, A., Behnke, E., Malkasian, D., and Desalles, A. A. F. (2007). Contralateral conjugate eye deviation during deep brain stimulation of the subthalamic nucleus. *Journal of Neurosurgery*, 107(1):37–42.

[Shimamoto et al., 2013] Shimamoto, S. a., Ryapolova-Webb, E. S., Ostrem, J. L., Galifianakis, N. B., Miller, K. J., and Starr, P. a. (2013). Subthalamic nucleus neurons are synchronized to primary motor cortex local field potentials in Parkinson's disease. *J Neurosci*, 33(17):7220–7233.

[Shin et al., 2007] Shin, D. S., Samoilova, M., Cotic, M., Zhang, L., Brotchie, J. M., and Carlen, P. L. (2007). High frequency stimulation or elevated K+ depresses neuronal activity in the rat entopeduncular nucleus. *Neuroscience*, 149(1):68–86.

[Shoulson et al., 1975] Shoulson, I., Glaubiger, G. A., and Chase, T. N. (1975). On-off response: Clinical and biochemical correlations during oral and intravenous levodopa administration in parkinsonian patients. *Neurology*, 25(12):1144–1144.

[Sled et al., 1998] Sled, J. G., Zijdenbos, A. P., and Evans, A. C. (1998). A nonparametric method for automatic correction of intensity nonuniformity in MRI data. *IEEE transactions on medical imaging*, 17(1):87–97.

[Smith, 2002] Smith, S. M. (2002). Fast robust automated brain extraction. *Hum. Brain Mapp.*, 17(3):143–155.

[Spiegel et al., 1962] Spiegel, E., Wycis, H., Szekely, E., Baird, H., Adams III, J., and Flanagan, M. (1962). Campotomy. *Trans Am Neurol Assoc*, 87:240–242.

[Spiegel et al., 1964] Spiegel, E., Wycis, H., Szekely, E., Soloff, L., Adams, J., Gildenberg, P., and Zanes, C. (1964). Stimulation of Forel's field during stereotaxic operations in the human brain. *Electroencephalography and Clinical Neurophysiology*, 16(6):537–548.

[Spiegel and Wycis, 1954] Spiegel, E. A. and Wycis, H. T. (1954). Ansotomy in Paralysis Agitans. *Archives of Neurology And Psychiatry*, 71(5):598.

[Spiegel et al., 1947] Spiegel, E. A., Wycis, H. T., Marks, M., and Lee, A. J. (1947). Stereotaxic Apparatus for Operations on the Human Brain. *Science*, 106(2754):349–350.

[Stikov et al., 2015] Stikov, N., Boudreau, M., Levesque, I. R., Tardif, C. L., Barral, J. K., and Pike, G. B. (2015). On the accuracy of T1 mapping: Searching for common ground. *Magnetic Resonance in Medicine*, 73(2):514–522.

[Sudhyadhom et al., 2009] Sudhyadhom, A., Haq, I. U., Foote, K. D., Okun, M. S., and Bova, F. J. (2009). A high resolution and high contrast MRI for differentiation of subcortical structures for DBS targeting: The Fast Gray Matter Acquisition T1 Inversion Recovery (FGATIR). *NeuroImage*, 47(SUPPL. 2):T44–T52.

[Sumanaweera et al., 1994a] Sumanaweera, T., Glover, G., Song, S., Adler, J., and Napel, S. (1994a). Quantifying MRI geometric distortion in tissue. *Magnetic Resonance in Medicine*, 31(1):40–47.

[Sumanaweera et al., 1994b] Sumanaweera, T. S., Adler, J. R., Napel, S., and Glover, G. H. (1994b). Characterization of spatial distortion in magnetic resonance imaging and its implications for stereotactic surgery. *Neurosurgery*, 35(4):696–703; discussion 703–4.

[Svennilson et al., 1960] Svennilson, E., Torvik, A., Lowe, R., and Leksell, L. (1960). Treatment of Parkinsonism by stereotactic thermolesions in the pallidal region. A clinical evaluation of 81 cases. *Acta Psychiatrica Scandinavica*, 35(3):358–377.

[Talairach et al., 1957] Talairach, J., David, M., Tournoux, P., Corredor, H., and Kvasina, T. (1957). *Atlas d'anatomie stéréotaxique. Repérage radiologique indirect des noyaux gris centraux des régions mésencephalosousoptique et hypothalamique de l'homme.* Masson & Cie, Paris, France.

[Talairach and Tournoux, 1988] Talairach, J. and Tournoux, P. (1988). *Co-planar stereotaxic atlas of the human brain*. Thieme, New York, 1 edition.

[Tardif et al., 2010] Tardif, C. L., Collins, D. L., and Pike, G. B. (2010). Regional impact of field strength on voxel-based morphometry results. *Human Brain Mapping*, 31(7):943–957.

[Tardif et al., 2015] Tardif, C. L., Schäfer, A., Waehnert, M., Dinse, J., Turner, R., and Bazin, P.-L. (2015). Multi-contrast multi-scale surface registration for improved alignment of cortical areas. *NeuroImage*, 111:107–122.

[Tasker et al., 1997] Tasker, R. R., Munz, M., Junn, F. S. C. K., Kiss, Z. H. T., Davis, K., Dostrovsky, J. O., and Lozano, A. M. (1997). Deep Brain Stimulation and Thalamotomy for Tremor Compared. In *Advances in Stereotactic and Functional Neurosurgery*, pages 49–53. Springer Vienna, Vienna.

[Thani et al., 2011] Thani, N. B., Bala, A., Swann, G. B., and Lind, C. R. P. (2011). Accuracy of postoperative computed tomography and magnetic resonance image fusion for assessing deep brain stimulation electrodes. *Neurosurgery*, 69(1):207–214.

[The Deep-Brain Stimulation for Parkinson's Disease Study Group, 2001] The Deep-Brain Stimulation for Parkinson's Disease Study Group (2001). Deep-Brain Stimulation of the Subthalamic Nucleus or the Pars Interna of the Globus Pallidus in Parkinson's Disease. *New England Journal of Medicine*, 345(13):956–963.

[Thompson et al., 1996] Thompson, P. M., Schwartz, C., Lin, R. T., Khan, A. A., and Toga, A. W. (1996). Three-dimensional statistical analysis of sulcal variability in the human brain. *The Journal of Neuroscience*, 16(13):4261–4274.

[Tomlinson et al., 2010] Tomlinson, C. L., Stowe, R., Patel, S., Rick, C., Gray, R., and Clarke, C. E. (2010). Systematic review of levodopa dose equivalency reporting in Parkinson's disease. *Movement Disorders*, 25(15):2649–2653.

[Tourdias et al., 2014] Tourdias, T., Saranathan, M., Levesque, I. R., Su, J., and Rutt, B. K. (2014). Visualization of intra-thalamic nuclei with optimized white-matter-nulled MPRAGE at 7T. *NeuroImage*, 84:534–545.

[Trampel et al., 2017] Trampel, R., Bazin, P.-L., Pine, K., and Weiskopf, N. (2017). In-vivo magnetic resonance imaging (MRI) of laminae in the human cortex. *NeuroImage*, (September):1–9.

[Tripoliti et al., 2008] Tripoliti, E., Zrinzo, L., Martinez-Torres, I., Tisch, S., Frost, E., Borrell, E., Hariz, M. I., and Limousin, P. (2008). Effects of contact location and voltage amplitude on speech and movement in bilateral subthalamic nucleus deep brain stimulation. *Movement Disorders*, 23(16):2377–2383.

[Truini et al., 2013] Truini, A., Garcia-Larrea, L., and Cruccu, G. (2013). Reappraising neuropathic pain in humans - How symptoms help disclose mechanisms. *Nature Reviews Neurology*, 9(10):572–582.

[Tustison et al., 2010] Tustison, N. J., Avants, B. B., Cook, P. A., Zheng, Y., Egan, A., Yushkevich, P. A., and Gee, J. C. (2010). N4ITK : Improved N3 Bias Correction. 29(6):1310–1320.

[Uğurbil, 2017] Uğurbil, K. (2017). Imaging at ultrahigh magnetic fields: History, challenges, and solutions. *NeuroImage*, (July):1–26.

[van der Kouwe et al., 2008] van der Kouwe, A. J. W., Benner, T., Salat, D. H., and Fischl, B. (2008). Brain morphometry with multiecho MPRAGE. *NeuroImage*, 40(2):559–569.

[Vanegas-Arroyave et al., 2016] Vanegas-Arroyave, N., Lauro, P. M., Huang, L., Hallett, M., Horovitz, S. G., Zaghloul, K. A., and Lungu, C. (2016). Tractography patterns of subthalamic nucleus deep brain stimulation. *Brain*, 139(4):1200–1210.

[Velasco et al., 2018] Velasco, F., Esqueda-Liquidano, M., Velasco, A. L., and García-Gomar, M. G. (2018). Prelemniscal Lesion for Selective Improvement of Parkinson Disease Tremor. *Stereotactic and Functional Neurosurgery*, 96(1):54–59.

[Velasco et al., 2001] Velasco, F., Jiménez, F., Pérez, M. L., Carrillo-Ruiz, J. D., Velasco, A. L., Ceballos, J., and Velasco, M. (2001). Electrical stimulation of the prelemniscal radiation in the treatment of Parkinson's disease: An old target revised with new techniques. *Neurosurgery*, 49(2):293–308.

[Velasco et al., 1975] Velasco, F., Velasco, M., and Machado, J. P. (1975). A Statistical Outline of the Subthalamic Target for the Arrest of Tremor. *Stereotactic and Functional Neurosurgery*, 38(1):38–46.

[Velasco et al., 1972] Velasco, F. C., Molina-Negro, P., Bertrand, C., and Hardy, J. (1972). Further definition of the subthalamic target for arrest of tremor. *Journal of neurosurgery*, 36(2):184–91.

[Wang et al., 2016] Wang, B. T., Poirier, S., Guo, T., Parrent, A. G., Peters, T. M., and Khan, A. R. (2016). Generation and evaluation of an ultra-high-field atlas with applications in DBS planning. In Styner, M. A. and Angelini, E. D., editors, *SPIE Medical Imaging*, volume 9784, page 97840H.

[Wang et al., 2005] Wang, J., Qiu, M., Yang, Q. X., Smith, M. B., and Constable, R. T. (2005). Measurement and correction of transmitter and receiver induced nonuniformities in vivo. *Magnetic Resonance in Medicine*, 53(2):408–417.

[Watanabe et al., 2006] Watanabe, Y., Lee, C. K., and Gerbi, B. J. (2006). Geometrical accuracy of a 3-tesla magnetic resonance imaging unit in Gamma Knife surgery. *Journal of neurosurgery*, 105 Suppl:190–3.

[Watson et al., 2014] Watson, C., Lind, C. R. P., and Thomas, M. G. (2014). The anatomy of the caudal zona incerta in rodents and primates. *Journal of Anatomy*, 224(2):95–107.

[Weiskopf et al., 2015] Weiskopf, N., Mohammadi, S., Lutti, A., and Callaghan, M. F. (2015). Advances in MRI-based computational neuroanatomy: from morphometry to in-vivo histology. *Current opinion in neurology*, 28(4):313–22.

[Weiskopf et al., 2013] Weiskopf, N., Suckling, J., Williams, G., Correia M., M. M., Inkster, B., Tait, R., Ooi, C., Bullmore T., E. T., and Lutti, A. (2013). Quantitative multi-parameter mapping of R1, PD*, MT, and R2* at 3T: A multi-center validation. *Frontiers in Neuroscience*, 7(7 JUN):1–11.

[Wertheimer et al., 1960] Wertheimer, P., Lapras, C., and Levy, A. (1960). Essais de chirurgie thalamique [Trials in thalamic surgery]. *Neuro-Chirurgie*, 6:105–12.

[Williams et al., 2010] Williams, A., Gill, S., Varma, T., Jenkinson, C., Quinn, N., Mitchell, R., Scott, R., Ives, N., Rick, C., Daniels, J., Patel, S., and Wheatley, K. (2010). Deep brain stimulation plus best medical therapy versus best medical therapy alone for advanced Parkinson's disease (PD SURG trial): a randomised, open-label trial. *The Lancet Neurology*, 9(6):581–591.

[Willie et al., 2014] Willie, J. T., Laxpati, N. G., Drane, D. L., Gowda, A., Appin, C., Hao, C., Brat, D. J., Helmers, S. L., Saindane, A., Nour, S. G., and Gross, R. E. (2014). Real-time magnetic resonance-guided stereotactic laser amygdalohippocampotomy for mesial temporal lobe epilepsy. *Neurosurgery*, 74(6):569–584.

[Xiao et al., 2017] Xiao, D., Vanni, M. P., Mitelut, C. C., Chan, A. W., LeDue, J. M., Xie, Y., Chen, A. C., Swindale, N. V., and Murphy, T. H. (2017). Mapping cortical mesoscopic networks of single spiking cortical or sub-cortical neurons. *eLife*, 6:e19976.

[Xiao et al., 2014] Xiao, Y., Fonov, V., Bériault, S., Subaie, F. A., Chakravarty, M. M., Sadikot, A. F., Pike, G. B., and Collins, D. L. (2014). Multi-contrast unbiased MRI atlas of a Parkinson's disease population. *International Journal of Computer Assisted Radiology and Surgery*, pages 329–341.

[Yarkoni et al., 2011] Yarkoni, T., Poldrack, R. A., Nichols, T. E., Van Essen, D. C., and Wager, T. D. (2011). Large-scale automated synthesis of human functional neuroimaging data. *Nature Methods*, 8(8):665–670.

[Zecca et al., 2004] Zecca, L., Stroppolo, A., Gatti, A., Tampellini, D., Toscani, M., Gallorini, M., Giaveri, G., Arosio, P., Santambrogio, P., Fariello, R. G., Karatekin, E., Kleinman, M. H., Turro, N., Hornykiewicz, O., and Zucca, F. A. (2004). The role of iron and copper molecules in the neuronal vulnerability of locus coeruleus and substantia nigra during aging. *Proceedings of the National Academy of Sciences*, 101(26):9843–9848.

[Zrinzo et al., 2012] Zrinzo, L., Foltynie, T., Limousin, P., and Hariz, M. I. (2012). Reducing hemorrhagic complications in functional neurosurgery: a large case series and systematic literature review. *Journal of neurosurgery*, 116(1):84–94.

Curriculum Vitae

Name

Jonathan C. Lau

Education and Degrees

Western University
London, Ontario, Canada
2017 - Present, PhD Candidate in Biomedical Engineering
2011 - Present, Resident in Neurosurgery

Queen's University
Kingston, Ontario, Canada
2007 - 2011, MD

Awards

Canadian Institutes of Health Research (CIHR) Frederick Banting and Charles Best Canada Graduate Scholarships Doctoral Award (2017-Present)

Canadian League Against Epilepsy, Mary Ann Lee Resident Research Prize (2018)

Department of Clinical Neurological Sciences, Resident Research Prize (2018)

Canadian League Against Epilepsy, Top Trainee Abstract Award (2017)

Department of Clinical Neurological Sciences, Resident Research Prize (2017)

Canadian Neurological Sciences Federation Congress, Best Resident Poster (2016)

Recent Manuscripts

(* - co-directed with Dr. Joseph Megyesi)

1. **Lau JC**, Parrent AG, Xiao Y, Demarco J, MacDougall KW, Cruckley C, Peters TM, Khan AR. Direct visualization and characterization of the human zona incerta and surrounding fiber tracts. In preparation.

2. **Lau JC**, Parrent AG, Demarco J, Ferko K, Gupta G, Khan AR, Peters TM. A framework for evaluating correspondence between brain images using anatomical fiducials. Human Brain Mapping. Under review.

3. DeKraker J, Ferko K, **Lau JC**, Kohler S, Khan AR. Hippocampal morphology and cytoarchitecture in 3D BigBrain histology. Cerebral Cortex. Submitted.

4. Gui C, **Lau JC***, Kosteniuk SE, Lee DH, Megyesi JF. Radiology reporting of low-grade glioma growth underestimates tumor expansion. Acta Neurochirurgica. Accepted.

5. **Lau JC**, Kosteniuk SE, Walker T, Iansavitchene A, Macdonald DR, Megyesi JF. Operative complications with and without image-guidance: systematic review and meta-analysis of the Ommaya reservoir literature. World Neurosurgery. 2019. 122:404-414.

6. Santyr BG, **Lau JC**, Mirsattari SM, Burneo JG, de Ribaupierre S, Steven DA, Parrent AG, MacDougall KW, Khan AR. Novel connectivity map normalization procedure for improved quantitative investigation of structural thalamic connectivity in temporal lobe epilepsy patients. Journal of Magnetic Resonance Imaging. 2018. 48:1529-1539.

7. Kosteniuk SE, **Lau JC***, Megyesi JF. The Impact of Functional Magnetic Resonance Imaging on Clinical Outcomes in a Propensity-Matched Low-Grade Glioma Cohort. World Neurosurgery. 2018. 120:1143-1148.

8. **Lau JC**, Khan AR, MacDougall KW, Parrent AG, Peters TM. Quantification of local geometric distortion in structural magnetic resonance images: application to ultra-high fields. NeuroImage. Special Issue: Neuroimaging with Ultra-High Field MRI: Present and Future. 2018. 168:141-151.

9. Gui C, Kosteniuk SE, **Lau JC***, Megyesi JF. Tumor growth dynamics in serially-imaged low-grade glioma patients. Journal of Neuro-Oncology. 2018. 139:167-175.

10. **Lau JC**, Kosteniuk SE, Macdonald DR, Megyesi JF. Image-guided Ommaya reservoir insertion for intraventricular chemotherapy. Acta Neurochirurgica. 2018. 160:539-544.

11. DeKraker J, Ferko K, **Lau JC**, Kohler S, Khan AR. Unfolding the hippocampus: applications in subfield segmentation and standardization. NeuroImage. 2018. 167:408-418.

12. **Lau JC**, MacDougall K, Peters TM, Parrent AG, Khan AR. Ultra-high field MRI template-assisted target selection for deep brain stimulation surgery. World Neurosurgery. 2017. 103:531-537.

13. Santyr BG, Goubran M, **Lau JC**, Kwan B, Salehi F, Lee DH, Mirsattari SM, Burneo JG, Steven DA, Parrent AG, de Ribaupierre S, Hammond RR, Peters TM, Khan AR. Investigation of hippocampal sub-structures in focal temporal lobe epilepsy with and without hippocampal sclerosis at 7T. Journal of Magnetic Resonance Imaging. 2017. 45(5):1359-1370.

14. **Lau JC**, Kosteniuk SE, Bihari F, Megyesi JF. Functional magnetic resonance imaging for preoperative planning in brain tumour surgery. Canadian Journal of Neurological Sciences. 2017. 44:59-68.